



Faculteit Wetenschappen
Departement Fysica

Vortex-antivortex molecules in mesoscopic quantum systems

Vortex-antivortex moleculen in mesoscopische kwantumsystemen

Proefschrift voorgelegd tot het behalen van de graad van

doctor in de wetenschappen

aan de Universiteit Antwerpen, te verdedigen door

Roeland GEURTS

Promotoren

Prof. dr. Milorad Milošević

Prof. dr. François Peeters

Antwerpen, 2011



Acknowledgments

In the first place I would like to thank my promoters Milorad and François for giving me the opportunity to prepare my PhD thesis in the CMT group. Due to their professional guidance and uncountable suggestions, this work has become what it is, something to be proud of.

Our group is a very international one and I am grateful for the experience to work with people from all over the world. I want to thank all my colleagues for the nice atmosphere at (and occasionally after!) work.

A big thank you also goes out to the guys with whom I daily had lunch. I really enjoyed the chats, the card games, the drinks after work, and the sporting activities! Also the support of my friends and family was an indispensable ingredient of the successful completion of my research. Thank you all!

The final remark is dedicated to my girlfriend An, who withstood my sometimes unbearable moods without any problem. You're amazing!

Contents

1	Introduction	1
1.1	Historical overview	3
1.1.1	London theory	7
1.1.2	Ginzburg-Landau theory	9
1.1.3	BCS theory	13
1.2	Types of superconductors	15
1.3	Vortices	18
1.4	Mesoscopic superconductors	22
1.5	Two-band superconductors	25
1.5.1	Interband coupling	26
1.5.2	Non-composite and fractional vortices	26
1.5.3	Type 1.5 superconductors	28
1.6	Probing the superconducting state	28
1.7	Ginzburg-Landau Theory	30
1.7.1	Energy functional	31
1.7.2	Derivation of GL equations	32
1.8	Methodology	36
1.8.1	Solving the first GL equation	37
1.8.2	Solving the second GL equation	39
1.8.3	Self-consistent solution	44
1.9	Bose-Einstein condensation	45
1.9.1	Theoretical description	47
1.9.2	Rotating BEC	50
1.9.3	Numerical method	51
2	V-Av molecules in mesoscopic single-gap superconductors	55
2.1	Symmetry induced V-Av state at T_c	58
2.1.1	Linear GL theory	58
2.1.2	Engineering of the artificial pinning sites	59
2.1.3	Influence of imperfections/defects	62

2.1.4	Competing symmetries	66
2.2	Symmetry induced V-Av for $T < T_c$	69
2.2.1	Full GL theory	69
2.2.2	Phase diagram	71
2.2.3	Influence of defects and imperfections	75
2.2.4	How to detect the vortex-antivortex state?	76
2.3	Molecular dynamics model	78
2.4	Second-generation V-Av state	80
2.5	Conclusions	86
3	Vortex matter in two-gap superconductors	89
3.1	Introduction	89
3.2	Josephson coupling	91
3.2.1	Theoretical formalism	91
3.2.2	Size of the vortex core	93
3.2.3	H-T phase diagrams	101
3.3	Magnetic coupling	108
3.3.1	Magnetic vs. Josephson coupling	110
3.3.2	Magnetization curves	113
3.3.3	Type-1.x vortex states	115
3.4	Conclusions	118
4	Enhanced stability of the vortex-antivortex molecule in two-gap mesoscopic superconductors	119
4.1	Theoretical formalism and sample parameters	120
4.2	Stability region of the V-Av state	121
4.3	Fractional antivortex states	124
4.4	Other conditions for enhanced V-Av state	125
4.5	Discussion on the validity of the two-gap GL formalism	126
4.6	Lawrence-Doniach model	128
4.6.1	Critical temperature	130
4.7	Conclusions	130
Appendix		133
	GL equations for two-gap superconductors using microscopic parameters .	133
5	Topologically trapped vortex molecules in Bose-Einstein condensates	143
5.1	Vortex-antivortex molecules as the ground state	145
5.2	Novel phase transitions	147
5.3	Stability and control of special vortex states	150
5.4	Conclusions	151

CONTENTS

Summary	153
Outlook	159
Samenvatting	161
Curriculum vitae	167
Bibliography	169

Chapter 1

Introduction

100 years have passed since the discovery of superconductivity. Whether this calls for celebration is somewhat questionable. While certainly progress is made, superconductors still have not found widespread usage in society. Nevertheless some applications exist: the most important one being the generation of ultrahigh magnetic fields, used for medical imaging techniques such as magnetic resonance imaging (MRI) now available in many hospitals over the world, or for the fundamental high-energy physics research carried out e.g. at CERN.

The ability of superconductors to transport electrical energy without dissipation was always expected to unleash a technological revolution, with an impact comparable to the one of the invention of the transistor. However, to date this has not happened, the main reason being that superconductors only superconduct when cooled to at least some hundred degrees Celsius below zero. The extra cost of the required cryogenic equipment currently can not compete with the readily available technology. In this respect, the excitement 25 years ago, generated by the discovery of the first high- T_c superconductor working at liquid nitrogen temperatures, is no wonder. To date, scientists remain in the dark concerning the exact mechanism behind superconductivity in these materials. The unraveling of this mystery could be the key to designing room-temperature superconductors. It is clear that a lot of work still has to be done, both experimentally and theoretically.

In the meantime, the ever ongoing process of downsizing and increasing the speed of digital electronic circuits, which are currently based on semiconductor technology, is reaching a physical limit. Instead, manufacturers of microchips currently focus on parallel architectures. The most reliable technology to succeed the semiconductor era is based on rapid single flux quantum (RSFQ) logic. There Josephson junctions (weakly coupled superconductors) are the active elements, like transistors are the active elements in semiconductor electronics. The power consumption is two orders of magnitude smaller, and speeds of several hundred GHz are easily attainable.

The 0's and 1's in this architecture are represented by the presence or the absence of a flux quantum inside the device. Such a flux quantum manifests itself as a microscopic whirlpool of electrons, called a *vortex* and it is the main physical object studied in this thesis.

RSFQ logic is still in its infancy and a lot of work remains to be done. In any case, a profound understanding of the behavior of vortices in nanoscale systems will be essential. To date, the theory which is best capable of describing these systems is the Ginzburg-Landau theory. In this thesis I will mainly discuss the behavior of vortices caused by the geometry of the system. A remarkable phenomenon is for instance the appearance of antivortices: vortices turning in the opposite direction and thus carrying opposite flux. When a vortex and an antivortex encounter each other, they annihilate each other.

Quantized vortices are a manifestation of the quantum properties of an electronic condensate in a material. They also appear in superfluids and in Bose-Einstein condensates. The latter system is a gas of identical particles which below a certain critical temperature start behaving collectively as a giant quantum mechanical matter wave. Multiquanta vortices and antivortices in this system are also studied in this thesis, providing evidence that such vortex states are of fundamental nature in mesoscopic quantum systems.

In 2001, superconductivity was discovered in the simple compound MgB_2 with an unusual high critical temperature. Soon after MgB_2 was shown to be the first unambiguously known two-band superconductor, simply put two-superconductors-in-one. The 50-year old paradigm of flux quantization in superconductors has to be revisited for two-band materials, at least in the case of mesoscopic systems, as will be shown in this thesis. This is also relevant to a number of other multiband superconductors, including recently discovered iron pnictides.

In this thesis, **Chapter 1** provides a broad overview starting with the history of superconductivity. Next, a general introduction to basic concepts of superconductivity is given; in order of appearance, type-I/II superconductivity, vortex matter and mesoscopic effects are discussed. Also the theoretical framework within the thesis is described in depth, and the methodology is outlined. Finally an introduction to Bose-Einstein condensation, a quantum state of matter exhibiting behavior in many aspects analogous to superconductors, is given.

In **Chapter 2**, the results of the investigation of vortex-antivortex molecules in mesoscopic single-gap superconductors is presented. The discussion starts by describing the situation at the critical temperature, where the influence of geometry is dominant, and a vortex-antivortex pair may be nucleated as a consequence of the discrete symmetry of the superconducting sample. I show how the inclusion of holes into the sample can lead to enhanced properties of the vortex-antivortex molecule. Both square and disk shaped samples are taken into account in this study. In the next step, the situation deeper in the superconducting state, i.e.

further from the critical temperature, is considered. Here the non-linearity of the equations describing superconductivity comes into play, together with the influence of the magnetic field generated by the superconductor. In this part, I also describe the effect of defects in and imperfections of the sample. Then we present a simple classical model, exhibiting behavior analogous to the vortex-antivortex state, which we simulated using molecular dynamics. Finally, a second-generation vortex-antivortex molecule is discussed which can exist in the strategically perforated superconducting samples, but is of completely different origin from the symmetry-induced vortex-antivortex molecule.

Chapter 3 presents our study of general properties of two-gap mesoscopic superconductors. Peculiar effects of the coupling between the two bands are presented, including the influence of coupling on the coherence length, mushroom shaped H-T stability regions, and fractional and asymmetric vortex states. The magnetic coupling is also considered and we present our findings concerning ‘mixed’-type superconductors.

In **Chapter 4**, the vortex-antivortex molecule in two-gap mesoscopic superconductors is studied. The main conclusion is that the temperature stability interval can be considerably enhanced in two-gap superconductors due to the interband coupling. The theoretical formalism is updated, to a version including microscopic parameters. The validity of this theory is discussed, and another system, a superconducting bilayer, is proposed as an alternative system in which the same phenomenology should occur.

The subject of **Chapter 5** are vortex-antivortex molecules in Bose-Einstein condensates. We show that the idea of adding holes to a superconductor to stabilize the vortex-antivortex has an analogue in Bose-Einstein condensates where pinning can be induced optically by laser beams. We provide phase diagrams, discuss the stability of states and find previously unobserved phase transitions. We also present an extensive parameter study of the vortex states depending on the pinning (laser beam) properties.

1.1 Historical overview

Superconductivity was discovered 100 years ago by the Dutch scientist Heike Kamerlingh Onnes in Leiden [1]. Being the first to liquify helium, he was the first able to perform measurements below 5 K. Onnes was interested in the behavior of metals at extremely low temperatures. Various speculations concerning the electrical conductivity at absolute zero circulated: Drude and Lorentz expected a steady decrease towards zero resistance, Lord Kelvin predicted an infinite resistance and others believed in a minimal but finite residual resistivity [2]. Obviously, it came as a total surprise when Onnes, while cooling down a mercury sample, observed

1.1. HISTORICAL OVERVIEW

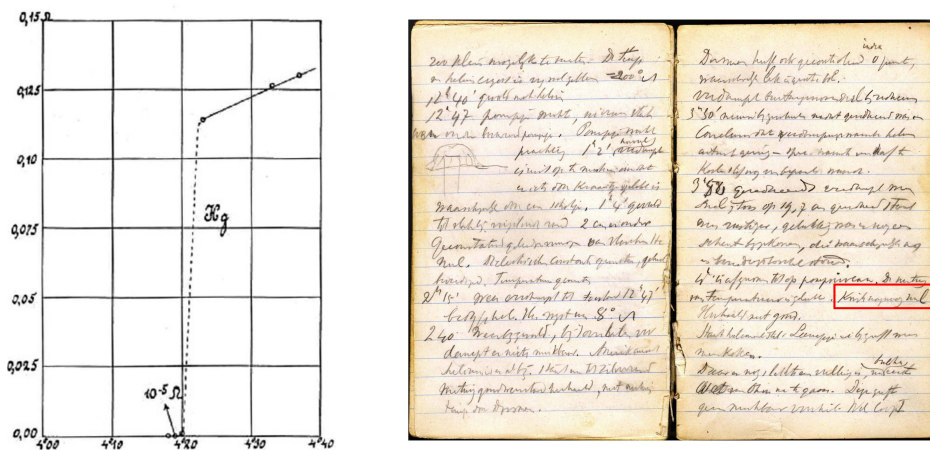


Figure 1.1: Left: The original plot of resistance versus temperature by Onnes from Ref. [1], indicating the discovery of superconductivity. Right: An extract of Onnes' lab notes. On April 8th, 1911, he wrote 'Kwik nagenoeg nul' which means 'Mercury virtually zero'.

that at 4.2 K the resistivity *abruptly* dropped to *exactly* zero. A current could flow through the sample without any dissipation: *superconductivity* was discovered. After reassuring that his remarkable finding was real, Onnes published his results in 1911. Subsequent experiments on tin and lead showed that superconductivity was a property of numerous metals, each with a different critical temperature. To nail down whether the resistance was *exactly* or just nearly zero, Onnes investigated the decay of a current in a superconducting ring. This experiment was later repeated with greater precision by File and Mills [3]. They found a lifetime of so called persistent currents, of more than 100000 years!

Twenty years after the discovery, superconductivity was still unexplained. The incomplete picture of a superconductor simply being an ideal superconductor probably impeded further progress. The real insight came after 1933, when Meissner and Ochsenfeld discovered a second feature: a superconductor *completely shields* out any (not too strong) magnetic field [4]. This expulsion of the field happens independently of the order of events: first cooling, then applying the field (zero-field cooled experiment) or first applying the field, then cooling (field-cooled experiment). However when the magnetic field is too strong, superconductivity is lost. For the superconducting materials known at that time this critical field was quite low, which was a disappointment to Onnes. Nowadays, perfect diamagnetism is considered as an even more fundamental signature of superconductivity than perfect conductivity.

Two years later the brothers London formulated the first phenomenological theory of superconductivity, now known as the London theory [5]. In essence it describes

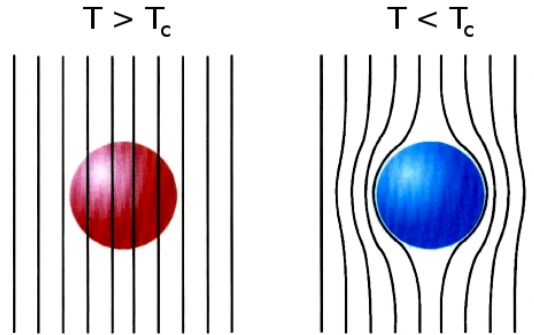


Figure 1.2: *Left: Above the critical temperature the magnetic field lines penetrate through the sphere. Right: Below the critical temperature the sphere becomes superconducting and magnetic field lines are expelled. This property is called the Meissner effect*

the electromagnetic field in a bulk superconductor by adding one extra equation, valid *inside* the superconductor, relating the current and the magnetic field, to the wellknown Maxwell equations. In this way, the theory successfully accounted for the zero resistance and the absolute diamagnetism. London theory proved the existence of a length scale λ , known as the penetration depth, over which a field can penetrate a superconductor. Therefore we state more correctly that a superconductor is a perfect diamagnet *up to a boundary layer* of thickness λ .

The next milestone in the theory of superconductivity was due to Ginzburg and Landau [6] in 1950. Anticipating the quantum nature of superconductivity, they associated an effective wave function Ψ with the superconducting electrons. This Ψ , known as the order parameter, is uniquely defined up to a constant phase factor $\exp(i\alpha)$ and is allowed to vary spatially. By applying Landau's theory of second-order phase transitions to this concept, they derived a set of two equations, one describing the spatial variation of Ψ and the other describing the magnetic field, now known as the Ginzburg-Landau (GL) equations. Besides the magnetic penetration depth λ , it features another fundamental length ξ , the coherence length, the scale over which variations of Ψ occur. Amongst other things, GL theory is able to describe the destruction of superconductivity by temperature and magnetic field and correctly predicts the energy of a superconducting-normal metal boundary. It can therefore be regarded as an improved version of the London theory. However it is still purely phenomenological and does not discuss the reasons *why* a material becomes superconducting.

Also in 1950, fluxoid quantization was predicted by F. London [7], based on the quantum nature of superconductivity. It was argued that the flux through a superconducting cylinder could assume only integer multiples of a quantity called the *flux quantum*. It would take another decade before the experimental confirmation

by Deaver and Fairbank [8] and Doll and Näbauer [9].

Still in the fifties, Abrikosov, a student of Landau, started studying the GL equations under the condition that the penetration depth is larger than the coherence length, $\lambda > \xi$. The results he obtained were quite a shock to the scientific community as even Landau, his mentor, at first did not believe in them. Abrikosov predicted the formation of a regular lattice consisting of *vortices*, small whirlpools of superconducting electrons with $\Psi = 0$ in the center, when a superconductor is put in a sufficiently high magnetic field. While Abrikosov originally predicted a square lattice, the triangular vortex lattice, which has slightly lower energy, became known as the Abrikosov lattice. He published his results in 1957 [10].

This was also the year of the major breakthrough by Bardeen, Cooper and Schrieffer. Being aware of the existence of a band gap, the similarity to superfluidity, the isotope effect and experimental results for the flux quantum suggesting two involved electrons, they were able to construct a microscopical theory with a great predictive power, now known as the BCS theory [11]. The main ingredient is that in a superconductor, electrons form pairs that do not break, unless a certain minimum energy is provided. This provided the band gap. The wave function of such a pair is symmetric under renumbering of the electrons and thus essentially represents a boson. Since bosons do not have to obey the Pauli-principle they can all occupy the same lowest energy state. This way a coherent sea of superconducting electrons is formed. When a current is generated in a superconductor, the Cooper pairs move collectively and unperturbed through the crystal lattice since they cannot absorb energies smaller than the Cooper pair binding energy.

An important contribution to the theory of superconductivity was made by Josephson in 1962 [12]. He predicted two remarkable effects which occur when two superconductors are brought into contact through a weak link (for instance, a thin insulator): the DC Josephson effect, predicting a current to flow across the junction without resistance, and the AC Josephson effect, predicting the emission of electromagnetic radiation upon applying voltage across the junction. These effects are caused by the interference of the individual wave functions and as such illustrated nicely the quantum nature of superconductors. The Josephson effect found practical applications in Superconducting Quantum Interference Devices (SQUIDs) to measure magnetic fields with unprecedented precision and in RSFQ electronics.

Just when the scientific community was considering superconductivity to be completely understood, the discovery by Bednorz and Müller in 1986 revived the interest in superconductors tremendously. In this year the first high- T_c superconductor, LaBaCuO with a critical temperature of about 30 K, was discovered [14]. This temperature is at the theoretical limit posed by BCS theory and thus hinted towards *unconventional* superconductivity. Few years later also YBCO with $T_c = 90$ K [15] and BSCCO with $T_c = 108$ K [16] were discovered. Their T_c just below the boiling temperature of liquid nitrogen, allowed for the use of a coolant much less

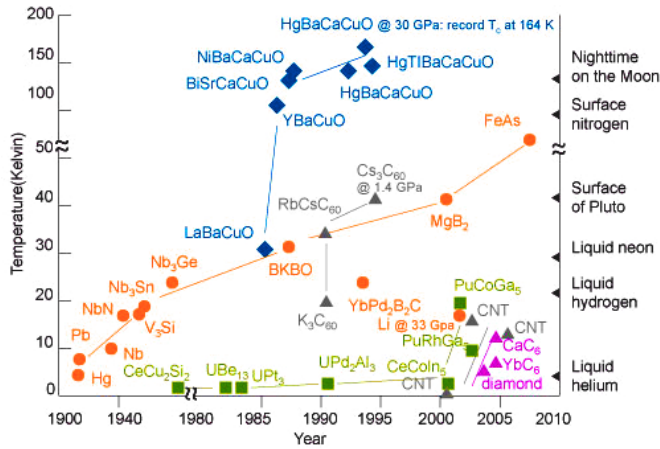


Figure 1.3: Timeline of the discovery of different superconductors showing the evolution of the critical temperature. The colors indicate several classes. Orange: conventional superconductors, blue: high- T_c superconductors, green: heavy-fermion superconductors, grey: fullerenes and purple: carbon-based superconductors. Adapted from Ref. [13].

expensive than helium. While Cooper pairing is still the mechanism for superconductivity in these superconductors, conventional BCS theory cannot account for the unusually high critical temperatures and scientists are still struggling to get an understanding of these materials. Above mentioned high- T_c superconductors all contain copper and are therefore referred to as cuprate superconductors. Recently also iron-based high- T_c superconductors have been discovered [17], very different materials, with a puzzling Cooper-pairing mechanism.

Nowadays, superconductors are widely used for medical imaging techniques such as magnetic resonance imaging (MRI), for generating and sustaining stable powerful magnetic fields, or for magnetoencephalography, using SQUIDS to detect the tiny variations of the magnetic in the human brain. Superconductors are also widely used in research facilities over the world, e.g. CERN and tokamak. The wide use of superconductors is partially hampered by the need for cryogenics, and partially by the mostly absent balance between the electronic and mechanical properties of superconducting materials.

1.1.1 London theory

In 1935, twenty-four years after the first discovery of superconductivity, and two years after the discovery of the Meissner effect, brothers London published the first phenomenological theory of superconductivity [5]. The theory describes the electromagnetic field inside a superconductor and does this by adding two equations

to the standard set of Maxwell equations. This way both the perfect conductivity as well as the expulsion of an applied magnetic field can be described.

The first London equation, valid in the inside of a superconductor, reads

$$\vec{E} = \frac{\partial}{\partial t} \left(\Lambda \vec{j}_s \right), \quad (1.1)$$

with $\Lambda = 4\pi\lambda^2/c^2 = m_e/n_s e^2$. \vec{E} is the electric field and \vec{j}_s is the superconducting current density, which is related to the superconducting electrons velocity \vec{v}_s by $\vec{j}_s = en_s \vec{v}_s$. The density of superconducting electrons, n_s , is assumed uniform, and λ is called the penetration depth. Eq. (1.1) is equivalent to Newton's second law applied to the superconducting electrons: the electrons are free and are accelerated by an electric field. It implies that when there is a stationary current, there is no electric field inside the superconductor. As such it functions as the replacement of Ohm's law for normal metals, $\vec{j} = \vec{E}/\rho$, with ρ the resistivity.

However, a superconductor is more than an ideal conductor; a superconductor is also an ideal diamagnet. Or put more carefully, a magnetic field can not penetrate a superconductor beyond a layer of thickness λ . This can be expressed mathematically by the equation

$$\vec{H} + \lambda^2 \vec{\nabla} \times \vec{\nabla} \times \vec{H} = 0, \quad (1.2)$$

which is valid inside the body of a bulk superconductor. From this the second London equation can be derived using a Maxwell equation:

$$\vec{\nabla} \times \vec{j} = -\frac{c}{4\pi\lambda^2} \vec{H}, \quad (1.3)$$

which in the London gauge ($\vec{\nabla} \cdot \vec{A} = 0$ and $\vec{A}_n = 0$ at the surface) is equivalent to

$$\vec{j} = -\frac{c}{4\pi\lambda^2} \vec{A}, \quad (1.4)$$

i.e. the supercurrent is proportional to the vector potential in the London gauge. This last equation can be considered as the summary of London theory since Eq. (1.1) and (1.3) follow from it, however its validity is restricted to the London gauge. The London theory does not intend to explain the origin or the mechanism of superconductivity, it merely provides a mathematical basis to describe the phenomenon. It is valid for extreme type-II superconductors, i.e. when the penetration depth is much larger than the characteristic length over which the superconducting wave function varies. Since it assumes n_s constant over the sample, and treats vortices as pointlike objects. Therefore it can not be used to study the vortex core, the latter being essential in this thesis as we investigate mesoscopic samples where the size of the sample can be of the same order as the size of the vortices.

Energy

In the London framework of superconductivity, the total energy of a given superconducting state is given by the energy stored in the magnetic field and the kinetic energy of the currents generated by it. The kinetic energy can be derived as

$$\begin{aligned}
 E_{kin} &= \int n_s \frac{1}{2} m \vec{v}_s^2 dV \\
 &= \int \frac{1}{2} \frac{m}{e^2 n_s} \vec{j}_s^2 dV \\
 &= \int \frac{\lambda^2}{8\pi} (\vec{\nabla} \times \vec{H})^2 dV,
 \end{aligned} \tag{1.5}$$

where we used $\vec{\nabla} \times \vec{H} = 4\pi \vec{j}/c$ in the last step. The magnetic energy density is:

$$E_{mag} = \frac{1}{8\pi} \int H^2 dV. \tag{1.6}$$

The total energy of a given state in London approximation equals the sum of the above two contributions:

$$E = \frac{1}{8\pi} \int [H^2 + \lambda^2 (\nabla \times H)^2] dV. \tag{1.7}$$

1.1.2 Ginzburg-Landau theory

In 1950, Russian scientists Vitaly L. Ginzburg and Lev D. Landau published their famous paper entitled ‘On the theory of superconductivity’ [6]. They found the existing phenomenological theory of superconductivity unsatisfactory, since it contained several caveats: the inability to determine the surface tension between a normal-superconducting boundary and the inability to describe the destruction of superconductivity by an applied magnetic field or current.

To tackle the problem they took a thermodynamic viewpoint. They noticed that the transition to the superconducting state at the critical temperature T_c was a phase transition of the second kind. In the general theory of such transitions there always enters a parameter which differs from zero in the ordered phase, but equals zero in the disordered phase. A known example was the spontaneous magnetization observed in ferromagnets below the Curie temperature. To represent the ordered phase in the superconducting state, they chose Ψ , the order parameter. Its physical meaning is to be understood as the amplitude of the wave function of the superconducting charge carriers (which at that time was still believed to be single electrons, rather than Cooper electron pairs). They formulated the free energy in a series expansion valid near the critical temperature, allowing for spatial variations. To date, the Ginzburg-Landau theory remains the best approach to describe superconducting systems of sizes comparable to the coherence length and

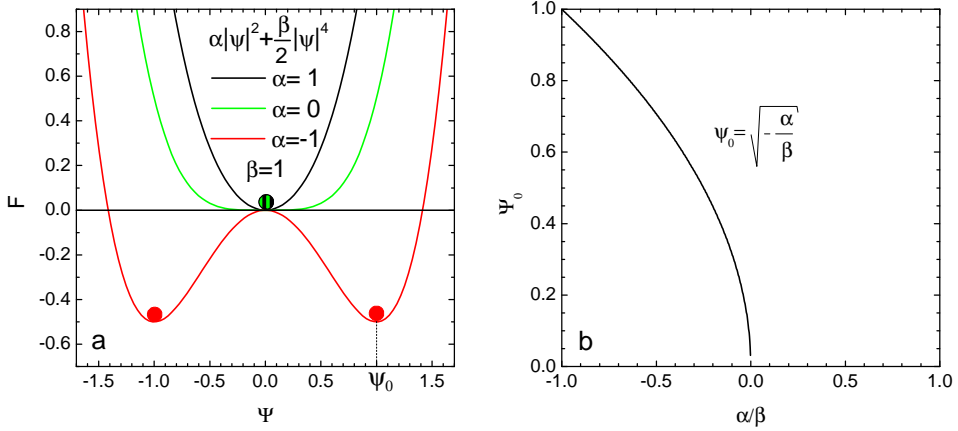


Figure 1.4: Left: Mexican hat potential used by Ginzburg and Landau to describe second order phase transitions. Right: The equilibrium value of the order parameter (in the absence of field) as a function of the ratio of the GL parameters α and β .

the penetration depth. It is the most powerful tool to investigate the behavior and structure of vortices and it is the basis of most of the calculations in this thesis. The general expression for the Ginzburg-Landau free energy is

$$\mathcal{G} = \int dV F_{s0} = \int dV \left[F_{n0} + \alpha |\Psi|^2 + \frac{\beta}{2} |\Psi|^4 + \frac{1}{2m} \left| -i\hbar \vec{\nabla} \Psi - \frac{2e}{c} \vec{A} \Psi \right|^2 + \frac{H^2}{8\pi} \right]. \quad (1.8)$$

F_{n0} (F_{s0}) is the free energy density of the normal (superconducting) state. α is a temperature dependent coefficient which changes sign at T_c , while β is temperature independent. m , α and β are material dependent parameters. The construction of the free energy with a square and a quartic term in Ψ , giving rise to the mexican hat potential, is a general method to describe spontaneous symmetry breaking through a second order transition. This principle is illustrated in Fig. 1.4. The gradient term in Ψ represents the (gauge invariant) kinetic energy, as prescribed by quantum mechanics, and the last term describes the magnetic energy density.

Eq. (1.8) is as a functional of Ψ , the order parameter, and \vec{A} , the vector potential, and by minimization with respect to these variables the two famous GL equations can be extracted:

$$\alpha \Psi + \beta |\Psi|^2 \Psi + \frac{1}{2m} \left(-i\hbar \vec{\nabla} - \frac{2e}{c} \vec{A} \right)^2 \Psi = 0, \quad (1.9)$$

$$\vec{j}_s = -\frac{i\hbar e}{m} \left(\Psi^* \vec{\nabla} \Psi - \Psi \vec{\nabla} \Psi^* \right) - \frac{4e^2}{mc} |\Psi|^2 \vec{A}, \quad (1.10)$$

where

$$\vec{j}_s = \frac{c}{4\pi} \vec{\nabla} \times \vec{\nabla} \times \vec{A}. \quad (1.11)$$

The derivation of these equations in detail is presented in a later section of this thesis.

From the GL equations some meaningful quantities can be defined. For a bulk superconductor in the absence of a magnetic field, Eq. (1.9) in one dimension reduces to

$$\alpha\Psi + \beta\Psi^3 - \frac{\hbar^2}{2m} \frac{\partial^2\Psi}{\partial x^2} = 0, \quad (1.12)$$

where we chose a gauge in which the order parameter is real. This has as non-trivial solution $|\Psi| = \Psi_0 \equiv \sqrt{-\alpha/\beta}$, the value of the order parameter far away from inhomogeneities. By expressing the order parameter in Ψ_0 by defining $\psi = \Psi/\Psi_0$, the GL equation reduces to

$$-\psi + \psi^3 - \frac{\hbar^2}{2m|\alpha|} \frac{\partial^2\psi}{\partial x^2} = 0, \quad (1.13)$$

and a characteristic length scale for variation of ψ emerges,

$$\xi^2 = \frac{\hbar^2}{2m|\alpha|}. \quad (1.14)$$

over which changes of ψ are expected happen. This fundamental length scale is called the coherence length. When we consider a normal metal-superconductor boundary at $x = 0$, the meaning of ξ becomes clear. We then have $\psi = 0$ at $x = 0$ and $\psi = 1$ at $x \rightarrow \infty$ as boundary conditions. The solution of Eq. (1.13) becomes

$$\psi = \tanh\left(\frac{x}{\sqrt{2}\xi}\right) \quad (1.15)$$

i.e. ξ represents the length over which the order parameter heals.

Another fundamental length scale emerges when considering the second GL equation. In a weak magnetic field the order parameter can be assumed constant and equal to Ψ_0 and in that case Eq. (1.10) reduces to

$$\vec{j}_s = -\frac{4e^2}{mc} |\Psi_0|^2 \vec{A},$$

which is simply the second London equation (Eq. (1.3)) describing that a magnetic field cannot penetrate a superconductor beyond a layer of thickness λ . Identification, after taking the curl of both sides, gives:

$$\lambda^2 = \frac{mc^2}{16|\Psi_0|^2\pi e^2},$$

which defines the second fundamental length scale of the GL formalism, the penetration depth λ . The meaning of ξ and λ is illustrated in Fig. 1.5.

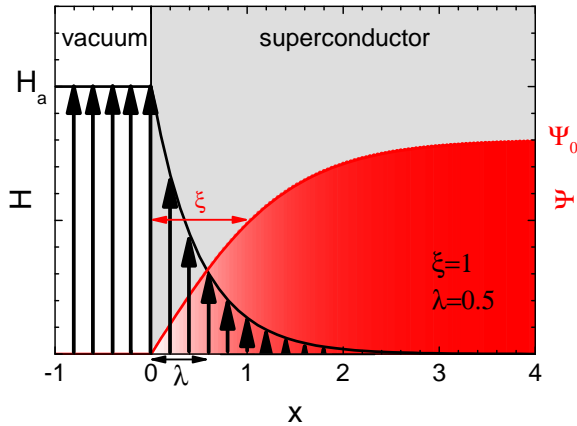


Figure 1.5: Semi-infinite type-I superconductor with boundary at $x = 0$. Black: magnetic field profile illustrating the penetration depth. Red: healing of the order parameter over a distance ξ , the coherence length, as described by Eq. (1.15).

Ginzburg and Landau also introduced a parameter $\kappa = \lambda/\xi$, equal to the ratio of the penetration depth and the coherence length, which later became known as the GL parameter. For all known materials at that time κ was much smaller than 1. Few years later, Abrikosov, a student of Landau, decided to study what happens if $\kappa > 1/\sqrt{2}$, when the normal metal-superconductor surface energy becomes negative. In his study he predicted the so-called mixed state in which a periodic vortex lattice is formed [10]. There was a lot of scepticism about this prediction and only ten years after Abrikosov's publication the vortex lattice was confirmed in experiment by Essmann and Trauble in 1967[18].

Here we must mention a few points concerning the validity of the GL theory. Since the derivation of Ginzburg and Landau is an expansion in powers of Ψ , it is only valid when Ψ is small, thus close to T_c . When later Gor'kov derived the GL equations from the microscopic theory he also found the GL equations valid only close to T_c . Ψ also must be a slowly varying function in terms of the BCS coherence length ξ_0 , i.e. for $\xi \gg \xi_0$, which is the case for high enough temperature. Pippard showed that the relation between the current and the vector potential should be non-local [19]. Therefore he proposed to average the vector potential over a distance ξ_0 before relating it to the supercurrent. The second GL equation (Eq. (1.10)) does assume a local relation between \vec{j}_s and \vec{A} and therefore, it can only be valid when \vec{A} is a slowly varying quantity with respect to ξ_0 , i.e. for $\lambda \gg \xi_0$. This is satisfied in type-II superconductors or in any superconductor when temperature is close enough to T_c , where both ξ and λ diverge.

1.1.3 BCS theory

Before the advent of superconductivity, the only current assumed to flow without resistance was the orbiting of an electron around the nucleus at a distance of a few Bohr radii. Although the length scale where this ‘perfect conductivity’ occurs differs by about 10 orders of magnitude with the currents realized in superconductors, some researchers saw a link between the two: quantization. The movement of the electron around the nucleus was quantized, so could the (macroscopic) current in a superconductor also be quantized? This hinted towards a quantum mechanical mechanism causing superconductivity, which as it turned out, proved to be correct. Superconductivity is a macroscopic manifestation of a quantum state.

Only 46 years after the original discovery of superconductivity, a microscopic theory of superconductivity was conceived by Bardeen, Cooper and Schrieffer [11]. The key experimental observations which led them to develop the theory [20] were (1) the existence of a band gap, as deduced from microwave absorption experiments, suggesting the existence of a state with lower energy than the Fermi sphere. This could have been caused by an attractive interaction between electrons. (2) The analogy between superconductivity and superfluidity (flow without resistance). The latter phenomenon was known to be related to Bose-Einstein condensation, where Bose particles collectively condense into the same quantum (ground) state. While electrons obey Fermi statistics, a pair of them will obey Bose-statistics, again hinting towards electron pairing. (3) The quantum of magnetic flux through a superconducting ring, measured experimentally, seemed to be described theoretically by a charge $2e$ instead of e , once again suggesting the formation of pairs. (4) The isotope effect, the relation between the critical temperature and the mass of the atomic nucleus. This indicated the relevance of lattice vibrations.

Therefore, BCS theory assumes an effective attraction between electrons, allowing them to form a bound state, called a Cooper pair. While electrons in vacuum are known to repel each other due to the Coulomb force, the situation changes inside a metal where the electrons are embedded in a lattice of positive ions. Already in 1954 Herbert Fröhlich demonstrated [22] that the interaction between two electrons could be attractive by exchange of phonons, i.e. the quantum particle representing lattice vibrations. This can be understood by realizing that an electron in a lattice attracts the ions near it, slightly deforms the ionic lattice, and thus leaves behind a positively charged cloud which in turn attracts another electron. There is an analogy to two marbles on a soft rubber sheet: while moving over the sheet the marbles locally indent the sheet causing them to stay close to each other, even if there is a repulsive force between them. The Cooper pairs act like bosons and, when the temperature is sufficiently low, undergo Bose-Einstein condensation. They do not have to obey the Pauli principle, and can all participate in the conduction. Being Bose particles, they all occupy the same energy state, i.e. the ground state.

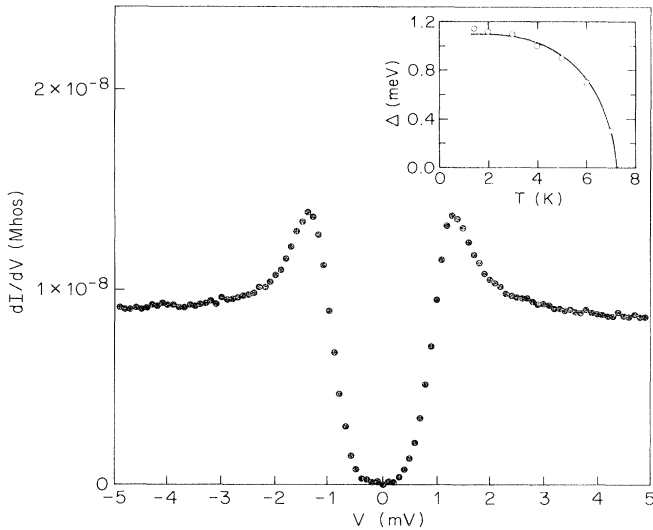


Figure 1.6: Direct observation of the band gap in NbSe_2 by scanning tunneling microscopy. From Ref. [21].

Thus they will establish a large scale phase coherence.

The BCS theory correctly predicts many superconducting properties, for instance the band gap, the critical temperature and the critical field, in terms of microscopic material parameters, such as the electron-electron interaction strength, the density of states and the Debye frequency. In Fig. 1.6 the direct experimental observation of the band gap of NbSe_2 , a BCS superconductor is depicted. The BCS theory also provides upper limits to the critical temperature and field [23]. Despite its wide range of applicability, there are superconductors which can not be described by BCS theory. The first ones were the high- T_c superconductors, discovered in 1986 [14] of which famous examples are YBCO and BSCCO. Nowadays even more non-BCS-superconductors are known, e.g. heavy fermion superconductors and the iron-pnictides.

In 1959 Gor'kov generalized the BCS theory to a gap locally varying in space, by applying the Green's function formalism [24]. This way the effect of the magnetic field could be included. The gap was found to be proportional to the GL order parameter ψ . He found the Ginzburg-Landau theory as a limiting case of his theory, valid near the critical temperature.

The expressions obtained by the BCS theory for the energy gap and the energy difference between superconducting and normal state are not analytic in terms of the pair interaction strength and can thus not be expressed as a power series expansion, as one would get from perturbation theory. This is (amongst others) one of the

reasons why it took so long to develop the microscopic theory of superconductivity.

1.2 Types of superconductors

Superconductors are usually classified as being either type-I or type-II. This distinction is based upon their behavior in an applied magnetic field. To explain this, we consider a long cylinder in a parallel field. When it is made of a type-I material, the field will be completely expelled until the applied field exceeds some critical value H_c , at which superconductivity is destroyed. This happens through a *first order* phase transition. In contrast, when the material is type-II, the total expulsion persists up to a critical field H_{c1} , when a small amount of magnetic flux will *enter* the superconductor in terms of vortices, and superconductivity survives everywhere except inside the vortex cores. When further increasing the applied field, gradually more vortices enter, until at a second critical field H_{c2} the material loses its superconductivity through a *second order* phase transition. The difference between the two types is most easily seen in the magnetization curves, which are depicted schematically in Fig. 1.7.

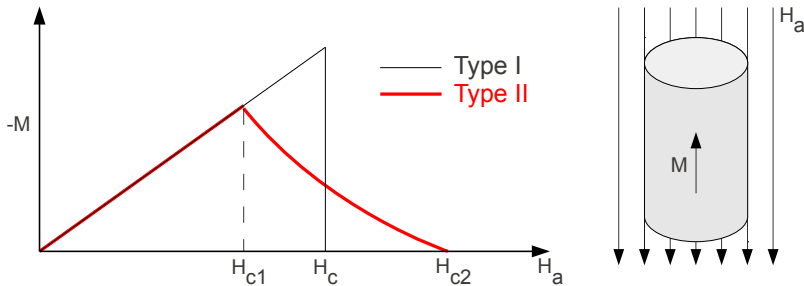


Figure 1.7: The magnetization (M) curves of a type-I and a type-II superconductor for the geometry of a long cylinder in longitudinal applied field H_a . The critical fields are indicated in the graph.

Within the GL theory, the distinction between the two types is simply determined by the ratio of the penetration depth and the coherence length, $\kappa = \lambda/\xi$ which is called the GL parameter. When $\kappa < 1/\sqrt{2}$ a material is a type-I superconductor, when $\kappa > 1/\sqrt{2}$ it is type-II. The energy of a superconducting/normal metal interface is positive for a type-I superconductor, and negative for a type-II one.

All critical fields can be expressed in terms of the fundamental length scales of the GL theory. The field at which a type-I superconductor abruptly loses supercon-

ductivity,

$$H_c = \frac{\Phi_0}{2\sqrt{2}\pi\lambda\xi},$$

is called the *thermodynamic* critical field, as it corresponds to an energy density equal to the condensation energy density of the superconducting state in the absence of a magnetic field.

A bulk type-II superconductor is in the Meissner state until the first critical field $H_{c1} < H_c$ is reached,

$$H_{c1} = \frac{\Phi_0}{4\pi\lambda^2} \ln(\kappa).$$

There the field is allowed to penetrate the sample stepwise by means of vortices, each carrying one magnetic flux quantum. The vortices arrange themselves in an Abrikosov lattice. When further increasing the field, vortices keep entering the sample, the mean Cooper pair density (CPD) gradually decreases, eventually leading to the loss of superconductivity at the second critical field

$$H_{c2} = \frac{\Phi_0}{2\pi\xi^2},$$

through a second order transition. Type-II superconductors can have a much higher critical field than type-I superconductors. Some examples of critical fields are given in Table 1.1.

Table 1.1: The (dimensionless) Ginzburg-Landau parameter κ , the thermodynamic, first and second critical fields of some superconductors, expressed in Tesla, and the critical temperature, expressed in Kelvin. From [25–27].

Metal	κ	H_c	H_{c1}	H_{c2}	T_c
Al	0.07	0.011			1.2
Sn	0.15	0.030			3.7
Pb	0.45	0.076			7.2
Nb	1.03	0.157	0.003	0.228	9.3
Nb ₃ Sn	22	1.95	0.12	29	18
MgB ₂ ($\parallel c$)	8.1	0.28	0.063	3.18	39
MgB ₂ ($\perp c$)	37.1	0.28	0.022	14.5	39
YBCO ($\parallel c$)	560	1.1	0.01	130	92

However, when the superconductor is not a long cylinder, the magnetization curve will look less trivial than shown in Fig. 1.7. For instance, in a type-I superconductor, the critical field H_c can be reached locally even when the applied field H_a is smaller than H_c . The reason is that the field generated by the Meissner currents,

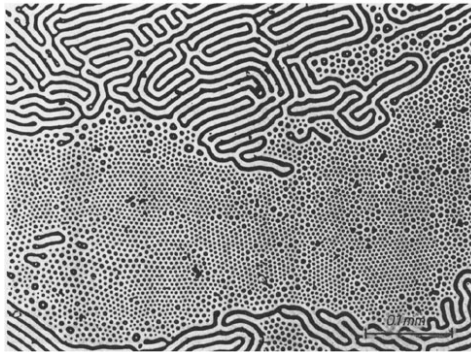


Figure 1.8: The intermediate state of a disk of Tantalum, a type-I superconductor. Coexistence of triangular lattice of flux tubes and laminar domains. Image made in 1969 by U. Essmann using Bitter decoration visualized by an optical microscope. From Ref. [28].

inside the sample *exactly cancels* the applied field, but outside the sample *reinforces* it. This leads to a coexistence of normal and superconducting regions, often arranged in laminar patterns or tubes, known as the type-I *intermediate state*. An experimental image is shown in Fig. 1.8. The field at which this state appears is determined by the geometry of the sample and is usually expressed by $(1 - n)H_c$ where n is called the *demagnetization* factor, which is minimal ($n = 0$) for a infinitely long cylinder in a longitudinal magnetic field and is maximal ($n = 1$) for a thin plate in a perpendicular magnetic field.

In the early years of superconductivity, the only known superconductors were type-I, as are most of the elemental superconductors. Though unnoticed by a large part of the scientific community, the first type-II superconductors were identified in 1937 by Shubnikov *et al.* [29] in experiments on single crystal leadthallium (PbTl_2) and leadindium (PbIn) alloys. They measured the magnetization curves and found drastically different behavior with increasing impurity concentration. They concluded the existence of two critical fields: H_{c1} , the field at which the Meissner state becomes unstable and flux tubes start to penetrate, and H_{c2} , the field at which a superconductor goes into the normal state.

Twenty years later, Abrikosov published his theoretical work on the GL equations in the case of $\lambda > \xi$ [10]. This case was never considered before as it featured a negative superconducting/normal surface tension, in contradiction with the available observations (for type-I superconductors). The solution he found was a *regular lattice* of *vortices* which he named the *mixed state*. It is fundamentally different from the type-I ‘intermediate state’, for one reason because it would appear even in a bulk superconductor. Additionally, he predicted critical fields and a shape of the magnetisation curve qualitatively different from the type-I case, and found good

agreement with the experimental observations by Shubnikov. This way Abrikosov was led to the prediction that there exists a second kind of superconductors, characterized by $\kappa = \lambda/\xi > 1/\sqrt{2}$, now known as type-II superconductors.

The real breakthrough happened in 1961 when Kunzler and collaborators [30] demonstrated type-II superconductivity in the alloy niobiumtin (Nb_3Sn), which has a high critical field and critical current, and as such is practical for applications. In fact, nowadays Nb_3Sn is still a very popular superconducting material: e.g more than 600 tons of it will be used in the International Tokamak Experimental Reactor (ITER) [31].

Recently, the existence of a new type of superconductivity, called type-1.5, has been suggested. It would manifest in two-gap superconductors where one band is effectively type-I and the other type-II. More discussion is left for the section 1.5.3.

1.3 Vortices

Fluxoid quantization

The best way to derive fluxoid quantization is starting from the second GL equation (1.10). With the order parameter split in phase and amplitude, $\Psi = \psi \exp(i\phi)$ (we choose ψ and ϕ real), the supercurrent can be written as:

$$\vec{j}_s = \frac{2\hbar e}{m} \psi^2 \nabla \phi - \frac{4e^2}{mc} \psi^2 \vec{A}.$$

We divide the supercurrent by the Cooper pair density and integrate this on a closed contour:

$$\oint \frac{\vec{j}_s}{\psi^2} \cdot d\vec{s} = \frac{2\hbar e}{m} \oint \nabla \phi \cdot d\vec{s} - \frac{4e^2}{mc} \oint \vec{A} \cdot d\vec{s}.$$

Since the start and endpoint of the contour are the same, the phase can only change in multiples of 2π ,

$$\oint \frac{\vec{j}_s}{\psi^2} \cdot d\vec{s} = \frac{2\hbar e}{m} n 2\pi - \frac{4e^2}{mc} \Phi, \quad (1.16)$$

where $\Phi = \oint \vec{A} \cdot d\vec{s} = \int \vec{B} \cdot d\vec{S}$, the magnetic flux through the contour, was introduced and n is an integer. Reordering the terms, the fluxoid Φ' can be defined as:

$$\Phi' = \frac{mc}{4e^2} \oint \frac{\vec{j}_s}{\psi^2} \cdot d\vec{s} + \Phi = n\Phi_0, \quad (1.17)$$

where the fluxoid quantum Φ_0 is defined as:

$$\Phi_0 = \frac{\hbar c}{2e} \approx 2.068 \times 10^{-15} Tm^2. \quad (1.18)$$

It is easily verified that for *any* contour inside and enclosing only superconducting material, the fluxoid is zero, by plugging in London equation (1.4) into (1.17).

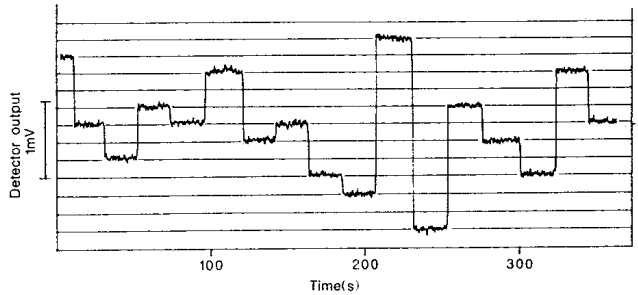


Figure 1.9: *Experimental verification of flux quantization through a ring made of a high- T_c superconductor. On the y-axis is the voltage that appears along a r.f. SQUID, which is proportional to the flux inside the ring. The flux jumps are caused by periodically exposing the ring to a local source of random electromagnetic noise. Horizontal lines are superposed as a guide to the eye, illustrating the discrete character of the possible flux values. From Ref. [34]*

Therefore, if the contour contains a hole or, in general, a non-superconducting region, the fluxoid is constant for any contour enclosing only that region. Consequently, a fluxoid can be uniquely associated with each non-superconducting region, and in particular, with a vortex. This is why each vortex carries a flux of exactly Φ_0 .

When the contour lies deep into the superconducting volume, the current is zero, (1.17) simplifies and *flux* quantization takes place:

$$\Phi' = \Phi = n\Phi_0$$

By generalizing his theory to accommodate the quantum nature of the superconducting wave function, i.e. that it has a macroscopical phase, London predicted fluxoid quantization in 1948 [32]. However, since he did not know the electrons formed Cooper pairs, his result for the flux quantum was wrong by a factor of 2. Flux quantization in a thick superconducting cylinder was confirmed in 1961 by two independent, yet almost simultaneously conducted experiments [8, 9, 33]. Another experiment in 1987 demonstrated nicely flux quantization in a high- T_c superconductor [34], giving evidence for the pairing of electrons in such superconductors. The experimental image is shown in Fig. 1.9.

Vortex interactions

Vortices interact with impurities, defects and boundaries but most importantly, with each other. The latter interaction is the subject of this subsection. To allow for a simple discussion we will first employ the London theory. However, to incorporate vortices, the second London equation (1.2) has to be modified. Vortices will

be treated as point-like objects, thus having no core. The validity of the derivation will thus be restricted to the situation in which $\lambda \gg \xi$, i.e. extreme type-II superconductors.

Vortices carry a flux of exactly one flux quantum. The London equation for an isolated vortex, centered at the origin, parallel to the z-axis, becomes:

$$\vec{H} + \lambda_L^2 \vec{\nabla} \times \vec{\nabla} \times \vec{H} = \Phi_0 \vec{e}_z \delta(r), \quad (1.19)$$

which leads directly to the condition of fluxoid quantization, Eq. (1.17) as can be checked by integration in an arbitrary region containing the vortex.

The modified London equation (1.19) can be solved analytically to get the magnetic field distribution of an isolated vortex line [35], as

$$H = \frac{\Phi_0}{2\pi\lambda^2} K_0\left(\frac{r}{\lambda}\right), \quad (1.20)$$

where $K_0(x)$ is the modified Bessel function of the second kind with asymptotic behavior $-\ln x$ for $x \ll 1$ and $\sqrt{\pi/2x} \exp(-x)$ for $x \gg 1$. When this is inserted into the expression for the energy, Eq. (1.7), and the integration is carried out over the vortex core with radius ξ , the energy per unit length of a flux line is found as:

$$E_v = \left(\frac{\Phi_0}{4\pi\lambda}\right)^2 \ln\left(\frac{\lambda}{\xi}\right). \quad (1.21)$$

This energy is a quadratic function of the flux. This result illustrates that energetically it is more favorable to have two separate flux lines (energy $2E_v$) than one with double flux (energy $4E_v$), i.e. multiquantum or giant-vortices are disfavored in bulk type-II superconductors.

When two vortices are far apart, the resulting current distribution can be approximated as a superposition of the individual current distributions. Then the vortex-vortex interaction can be calculated analytically. For a bulk superconductor the result is [35]:

$$U_{vv} = \frac{\Phi_0^2}{8\pi^2\lambda^2} K_0\left(\frac{r}{\lambda}\right). \quad (1.22)$$

It decays exponentially for $r > \lambda$, thus it is a short range interaction. In a thin superconducting film the interaction energy is [36]:

$$U_{vv} = \frac{\Phi_0^2}{4\pi^2} \frac{1}{r}, \quad (1.23)$$

i.e. vortices in films have a long range interaction. This is due to the fact that most of the interaction takes place not inside the superconductor, but through the space above and below it. The vortex-vortex interaction is always repulsive (attractive) between vortices of same (different) sign. Note that both interaction energies diverge at zero distance.

A vortex however has a finite core, a region of size ξ in which the order parameter is suppressed. Using the GL theory this can be taken into account. This was done by Kramer [37], Brandt [38] and Chaves [39]. This results in an extra term in the interaction energy which for two vortices in bulk now becomes:

$$U_{vv} = \frac{\Phi_0^2}{8\pi^2\lambda^2} \left[K_0\left(\frac{r}{\lambda}\right) - K_0\left(\frac{r}{\xi/\sqrt{2}}\right) \right]. \quad (1.24)$$

While the previous result of London theory took only the magnetic field energy into account, the above result also considers the gain of condensation energy, which occurs when vortex cores overlap. Note also that this vortex interaction does not diverge at zero distance but takes a finite value, $U_{vv}(0) \propto \ln(\sqrt{2}\lambda/\xi)$, similar to the finite vortex self-energy of the London theory, Eq. (1.21).

When $\kappa > 1/\sqrt{2}$, we are in the type-II regime, $U_{vv} > 0$ and vortices repel. When $\kappa < 1/\sqrt{2}$, in the type-I regime, the vortex interaction changes sign and becomes attractive. At $\kappa = 1/\sqrt{2}$ (which is called the Bogomolnyi limit), vortices do not interact, at least according to this model. Detailed calculations up to higher order in temperature have shown that this is however not always the case [40]. For instance one can get a non-monotonous interaction, featuring long-range attraction and short-range repulsion. In Fig. 1.10 the force between vortices for different values of the GL parameter is illustrated.

One can also consider the interaction of a vortex and an antivortex. This corresponds to reversing the sign of the magnetic interaction term. The condensation term is not influenced. This always results in an attractive interaction, both in type-I and type-II superconductors. This can be understood from a very simple argument: when a vortex and an antivortex are far from each other the energy of the system is non-zero, as it is the sum of the energy of one vortex and one antivortex; on the other hand, when they approach each other they will annihilate, giving zero energy. Hence at least at some distance, the energy of the vortex-antivortex (V-Av) pair must decrease as the V-Av distance approaches 0, and as a consequence the interaction potential is attractive [39].

Above examples all considered monotonous interactions, i.e. interaction which are either repulsive or attractive over the whole range of distances from zero to infinity. A non-monotonous interaction can however arise due to e.g. higher order corrections of London or GL theory, in anisotropic or layered superconductors, etc. [28]. Actually Brandt also introduced type II/1 and type II/2, with competing interactions out of the GL model. Recently the suggestion has been made that a long range attractive and short range repulsive vortex interaction might manifest in certain two gap superconductors [41], as will be discussed in chapter 3.

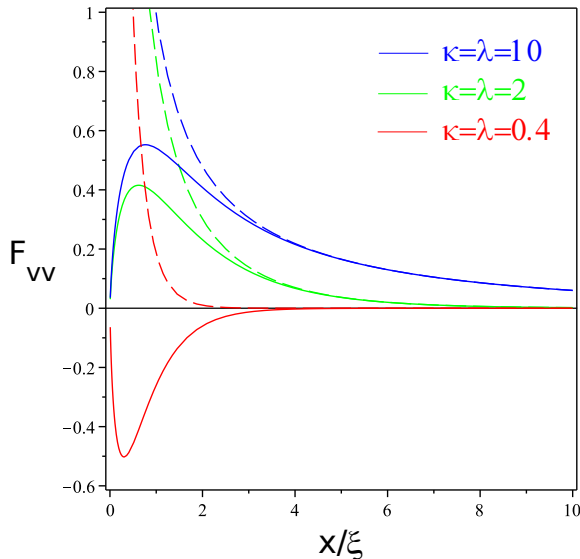


Figure 1.10: The force between vortices in the GL (solid lines) and London (dashed lines) approach for different values of the GL parameter. Calculated by $F_{vv} = -\partial U_{vv}/\partial x$, with U_{vv} from Eq. (1.24) and (1.22). Positive values indicate repulsion, negative values attraction.

1.4 Mesoscopic superconductors

A superconducting sample is called mesoscopic when at least one of its dimensions is of the order of the coherence length or the penetration depth. While in bulk samples the surface to volume ratio is small and boundary effects only have minor influence, in mesoscopic superconductors these effects are - by definition - essential. The vortex physics in mesoscopic superconductors is dominated by boundary effects. The interaction of a vortex with a boundary was first calculated by Bean and Livingston in 1964 [42]. They found that at low applied fields a vortex at the boundary experiences a barrier to enter the sample, which can be lifted by increasing the field. Vortices that are already inside the sample are pushed inwards, for any non-zero field. This way the boundary will try to impose its geometry onto the vortex lattice.

Clearly the triangular Abrikosov vortex lattice, arising due to the repulsive forces of vortices, is not stable in a mesoscopic superconductor. Instead, observations have been done of circular shell structures of vortices in mesoscopic disks [43] and a square arrangement of vortices in a superconducting square [44].

Other peculiar vortex states can be found in mesoscopic samples. For instance multiquanta or *giant* vortices, which are unstable in bulk superconductors, were

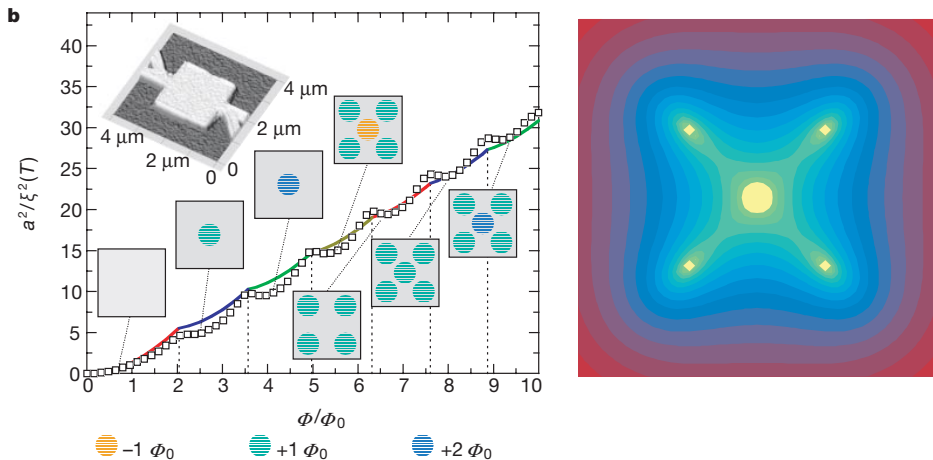


Figure 1.11: Left: Calculated (lines) and experimental (dots) T_c - H phase boundary for a mesoscopic square. The V-Av state at T_c occurs for $5 < \Phi/\Phi_0 < 6.3$. The y-axis is essentially a negative temperature since $a^2/\xi^2(T) \propto (1 - T/T_c)$. Right: Cooper pair density of the symmetry-induced V-Av state exhibiting five minima corresponding to one antivortex and four surrounding vortices. The picture has a magnification of $8\times$. From Ref. [47].

observed in mesoscopic disks in 2004 [45]. Theoretically these states were investigated as early as in 1966 [46].

In 2000, an even more exotic vortex state was predicted to exist in mesoscopic samples with a discrete symmetry (e.g. triangles, squares, regular polygons): the *vortex-antivortex* (V-Av) state [47] (see Fig. 1.11), where vortices and antivortices co-exist and form the thermodynamically stable ground state. In normal conditions vortex and antivortex would be attracted to each other and annihilate each other. In the mesoscopic case however, the V-Av pair is generated to allow the vortex arrangement to conform better with the sample geometry when the number of vortices normally would not allow this. The symmetry-induced V-Av state is however not yet confirmed by experiment.

In mesoscopic superconductivity, the distinction between type-I and type-II can no longer be made by only the bulk value of the GL parameter. In fact the type is dependent both on the thickness as on the lateral dimensions of a sample. For instance, in a thin film with thickness $d \ll \lambda$ in a perpendicular magnetic field, an effective penetration depth can be defined as a function of the thickness and its bulk value [35, 48]:

$$\lambda_{eff} = \frac{\lambda^2(T)}{d} \quad (1.25)$$

This also affects effective $\kappa = \lambda_{eff}/\xi$, and consequently thin films of a type-I

material will behave effectively as type-II. A numerical, more exact treatment of the thickness of the sample, which we used for our calculations is presented in Sec. 1.8.2.

The $T_c(H)$ boundary of a mesoscopic sample (see Fig. 1.11), separating the normal and the superconducting state, exhibits oscillations similar to the Little-Parks (LP) oscillations. The latter oscillations were predicted for a thin cylinder as a consequence of fluxoid quantization and have a period of Φ_0 [49]. Their amplitude increases with decreasing radius of the cylinder, which suggests that the effect becomes relevant for mesoscopic samples.

While the LP effect is originally predicted for a cylinder (or a ring), all singly connected superconductors exhibit oscillations with essentially the same origin [50]. The main difference with the LP oscillations is that for small applied fields the oscillation period is larger than Φ_0 , while for larger fields the oscillation period still converges to Φ_0 . Every oscillation corresponds to the entrance of a vortex into the system. For a singly connected superconductor, vortex entrance is hampered by e.g. the Bean-Livingstone barrier. Additionally, there is the interaction with the vortices already present in the sample. In an infinitely thin cylinder these mechanisms do not occur, which explains the different oscillation period.

To help describe the plethora of vortex configurations, consisting of vortices, giant- and antivortices, which appear in mesoscopic superconductors, we introduce a single quantity, the *vorticity* L . It corresponds to the number of flux quanta inside the outer contour with zero supercurrent, and is integer due to fluxoid quantization. Such a contour always exists in a mesoscopic superconductor containing some vortices since at some contour the Meissner currents at the outer boundary will cancel with the vortex currents in the center (which run in opposite direction). There is however an easier way to determine L , by counting the number of times that the phase of the order parameters changes by 2π at the sample boundary. Consequently, when no giant or anti-vortices are present in the sample, the vorticity L equals simply the number of vortices, since the phase changes by 2π around each vortex. When two or more vortices merge into a giant vortex state, or a vortex-antivortex pair is nucleated, the vorticity is left invariant. Mathematically, the vorticity of a flat mesoscopic sample with outer boundary C in perpendicular magnetic field can be expressed as:

$$L = \frac{1}{2\pi} i \oint_C d\vec{s} \cdot \vec{\nabla} \ln \left(\frac{\psi}{|\psi|} \right).$$

The geometry of a mesoscopic sample can strongly influence the critical field and the current. The critical temperature in the absence of magnetic field is not influenced by sample geometry, but its evolution with field and current is.

By *nanstructuring* i.e. the introduction of nanoscale structures (e.g. holes, pinning centers, magnetic inclusions...) in a superconductor, macroscopic superconductors

can be tuned to exhibit mesoscopic effects. In this way, a considerable increase of the critical currents of superconducting films was achieved.

1.5 Two-band superconductors

Two-band superconductors have been considered since 1959, when Suhl, Matthias and Walker presented a BCS theory for two-band superconductivity, which they speculated could occur in some of the transition metals [51]. Six years later the first evidence that Nb was a superconductor with two energy gaps was reported [52, 53], but was questioned later [54, 55].

MgB₂, a material in which superconductivity is discovered only 10 years ago [56], is the first superconductor unambiguously shown to possess two energy gaps [57, 58]. The material immediately caught scientific attention due to some remarkable properties: it has a critical temperature of about 40K, the highest within its class of binary compounds, and moreover, a value above the theoretical BCS limit [59, 60]. Remarkably, the Cooper pairing happens via the conventional electron-phonon coupling mechanism, as is shown by e.g. the isotope effect [61], photoemission spectroscopy, scanning tunneling microscopy and neutron scattering measurements. MgB₂ possesses two energy gaps: one with $\Delta(0) \sim 2\text{meV}$ and another with $\Delta(0) \sim 7\text{meV}$. Both gaps follow the temperature dependence predicted by the BCS theory, and disappear at the same T_c . According to the BCS formula $2\Delta(0) = 3.53k_B T_c$ the energy gaps should correspond to critical temperatures of 15K and 45K. Due to the interband coupling however both gaps disappear at the same temperature of 40K. The two bands existing in MgB₂ correspond to σ and π orbitals. The σ -band is 2D and the π one 3D. Because of the small overlap the interband scattering is weak, which results in two separate energy bands. The reason why MgB₂ is a clear example of a two-gap superconductor is exactly this weak coupling.

Until today, the evidence of multiband superconductivity has been reported in many other materials. Examples include NbSe₂ [62], Nb₃Sn [63], Lu₂Fe₃Si₅ [64], MgCNi₃ [65], PrOs₄Sb₁₂ [66, 67] and URu₂Si₂ [68], and the newly discovered iron pnictide superconductors [69].

The first GL theory of multigap superconductors, derived from first principles and following the approach of Gor'kov, was done by Tilley, dating back to 1964 [70]. During the last decade, several other GL descriptions of multigap superconductors have been developed. For instance, Zhitomirsky and Dao derived the GL equations for a clean two-gap superconductor from the microscopic BCS model using the Green function approach of Gor'kov [71]. Fitting their theory to experimental data, they were able to estimate several unknown GL parameters within the two-gap model, such as the Josephson coupling strength. In the dirty limit, a GL theory was derived by Gurevich, using the quasiclassical Usadel equations [72], first

by neglecting interband impurity scattering. Later this effect, responsible for two new coupling terms in the GL functional, one of which is interband supercurrent interaction, was included in the theory [73].

1.5.1 Interband coupling

The two condensates in a two gap superconductor do not behave independently of each other. Firstly it is evident that they are coupled magnetically: the supercurrents in one band induce a magnetic field that is also felt by the other band.

Secondly they are coupled through the Josephson coupling. This name is inherited from the British physicist B. Josephson who in 1962 predicted that a current will flow across the link of two weakly coupled superconductors. The principle that Cooper pairs can tunnel from one superconductor to the other through a thin insulating layer is translated to two gap superconductors, so that a Cooper pair from one band can be scattered to the other band.

Thirdly there is the scattering of Cooper pairs on impurities. This modifies the strength of the Josephson coupling and additionally introduces a direct coupling of the supercurrents and an extra non-linear interaction.

All three interactions apart favor the Cooper pair distributions to be similar. When combined, these interactions can lead to novel effects, and this is currently the subject of intense theoretical work.

1.5.2 Non-composite and fractional vortices

In a mesoscopic two-gap superconductor, non-composite vortex states can occur. These are states in which the cores of one vortex in the two condensates are spatially separated. In a bulk superconductor non-composite vortices can never be stable. The equilibrium position of the cores is on top of each other, since this minimizes the energy. However, in mesoscopic samples, as a consequence of different inherent length scales and the resulting different influence of the boundary on each condensate, non-composite states are more likely to occur. In Ref. [74] these vortex states were first studied using the GL theory. and a phase diagram, showing the range of temperatures and magnetic flux for which the non-composite state is thermodynamically stable, was determined.

In addition, mesoscopic two gap superconductors allow for so-called fractional vortex states. These states comprise vortices carrying non-integer multiples of the flux quantum Φ_0 . This situation occurs when condensates in different bands have different vorticity ($L_1 \neq L_2$). In the ground state this can only occur when the intrinsic length scales of the condensates are significantly different.

Let us now work out fluxoid quantization for two band superconductors, starting

from the expression for the supercurrent:

$$\vec{j}_s = \frac{2he}{2\pi} \left(\frac{\psi_1^2}{m_1} \vec{\nabla} \phi_1 + \frac{\psi_2^2}{m_2} \vec{\nabla} \phi_2 \right) - \frac{4e^2}{c} \left(\frac{\psi_1^2}{m_1} + \frac{\psi_2^2}{m_2} \right) \vec{A}. \quad (1.26)$$

In the next step we will switch to different variables: $\psi'_i = \psi/\sqrt{m_i}$, $j'_s = cj_s/4e^2$ but immediately drop the accents:

$$\vec{j}_s = \Phi_0 \left(\psi_1^2 \frac{\vec{\nabla} \phi_1}{2\pi} + \psi_2^2 \frac{\vec{\nabla} \phi_2}{2\pi} \right) - (\psi_1^2 + \psi_2^2) \vec{A}. \quad (1.27)$$

We divide this by the sum of the renormalized Cooper pair densities and integrate around a closed contour lying inside the superconducting material:

$$\oint \frac{\vec{j}_s}{\psi_1^2 + \psi_2^2} \cdot d\vec{s} + \Phi = \Phi_0 \oint \left(\frac{\psi_1^2}{\psi_1^2 + \psi_2^2} \frac{\vec{\nabla} \phi_1}{2\pi} + \frac{\psi_2^2}{\psi_1^2 + \psi_2^2} \frac{\vec{\nabla} \phi_2}{2\pi} \right) \cdot d\vec{s}, \quad (1.28)$$

where Φ , the total flux through the contour, was moved to the left-hand side. We see that if the phase change in both condensates are equal, i.e. $\vec{\nabla} \phi_1 = \vec{\nabla} \phi_2$, we recover the conventional condition of fluxoid quantization:

$$\oint \frac{\vec{j}_s}{\psi_1^2 + \psi_2^2} \cdot d\vec{s} + \Phi = n\Phi_0, \quad (1.29)$$

with n integer. However, in the general case, fluxoid quantization in two band superconductors is not warranted.

Nevertheless, when we assume that both Cooper pair densities are proportional, i.e. $\psi_1^2 = \delta^2 \psi_2^2$, we obtain:

$$\begin{aligned} \oint \frac{\vec{j}_s}{\psi_1^2 + \psi_2^2} \cdot d\vec{s} + \Phi &= \Phi_0 \oint \left(\frac{\delta^2}{1 + \delta^2} \vec{\nabla} \phi_1 + \frac{1}{1 + \delta^2} \vec{\nabla} \phi_2 \right) \cdot d\vec{s} \\ &= \Phi_0 (\delta^2 m + n) \frac{1}{1 + \delta^2}, \end{aligned} \quad (1.30)$$

with m (n) the number of phase windings of 2π in ϕ_1 (ϕ_2). This approach is valid when the contour is located sufficiently far away from condensate inhomogeneities (e.g. vortices), where the Cooper pair densities in two bands heal to their equilibrium value. Moreover, it becomes valid for *any* contour, if the temperature is near the critical temperature [75] (i.e. the strict validity region of the GL equations), and with increasing Josephson coupling.

We conclude that when the vorticity is the same in both bands, the fluxoid is still quantized. When the vorticity differs, the flux carried by the fluxoid is fractional and lies somewhere between m and n , determined by a weighted average, the weights being the corresponding Cooper pair densities.

Fractional vortices have been considered before. For instance, half-quantum vortices can occur on boundaries between 2 superconductors separated by a weak insulating link (i.e. a Josephson junction), but as such are conceptually different from the fractional vortices in two gap superconductors, which carry an arbitrary amount of flux and appear inside the superconductor.

Both non-composite and fractional vortex states are destabilized by an increasing interband coupling such as Josephson or magnetic coupling.

1.5.3 Type 1.5 superconductors

Recently, the existence of a new type of superconductivity, called type-1.5, has been suggested by Moshchalkov *et al.* [41] based on unusual vortex behavior. It is supposed to manifest itself in certain two-gap superconductors where one band is type-I and the other type-II. This leads to the so-called semi-Meissner state [76], where vortices have a non-monotonic vortex-vortex interaction (repulsive at short and attractive at long range) and as a consequence arrange themselves in clusters containing Abrikosov vortex lattices within. However as suggested by Brandt [28], a non-monotonic vortex-vortex interaction can also occur due to other mechanisms. Furthermore, in the past several observations have been made of states of clusters of Abrikosov lattices in e.g. the type-I superconductor Tantalum. As a result, a more precise definition of a new type of superconductivity is necessary.

1.6 Probing the superconducting state

To directly verify the vortex states predicted in this thesis, experiments that visualize vortices should be carried out. This can be accomplished by imaging either the order parameter (Cooper pair density) or the magnetic field profile. The vortex size in each approach is determined by respectively the coherence length and the penetration depth, imposing some constraints to the necessary spatial resolution of the particular imaging technique. Note that while both length scales diverge near the critical temperature, the amplitude of the variations in density and field decreases. Due to the small sizes of these fundamental length scales, the use of microscopic techniques is necessary. It is the purpose of this section to give a brief overview of the currently available techniques. An in-depth review of the magnetic probing of a superconductor is given in Ref. [77].

The first image of an Abrikosov vortex lattice was made in 1967 by Essmann and Trauble using *Bitter decoration* [18]. This technique comes down to sprinkling small ferromagnetic particles (e.g. fine iron powder) onto the surface of a superconductor. During the procedure, the particles experience a force in the direction of the field gradient and therefore finally reside at locations with high magnetic field, i.e. the vortices. Afterwards the distribution of particles is imaged optically, or using

scanning electron microscopy (SEM). This decoration technique is limited to low fields, typically smaller than 10 mT, since the vortex spacing has to be much larger than the penetration depth. It has a very good spatial resolution ($\sim 0.1\mu\text{m}$), but a quite poor field sensitivity ($\sim 10^{-3}$ T). Moreover, to repeat a measurement, the sample surface has to be cleaned each time.

Another method with very high spatial resolution is *magnetic force microscopy* (MFM). It is one particular realization of scanning probe microscopy (SPM), a class of microscopic techniques that involve a very sharp tip in motion just above the surface, scanning the surface line by line, creating a two dimensional image containing information about the surface. In MFM the tip is made of a ferromagnetic material. MFM is an invasive technique in the sense that it can influence the number of vortices and their position, due to the force exerted by the tip on the vortices. The spatial resolution is slightly better than Bitter decoration. It is however still quite insensitive to the exact value of the magnetic field, as the exact magnetization of the tip itself is difficult to determine.

A technique with slightly worse spatial resolution, but better sensitivity to the magnetic field is *scanning Hall probe microscopy* (SHPM). It is based on the Hall effect: a voltage difference will be produced across an electrical conductor, transverse to an electric current in the conductor and a magnetic field perpendicular to the current. Modern Hall probes are made of semiconducting material and are essentially two-dimensional. They are produced as a cross, by two intersecting wires. The area of the intersection determines the spatial resolution which can be as low as $0.1\mu\text{m}$. When placed parallel and close to the surface, the voltage will be proportional to the magnetic flux density passing through the Hall probe and is - in a first approximation - independent of the parameters of the Hall probe. Due to inevitable imperfections, SHPM is not aimed at determining the absolute value of the magnetic field. However, it excels in measuring relative changes of the magnetic field with a precision of about 10^{-8} T.

Currently the method with the highest sensitivity to the magnetic field is *scanning SQUID microscopy*. A DC SQUID consists of two Josephson junctions connected in a loop. Since they are made of a superconducting material, they have to be operated at low temperatures, below their T_c . The voltage across the loop depends on the flux threading the loop. The spatial resolution is thus limited to the size of the loop, which currently is the main weakness of this method.

The first among SPM techniques is *scanning tunneling microscopy* (STM). Its invention in 1981 by Binnig and Rohrer [78] yielded them the Nobel Prize in Physics only five years later. The working principle is based on quantum tunneling: when a conductor (the probe) is brought very close to a surface (the specimen) and a voltage difference is applied, electrons can tunnel through the vacuum between them. This tunneling current can be measured and is a function of the tip position, applied voltage and local density of states (LDOS). The tip of the probe is mounted

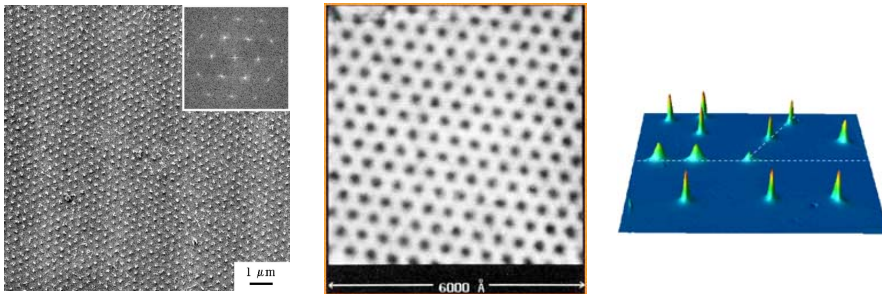


Figure 1.12: Left: Bitter decoration on MgB_2 , from Ref. [79]. Middle: STM on $NbSe_2$, from Ref. [80] Right: Scanning SQUID microscopy image of vortices near a tricrystal point in YBCO, showing whole and half integer quantized vortices, from Ref. [81].

onto a piezoelectric tube, allowing for precise positioning. By an electronic feedback loop, the height of the tip above the sample can be adjusted to maintain a constant tunneling current. This way the sample roughness can be mapped with atomic precision. Other SPM techniques are often combined with STM, to ensure that the actual probe does not crash onto the sample surface. Since Gor'kov showed that the superconducting order parameter is proportional to the LDOS, STM can be employed to directly image the Cooper pair density.

When the dynamics of vortices needs to be studied, none of the above SPM techniques can be used due to the time needed to complete an entire scan of the surface. For real-time imaging, *magneto-optical* (MO) imaging [82] or *Lorentz microscopy* [83] can be utilized. The MO imaging technique is based on the Faraday effect, i.e. the rotation of the polarization of light induced by a magnetic field. Lorentz microscopy is based on the principle of transmission electron microscopy. The sample surface is tilted and electrons are fired on it. They get deflected by the local magnetic field and absorbed elsewhere. This procedure gives fast information about the magnetic field profile.

1.7 Ginzburg-Landau Theory

The Ginzburg-Landau (GL) theory is the main tool I used to study vortex matter in mesoscopic superconductors. The theory is based on the assumption that in the vicinity of T_c , the free energy can be expressed as a series expansion of the order parameter Ψ , a spatially varying complex quantity with its modulus equal to the Cooper pair density (CPD).

The free energy is a functional of Ψ , the order parameter, and \vec{A} , the vector potential. Consequently, a thermodynamically stable state is found when Ψ and \vec{A} simultaneously minimize the free energy. By variational analysis, the equations to which Ψ and \vec{A} obey can be derived. It is the purpose of this section to show this

derivation.

1.7.1 Energy functional

The free energy functional is given by:

$$\mathcal{F} = \int dV \left[\alpha |\Psi|^2 + \frac{\beta}{2} |\Psi|^4 + \frac{1}{2m} \left| \left(-i\hbar \vec{\nabla} - \frac{2e}{c} \vec{A} \right) \Psi \right|^2 + \frac{(\vec{H} - \vec{H}_0)^2}{8\pi} \right], \quad (1.31)$$

with $\vec{H} = \vec{\nabla} \times \vec{A}$ and \vec{H}_0 the applied field. We have cast the free energy into dimensionless form. This is done by introducing a length scale ξ , a scale for the order parameter Ψ_0 and an energy scale F_0 . We transform the variables as:

$$\begin{cases} \vec{r}' = \vec{r}/\xi \\ \vec{\nabla}' = \xi \vec{\nabla} \\ \psi(\vec{r}') = \Psi(\vec{r})/\Psi_0 \\ \vec{A}'(\vec{r}') = \vec{A}(\vec{r})/A_0 \\ \vec{H}'(\vec{r}') = \vec{H}(\vec{r})/H_{c2} \end{cases} \quad (1.32)$$

with

$$\begin{cases} \xi = \sqrt{-\hbar^2/2m\alpha} \\ \Psi_0 = \sqrt{-\alpha/\beta} \\ A_0 = c\hbar/2e\xi \\ H_{c2} = c\hbar/2e\xi^2 \\ F_0 = V\alpha^2/\beta \end{cases} \quad (1.33)$$

In the conventional GL theory, the temperature dependence is taken into account by $\alpha = \alpha_0(1 - T/T_c)$ where α_0 is a negative number and T_c is the critical temperature. This makes the coherence length temperature dependent as $\xi \propto (1 - T/T_c)^{-1/2}$. By substitution we get the dimensionless expression for the free energy $\mathcal{F}' = \mathcal{F}/\xi^3 F_0$, which becomes (after dropping all the accents):

$$\mathcal{F} = \frac{1}{V} \int dV \left[-|\psi|^2 + \frac{1}{2} |\psi|^4 + \left| (-i\vec{\nabla} - \vec{A}) \psi \right|^2 + \kappa^2 (\vec{H} - \vec{H}_0)^2 \right], \quad (1.34)$$

where $\kappa^2 = H_{c2}^2/8\pi F_0 = m^2 c^2 \beta / 8\pi \hbar^2 e^2$.

1.7.2 Derivation of GL equations

The first GL equation

When ψ is a minimum of the free energy (Eq. (1.34)), any infinitesimal variation $\delta\psi$ should leave the free energy invariant, i.e.

$$\delta\mathcal{F} = \int_{V_s} dV \left[-\psi\delta\psi^* + |\psi|^2\psi\delta\psi^* + (\vec{\Pi}\psi)(\vec{\Pi}^*\delta\psi^*) \right] + c.c. = 0, \quad (1.35)$$

where we kept only the leading terms, proportional to $\delta\psi^*$. We also introduced the dimensionless canonical momentum operator $\vec{\Pi} = -i\vec{\nabla} - \vec{A}$. The integration has to be carried out over the superconducting volume V_s since the solution outside is already known ($\psi = 0$).

The last term in Eq. (1.35) can be rewritten as:

$$\begin{aligned} (\vec{\Pi}\psi)(\vec{\Pi}^*\delta\psi^*) &= (\vec{\Pi}\psi)([i\vec{\nabla} - \vec{A}]\delta\psi^*) \\ &= i(\vec{\Pi}\psi)(\vec{\nabla}\delta\psi^*) - (\vec{\Pi}\psi)\vec{A}\delta\psi^* \\ &= i\vec{\nabla}(\delta\psi^*\vec{\Pi}\psi) - i\delta\psi^*\vec{\nabla}\vec{\Pi}\psi - (\vec{\Pi}\psi)\vec{A}\delta\psi^* \\ &= i\vec{\nabla}(\delta\psi^*\vec{\Pi}\psi) - \delta\psi^*\vec{\Pi}^2\psi \end{aligned} \quad (1.36)$$

When we substitute this into the the expression for $\delta\mathcal{F}$ and apply the Gauss' theorem to the first term above, we obtain

$$\delta\mathcal{F} = \int_{V_s} dV \delta\psi^* \left[-\psi + |\psi|^2\psi - \vec{\Pi}^2\psi \right] + i \oint_{S_s} dS \delta\psi^* \left[\vec{n} \cdot \vec{\Pi}\psi \right] + c.c. = 0 \quad (1.37)$$

where \vec{n} is the unit vector perpendicular to the surface S_s of the superconductor. Since the equation above has to apply to arbitrary $\delta\psi^*$, the terms between brackets must be zero. This gives the first GL equation:

$$-\psi + |\psi|^2\psi - \vec{\Pi}^2\psi = 0, \quad (1.38)$$

together with the boundary condition

$$\vec{n} \cdot \vec{\Pi}\psi|_{S_s} = 0, \quad (1.39)$$

which implies no supercurrent can pass through the sample boundary.

The second GL equation

When the vector potential is varied by an amount $\delta\vec{A}$, the part of the free energy containing the magnetic field reads:

$$\mathcal{F}_M(\vec{A} + \delta\vec{A}) = \int dV \left[|(\vec{\Pi} - \delta\vec{A})\psi|^2 + \kappa^2 \left(\vec{\nabla} \times (\vec{A} + \delta\vec{A} - \vec{A}_0) \right)^2 \right], \quad (1.40)$$

with $\vec{\nabla} \times \vec{A}_0 = \vec{H}_0$. The integration is now carried out over the entire space. In the variation of the free energy with respect to \vec{A} , only the mixing terms of the squared terms of Eq. (1.40) occur, since they are linear in $\delta\vec{A}$:

$$\delta\mathcal{F} = \int dV \left[-2 \cdot \delta\vec{A} \cdot \Re(\psi^* \vec{\Pi}\psi) + 2\kappa^2 \cdot \vec{\nabla} \times (\vec{A} - \vec{A}_0) \cdot (\vec{\nabla} \times \delta\vec{A}) \right]. \quad (1.41)$$

The second term in Eq. (1.41) can be rewritten by means of the vector identity $\vec{\nabla} \cdot (\vec{a} \times \vec{b}) = \vec{b} \cdot (\vec{\nabla} \times \vec{a}) - \vec{a} \cdot (\vec{\nabla} \times \vec{b})$ with $\vec{a} = \delta\vec{A}$ and $\vec{b} = \vec{\nabla} \times (\vec{A} - \vec{A}_0)$ as:

$$\int dV \left[2\kappa^2 \cdot \left(\vec{\nabla} \cdot (\delta\vec{A} \times \vec{\nabla} \times (\vec{A} - \vec{A}_0)) + \delta\vec{A} \cdot (\vec{\nabla} \times \vec{\nabla} \times (\vec{A} - \vec{A}_0)) \right) \right]. \quad (1.42)$$

By using the Gauss' theorem, the first term can be cast into a surface integral. Since the surface lies at infinity where $\vec{A} = \vec{A}_0$, this contribution vanishes. The free energy variation thus becomes:

$$\delta\mathcal{F} = 2 \int dV \delta\vec{A} \cdot \left[-\Re(\psi^* \vec{\Pi}\psi) + \kappa^2 (\vec{\nabla} \times \vec{\nabla} \times (\vec{A} - \vec{A}_0)) \right], \quad (1.43)$$

which has to be satisfied for arbitrary $\delta\vec{A}$. This can only be true when the term between brackets itself is zero, and this gives the second GL equation:

$$\vec{j}_s = (\vec{\nabla} \times \vec{\nabla} \times (\vec{A} - \vec{A}_0)) = \frac{1}{\kappa^2} \Re(\psi^* \vec{\Pi}\psi), \quad (1.44)$$

with \vec{j}_s the supercurrent induced in the superconductor by the applied field. If we choose the Coulomb gauge in which $\vec{\nabla} \cdot (\vec{A} - \vec{A}_0) = 0$, Eq. (1.44) reduces to

$$-\Delta(\vec{A} - \vec{A}_0) = \frac{1}{\kappa^2} \Re(\psi^* \vec{\Pi}\psi). \quad (1.45)$$

Useful expression for the free energy

For arbitrary ψ and \vec{A} the free energy has to be calculated by an integration over the entire space. However when ψ and \vec{A} satisfy the GL equations, the free energy can be rewritten as an integral over the sample volume, which is useful for numerical simulations. First consider the kinetic part of the free energy:

$$\begin{aligned} \mathcal{F}_{\Pi} &= \int_{V_s} dV \left| \vec{\Pi}\psi \right|^2 \\ &= \int_{V_s} dV \left[i\vec{\nabla}(\psi^* \vec{\Pi}\psi) - \psi^* \vec{\Pi}^2 \psi \right] \\ &= \int_{V_s} dV \left[-\psi^* \vec{\Pi}^2 \psi \right] \\ &= \int_{V_s} dV \left[|\psi|^2 - |\psi|^4 \right] \end{aligned} \quad (1.46)$$

where in the first step we rewrote the term as in Eq. (1.36), now with $\delta\psi^* \equiv \psi^*$. In the second step we dropped the divergence term since it is zero when the GL boundary condition (1.39) is fulfilled. In the third step we substituted the first GL equation (1.38). When this is entered in the GL free energy we obtain:

$$\mathcal{F} = \int dV \left[-\frac{1}{2}|\psi|^4 + \kappa^2(\vec{H} - \vec{H}_0)^2 \right]. \quad (1.47)$$

The second term in (1.47), i.e. the magnetic part of the free energy, can also be rewritten:

$$\begin{aligned} \mathcal{F}_M &= \kappa^2 \int dV \left[\vec{\nabla} \times (\vec{A} - \vec{A}_0) \right]^2 \\ &= \kappa^2 \int dV \left[\left(\vec{\nabla} \cdot \left((\vec{A} - \vec{A}_0) \times \vec{\nabla} \times (\vec{A} - \vec{A}_0) \right) + (\vec{A} - \vec{A}_0) \cdot \left(\vec{\nabla} \times \vec{\nabla} \times (\vec{A} - \vec{A}_0) \right) \right) \right] \\ &= \kappa^2 \int dV \left[(\vec{A} - \vec{A}_0) \cdot \left(\vec{\nabla} \times \vec{\nabla} \times (\vec{A} - \vec{A}_0) \right) \right] \\ &= \kappa^2 \int_{V_s} dV \left[(\vec{A} - \vec{A}_0) \cdot \vec{j}_s \right] \end{aligned} \quad (1.48)$$

In the first step we rewrote the term as in (1.42), now with $\delta\vec{A} \equiv \vec{A} - \vec{A}_0$. In the second step the term with divergences vanishes since it can be written as a surface integral at infinity where $\vec{A} = \vec{A}_0$. In the third step we substituted the second GL equation (1.44). Since the supercurrent is zero outside the sample volume, the integration is reduced to an integral inside the sample. When this is entered in the GL free energy we finally obtain:

$$\mathcal{F} = \int_{V_s} dV \left[-\frac{1}{2}|\psi|^4 + \kappa^2(\vec{A} - \vec{A}_0) \cdot \vec{j}_s \right]. \quad (1.49)$$

Alternative form of the GL equations

Adding the gradient of a function f to the vector potential \vec{A} leaves the magnetic field \vec{H} invariant, since $\vec{H} = \vec{\nabla} \times \vec{A}$ and the curl of a gradient equals zero. However to describe the same physical situation (same supercurrent and CPD), the phase of the wave function should be rotated with an amount f . Mathematically this is expressed by:

$$\begin{aligned} \vec{A} &\rightarrow \vec{A} + \vec{\nabla}f \\ \psi &\rightarrow \psi \exp(if), \end{aligned} \quad (1.50)$$

This transformation rule ensures that no observable quantities are affected by a change of gauge. This principle is called gauge invariance, and the canonical momentum operator $\vec{\Pi}$ ensures that our results obey this fundamental requirement.

The canonical momentum operator $\vec{\Pi}$ can be written as the standard gradient of a phase-rotated order parameter in the following way:

$$\vec{\Pi}_\mu \psi = \frac{1}{U_\mu} \vec{\nabla}_\mu (U_\mu \psi), \quad (1.51)$$

with $\mu = x, y$ or z and introducing the phase rotation variables U_μ defined as:

$$\begin{cases} U_x(x, y, z) = \exp\left(-i \int^x dx' A_x(x', y, z)\right) \\ U_y(x, y, z) = \exp\left(-i \int^y dy' A_y(x, y', z)\right) \\ U_z(x, y, z) = \exp\left(-i \int^z dz' A_z(x, y, z')\right) \end{cases} \quad (1.52)$$

as can be checked by substitution. The square of the canonical momentum term can be easily derived by applying (1.51) twice:

$$\begin{aligned} \vec{\Pi}_\mu^2 \psi &= \Pi_\mu \left[\frac{1}{U_\mu} \vec{\nabla}_\mu (U_\mu \psi) \right] \\ &= \frac{1}{U_\mu} \vec{\nabla}_\mu^2 (U_\mu \psi), \end{aligned} \quad (1.53)$$

and the GL equations can be rewritten as:

$$\begin{cases} -\psi + |\psi|^2 \psi - \sum_\mu \frac{1}{U_\mu} \frac{\partial^2}{\partial \mu^2} (U_\mu \psi) = 0, \\ \frac{1}{\kappa^2} \frac{1}{U_\mu} \Re \left(\psi^* \frac{\partial}{\partial \mu} (U_\mu \psi) \right) = j_{s\mu}. \end{cases} \quad (1.54)$$

This form of the GL equation will prove to be very useful for numerical simulations, as is explained in detail in Section 1.8.1.1, where the link variable approach is presented.

The GL equations split in amplitude and phase of the order parameter

By expressing the order parameter as $\Psi = \psi \exp(i\phi)$, two separate GL equations can be obtained, one for the amplitude ψ and one for the phase ϕ . When we substitute this into the GL equation (1.38) we obtain an imaginary and a real part which both have to equal zero. This delivers the following equations:

$$\begin{cases} -\psi + \psi^3 - \Delta\psi + \psi(\nabla\phi - A)^2 = 0, \\ \Delta\phi + 2\frac{\nabla\psi}{\psi}(\nabla\phi - A) = 0, \end{cases} \quad (1.55)$$

and the Neumann boundary condition becomes:

$$\begin{cases} \vec{n} \cdot \nabla \psi = 0, \\ \vec{n} \cdot (\nabla \phi - A) = 0. \end{cases} \quad (1.56)$$

The free energy can also be derived for this case, as:

$$F = -\psi^2 + \frac{1}{2}\psi^4 + (\nabla\psi)^2 + \psi^2(\nabla\phi - A)^2, \quad (1.57)$$

and the current is equal to:

$$\vec{j}_s = \psi^2(\vec{\nabla}\phi - \vec{A}). \quad (1.58)$$

1.8 Methodology

The GL equations are a set of non-linear coupled differential equations. An analytic solution is not available except for a few trivial situations. Therefore we will solve the GL equations numerically. The main method used in this work is based on a finite difference (FD) approximation. We map the order parameter ψ and the vector potential \vec{A} onto a regular Cartesian grid with spacing h as illustrated in the left of Fig. 1.13. ψ is defined on the nodes, while \vec{A} is defined on the bonds of the grid. In some cases we employed a finite element method, to solve the linearized first GL equation on more complex geometries.

First we will discuss two methods to solve the first GL equation. Then we show how the second equation can be solved. Finally we outline our approach to obtain a self-consistent solution, thus satisfying both GL equations simultaneously.

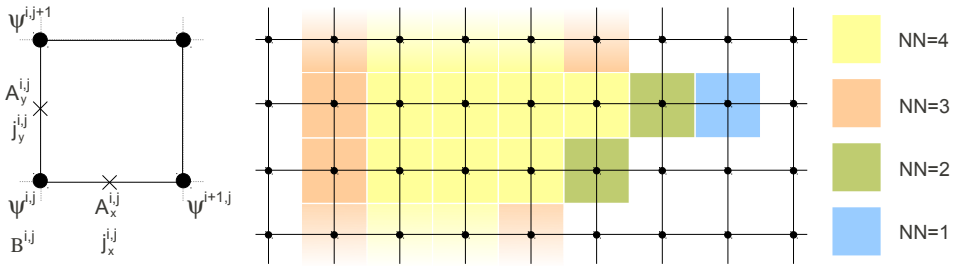


Figure 1.13: The finite difference grid used to solve the GL equations. Left: One unit cell showing the position where all relevant GL variables are defined. Right: Snapshot of a full grid. The colored cells are inside the superconductor, where the color shows the number of nearest neighbours a cell has. The white cells are outside the superconductor.

1.8.1 Solving the first GL equation

1.8.1.1 Finite difference method

To solve the first GL equation, a relaxation method is used. This means that we add an artificial time dependence $\partial\psi/\partial t$ to the right-hand side of Eq. (1.38) and let the system evolve in ‘time’ until a stationary solution is found. Since most of the calculations in this thesis were done in two dimensions, we will show the derivation for this case. However, the extension to three dimensions is trivial. Starting point for the discretization scheme is the first GL equation in the form of Eq. (1.54), i.e. using link variables. This ensures discretized gauge invariance [84–86] and allows for a better numerical convergence [87]:

$$-\psi + |\psi|^2\psi - \frac{1}{U_x} \frac{\partial^2}{\partial x^2}(U_x\psi) - \frac{1}{U_y} \frac{\partial^2}{\partial y^2}(U_y\psi) = \frac{\partial\psi}{\partial t} \quad (1.59)$$

Only the kinetic term contains derivatives and therefore it is the only term that couples the order parameter at one node to its value at the neighboring nodes. We will first show how the term with the second derivative with respect to x can be discretized. The case for y (and z) is completely analogous and we will add it later.

$$\begin{aligned} \frac{1}{U_x} \frac{\partial^2}{\partial x^2}(U_x\psi) &\approx \frac{1}{h^2} \frac{1}{U_x^i} [(U_x^{i+1}\psi^{i+1} - U_x^i\psi^i) - (U_x^i\psi^i - U_x^{i-1}\psi^{i-1})] \\ &= \frac{1}{h^2} [(T_{xp}^i\psi^{i+1} - \psi^i) - (\psi^i - T_{xn}^i\psi^{i-1})], \end{aligned} \quad (1.60)$$

where we introduced the link variables T_{xp} and T_{xn} defined as:

$$\begin{aligned} T_{xp}^i &= \frac{U_x^{i+1}}{U_x^i} = \exp\left(-i \int_{x_i}^{x_{i+1}} dx' A_x(x', y)\right) \\ &\approx \exp(-ihA_x(x_{i+1/2}, y)) \\ T_{xn}^i &= \frac{U_x^{i-1}}{U_x^i} \approx \exp(ihA_x(x_{i-1/2}, y)) = \frac{1}{T_{xp}^{i-1}}, \end{aligned} \quad (1.61)$$

where we approximated the integrals by the value of the integrand in the center times the grid spacing h . x_i represents the x -coordinate of i -th lattice node. Clearly, for the numerical simulation we only need the vector potential at coordinates $x_{i+1/2}$, i.e. on the node links.

The discretized boundary condition in the x -direction reads:

$$\begin{aligned} 0 = \Pi_x\psi &= \frac{1}{U_x} \frac{\partial}{\partial x}(U_x\psi) \\ &\approx \frac{1}{U_x^i} \frac{1}{h} (U_x^{i+1}\psi^{i+1} - U_x^i\psi^i), \\ &= \frac{1}{h} (T_{xp}^i\psi^{i+1} - \psi^i), \end{aligned} \quad (1.62)$$

or equivalently,

$$0 = \frac{1}{h} (\psi^i - T_{xn}^i \psi^{i-1}) \quad (1.63)$$

We can ensure that these boundary conditions are met by incorporating them directly into Eq. (1.60). This can be done by introducing a new variable N_x that counts the number of nearest neighbors *inside* the sample in the x -direction. The link variables need no modification, provided that ψ_i is and stays zero during the relaxation process, when located outside the sample. The discretized kinetic term then becomes:

$$\frac{1}{h^2} (T_{xp}^i \psi^{i+1} - N_x^i \psi^i + T_{xn}^i \psi^{i-1}). \quad (1.64)$$

The complete two dimensional discretized scheme thus becomes:

$$\begin{aligned} \frac{\partial \psi^{i,j}}{\partial t} = & -\psi^{i,j} + |\psi^{i,j}|^2 \psi^{i,j} \\ & - \frac{1}{h^2} (T_{xp}^{i,j} \psi^{i+1,j} + T_{xn}^{i,j} \psi^{i-1,j} + T_{yp}^{i,j} \psi^{i,j+1} + T_{yn}^{i,j} \psi^{i,j-1} - N^{i,j} \psi^{i,j}), \end{aligned} \quad (1.65)$$

with $N^{i,j} = N_x^{i,j} + N_y^{i,j}$. An illustration of the variable N is given in the right panel of Fig. 1.13. The time derivative at left-hand side of Eq. (1.65) should also be replaced by a discretization $\frac{1}{\Delta t}(\psi_{n+1}^i - \psi_n^i)$ with Δt the time step (which is small, but chosen as large as possible in the simulations).

1.8.1.2 Finite element method

We typically used the finite element method to solve the *linearized* first GL equation.

Near the critical temperature both fundamental length scales (ξ and λ) diverge and the influence of the boundary is felt with maximal strength. Mesoscopic phenomena induced by geometry of the sample, such as the formation of giant- or antivortices are then most likely to occur. Near T_c the CPD is very low, and the first GL equation becomes essentially linear. The second GL equation can be neglected, since the supercurrents are weak and do not generate an important contribution to the magnetic field. The GL theory is thus simplified considerably. For this reason it is instructive to use the linear GL theory as a first step to estimate which potential symmetry-induced phenomena could manifest for a certain sample geometry. In a next step, the full GL theory can then be employed to assess the temperature-stability of the found states.

The linearized GL equation reads:

$$\left(-i\vec{\nabla} - \vec{A}\right)^2 \psi = \left(1 - \frac{T_c(H)}{T_c(0)}\right) \psi, \quad (1.66)$$

with the standard GL boundary condition Eq. (1.39). It is equivalent to the Schrödinger equation for a charged particle. $T_c(H)$ is the critical temperature for a

given magnetic field. The temperature appears by explicitly extracting the temperature dependence out of α before making the GL equations linear. The solutions of (1.66) are represented by the eigenstates of the $\vec{\Pi}^2$ operator with eigenvalues $1 - T_c(H)/T_c$. Consequently these eigenvalues determine the critical temperature at a given field, i.e. the superconducting/normal phase boundary.

We solved the linear GL equation using a software package ‘Comsol Multiphysics’, which is able to solve a multitude of differential equations with given boundary conditions. One just has to map the differential equation into a shape convenient for the software. The numerical method used is the finite element (FE) one. The main difference with FD is that, instead of using equal-sized rectangles to divide the simulation region, FE uses triangles, *not* necessarily with the same size or shape. FE has the advantage that complex geometries and boundary conditions become more easy to implement and at points of interest the grid density can be increased locally.

To implement the linear GL equation we use the ‘coefficient form PDE’ which has the shape:

$$d_a \frac{\partial u}{\partial t} + \vec{\nabla} \cdot (-c\vec{\nabla}u - \vec{\alpha}u + \gamma) + \vec{\beta} \cdot \vec{\nabla}u + au = f, \quad (1.67)$$

with boundary condition:

$$\vec{n} \cdot (-c\vec{\nabla}u - \vec{\alpha}u + \gamma) = 0. \quad (1.68)$$

This we cast into the linear GL equation by putting:

$$\left\{ \begin{array}{ll} c = 1 & \text{(diffusion coefficient)} \\ \alpha_x = -iA_x \\ \alpha_y = -iA_y & \text{(conservative flux convection coefficient)} \\ \beta_x = iA_x & \text{(convection coefficient)} \\ \beta_y = iA_y \\ d_a = 1 & \text{(damping/mass coefficient)} \end{array} \right. \quad (1.69)$$

and the other coefficients equal zero. The vector potential is chosen in a gauge with $\vec{\nabla} \cdot \vec{A} = 0$.

In Fig. 1.14 the triangulation of a disk containing a defect in the edge is shown. The grid consists of 757 elements. Also the phase boundary is plotted. It was obtained by solving the linear system for the lowest eigenvalue at 40 different magnetic fields. The total time needed for this calculation on a normal desktop PC was only 90 seconds.

1.8.2 Solving the second GL equation

The second GL equation, calculating the magnetic response of the superconducting sample, is just the Maxwell equation, relating the magnetic vector potential with

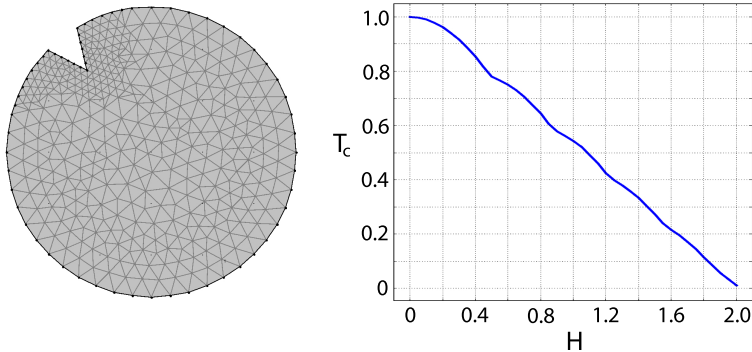


Figure 1.14: Left: Triangulation of a disk (area= $25\xi^2$) with a defect. The grid is refined near the defect. Right: $T_c(H)$ phase boundary computed from this geometry by COMSOL. Every cusp corresponds to a state with different vorticity.

the supercurrents. In the Lorentz gauge, $\vec{\nabla} \cdot \vec{A} = 0$, this equation reduces to 3 ordinary partial differential equations of the Poisson type. In other words, we have to solve three equations, one for each spatial direction, of the shape:

$$-\kappa^2 \Delta A = j. \quad (1.70)$$

When a thin slab is placed in a perpendicular applied magnetic field (say $H \perp z$), one can assume the CPD and supercurrent distribution to be uniform over the sample thickness [88]. Effectively we can thus reduce the numerical problem from three to two dimensions, gaining both in accuracy and performance. Below we will demonstrate how to compute the 3D magnetic field distribution using discrete Fourier transformations in x- and y-direction and an analytic Fourier transform in the z-direction.

In continuous Fourier theory the correspondence between the real (x) and Fourier-space (k) is defined as:

$$\begin{cases} F(k) = \int_{-\infty}^{\infty} f(x) \exp(-2\pi i x k) dx, \\ f(x) = \int_{-\infty}^{\infty} F(k) \exp(2\pi i x k) dx. \end{cases}$$

This, we use to solve the equation analytically in the z-direction. In the x- and y-directions, we will solve the Poisson equations numerically using a Fast Fourier

Transform (FFT) which is based on discrete Fourier relations:

$$\begin{cases} b_n = \frac{2}{N} \sum_{j=1}^{N-1} f_j \sin(j\pi \frac{x_n}{L}), \\ f_j = \sum_{n=1}^{N-1} b_n \sin(j\pi \frac{x_n}{L}), \end{cases}$$

where we have chosen the sine transform, in order to obey the boundary condition $\vec{A}(r \rightarrow \infty) \rightarrow 0$, appropriate for mesoscopic samples. When simulating infinite films the real Fourier transform is used instead. Notice that the vector potential \vec{A} , which is solved for here, represents solely the electromagnetic field induced by the supercurrents of the sample, and does not include the applied magnetic field. N is the number of grid points, and L the size of the simulation region.

The x - or y -components of the vector potential can thus be written in the Fourier expansion as:

$$A(x_m, y_n, z) = \sum_{i=1}^{N-1} \sum_{j=1}^{N-1} \int_{-\infty}^{\infty} dk a_{ij}(k) \exp(2\pi izk) \sin(\frac{i\pi x_m}{L}) \sin(\frac{j\pi y_n}{L}), \quad (1.71)$$

where $1 \leq m, n \leq N$ are integer numbers, $x_m = mL_x/N$, $y_n = nL_y/N$, z is a real number and $a_{ij}(k)$ are the Fourier coefficients of the vector potential. Below the expression for $a_{ij}(k)$ will be derived and the integration over k can thus be done analytically, to give

$$A(x_m, y_n, z) = \sum_{i=1}^{N-1} \sum_{j=1}^{N-1} a_{ij}(z) \sin(\frac{i\pi x_m}{L}) \sin(\frac{j\pi y_n}{L})$$

with the z -dependent Fourier coefficients $a_{ij}(z)$, defined as:

$$a_{ij}(z) = \int_{-\infty}^{\infty} dk a_{ij}(k) \exp(2\pi izk) \quad (1.72)$$

It is the aim of this section to determine these coefficients.

The Laplacian of A can be computed analytically from Eq. (1.71) and reads:

$$\Delta A(x_m, y_n, z) = \sum_{i=1}^{N-1} \sum_{j=1}^{N-1} \int_{-\infty}^{\infty} dk [-(2\pi k)^2 - ij^2] a_{ij}(k) \exp(2\pi izk) \sin(\frac{i\pi m}{N}) \sin(\frac{j\pi n}{N}), \quad (1.73)$$

where we introduced $ij^2 \equiv (i\pi/N)^2 + (j\pi/N)^2$.

We assume the sample with thickness d to be centered at $z = 0$. Now we introduce $j(x, y)$ as the current averaged over the z -direction:

$$j(x, y) = \frac{1}{d} \int_{-d/2}^{d/2} j(x, y, z) dz,$$

and assume that this current is constant over the thickness the sample:

$$j(x, y, z) = j(x, y)\Pi(z, -d/2, d/2),$$

where Π represents the rectangular function which is 1 inside the interval $[-d/2, d/2]$ and 0 outside. It has the Fourier transform:

$$\Pi(k) = d \frac{\sin(\pi kd)}{\pi kd}. \quad (1.74)$$

The 2D averaged current can also be expressed as a sine transform:

$$j(x_m, y_n) = \sum_{i=1}^{N-1} \sum_{j=1}^{N-1} b_{ij} \sin(i\pi m/N) \sin(j\pi n/N), \quad (1.75)$$

with

$$b_{ij} \equiv \frac{4}{N^2} \sum_{m=1}^{N-1} \sum_{n=1}^{N-1} j(x_m, y_n) \sin(i\pi \frac{m}{N}) \sin(j\pi \frac{n}{N}),$$

being the Fourier coefficients, which can be computed by a FFT algorithm as provided in e.g. the Numerical Recipes.

Substituting Eqs. (1.73), (1.74) and (1.75) in Eq. (1.70) we get:

$$\sum_{i=1}^{N-1} \sum_{j=1}^{N-1} \int_{-\infty}^{\infty} dk \exp(2\pi izk) \left(\kappa^2 [(2\pi k)^2 + ij^2] a_{ij}(k) - b_{ij} d \frac{\sin(\pi kd)}{\pi kd} \right) = 0,$$

which can only be satisfied if the term in the brackets is zero. This leads to an expression of the coefficients $a_{ij}(k)$ of the vector potential:

$$a_{ij}(k) = \frac{d}{\kappa^2} \frac{b_{ij}}{(2\pi k)^2 + ij^2} \frac{\sin(\pi kd)}{\pi kd}.$$

This can be substituted into Eq. (1.72) to get the z-dependent Fourier coefficients for which this integral has to be solved:

$$\int_{-\infty}^{\infty} dk \exp(2\pi izk) \frac{1}{(2\pi k)^2 + ij^2} \frac{\sin(\pi kd)}{\pi kd}.$$

We get:

$$\begin{cases} \frac{1}{dij^2} (1 - \cosh(ijz) \exp(-dij/2)) & \text{if } z \leq d/2, \\ \frac{1}{dij^2} (\sinh(dij/2) \exp(-ijz)) & \text{if } z \geq d/2. \end{cases} \quad (1.76)$$

A plot of these expressions is shown in Fig. 1.15. Both expressions and their derivatives are equal at the point $z = d/2$, as they should be. The full expression

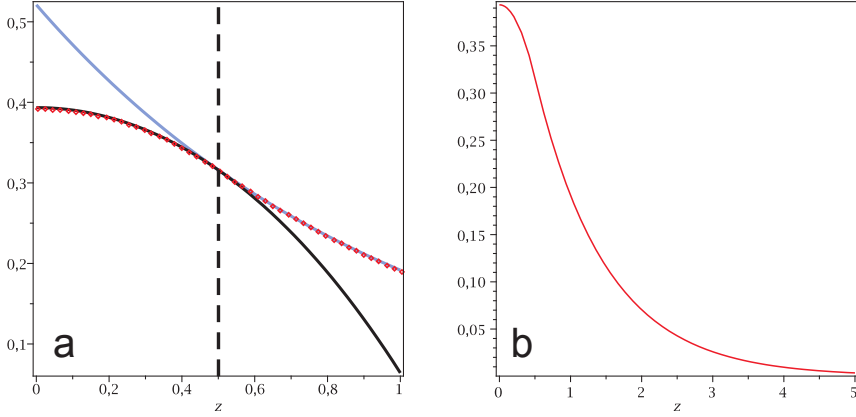


Figure 1.15: A plot of the functions of Eq. (1.76) in black for $z < d/2$, in blue for $z > d/2$. The red dots/line represent the solution valid for all z . In these figures, $ij = d = 1$.

for the z -dependent Fourier coefficients thus reads:

$$a_{ij}(z) = \begin{cases} \frac{b_{ij}}{\kappa^2 ij^2} (1 - \cosh(ijz) \exp(-dij/2)) & \text{if } z \leq d/2, \\ \frac{b_{ij}}{\kappa^2 ij^2} (\sinh(dij/2) \exp(-ijz)) & \text{if } z \geq d/2. \end{cases} \quad (1.77)$$

A full 3D magnetic field profile obtained by this coefficients is shown in Fig. 1.16. For our self-consistent method that simultaneously solves the order parameter and the vector potential however we only need to know the vector potential inside the superconductor, which we can approximate be the value in the center, i.e. at $z = 0$, both for the case of thin and infinitely thick samples. The Fourier coefficients then read:

$$a_{ij} = \frac{b_{ij}}{\kappa^2} \frac{1 - \exp(-d|ij|/2)}{ij^2}. \quad (1.78)$$

From this two limits can be considered: When the sample is an infinite prism, or a bulk sample, i.e. $d \rightarrow \infty$, we get:

$$a_{ij} = \frac{1}{\kappa^2} \frac{b_{ij}}{ij^2}. \quad (1.79)$$

For the case of a thin sample, i.e. $d \ll 1$, we have:

$$a_{ij} = \frac{d}{\kappa^2} \frac{b_{ij}}{2|ij|}, \quad (1.80)$$

which leads to the definition of an effective κ , dependent on the sample thickness, defined as $\kappa_{eff}^2 = \kappa^2/d$.

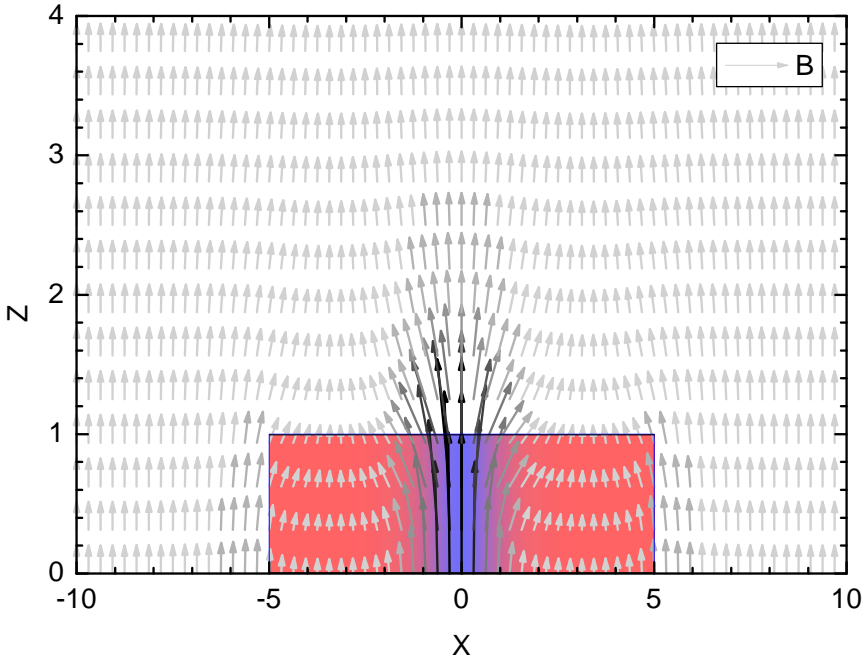


Figure 1.16: A x - z cut at $y = 0$ through a superconducting square with lateral sizes $L_x = L_y = 10\xi$ and thickness $d = 2\xi$ in a perpendicular homogeneous applied magnetic field. The state with one central vortex is shown. The colors red to blue on the superconductor represent high to low CPD. The vector plot represents the local magnetic field, grey to black representing the magnetic field amplitude. Calculated using the Fourier coefficients of Eq. (1.76)

1.8.3 Self-consistent solution

In our procedure, after hundreds of time-steps of solving the first GL equation, the iteration loop is interrupted and the supercurrent is calculated from the new value of the order parameter. This is the input for the second GL equation which returns the magnetic field associated with these currents. To ensure a self-consistent convergence to the solution, the vector potential is only updated slowly by taking a weighted average consisting typically 95% of the old value and 5% of the newly obtained value. Subsequently the link variables are updated with the new vector potential, and the iterations for the first GL equation are resumed. Eventually, the iteration loop will be stopped when the residuals of both GL equations reach the desired relative error threshold, typically of the order of 10^{-5} . For the finite difference method, the magnetic field on the grid is finally calculated as

$$B^{i,j} = \frac{1}{h} (A_y^{i,j} - A_y^{i-1,j} - A_x^{i,j} + A_x^{i,j-1}). \quad (1.81)$$

1.9 Bose-Einstein condensation

Bose-Einstein condensation is a state of matter first predicted by Bose [89] and Einstein [90] in 1924-1925. Just like superconductors, a Bose-Einstein condensate (BEC) is a macroscopic manifestation of a quantum state. In fact superconductivity is a BEC of Cooper pairs. BEC can be realized at ultralow temperatures, when a macroscopic number of identical particles condense into the ground state.

The original prediction was based on a thought experiment that features a system consisting of exactly two energy levels that are populated by a large number of identical particles. From the simple thermodynamic consideration that the probability for the system to be in a certain configuration is proportional to $\exp(-NE/k_B T)$, one can conclude that for a macroscopic number of identical - and thus *indistinguishable* - particles, essentially all of them will populate the state with lowest energy, no matter how small the energy difference between the two states.

In a system of Bose particles, a similar situation occurs when the temperature is sufficiently low and the number of thermally available states becomes smaller than the total number of particles. In contrast to Fermi particles, which are characterized by half-integer spin, Bose particles, which carry integer spin, are not hampered by the Pauli principle and can all occupy the same quantum state; therefore a macroscopic portion will condense into the ground state of the system and form a giant wavelike state of matter, the BEC.

In contrast to the statistical argument given above, a more intuitive explanation, which is based on the particle-wave duality, can be outlined. In the same year of the prediction of BEC, de Broglie presented his hypothesis that every particle has a wavelike character, and vice versa, that every wave has a particle-like character. The corresponding wavelength he predicted to be h/p , the ratio of Planck's constant and the momentum. For an ideal gas, with Maxwell-Boltzmann velocity distribution, the mean wavelength can be derived as $\lambda_{dB} = \sqrt{2\pi\hbar^2/mk_B T}$, known as the thermal de Broglie wavelength. From this it follows that decreasing the temperature will increase the wavelength. The wave nature of matter will become apparent when the de Broglie length becomes of the order of the interparticle distance, the latter which is proportional to $n^{-1/3}$ (n is the particle density). The critical temperature at which the phase transition to a BEC occurs will therefore be proportional to $n^{2/3}$ and in fact equals $T_c = 3.3\hbar^2 n^{2/3}/mk_B$ for a uniform three-dimensional non-interacting gas. Note that for a BEC confined in a trap, this relation is altered significantly: the critical temperature becomes proportional to $n^{1/3}$.

A BEC was first realized in superfluid helium in 1937, however, in ^4He only a small part of the superfluid is condensed which makes it hard to directly observe the Bose-Einstein condensation. Furthermore a superfluid is, as the name says, *fluid*, and the high particle density causes the particles to interact strongly, contrary to

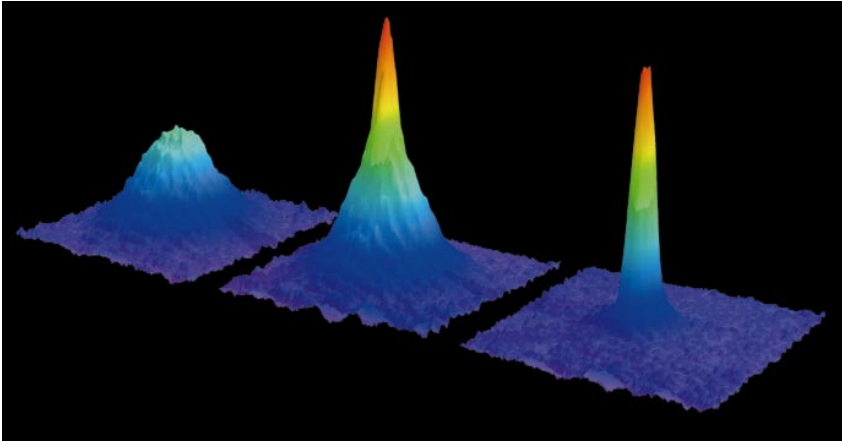


Figure 1.17: Observation of Bose-Einstein condensation by absorption imaging. Shown is absorption vs. two spatial dimensions. The Bose-Einstein condensate is characterized by its slow expansion observed after 6 ms time of flight. The left picture shows an expanding cloud cooled to just above the transition point; middle: just after the condensate appeared; right: after further evaporative cooling has left an almost pure condensate. The total number of atoms at the phase transition was about 7×10^5 , the temperature at the transition point was $2 \mu K$. From Ref. [91].

the case of the ideal gas for which the BEC was originally predicted. The first gaseous BEC was only realized in 1995, with ^{87}Rb atoms by Wiemann and Cornell [92] and with ^{23}Na atoms by Ketterle and co-workers [93] (see Fig. 1.17), 70 years after the theoretical prediction! The reason for this big delay are the technical difficulties encountered when cooling to extreme temperatures. A first obstacle is that at the temperature required for BEC, almost all substances solidificate and form a crystal structure. A BEC is thus metastable and one had to find a way to increase its lifetime. This can be done by minimizing the interparticle interaction, which can be expressed as the condition $na^3 \ll 1$ (a is the scattering length). This required experimentalists to work with even lower densities, pulling the critical temperature even further downwards. The density of a sodium BEC is typically 10^{14} cm^{-3} and $T_c = 2 \mu K$. New technologies for cooling thus had to be developed. It was the combination of two techniques, called *laser* and *evaporative* cooling that eventually led to the realization of a BEC. Additionally, the (electrically neutral) particles have to be confined, and should be thermally isolated from all material walls. This is done by trapping atoms inside ultrahigh vacuum chambers with magnetic fields or with laser light.

One of the most convincing arguments of the BEC as a macroscopic manifestation of a quantum state was provided by an experiment in which two condensates were allowed to overlap [94]. Since each condensate has its own phase, the overlap of two

condensates causes regions of destructive and constructive interference to appear, visible as fringes, a property exclusively reserved for waves. A second demonstrative experimental fact of the quantum nature is that by rotating a BEC (by e.g. stirring it with a laser beam) vortices appear [95], and penetrate the condensate arranged as an Abrikosov lattice, a phenomenon that could not happen in any classical system.

1.9.1 Theoretical description

In a non-interacting (ideal) Bose gas, at temperature absolute zero, all bosons occupy the same single-particle ground state, uniquely determined by the trapping potential. The confinement potential of the trap can usually be approximated by a quadratic expression,

$$V_{trap} = \frac{m}{2}(\omega_x^2 x^2 + \omega_y^2 y^2 + \omega_z^2 z^2),$$

for which the ground state is well known, and is a Gaussian:

$$\phi_0(\vec{r}) = \left(\frac{m\omega_{ho}}{\pi\hbar}\right)^{3/4} \exp\left[-\frac{m}{2\hbar}(\omega_x x^2 + \omega_y y^2 + \omega_z z^2)\right], \quad (1.82)$$

with $\omega_{ho} = (\omega_x \omega_y \omega_z)^{1/3}$. The BEC density distribution then becomes $n(\vec{r}) = N|\phi_0(\vec{r})|^2$, with N the number of bosons. Clearly, the shape is independent of the number of particles and depends only on the trap. However, this contrasts strongly with the observations done in experiment. The condensed cloud appears to be dependent on the number of atoms and for ^{87}Rb and ^{23}Na proves to be much larger than the above prediction. The reason for this is that despite the gas is dilute, interactions do play an essential role in describing many properties of a BEC. In 1961, Gross [96] and Pitaevskii [97] developed a mean-field approach that includes the effect of these interactions, making it possible to describe BEC's fairly accurate without the need for solving a many-body Schrödinger equation. The Gross-Pitaevskii (GP) formalism will be the main tool to investigate BEC's in this thesis.

The GP equation is derived by introducing an order parameter Ψ which is often called the "wave function of the condensate". An essential ingredient of the GP theory is to replace the interparticle interaction by an effective one, $V(\vec{r}' - \vec{r}) = g\delta(\vec{r}' - \vec{r})$, where the coupling constant g is related to the scattering length a through $g = 4\pi\hbar^2 a/m$. This is justified because in a dilute and cold gas only binary collisions at low energy are relevant and these collisions are characterized by a single parameter, the s-wave scattering length a . The time-dependent GP equation reads:

$$i\hbar \frac{\partial}{\partial t} \Psi(\vec{r}, t) = \left(-\frac{\hbar^2 \nabla^2}{2m} + V_{trap}(\vec{r}) + g|\Psi(\vec{r}, t)|^2 \right) \Psi(\vec{r}, t).$$

It can be used to explore the macroscopic behavior of the system, characterized by variations of the order parameter over distances larger than the mean distance between atoms. By substituting $\Psi(\vec{r}, t) = \psi(\vec{r}) \exp(-i\mu t/\hbar)$, with μ the chemical potential, the ground state can be obtained by the solution of

$$\left(-\frac{\hbar^2 \nabla^2}{2m} + V_{trap}(\vec{r}) + g|\psi(\vec{r})|^2 \right) \psi(\vec{r}) = \mu\psi(\vec{r}), \quad (1.83)$$

which is called the time-independent GP equation and has the form of a non-linear Schrödinger equation. The proper normalization condition reads $\int d\vec{r} |\psi|^2 = N$. The chemical potential, μ , is necessary to keep the number of particles constant. When the GP ground state is derived by a variational approach the meaning of μ becomes clear. The energy functional is given by

$$E[\psi] = \int d\vec{r} \left[\frac{\hbar^2}{2m} |\nabla\psi|^2 + V_{trap}(\vec{r})|\psi|^2 + \frac{g}{2} |\psi|^4 \right]. \quad (1.84)$$

To find the ground state, E has to be minimized with constraint that the number of particles stays equal to N . This can be routinely done by the method of Lagrange multipliers, for which we consider the extrema of

$$E[\psi] - \mu \int d\vec{r} |\psi|^2,$$

where μ , the chemical potential, now plays the role of Lagrange multiplier, i.e. it assures the proper normalization of Ψ . From this, Eq. (1.83) can be recovered. A simplified expression for the energy can be obtained by multiplying Eq. (1.83) by ψ^* , doing integration by parts, and identifying the result with Eq. (1.84) after which we get the energy per particle:

$$\frac{E}{N} = \mu - \frac{g}{2N} \int dV |\psi|^4. \quad (1.85)$$

The ground state solution in the case of no interaction was already given in Eq. (1.82). The solution in the case of a very strong interaction (N large) is called the Thomas-Fermi approximation and can easily be obtained from the GP equation by neglecting the kinetic energy contribution. The density then reads

$$n(\vec{r}) = |\psi(\vec{r})|^2 = g^{-1} [\mu - V_{trap}(\vec{r})] \quad (1.86)$$

in the region where $\mu > V_{trap}(\vec{r})$ and $n = 0$ outside.

In the case of an anisotropic trapping potential with $\omega_z \gg \omega_\perp \equiv \omega_x = \omega_y$, the condensate will be pancake-shaped and can effectively be described by a 2D GP equation. The approximation is based on the assumption that in the z -direction, the condensate is in the ground state. The derivation to 2D will be given after casting the 3D equations in a dimensionless shape.

The GP equation can be cast into dimensionless units by introducing $l_{\perp} = \sqrt{\hbar/m\omega_{\perp}}$, the length scale of the harmonic confinement in the xy -plane, and $|\phi|^2 = |\psi|^2 l_{\perp}^3 / N$, the dimensionless BEC density, normalized to unity. Energy and the chemical potential are then expressed in $E_0 = \hbar\omega_{\perp}$. Thus,

$$\left(-\frac{1}{2}\Delta + \frac{1}{2}r^2 + \frac{1}{2}\left(\frac{\omega_z}{\omega_{\perp}}\right)^2 z^2 + g_{3D}|\phi|^2 - \mu \right) \phi = 0 \quad (1.87)$$

with $g_{3D} = 4\pi Na/l_{\perp}$ and $r^2 = x^2 + y^2$.

Now, we make the ansatz that the BEC wave function can be written as $\phi(x, y, z) = R(x, y)Z(z)$ [98, 99]. R and Z are normalized to 1 and are substituted in Eq. (1.87). After multiplication by Z^* and integration over the z -axis, the two-dimensional GP equation is found:

$$\left(-\frac{1}{2}\Delta_{2D} + \frac{1}{2}r^2 - \mu + E_z \right) R + g_{3D}|R|^2 R \int dz |Z|^4 = 0, \quad (1.88)$$

with

$$E_z = \int dz Z^* \left(-\frac{1}{2}\frac{\partial^2}{\partial z^2} + \frac{1}{2}\left(\frac{\omega_z}{\omega_{\perp}}\right)^2 z^2 \right) Z,$$

being the energy of the solution in the z -direction. Thus we arrive at the definition of an effective 2D interaction strength:

$$g_{2D} = g_{3D} \int dz |Z|^4.$$

In the case of condensates with few atoms, the interaction is weak, and a good approximation in the z -direction is just the ground state of the harmonic oscillator:

$$Z = \left(\frac{1}{\pi} \frac{\omega_z}{\omega_{\perp}} \right)^{1/4} \exp\left(-\frac{z^2}{2} \frac{\omega_z}{\omega_{\perp}} \right),$$

so that

$$g_{2D} = g_{3D} \frac{1}{\sqrt{2\pi}} \sqrt{\frac{\omega_z}{\omega_{\perp}}} = 2\sqrt{2\pi} N \frac{a}{l_z} \quad (1.89)$$

with $l_z = \sqrt{\hbar/m\omega_z}$. Summarizing, the 2D GP equation reads:

$$\left(-\frac{1}{2}\Delta + \frac{1}{2}r^2 + g_{2D}|\psi|^2 - \mu \right) \psi = 0 \quad (1.90)$$

where E_z was absorbed into μ , R was replaced by ψ , and $\int dx dy |\psi|^2 = 1$. It is valid when $a \ll l_z \ll l_{\perp}$.

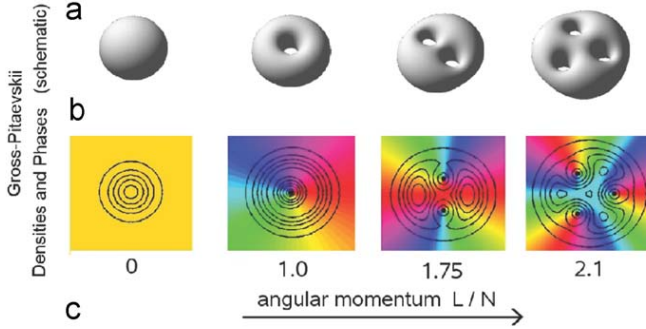


Figure 1.18: Vortices in a rotating BEC. The top row schematically shows the vortex holes that penetrate the boson cloud with increasing angular momentum. The bottom row shows the corresponding phase of the order parameter and the density contours (the black dots indicate the vortex positions). From Ref. [100].

1.9.2 Rotating BEC

A BEC is a superfluid and therefore behaves quite differently from a normal fluid when subjected to rotation. To transfer angular momentum to a BEC one can for instance stir it by a laser beam or apply a (slightly) asymmetric rotating confinement potential. Nevertheless, below a certain threshold angular velocity, the BEC will remain at rest, since a superfluid can not perform rigid rotations. Above this threshold however, the applied rotation will manifest itself by a single vortex entering the condensate. This vortex is characterized by a zero density at its center and a phase difference of 2π for any path around it. The angular momentum per particle of the condensate is now exactly equal to \hbar . By increasing the angular speed above a second threshold, an extra vortex penetrates the cloud. They will take non-central positions, and the angular momentum per particle will be about $1.75\hbar$. Increasing the speed more, one successively finds transitions between states carrying a different number of vortices, as illustrated in Fig. 1.18.

When a lot of vortices are generated in a BEC, they form a triangular *Abrikosov* lattice. Just as in type-II superconductors vortices repel and multiquanta vortices are not favored (in the homogeneous case). Due to the strong interaction of atoms with light of the right frequency, an optical lattice can serve as a grid of pinning centers, making it possible to switch from a triangular to a square lattice configuration as demonstrated by the experiment of Tung *et al.* in 2006.

Due to the centrifugal forces induced by rotation, the BEC clouds expands in the radial direction and becomes more dilute. This poses a maximum to the rotation speed: for a purely harmonic confinement potential $\Omega_{max} = \omega_{\perp}$ as then the centrifugal force overcomes the confining force and the gas flies apart. The critical velocities at which vortices enter the condensate are strongly dependent on

the coupling strength g . In a linear system with $g = 0$, the first critical angular velocity equals the centrifugal force, thus disallowing vortices. When the system becomes more non-linear, i.e. g increases, the critical angular velocity decreases and the formation of vortices becomes energetically favorable. Nevertheless, to study a weakly interacting BEC in rotation it is possible to choose the confinement stronger than parabolic. By optical beams it is possible to additionally generate a quartic component in the confinement potential, allowing the gas to stay together for even higher angular velocities.

In the GP formalism, the energy of a BEC rotating with angular velocity Ω around the z -axis, in the co-rotating frame becomes:

$$E_r = E - \Omega L_z$$

with $L_z = (\vec{r} \times \vec{p})_z = -i\hbar(\vec{r} \times \vec{\nabla})_z$. The GP equation in dimensionless units thus becomes:

$$\left(-\frac{1}{2}\Delta + \frac{1}{2}r^2 + g_{2D}|\psi|^2 - \omega L_z - \mu \right) \psi = 0 \quad (1.91)$$

with $\omega = \Omega/\omega_\perp$ and $L_z = -i(x\partial/\partial y - y\partial/\partial x)$. The Laplacian, the confinement and the angular momentum term can be combined, and we obtain:

$$\left(\frac{1}{2}(-i\vec{\nabla} - \vec{A})^2 + \frac{1}{2}(1 - \omega^2)r^2 + g_{2D}|\psi|^2 - \mu \right) \psi = 0 \quad (1.92)$$

with $A_x = \omega y$ and $A_y = -\omega x$. This formulation shows clearly that the confinement is lost when $|\omega| \geq 1$. Additionally it is very similar to the first Ginzburg-Landau equation, only difference being the extra confinement potential and the chemical potential. The non-linearity g_{2D} of the BEC corresponds to the temperature dependence $1 - T$ of the superconductor.

1.9.3 Numerical method

To solve the GP equation numerically, the same algorithm that solves the first GL equation can be used after adding the confinement and chemical potential. Link-variables, containing the rotation as a gauge field, are used and simple Euler time steps are performed to let the solution relax to a stable state. The difference with the GL equation is that the only boundary condition is that ψ has to be normalized to unity. Therefore after every time step the chemical potential μ has to be adapted to ensure the proper normalization.

To find the μ that features a ψ normalized to unity, three quantities are relevant for our algorithm: (1) $N(t) = \int dx dy |\psi(t)|^2$, the current normalization at time t , (2) $\delta N(t) = N(t) - N(t - \delta t)$, the change of the normalization over the last time step δt and (3) $r(t) = |\delta N(t)/(N(t) - 1)|$, the rate at which N approaches 1. This rate we want to keep lower than a threshold rate r_t to avoid overshooting the correct

μ . r_t is chosen in order to minimize the convergence time. In every time step, μ is adjusted by an amount of the order of $\delta\mu = |N(t) - 1|$. From the GP equations it is easily seen that increasing (decreasing) μ also increases (decreases) N .

To outline the algorithm, we start by assuming a high normalization, $N > 1$. Two situations can occur: either the normalization is decreasing, as it should, or it is increasing. The latter case is simple: μ must be decreased and we do this by an amount $\delta\mu$. In the former case we must avoid, or at least counteract, possible overshooting. This we do based on the rate r : when $r > r_t$, we are approaching $N = 1$ too fast and we will precautionary decrease μ by $\delta\mu/2$; when $r < r_t$, we will speed up the rate by increasing μ by $\delta\mu$. The case of a too low normalization ($N < 1$) is analogous, only the signs in front of $\delta\mu$ are reversed. We solve ψ and μ self-consistently until both quantities are below a certain error threshold. The pseudocode is given in Algorithm 1.

Algorithm 1 Solving the GP equation

```

1: procedure SOLVEGP
2:   repeat
3:      $\psi \leftarrow \psi + \delta t \cdot GP(\psi, \mu)$            ▷ Do one (or more) time step(s)
4:      $N \leftarrow \int dx dy |\psi|^2$                    ▷ Compute the normalization  $N$ 
5:      $\delta N \leftarrow N - N_{prev}$ 
6:      $\delta\mu \leftarrow (N - 1)$ 
7:      $r \leftarrow |\delta N / \delta\mu|$ 
8:     if  $\delta N \cdot \delta\mu < 0$  then                       ▷ If  $N$  evolves in the right direction
9:       if  $r < r_s$  then                               ▷ If convergence rate is slow
10:         $\mu \leftarrow \mu - \delta\mu$                    ▷ Speed up the change of  $N$ 
11:       else                                          ▷ Convergence rate is too fast
12:         $\mu \leftarrow \mu + \frac{1}{2}\delta\mu$            ▷ Slow down the change of  $N$ 
13:       end if
14:     else                                          ▷  $N$  evolves in the wrong direction
15:        $\mu \leftarrow \mu - \delta\mu$                    ▷ Change  $\mu$  to counteract this
16:     end if
17:      $N_{prev} \leftarrow N$ 
18:   until  $|GP(\psi, \mu)/\psi| < e_\psi$  and  $|N - 1| < e_N$ 
19: end procedure

```

Fig. 1.19A illustrates how the algorithm converges to the solution, and its dependence on r_t , the threshold rate at which the convergence is damped. When allowing for high rates (e.g. $r_t = 0.10$), the algorithm converges rather slowly by a damped out-of-phase oscillation of μ and N resulting in a spiraling convergence curve in the $\mu - N$ plane. Lowering the threshold rate (e.g. $r_t = 0.05$) results in a stronger damping of the oscillations, while the frequency decreases only slightly.

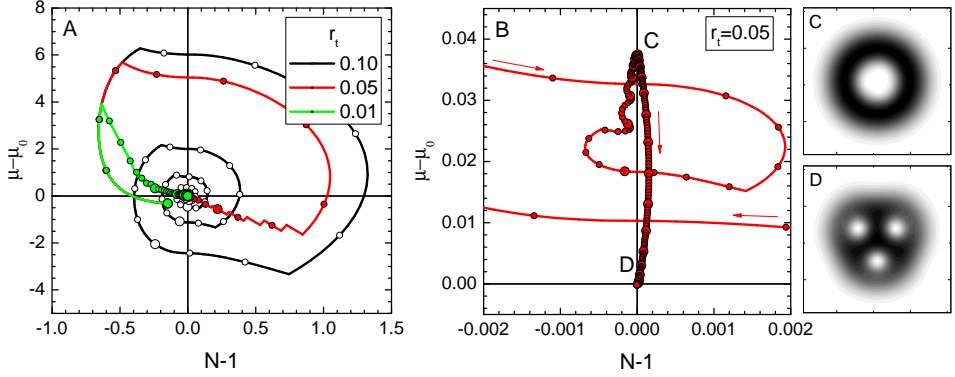


Figure 1.19: A: $(\mu - \mu_\infty)$ vs $(N - 1)$ plot showing the convergence of the algorithm (1) using different values of r_t the threshold rate. Small (large) circles are drawn every 10 (100) time steps. B: The same plot, zoomed in for $r_t = 0.05$. First the algorithm is led to a metastable state C, with giant vortex in the center. Later it converges to the ground state D, the $L = 3$ multivortex. Panels C and D show the corresponding density plots. A radial symmetric phase winding of $3 \times 2\pi$ was imprinted on the initial state. Parameters in the simulations were $g = 40$, $\omega = 0.85$, $\delta t = 0.001$.

When being even more restrictive on the convergence rate (e.g. $r_t = 0.01$), the correct normalization is reached directly, without oscillation. However the correct ψ is not necessarily found faster than for the case with $r_t = 0.05$. The choice of r_t , in combination with the characteristic parameters of the system and the time step, determines the eventual time required to find a stable solution. Fig 1.19B is a zoom-in of A for $r_t = 0.05$ and demonstrates that the algorithm initially might converge towards a metastable solution, fix the proper normalization, afterwards making the transition to a lower energy state, and fixing the normalization again.

Chapter 2

V-Av molecules in mesoscopic single-gap superconductors

All sub-atomic particles have a fraternal twin: an antiparticle, exactly alike except for e.g. opposite charge or helicity. However, as a general rule, matter and antimatter cannot coexist without excess energy and annihilate each other.

This universal duality has its analogue in the physics of superconductors, where vortices as the carriers of magnetic flux play the role of charged particles. Namely, vortex-antivortex pairs in superconducting films can be induced in a local hot-spot, created by thermal fluctuations [101–103], photon absorption [104], or driving current [105, 106]. Intuitively, vortex-antivortex pairs are easily stabilized in an inhomogeneous magnetic field, such as one resulting from dipolar magnetic objects in the vicinity of the superconductor [107–111].

Contrary to latter examples, during the last decade theoretical studies [47, 112–117] have shown that vortex-antivortex (V-Av) structures can be stabilized in submicron superconductors even in *homogeneous* magnetic field, and *without any apparent energy input*.

V-Av states are counterintuitive and rather difficult to explain in usual terms. Nevertheless, by analyzing the solutions of the linearized Ginzburg-Landau (GL) theory, Chibotaru *et al.* [47] predicted their stability in flat superconducting squares as a consequence of the symmetry of the sample. Namely, in linear theory, the geometry of the sample boundaries directly translates on the vortex states. As a consequence, for three fluxons captured by a square sample (i.e. vorticity $L = 3$), the vortex state with four vortices and one antivortex can be energetically more favorable than the triangular configuration of single vortices. Still, one should bear

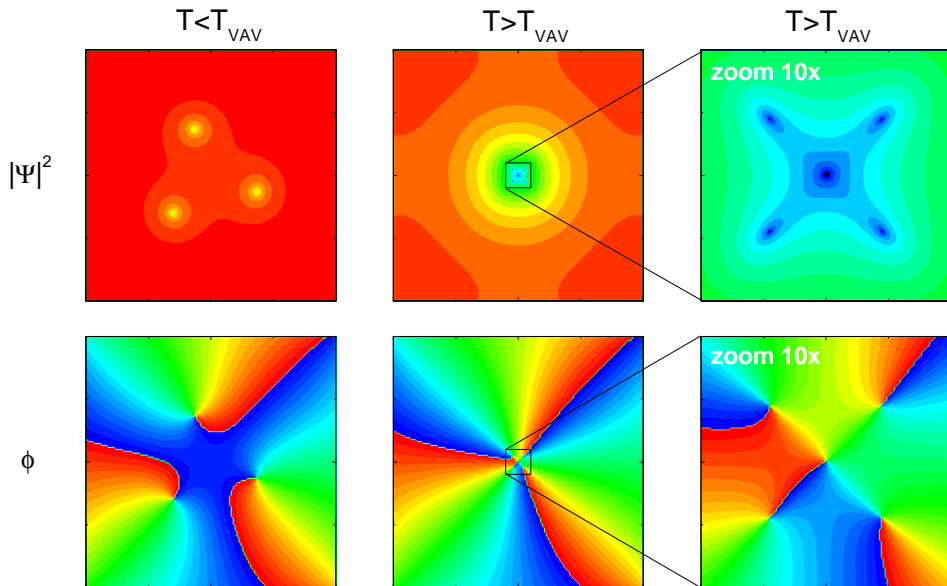


Figure 2.1: Cooper pair density (top) and phase distribution (bottom) for the state with vorticity $L = 3$ at two different temperatures: below and above the V-Av pair nucleation temperature T_{V-Av} . In the colorscale, blue to red represent low to high for the Cooper pair density and $-\pi$ to π for the phase. The phase changes clockwise from blue to red around ‘normal’ vortices while it goes counterclockwise around antivortices.

in mind that the linear approach of Ref. [47] is only valid at the superconducting/normal (S/N) boundary, where Ψ is extremely small and the non-linear term in the GL theory becomes negligible.

In a further step [113, 115], by taking into account the non-linearity of the first GL equation, the existence of V-Av states was predicted to persist even away from the S/N phase boundary. The antivortex for $L = 3$ in a square of size $10\xi_0 \times 10\xi_0$ was shown to be stable in a temperature range of about $\Delta T = 0.3T_c$ (with ξ_0 being the coherence length at $T = 0$, and T_c the critical temperature).

An antivortex is defined as a vortex rotating in the opposite direction of a *usual* vortex. In a homogeneous magnetic field, usual vortices enhance the magnetic field inside their core, and oppose it outside their core. Their purpose is to allow the flux to penetrate the superconductor locally, while keeping the bulk of the superconductor flux free. An individual vortex carries a flux equal to the flux quantum, Φ_0 . The usual vortices form the Abrikosov lattice in a bulk type-II superconductor. Above the first critical field, the nucleation of these vortices lowers the energy of the superconductor, and therefore they are thermodynamically stable objects. An antivortex instead has currents rotating in the opposite direction and

carries a flux $-\Phi_0$. By itself it is not thermodynamically stable in bulk: it will be pushed out of the sample due to interaction with the magnetic field or it will annihilate with a nearby ‘usual’ vortex. However in certain mesoscopic systems and due to the important influence of sample geometry therein, coexistence of vortices and antivortices is predicted by GL theory.

In the top row of Fig. 2.1 contour plots of the Cooper density of the state with vorticity $L = 3$ in a mesoscopic square are depicted for two different temperatures: below and above the V-Av pair nucleation temperature T_{V-Av} . For $T < T_{V-Av}$, the multivortex state is stable and three minima can be distinguished, each corresponding to a usual vortex. However for $T > T_{V-Av}$, instead of three minima, five minima are observed, corresponding to four vortices surrounding one central antivortex. To determine which minima correspond to vortices and which to antivortices it is convenient to look at the phase of the order parameter, depicted in the second row of Fig. 2.1, as its gradient gives the direction of the supercurrent. The phase changes clockwise from blue to red around ‘usual’ vortices while it goes counterclockwise around antivortices.

Up to now, such V-Av configurations have not been visualized in experiment. From a theoretical viewpoint, there are several reasons why these novel vortex states escaped experimental observation: first, even a tiny defect at the boundary ($< 1\%$) destroys the vortex-antivortex state [114]. Second, the vortices and the antivortex are all confined in a small area of typical size less than the coherence length $\xi(T)$. As a consequence, this proximity results in a strong local suppression of the order parameter Ψ which makes the separate minima experimentally undistinguishable - the vortex configuration as a whole is very similar to a single giant-vortex. Third, imaging of the magnetic field profile is also shortcoming: the field generated is proportional to the supercurrent which is rather weak in the V-Av region (being directly related to Ψ).

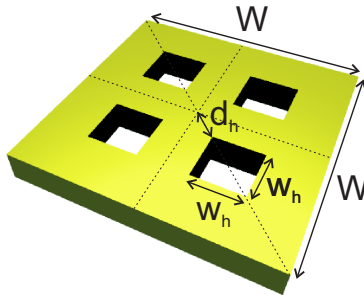


Figure 2.2: Superconducting square with four nanoholes (i.e. antidots).

To solve these issues, we introduced [118] the idea of strategically made perfora-

tions (also called holes or antidots) in a square mesoscopic superconductor (see Fig. 2.2) which act as pinning centers for the vortices. The pinning force is supposed to pull the vortices further from the sample center and thus create a larger separation between the vortices and the central antivortex. In what follows, we will elaborate further on this concept, and demonstrate a number of its advantages. While previous studies [47, 112, 113, 115] only studied V-Av configurations in extremely thin samples, we consider samples of finite (though relatively small) thickness, by incorporating magnetic screening effects in the calculation.

2.1 Symmetry induced V-Av state at T_C

2.1.1 Linear GL theory

Since the V-Av state is a consequence of the symmetry of the sample boundary and because of the most efficient reflection of this symmetry into the solutions of the linearized Ginzburg-Landau (LGL) theory, the LGL formalism is the ideal instrument to study the influence of the geometry on the V-Av state. From a numerical point of view, the linear approach is far less demanding than the full non-linear treatment, and can still provide us with the minimal requirements for the realization of the V-Av states.

The linear theory is *exactly valid only on the S/N boundary*, i.e. when the $|\Psi|^3$ term can be neglected. Due to the weak superconducting order parameter, the magnetic field equals the applied one and the second GL equation can be disregarded. The linear GL equation was discussed in section 1.8.1.2 and reads

$$(i\nabla + \mathbf{A})^2\psi = \alpha\psi, \quad (2.1)$$

(in dimensionless units) where α is equivalent to an eigenvalue. The shape of the sample boundaries is introduced in our calculation through the Neumann boundary condition, which sets the supercurrent perpendicular to the boundary equal to zero:

$$\mathbf{n} \cdot (-i\nabla - \mathbf{A})|_{\text{boundary}} = 0, \quad (2.2)$$

where \mathbf{n} is the normal unit vector on the surface. In Refs. [47, 112, 119] a unitary transformation was used in combination with a certain gauge for the vector potential such that for the linear GL equation $\mathbf{A} = 0$ on the sample boundary. This approach is restricted to simple geometries (i.e. polygons) and cannot be applied to our multiply connected samples that contain holes.

An important property of Eq. (2.1) is that its solution is independent of the size of the sample, as long as the applied flux is held constant, i.e. the LGL method is a scalable theory.

To be able to compare the solutions of the LGL obtained for different geometries, one has to make sure that they have the same normalization. We use the following

normalization of the wave function, $\frac{1}{V} \int_V dV |\Psi|^2 = 1$, or equivalently $\langle |\Psi|^2 \rangle = 1$, where the integration is performed over the sample volume V . This matches the uniform solution of $|\Psi| = 1$ in the whole sample in the absence of a magnetic field. Our aim is to use the LGL model deeper inside the superconducting state, even though it is strictly not valid, simply as a limiting case of the full GL theory. For that purpose we still calculate the generated magnetic field profile using the second GL equation, Eq. (1.45). Although the LGL theory is not able to determine an absolute order of magnitude of the field (because $\Psi \approx 0$), it gives the correct magnetic field up to a multiplying constant, and thus allows for comparison of field profiles for different sample geometries.

We compute the vector potential \mathbf{A} from the calculated distribution of supercurrents, for taken effective $\kappa_{eff} = 1$. For this purpose, we solve two independent Poisson equations (for A_x and A_y) using the Fast Fourier Transform. Magnetic field is then obtained as $\mathbf{B} = \nabla \times \mathbf{A}$. The relative magnetic field profile found in this way turns out to be rather accurate, even when going deeper in the superconducting state (e.g. by decreasing temperature). When compared with a calculation based on the full non-linear GL theory, the main effect of the second equation is to enhance the magnetic field generated by the sample.

As an advantage, to solve Eq. (2.1) is computationally not very demanding, and we use the numerical package COMSOL (formerly known as Femlab) for this purpose. This software package uses the finite element method to solve differential equations. Its high precision in solving linear equations allows us to significantly increase the grid resolution, for instance, in the neighborhood of the V-Av molecule. The use of triangular finite elements proved as a more accurate treatment of the sample geometry than we could achieve with a rectangular grid, for any arbitrary sample geometry.

Therefore, our linear approach is well suited for comparison of the V-Av state in different samples. We will use it to determine the optimal hole parameters and to study the influence of imperfections and defects. We will also treat the competition of different pinning symmetries and samples with different geometries, like e.g. perforated disks, in search for novel V-Av states.

2.1.2 Engineering of the artificial pinning sites

In what follows, we will study the optimal parameters of the artificial pinning centra, i.e. size and position of the holes introduced in the mesoscopic sample, using the linear GL theory. Later on, the influence of the non-linearity of the GL equations and the inclusion of the second GL equation will be systematically investigated.

Our aim is to enhance the parameters that characterize the V-Av state. These are: (i) the maximal Cooper-pair density (CPD) between the V and Av ($|\psi|_{max}^2$)

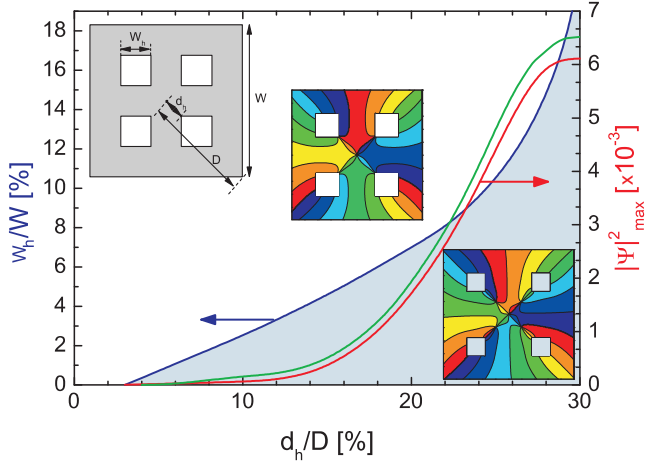


Figure 2.3: Blue: The minimum size W_h of the hole for the vortices to be fully captured by the holes at distance d_h . Above the blue line, vortices are contained in the holes. Below the blue line, vortices are outside and between the holes. Red: The maximum CPD between the vortex and the antivortex when the holes are minimum sized. Green: Dimensionless quantity ΔB_{V-Av} , expressing the strength of the magnetic field difference measured in the vortex and in the antivortex. Insets are contour plots of the phase of the wave function (blue/red corresponds to $0/2\pi$) for $d_h/D = 28\%$ and $w_h/W = 18\%$ (upper) and $d_h/D = 36\%$ and $w_h/W = 14\%$ (lower). The applied flux is $\phi = 5.5\phi_0$.

because of the need of imaging techniques like STM for a sufficient contrast in the local density of states, (ii) the distance between V and Av (d_{V-Av}) which has to be larger than the spatial resolution of the measurements, and (iii) the magnetic field difference between V and Av (ΔB_{V-Av}) relevant for magnetic measurements.

The influence of the holes on the vortices is determined by their position and their size. How can we enhance e.g. the vortex-antivortex separation by manipulating these parameters? Holes are known to be pinning sites, i.e. they attract vortices. By placing four holes in the sample, we can attempt to pull the vortices, which surround the antivortex, away from the antivortex. The larger the holes, the stronger the pinning. The forces on the antivortex are exactly cancelled because of the symmetric position of the holes. However, the vortices also experience inward forces, i.e. they are attracted by the antivortex and additionally the Meissner current also compresses the vortices to the inside of the sample. The vortices eventually will find an equilibrium position, in which the inward and outward forces cancel exactly. This position depends on the distance of the holes to the center and on the size of these holes.

To understand the influence of the hole parameters (size and position) we introduce a criterium to determine the optimal hole parameters. This criterium is the

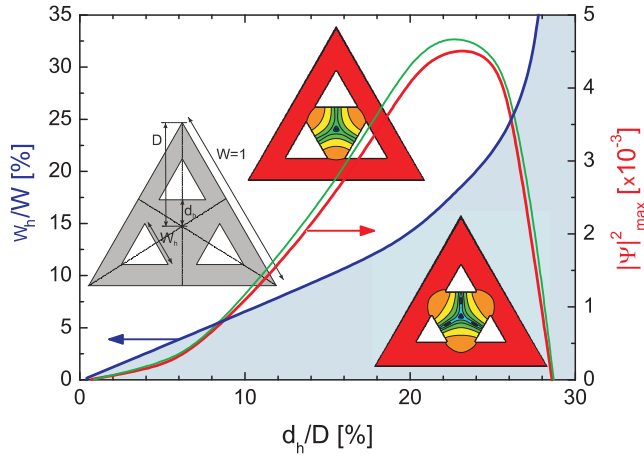


Figure 2.4: Blue: The minimum size w_h of the hole for the vortices to be fully captured by the holes at distance d_h . Above the blue line, vortices are contained in the holes. Below the blue line, vortices are outside and between the holes. Red: The maximum CPD between the vortex and the anti vortex when the holes are minimum sized. Green: Dimensionless quantity ΔB_{V-Av} , expressing the strength of the magnetic field difference measured in the vortex and in the antivortex. Insets are contour plots of the CPD of the wave function (blue/red corresponds to low/high density - logarithmic color scale) for $d_h/D = 22\%$ and $w_h/W = 24\%$ (upper) and $d_h/D = 24\%$ and $w_h/W = 18\%$ (lower). The applied flux is $\phi = 3.5\phi_0$.

minimum hole size for a given hole position, such that the vortex is still captured by the hole. It appears that when holes are made larger, they attract the vortices more strongly and eventually the vortex will be captured by the hole, when the holes are placed not too close to the boundary of the sample. We show our results in Fig. 2.3 and Fig. 2.4 for the square and the triangle geometry, respectively. The insets show the setup and the definition of the hole parameters. The characteristic variables $d_h (= d_{V-Av})$, $|\psi|_{max}^2$ and ΔB_{V-Av} are also shown in Figs. 2.3 and 2.4. We note that the curves of $|\psi|_{max}^2$ and ΔB_{V-Av} are isomorphous. We expected this, because $|\psi|_{max}^2 \propto |\psi|^2 \propto j_s \propto \Delta B \propto \Delta B_{V-Av}$. The maximum $|\psi|_{max}^2$ and, as a consequence, maximum ΔB_{V-Av} , in a triangle appear to be 40 % smaller than for the square.

From these figures, we can conclude that, for both the square and the triangle shaped samples, moving the holes further from the center implies enlarging them, in order to keep the vortices trapped by the holes. From a certain distance d_h , the needed hole size w_h diverges, i.e. from a certain distance of the holes, they can never be made large enough to trap the vortices that surround the antivortex. For both the square and the triangle, this threshold distance d_h/D is about 30%. While for the square increasing the distance always implies an increase of $|\psi|_{max}^2$

and ΔB_{V-Av} , this is not true for the triangle: from a distance $d_h/D \approx 23\%$ these observables start degrading.

Note that these results apply to a specific shape of the holes, and in principle it is not justified to compare the perforated square with the perforated triangle, since the holes have different shape. For the square, the trapped vortex is located in the corner of the square hole; for the triangle this vortex is located in the middle of a side. Thus, as an alternative approach we reinvestigated both samples, now with circular holes, and noticed that qualitatively these results do not differ from the ones with the differently shaped holes. Consequently, the general conclusions for square and triangle are independent of the shape of the holes.

When, in a realistic situation, one is interested in capturing the vortices by the holes, one has to choose a somewhat bigger hole size than the minimal one since small defects will distort the V-Av state and drive a V-Av pair closer to each other, thereby the vortex leaving the hole.

For holes at a distance of $d_h/D = 28\%$, the influence of the hole size is depicted in Fig. 2.5. Although a larger hole size does not increase the V-Av distance, it will increase $|\psi|_{max}^2$ which is important for the needed experimental resolution.

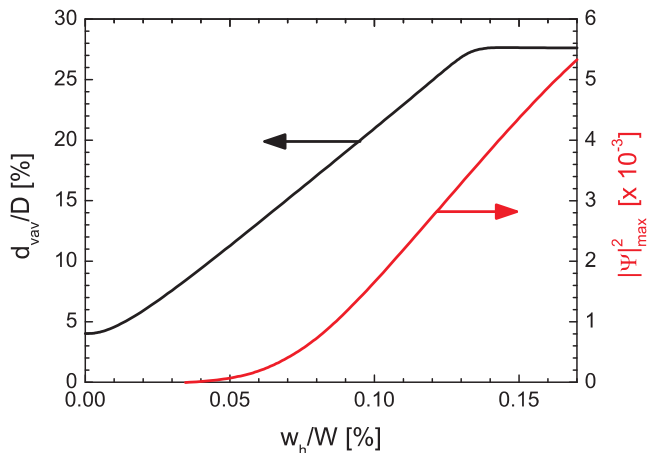


Figure 2.5: V-Av distance (d_{V-Av}) and the maximal value of the CPD between the V and the Av ($|\psi|_{max}^2$) versus the hole size w_h for a square with square holes at position $d_h/D = 28\%$. Applied flux $\phi = 5\phi_0$.

2.1.3 Influence of imperfections/defects

By introducing nano-engineered holes, we improved the observability of the V-Av state. Now the question of its stability against defects remains.

It is generally known that the V-Av state in a plain square is very vulnerable to defects at the edge of the sample [114]. We will show how this situation dramatically changes (improves) when fourfold symmetric holes are introduced into the sample. We will consider defects as slight modifications of the geometry using the linear GL theory. We observe that when the linear theory predicts that the vortex-antivortex pair annihilates, it will surely be the case in the non-linear theory, which justifies the use of the LGL theory, to determine the minimal requirements for the stability of the V-Av state.

2.1.3.1 A defect at the edge

As a starting point for comparing the perforated sample with the plain sample we will study the influence of defects at the edge of the sample. It is generally known that a small defect at the boundary will destroy the V-Av state in a plain square [114]. In the present study we restrict ourselves to defects that are indentations and bulges at the surface of the sample. We will present here the results for a square for two different defects positioned at the center of the edge of the sample. The defect under study is placed at the center of the edge of the square and is taken to be a square itself with side w_d . We considered a small bulge and a small indentation. It is known that such defects may influence the penetration and expulsion of vortices as was demonstrated experimentally by A. K. Geim *et al.* in Ref. [120]. For theoretical studies we refer to Refs. [121] and [122].

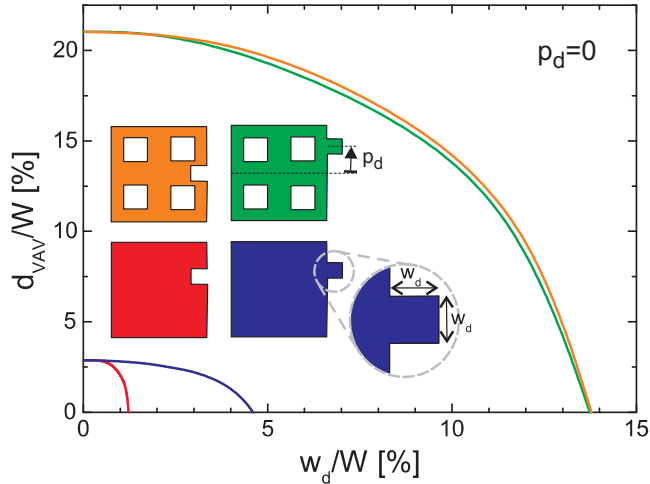


Figure 2.6: The vortex-antivortex distance vs defect size for a plain and a perforated square, with a square defect at the middle of one edge (red=indentation, black=bulge). The applied flux for the plain square is $\phi = 5.5\phi_0$ and for the perforated square it is $\phi = 4.0\phi_0$.

We now focus on the V-Av separation d_{V-Av} to compare the influence of defect size between the perforated square and the plain square. When this distance equals zero, the V-Av pair annihilates and the V-Av configuration disappears. The results for the plain square are shown by the two curves at the lower left part of Fig. 2.6. The results for the perforated square are shown by the two curves at the upper right part of Fig. 2.6. The hole size and position used for the perforated square are $W_h/W = 20\%$ and $d_h/D = 28\%$. For the plain square we applied a flux $\phi = 5.5\phi_0$, for the perforated square $\phi = 4.0\phi_0$. We had to apply different fluxes since the stability ranges of the L=3 state in two samples do not overlap (the introduction of holes shifts the phase diagrams to lower flux).

For a plain square with a bulge defect, we conclude that the V-Av configuration exists up to a size $w_d/W \sim 5\%$. The V-Av state is even more sensitive to an indentation: a size of $\sim 1\%$ is sufficient for the disappearance of the V-Av. However, we found that the V-Av state in a perforated square is much more resistant to defects. Bulge and indentation defects, up to 14% in size (comparable to the size of the nano-holes), now coexist with a V-Av configuration. Bulge and indentation defects have a similar effect on the V-Av stability, in contrast to the plain square case. We conclude that the 4-fold symmetrically placed pinning centers are much more efficient in imposing their symmetry than the outer boundary of the sample. As a consequence, small defects at the edge have little effect and only distort the V-Av molecule

One may argue that this effect is possibly only since the defect is located exactly in the center of the edge, therefore imposing mirror symmetry. Because of this symmetry, the antivortex is prohibited to choose one of the two vortices of the holes to annihilate with and it stays on the mirror line.

To turn off this stabilization effect due to symmetry, we also investigated defects which are displaced from the middle of the edge. We studied the influence of the position and size of an edge defect on the characteristic parameters d_{V-Av} , $|\psi|_{max}^2$ and ΔB_{V-Av} . The result is summarized in Fig. 2.7 for a perforated square with hole parameters $w_h/W = 20\%$ and $d_h/D = 28\%$ under an applied flux of $4\phi_0$. On the left side, the influence of the defect size is depicted for both a bulge and an indentation defect, positioned at a distance $p_d/W = 3\%$ from the edge center. On the right side, the influence of the position of a defect of size $w_d/W = 7\%$ is shown. Concerning the influence of the size of the defect, we notice that bulge and indentation defect act similarly: Increase of the defect size implies degradation of all three observables $|\psi|_{max}^2$, d_{V-Av} and ΔB_{V-Av} . However, for the position of the defect, we predict different behavior for bulge and indentation. For a bulge defect, we notice that the stability of the V-Av configuration decreases as the defect moves further from the center of a side, while for the indentation we observe a decrease followed by an increase. However, for both types of defects, the V-Av configuration survives best when the defect is centered at an edge. We also conclude that a bulge

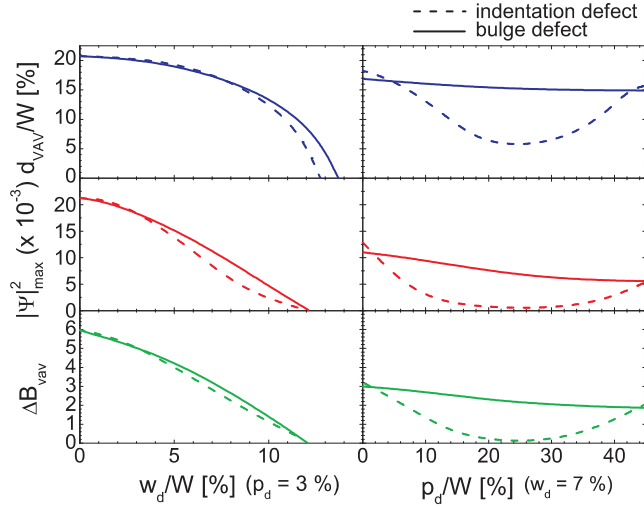


Figure 2.7: The influence of a defect on the V-Av distance (d_{V-Av}), CPD between vortex and antivortex ($|\psi|_{max}^2$) and the magnetic field difference between vortex and antivortex (ΔB_{V-Av}). The hole parameters are $w_h/W = 20\%$ and $d_h/D = 28\%$ and the applied flux is $\phi = 4\phi_0$.

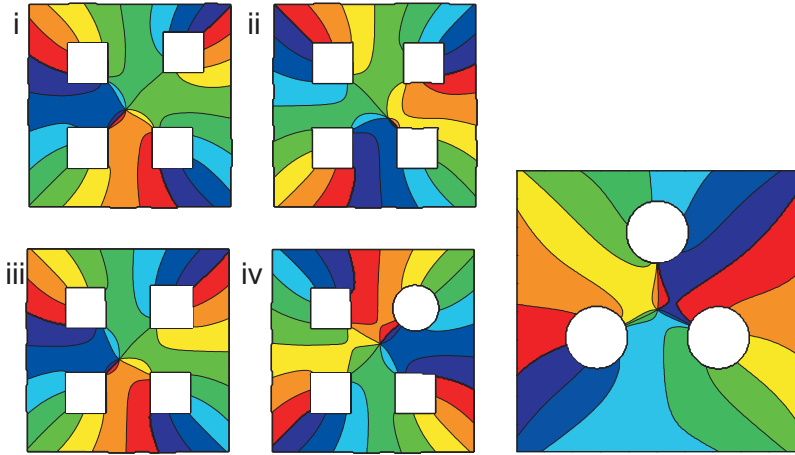
defect is less destructive than an indentation, unless it is placed near the center of an edge. The antivortex acts like being attracted to the indentation and repelled by the bulge defect.

2.1.3.2 Other kinds of defects

The V-Av stability against edge defects is strongly improved by the introduction of the fourfold symmetrically placed holes. However, in actual experiments these holes themselves can contain defects or imperfections such as non-uniform sized holes, holes which are a little displaced with respect to their high symmetry position, or holes with a slightly different shape.

In Fig. 2.8a four examples are shown. In all pictures the ‘usual’ holes have parameters $w_h/W = 20\%$, $d_h/D = 22\%$ and we apply a magnetic flux $\phi = 4.1\phi_0$. The plots in Figs. 2.8a (i) and (ii) illustrate the effect of imperfectly positioned holes. In Fig. 2.8a (i), a diagonal displacement of the upper right hole over a distance $d/W = 6\%$ is shown. The V-Av survives such displacements in the range of -4% to $+12\%$. For a horizontal displacement, as illustrated in (ii), the range is smaller: from -3.5% to $+3.5\%$. The fact that the V-Av configuration is more stable for a diagonal displacement, we attribute to the existence of mirror symmetry along one diagonal, forcing the AV on this diagonal.

In Fig.2.8a (iii) the upper right hole has a 5 % larger size than the other holes.



(a) $L = 3$ state in an imperfectly perforated square. The hole parameters are: $w_h/W = 20\%$, $d_h/D = 22\%$ and applied flux $\phi = 4.1\phi_0$. The defects include: a) a diagonally displaced hole, b) a horizontally displaced hole, c) a bigger hole and d) a different shaped hole.

(b) $L = 2$ state in a square sample with three circular holes. Not the square outer sample boundary, but the symmetric positioning of the holes induces an antivortex in the center.

Figure 2.8: Contourplots of the phase of the order parameter.

This kind of hole size defect does not destroy the V-Av state, when in the range of -8% to +9%.

In Fig. 2.8a (iv) the upper right hole is circular. It has the same area as the square holes and is centered like the square holes. The V-Av survives, which illustrates that it's not the exact shape of the holes which matters, but rather its size. This implies that non perfect holes, i.e. holes with defects, will not destroy the V-Av state as long as the imperfection is not too large.

2.1.4 Competing symmetries

2.1.4.1 Superconducting samples with polygonal pinning

Several interactions compete with each other when the V-Av state nucleates. First we have the vortex-vortex interaction through which the vortices will try to form the Abrikosov triangle lattice. Second there is the sample boundary which tries to impose its symmetry, and third there are the pinning centers (i.e. the holes) which will also try to impose their own symmetry on the vortex state.

For small samples of the order of several coherence lengths, like the ones we studied up to now, the symmetry of the sample boundary opposes the Abrikosov lattice. In this subsection we will point out that the symmetry of the pinning sites is usually dominating the symmetry of the boundary.

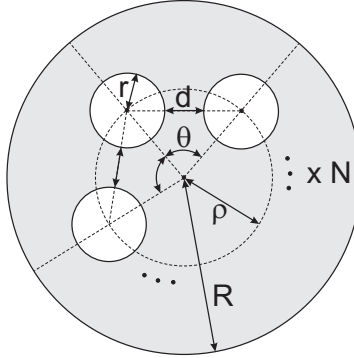


Figure 2.9: The parameters R , ρ , r , d and θ , used to characterize the geometry of the disk with N holes.

For example we show the V-Av state with vorticity $L = 3 - 1 = 2$ in a square with three holes in Fig. 2.8b. Although the outer edge has a square geometry it is the triangular arrangement of the circular holes which imposes its symmetry on the superconducting wave function in the center of the square. This leads to 3 vortices trapped in the holes and a single antivortex in the middle of the sample.

2.1.4.2 Superconducting disk with many holes

The arrangement of holes, instead of the sample outer boundary, seems to be the geometry element which is most effective in imposing its geometry on the wave function. For this reason, we can as well use circular symmetric disks, perforated by N symmetrically placed holes, and expect an N -fold symmetric vortex state. A large variety of symmetry-induced antivortex configurations can be created in this way. Following this approach we found that it was possible to even create giant anti-vortices with vorticity L up to -7 .

The parameters which define the geometry are depicted in Fig. 2.9. d is the distance between holes, θ the angle between holes which is set equal to $2\pi/N$, to impose the N -fold symmetry. ρ is the distance of the holes' center to the disks center, R is the radius of the disk and r is the radius of the holes. Imposing that the distance between the holes equals the hole's diameter is equivalent to the condition $r = (1/2)\rho\sin(\theta/2)$.

To illustrate this conjecture, we give some examples. In Fig. 2.10a the CPD and the phase plot of a disk with 20 holes is shown. The parameters are $r/R = 4.3\%$, $\rho/R = 55\%$, so that the distance between the holes $d = 2r$. The applied flux is $\phi = 26\phi_0$. The vorticity $L = 19$, is one less than the number of holes and consequently an additional vortex-antivortex pair is created. The alternative solution to obey the symmetry would be to create a $L = 19$ giant vortex, but it turns out that the

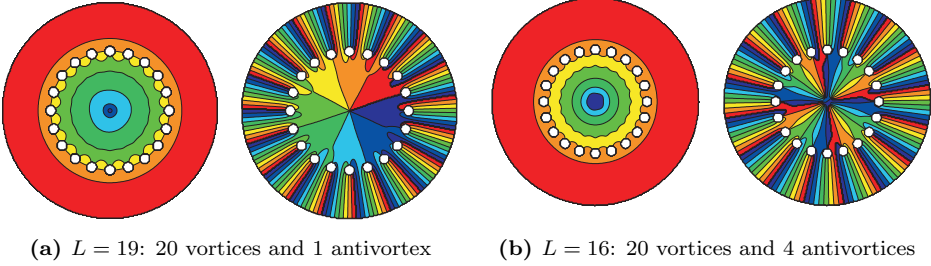


Figure 2.10: Two V-Av states in a disk with 20 holes. Left: logarithmic CPD contour plot (red/blue=high/low density). Right: phase contour plot (red/blue= $0/2\pi$).

creation of one V-Av pair is energetically more favorable.

Additionally, here clearly exists a competition between the formation of a giant vortex - the merging of several vortices in one point - and the formation of a giant antivortex - consisting of the creation of vortex-antivortex pairs and then merging of all anti-vortices in a singular point.

For the same disk, with an applied flux of $\phi = 21\phi_0$ and slightly modified parameters $\rho/R = 0.5$ and $r/R = 4.73\%$ the CPD and the corresponding phase plot is shown in Fig. 2.10b. The phase plot indicates a giant antivortex in the center with winding number -4. We found that the giant antivortex is highly unstable with respect to sample imperfections. Therefore, in experiment, it will be very difficult to observe these giant antivortices, and most likely they will fall apart in 4 single antivortices. Small imperfections will cause the giant AV to disassociate into separate antivortices and larger imperfections will cause the V-Av pairs to annihilate.

To generalize the concept of giant-antivortices and their appearance in disks with N symmetrically placed holes, we investigated the relation between the symmetry order N and the vorticity L . The result is the L - N phase diagram shown in Fig. 2.11 where we used the following parameters: $\rho/R = 0.55$, $r = 2d$ and $\phi = 1.2N\phi_0$. The anti-vorticity of the state is indicated by the different colors. When $L < N$, and there are no anti-vortices, a giant vortex of vorticity L is located at the disk center, since this is the only solution which is able to obey the symmetry. However, because of the finite grid resolution, these vortices split up in separate ones, analogous to the fate of the giant antivortex described before.

For vorticities $L \geq nN$ (where n is the largest integer obeying the condition) another property is observed: every hole pins n vortices, which are not necessarily captured inside the holes, but clearly belong (i.e. are attached) to the specific hole. The L - N phase diagram is not uniquely determined by N . The choice between giant- or anti-vortices is strongly dependent on the exact choice of the geometry (i.e. of r , ρ , d) which strongly affect the free energy, and also on the applied flux, because

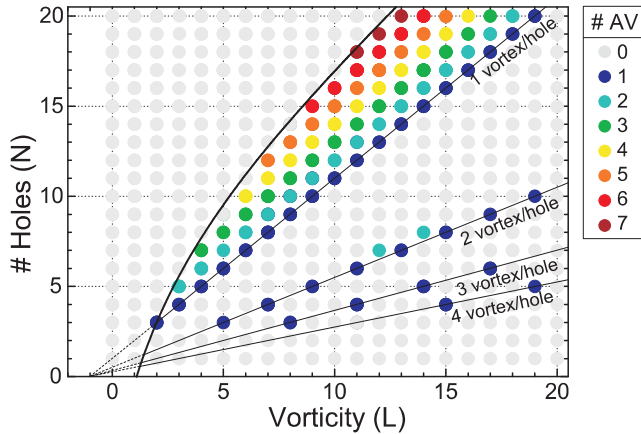


Figure 2.11: For each vorticity and for each number of holes N , the number of anti-vortices is shown. Due to the symmetry the antivortices combine to a giant antivortex. Left of the thick line no antivortices are observed.

of the Meissner current compressing the (anti-)vortices inwards.

2.2 Symmetry induced V-Av for $T < T_c$

2.2.1 Full GL theory

The non-linearity of the GL equations and the coupling to the magnetic field will now be taken into account. This means that from now on, we will use the full non-linear GL theory. We will focus only on the square geometry, but all conclusions can be extrapolated to other geometries/symmetries. We remind the reader that the thickness of the sample throughout this chapter is chosen to be $1\xi(0) \equiv \xi(T=0)$. It is already well established that the Ginzburg-Landau (GL) formalism gives an accurate description of the superconducting state of low- T_c superconductors, and is well suited to incorporate boundary effects in the treatment of the mesoscopic superconductors. The GL theory postulates the following expression for the free energy of the system (in dimensionless form):

$$\mathcal{F} = \int d\mathbf{r} \left[-|\Psi|^2 + \frac{1}{2}|\Psi|^4 + |(-i\nabla - \mathbf{A})\Psi|^2 + \kappa^2 (\mathbf{B} - \mathbf{B}_{appl})^2 \right]. \quad (2.3)$$

Here all distances are measured in units of the coherence length $\xi(T) = \xi(0)/\sqrt{1 - T/T_c}$. The vector potential \mathbf{A} is expressed in units of $c\hbar/2e\xi$, the magnetic field in units

of $H_{c2} = \hbar/2e\xi^2$, and the complex order parameter Ψ in units of $\Psi_0 = \sqrt{-\alpha/\beta}$, such that $|\Psi| = 1$ in the pure Meissner phase and $|\psi| = 0$ in the normal conducting state (with α, β being the GL coefficients [48]). $|\Psi|^2$ represents the local Cooper-pair density. \mathbf{B}_{appl} denotes the applied magnetic field, while \mathbf{B} stands for the total magnetic field. κ is the ratio between penetration depth and coherence length, i.e. $\kappa = \lambda/\xi$ and is assumed to be temperature independent in this model.

To find stable solutions, one has to find the wave function and the vector potential which minimize the free energy functional. Two coupled non-linear differential equations, one for the order parameter and one for the vector potential, can be derived using variation analysis. We are interested in thin, but finite-thickness, samples in a perpendicular applied field, where we may neglect the variation of the magnetic field and order parameter over the thickness of the sample. Accordingly, we average the GL equations over the sample thickness [48, 88, 123, 124], and write them as

$$(-i\nabla - \mathbf{A})^2 \Psi = \Psi (1 - |\Psi|^2), \quad (2.4)$$

$$-\kappa^* \Delta \mathbf{A} = \mathbf{j}_s = \Re(\Psi^* (-i\nabla - \mathbf{A}) \Psi), \quad (2.5)$$

where \mathbf{j}_s denotes the supercurrent density, and $\kappa_{eff} = \kappa^2/(d/\xi)$ is the effective Ginzburg-Landau parameter, the consequence of averaging over sample thickness d . It's worth emphasizing that κ_{eff} is temperature dependent (e.g. through $\xi(T)$ in the denominator). All samples in this chapter, treated with the full non-linear GL theory, have the same thickness $d = \xi_0$. Consequently κ_{eff} takes the temperature dependence $\kappa_{eff}(T) = \kappa^2/\sqrt{1-T}$. To address properly the influence of T , all results obtained by the full GL theory will be expressed in units of ξ , ψ_0 and H_{c2} at zero temperature.

While authors of Refs. [47, 112, 113, 115] solved only the first GL equation, and restricted themselves to the limit of $d \rightarrow 0$, or extreme type II superconductors, we solve numerically *both* equations. The strength of the influence of the second GL equation is governed by κ_{eff} . When $\kappa_{eff} \gg 1$ (thus for $d \ll 1$ and/or $\kappa \gg 1$), Eq. (2.5) can indeed be neglected. However, when $\kappa_{eff} \approx 1$, we found it can have a tremendous influence and provide us with some interesting and novel behavior of the superconducting state.

Our numerical approach is based on a finite difference Gauss-Seidel relaxation for the time dependent GL equations. The numerical technique we applied was described in the introduction in section 1.8. Additionally, a convenient iterative expansion of the non-linear term explained in Ref. [123, 124], to speed up convergence, was added. We solve the GL equations on a uniform Cartesian grid typically with 128×128 points.

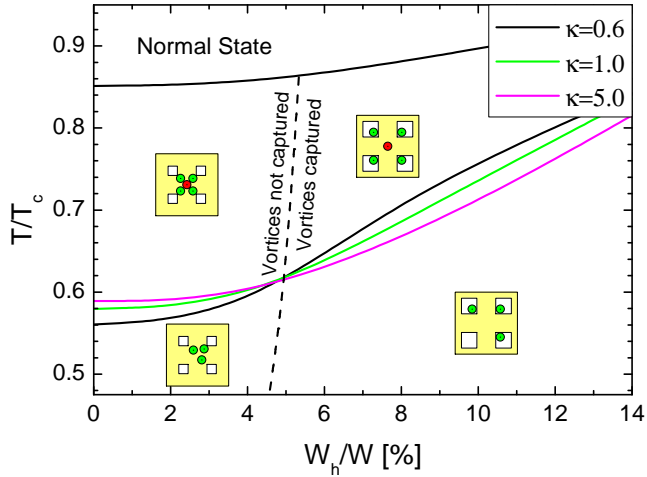


Figure 2.12: Transition temperatures T_{V-Av} , $T_{V-Av-symm}$, $T_{S/N}$ vs. the size of the hole for a square of sizes $10\xi_0 \times 10\xi_0$ and an applied field of $\phi/\phi_0 = 5.0$. The corners of the holes are at a distance $d_h/D = 25\%$. On the left side of the thick line, the vortices are captured by the holes, on the right side they reside outside the holes.

2.2.2 Phase diagram

The V-Av state can be reached by, for instance, increasing the temperature. In this case the multivortex state will, through a second order transition, transform into the symmetric V-Av state. In between these two phases, a new state arises: the *asymmetric* V-Av state. This is a stable ground state configuration, consisting of several vortices and one antivortex, but they are not positioned symmetrically. The area in a $\phi - T$ phase diagram, where these asymmetric symmetry-induced states are the ground state configuration is extremely small. The size of the temperature interval is of the order of $10^{-3}T_c$ for a perforated square or $10^{-4}T_c$ for a plain square.

We state that a V-Av state is symmetric, when a , our measure of asymmetry is smaller than 0.05, which is defined as $a = \sum_i \min_{j \neq i} |\mathbf{x}_i - \mathbf{R}\mathbf{x}_j| / \left(\sum_i |\mathbf{x}_i| \right)$. Here, \mathbf{R} is the rotation operator, which rotates a vector over 90 degrees, \mathbf{x}_i are the positions of (anti-)vortices (when they are residing in holes, the position is taken to be in the inner corner pixel of the hole). The origin of the axes is chosen in the middle of all vortices, i.e. $\sum_i \mathbf{x}_i = 0$.

In the non-linear theory we will now review the role played by the hole size. The phase diagram in Fig. 2.12 shows the dependence of the V-Av stability temperature interval of the hole size. In this figure the total applied flux ϕ equals $5\phi_0$. The position of the inner corner of the holes was fixed at $d_h/D = 25\%$. Although in-

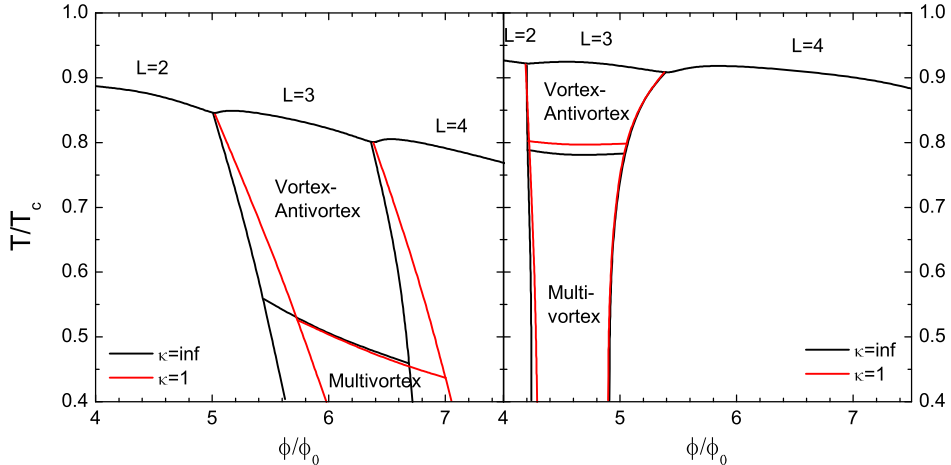


Figure 2.13: $\phi - T$ phase diagram for a plain (left) and perforated (right) square, illustrating the ground state regime of the $L=3$ state. Grey represents $\kappa = \infty$, red $\kappa = 1$. Hole parameters: $w_h/W = 12.5\%$ and $d_h/D = 25\%$.

creasing the hole size, enhances the characteristic observables $|\psi|_{max}^2$ and ΔB_{V-Av} and as well stabilizes the V-Av state against all kinds of defects, we notice one disadvantage of large holes: the V-Av temperature interval shrinks.

When the influence of magnetic screening grows, i.e. κ decreases, the temperature interval in which the V-Av is stable expands if the holes are small ($W_h/W < 5\%$), but shrinks when the holes are large ($W_h/W > 5\%$). This is explained by the constraining effect of the holes on the κ -dependent natural size of the V-Av molecule. In the absence of holes (pinning centers), the vortex distance is determined mainly by the vortex-vortex interaction. This interaction is repulsive for large κ , but becomes weaker when κ is lower. As a consequence, for the same temperature, vortices will be closer to each other when κ is lower. Also, the natural size of an V-Av molecule is smaller for low values of κ as is illustrated in Fig. 2.14. When the holes are small, their influence is still weak and the V-Av is fairly free to adjust its size according to the changing vortex interactions with changing κ and T . Moreover for lower κ , vortices are closer and will overlap at lower temperature. The associated suppression of the order parameter causes the nucleation of the additional V-Av pair. When the holes are larger, their pinning force becomes stronger, pulling the vortices farther from the center. When they pull the vortices too far away from their natural positions, the order parameter is no longer sufficiently suppressed and the V-Av state can not be sustained. The V-Av transition temperature is thus higher, since only then the influence of magnetic screening diminishes.

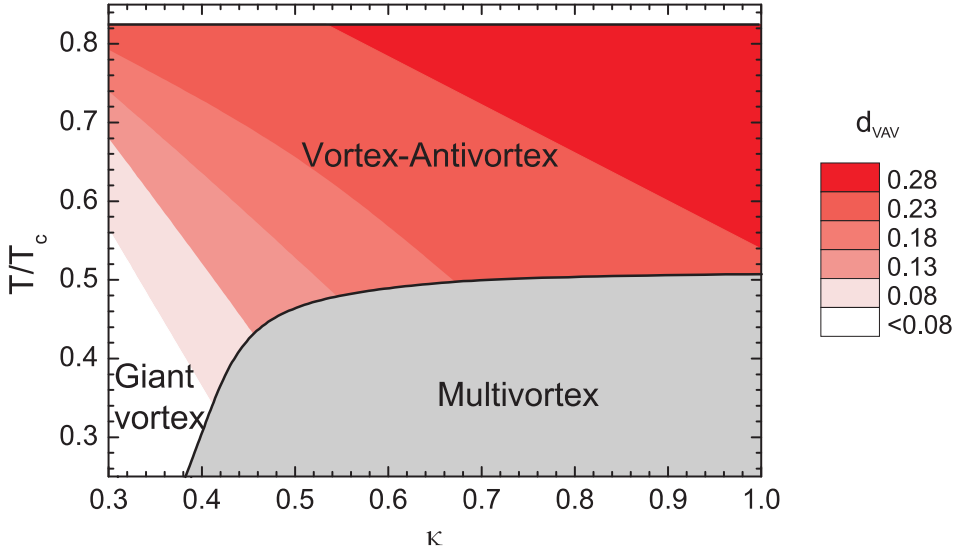


Figure 2.14: κ - T phase diagram showing the three different states (V-Av, multivortex and giantvortex) for a plain square with size $10\xi(0) \times 10\xi(0)$ and flux $\phi/\phi_0 = 6$. For the V-Av state the V-Av distance d_{V-Av} is given in the color scale from red to white.

$\phi - T$ phase diagrams are shown in Fig. 2.13a for a plain square and in Fig. 2.13b for a perforated square, both of size $10\xi(0) \times 10\xi(0)$. Both figures contain two superimposed phase diagrams, one for $\kappa = \infty$ (indicated by grey) and one for $\kappa = 1$ (shown in red). The diagrams illustrate the ground state region of the L=3 state, so only the neighboring L=2 and L=4 states are taken into account.

Comparing these two phase diagrams with and without holes, one can clearly see that the introduction of holes of size $w_h/W = 12.5\%$ at the position $d_h/D = 25\%$ causes the total V-Av region to shrink, even more for $\kappa = 1$.

For both samples a decrease of κ causes a shift of the vorticity to higher fields which is large for low temperatures and smoothly decreases to zero at the S/N boundary. The reason for the latter is that the larger currents ($j_s \propto |\psi|^2 \propto 1 - T/T_c$) generate a stronger magnetic field and thus are more effective in expelling and concentrating the magnetic flux. This shift for decreasing κ can be understood in the limit to type I superconductivity, where L=0 (i.e. the Meissner state) is the only stable state. The S/N boundaries for both κ coincide, since at the S/N boundary the second equation does not have any influence.

Fig. 2.14 depicts the κ -dependence of the temperature range in which the V-Av state in a plain square is stable. The vortex-antivortex distance is superposed in the red-to-white color scale. One notices three regions in this diagram: vortex-antivortex, giant vortex and multivortex state. For $\kappa < 0.4$ it is possible to obtain

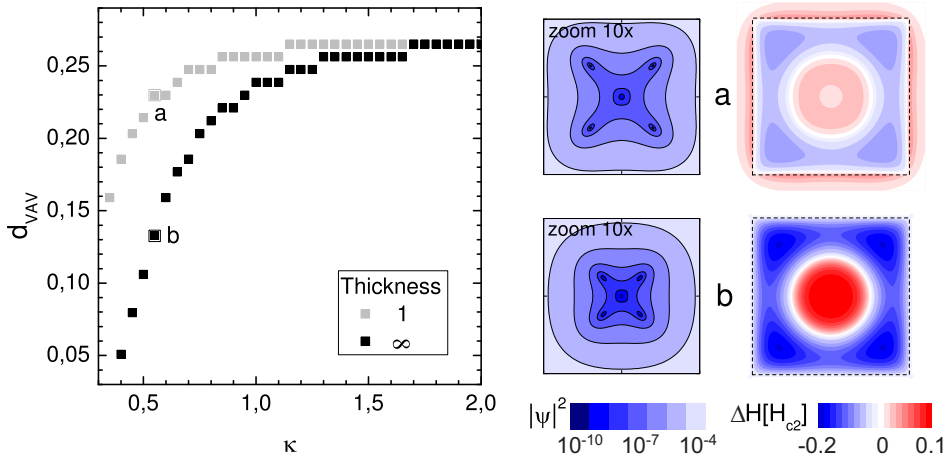


Figure 2.15: Vortex-antivortex distance versus κ for a thin square sample ($d = 1\xi(0)$) and an infinitely thick sample ($d = \infty$). Used parameters are $\phi/\phi_0 = 6$ and $T/T_c = 0.7$. For the datapoints indicated by the letters a and b, the zoomed in the Cooper pair density distribution, together with the induced magnetic field profile is shown on the right. The sample border is indicated by the dashed line.

a transition from multi- to giant- to vortex-antivortex-state by sweeping the temperature.

The results suggest that the temperature range of the V-Av state grows for decreasing κ . Also it is shown that the decrease of κ makes the vortices approach the antivortex, eventually leading to the formation of a giantvortex: decreasing κ thus disfavours the vortex-antivortex nucleation.

This conclusion is opposite to the findings of Ref. [125] where a mesoscopic type-I triangle was studied. There the authors reported a strong expansion of the V-Av molecule around $\kappa \sim 0.70$. They considered a prism with infinite thickness, which considerably affects the magnetic field distribution and might be responsible for the discrepancy. To check this we investigated infinite prisms as well, of triangle and square shape, but could not confirm the results of Ref. [125]. We therefore stick to the statement that the decrease of κ shrinks the V-Av molecule and consequently disfavors it. Our conclusion is in fact expected, as decreasing κ decreases the vortex-vortex repulsion, but does not turn the vortex-antivortex interaction into a repulsive one, as explained in Section 1.3.

In an infinitely thick sample, all the induced magnetic field is forced into the sample, while for a thin sample the induced magnetic field can spill out the sample. Therefore, the induced magnetic field inside a thick sample is stronger than in a thin sample. This way we understand Fig. 2.15 showing that the effect on the vortex-antivortex state of taking an infinitely thick sample, is similar to taking a

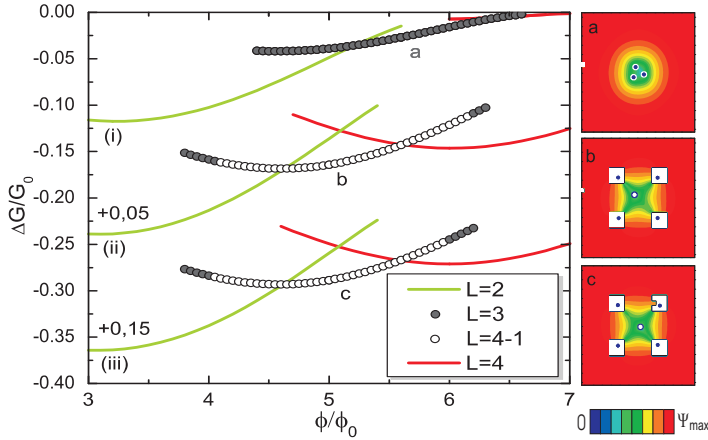


Figure 2.16: Gibbs free energy for $T = 0.78T_c$ and (i) plain square sample with an edge-defect (size $0.5\xi_0$), (ii) sample with 2×2 holes and an edge-defect, and (iii) sample with 2×2 holes and a defect in hole-edges. Insets (a-c) show the Cooper-pair density plots of found states with total vorticity 3, in cases (i-iii).

thin sample with a smaller value of κ .

Since the vortex-antivortex state is already a state which is rather unstable and sensitive to defects, it is normal that this subtle equilibrium of the coexistence of vortex and antivortex disappears and that the V-Av pair annihilates.

From a theoretical viewpoint, there are several ways to make the second order transition from the highly symmetric V-Av state to the multivortex state: by decreasing temperature, the magnetic field or κ . In all these three scenarios the same transition takes place: the antivortex moves towards one of the vortices, they approach and eventually annihilate. This is clearly a manifestation of spontaneous symmetry breaking.

2.2.3 Influence of defects and imperfections

We already investigated the influence of defects and imperfections in section 2.1.3 at T_c where the symmetry is felt the strongest. Here we show the results of simulations for the plain and the perforated square deeper into the superconducting state.

While the ground-state strongly depends on symmetry, the analysis of Ref. [114] has shown that defects as small as $0.01w$ at the edges of a plain superconducting square disable vortex-antivortex nucleation. We found that 2×2 nanoholes significantly strengthen the $L = 4 - 1$ state. Fig. 2.16 shows the free energy diagrams of (i) a plain square with a small edge defect, (ii) a square with nanoholes and an edge defect, and (iii) square with nanoholes and a defect at one of the holes. Whereas in case (i) no vortex-antivortex state is found, in both cases (ii) and (iii) we found

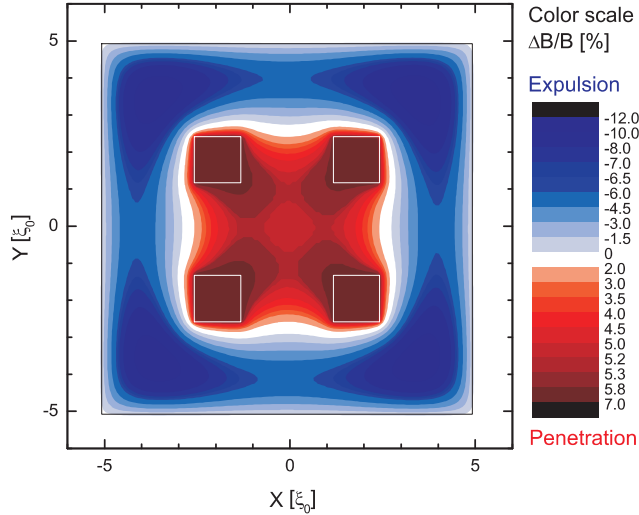


Figure 2.17: Contourplot of the quantity $\Delta B = (B - B_{appl})/B_{appl}$ for $\phi = 5.8$, $T = 0.84$ and $\kappa = 0.7$ in a $10\xi_0 \times 10\xi_0$ superconducting square with holes in the $L=4-1$ state. Hole parameters: $w_h/W = 12.5\%$ and $d_h/D = 25\%$.

stable $L = 4 - 1$ state. Our numerical experiment shows that vortex-antivortex states in latter cases can survive for defects in edges *up to 10% of the sample size* and defects in nanoholes up to *remarkable 40% of their size*. Note also that the presence of defects changes the current profile of the sample, which again results in asymmetric vortex-antivortex configurations [see Fig. 2.16(b,c)].

2.2.4 How to detect the vortex-antivortex state?

Essentially, we see two ways to prove experimentally the existence of stable antivortex states: through magnetic field imaging (e.g. using SHPM) and through Cooper pair density imaging (e.g. using Scanning Tunneling Microscopy). In this section we will highlight the advantages and disadvantages of both approaches.

An antivortex is characterized by the following properties: i) the CPD in the center is suppressed to be exactly zero, and ii) its supercurrent circulates opposite to the one of the vortices. Unfortunately, the first property also applies to a conventional vortex, so it cannot be used to discriminate between a vortex and an antivortex. This means that the magnetic field, generated by the supercurrents, is the only observable to distinguish between a vortex and an antivortex.

In our study of superconductors in a homogeneous field, antivortices always seemed to appear surrounded by vortices. However, (multi)vortex currents always generate in the center of the sample an antivortex-like current, in a cogwheels motion of the

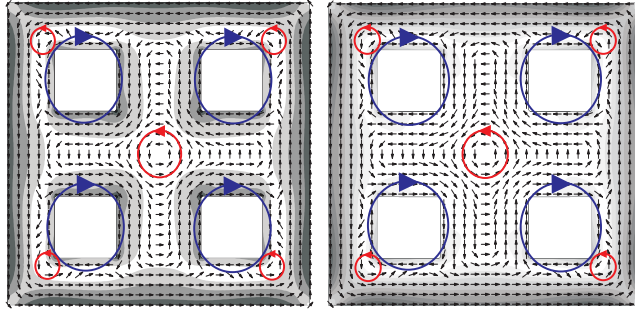


Figure 2.18: The distribution of the supercurrent in a perforated square. The black arrows indicate the direction of the current, the background greyscale map depicts the magnitude of the local supercurrent density (white/black represents low/high). The main characteristics of the current flow pattern are indicated by the blue and red circles. Left: $L = 4$ state with applied flux $\phi = 7\phi_0$. Right: $L = 4 - 1 = 3$ (V-Av) state with applied flux $\phi = 5.5\phi_0$.

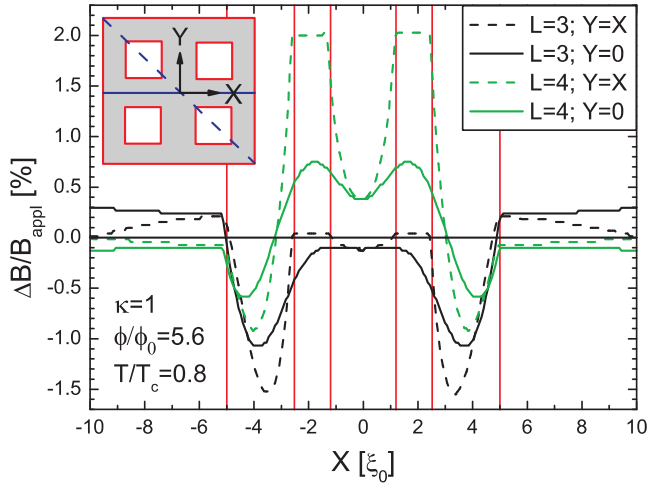


Figure 2.19: Magnetic field profiles (diagonal and vertical cut) for the $L=4-1=3$ and $L=4$ states in a perforated square. $\Delta B \equiv B - B_{\text{appl}}$.

condensate. This current masks the current profile of a possible antivortex which could be present since it has the same direction. As a consequence, we can not get evidence for the existence of an antivortex by looking in a qualitative way at the magnetic field profile of the sample. As an example, there is no qualitative difference of the supercurrent and the magnetic field profile between the $L=4$ and $L=3$ V-Av state, as shown in Figs. 2.18 and 2.19. Of course there is a quantitative difference, which could possibly be exploited.

Nonetheless, one can make use of qualitative differences of both the CPD and the magnetic field profile, at different temperatures. Here the challenge is to control the vorticity of the sample and to assure that it stays constant while measuring and sweeping the temperature. This way one can either measure the CPD or the magnetic field profile. At low temperature the magnetic field profile should clearly exhibit the penetration of the field through the three vortices residing in three of the holes, while at a higher temperature the magnetic field should be penetrating the four holes equally, since a V-Av pair is then created, with the vortex occupying the remaining hole.

2.3 Molecular dynamics model

In this section we outline an analogy in classical systems of vortex-antivortex nucleation due to sample symmetry.

The model system was defined in Ref. [126], where Hamiltonian is given by

$$\mathcal{H} = \sum_{i>j}^N U_{ij} + \sum_i^N V(x, y), \quad (2.6)$$

with N being the number of particles. We took square-parabolic confinement potential of size w_c , i.e.

$$V(x, y) = \frac{1}{2}m\omega_0^2 \frac{x^2 + y^2}{w_c^2} \left[1 + \sqrt{\delta + \cos^2 \left(2 \arctan \frac{y}{x} \right)} \right] \quad (2.7)$$

(m -mass of particle, ω_0 -confinement frequency) with a nonzero $\delta \ll 1$, ensuring the existence of the derivatives of this potential in the corners of the square. To further translate this system to vortices in mesoscopic superconductors, one has to choose properly the vortex-(anti)vortex interaction energy (U_{ij}). Firstly, this interaction must be of long range (and diminishing far from the source), knowing that supercurrents decay $\sim 1/r$ away from the vortex. Secondly, U_{ij} may not diverge for $r_{ij} \leq \alpha$ but saturate, allowing for realistic merging of vortices into a giant vortex [45], or a vortex-antivortex annihilation. In this scenario, α roughly corresponds to the finite size of the vortex core.

Though any interaction energy of described profile would suit our analysis, we used a modified logarithmic and modified Coulomb interaction, more specifically

$$\begin{aligned} dU/dr(r_{ij}) &= \beta(1 - e^{-r_{ij}/\alpha})^2/r_{ij} \quad \text{and} \\ dU/dr(r_{ij}) &= \frac{q_i q_j}{\epsilon} (1 - e^{-r_{ij}/\alpha})^3 / r_{ij}^2, \end{aligned} \quad (2.8)$$

respectively. Notice that the modified Coulomb interaction is a quality fit for $\alpha^{-1} = \sqrt{2}\kappa$ (up to a multiplying constant) to the realistic vortex-vortex interaction in type-II samples (see e.g. Ref. [127]).

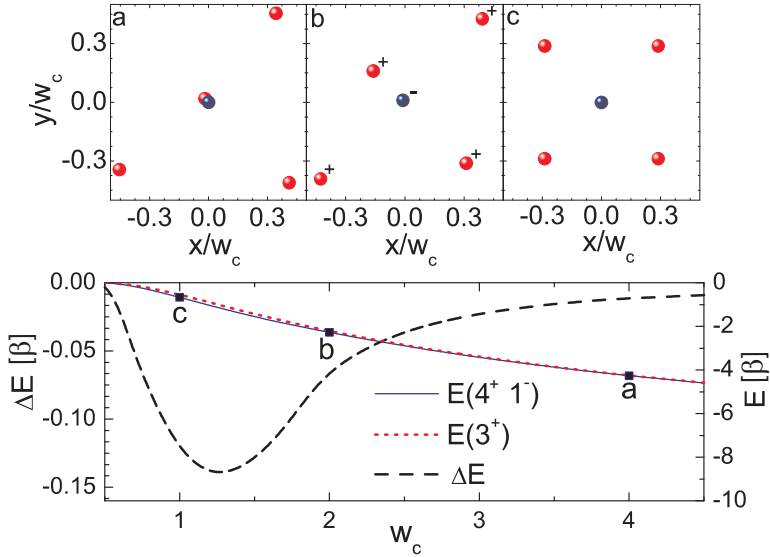


Figure 2.20: Energy of the 3-particle cluster compared to the cluster of 4 particles and one antiparticle, as a function of the size of the square confinement w_c , for modified logarithmic inter-particle interaction (of strength β , and with $\alpha = 1$). (a-c) are snapshots of the ground state configuration of the latter cluster with decreasing w_c (x, y in units of $\sqrt{\frac{2\beta}{m\omega_0^2}}$).

Next we employed molecular dynamics simulation, a relatively simple and rapidly convergent technique that gives a reliable estimate of the energy for small clusters of interacting particles. The obtained energy versus confinement size (w_c) is shown in Fig. 2.20, for a cluster containing three particles of the same charge (i.e. $U_{ij} > 0$) and a cluster of four particles and an antiparticle, with clear analogy to our $L = 3$ and $L = 4 - 1$ vortex state. For large w_c , the ground states of the two clusters have identical energy, as one particle and the antiparticle sit on top of each other. However, for tighter confinement, the $N = 4^+ 1^-$ cluster attains lower energy than the $N = 3^+$ one. Namely, particle and antiparticle gradually separate causing the rearrangement of the remaining 3 particles. Figs. 2.20(a-c) show snapshots of this dynamical transition in the ground state. To our knowledge, this symmetry breaking in the crystallization of confined systems is novel and applies to classical particles interacting with charged impurities in the substrate [128], and potentially to small ionic crystals under pressure [129]. Note also that colloidal molecules have recently been realized experimentally on hydrophilic square templates [130].

2.4 Second-generation V-Av state

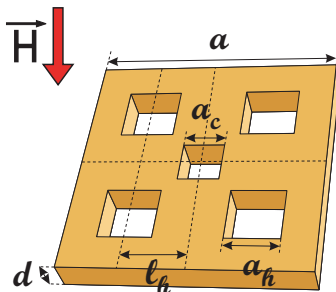


Figure 2.21: A schematic drawing of a polygonal mesoscopic superconductor (side a , thickness d) with corresponding arrangement of perforations (spacing l_h , characteristic size of each hole a_h and of the central hole a_c) in a perpendicular magnetic field H .

In last several years, two methods were proposed to improve the stability and the observability of the vortex-antivortex states in mesoscopic polygons. In one, the magnetic field profile was altered by a magnetic dot placed on top of the superconductor [131]. The bipolar field of the added magnet favors the antivortex underneath, and repels vortices further apart. However, this method: (i) interferes with the key concept of an antivortex in opposite, unipolar field, (ii) makes the structure more complicated, three-dimensional, and inaccessible for scanning probe techniques, and (iii) poses difficulties for any magnetic (magnetic-force, Hall-probe) measurements. In the previous sections we presented the second method: structural engineering of the sample itself, by strategically placed holes in the sample, mimicking the sample symmetry and the expected symmetry of the vortex-antivortex state. In such realization each hole hosts (pins) one vortex, where the pinning force is effectively stronger than the vortex-antivortex attraction. As a consequence, vortices remain in the holes even when placed at further distances from the antivortex, and the whole molecule can be made significantly larger.

In this section, we show that not only vortices can be pinned in the latter concept, but an antivortex as well. We therefore introduced an additional, central hole in the sample, in which the antivortex can reside. Intuitively, this facilitates the quantization of negative stray flux between the vortices in a cluster, and leads to a more stable antivortex. Vortices and antivortices in holes are just quantized magnetic field, screening prevents their annihilation, and the fact that they have no core reduces their attractive interaction. As will be shown, this indeed leads to an enhanced stabilization of the vortex-antivortex molecule, even deep into the superconducting state, but with significantly altered overall properties. Although this generally applies to any polygonal setting of the holes and various shapes of

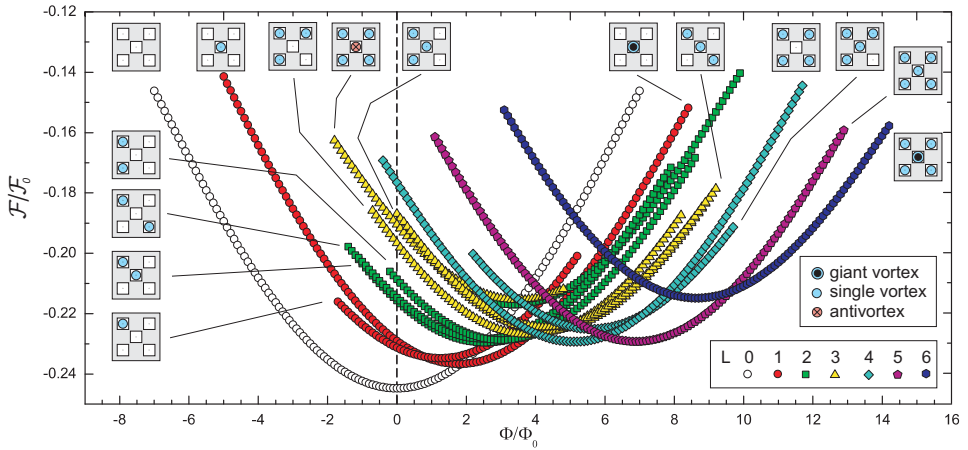


Figure 2.22: The Gibbs free energy spectrum, showing the energy levels and stability of different vortex states as a function of applied magnetic field at $T = 0.3T_c$. Insets cartoon the vortex arrangement for selected states.

the sample, as was discussed in section 2.1.4, in what follows we show the proof of principle for a square superconducting geometry, as shown in Fig. 2.21.

In Fig. 2.22 we show the free energy of vortex states with vorticities from $L = 0$ to $L = 6$ as a function of the applied magnetic flux $\Phi = a^2H$. The simulation is performed by sweeping the magnetic field up and down, and then back-tracking of all found vortex states so that their complete stability range is obtained. In addition, we performed the calculation starting from different initial conditions, some of which included reasonable guesses of possible vortex configurations. Fig. 2.22 summarizes all the found stable states, but we may not rule out the possibility of some more complex, higher energy, vortex states. For this simulation a square of size $20\xi(0) \times 20\xi(0)$ was used with holes of size $3.5\xi(0) \times 3.5\xi(0)$, four of which are horizontally and vertically displaced by $5\xi(0)$ from the center of the sample. Temperature was fixed at $0.3T_c$ (corresponding to Al samples below 400 mK [132]) and an extreme type-II behavior was assumed, typical for thin samples ($\kappa = \infty$). The combinatorial number of possible vortex configurations for given vorticity is quite high, and many of them are indeed found stable due to both the large size of the sample and that of the central hole. Starting from zero field, the Meissner state, $L = 0$, is the lowest energy state in the flux band of $\Delta\Phi = 1.85\Phi_0$, which is larger than a flux quantum, but significantly smaller than in non-perforated mesoscopic samples [116]. The reason is that the first vortex penetrates easier, and is more stable in the present system due to the central hole (central $L = 1$ is in the ground state in $\Delta\Phi = 1.92\Phi_0$). States with an off-center vortex have mostly higher energy, smaller stability range, and are fourfold degenerate (which makes them interesting for logic applications [133]). $L = 2$ shows the *broken symmetry* in the ground

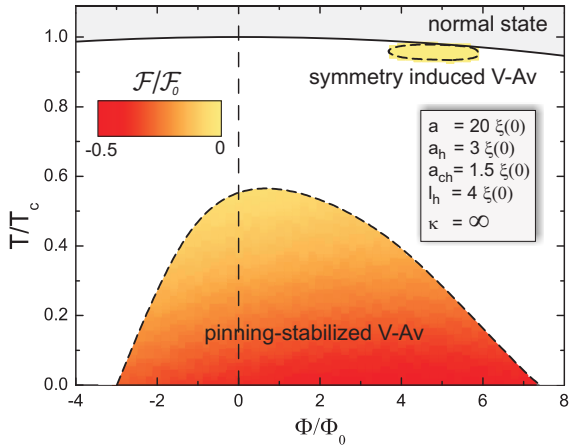


Figure 2.23: The superconducting state in the Φ - T diagram (solid line shows the superconducting/normal state boundary) comprising the areas of stability of the $L = 3$ vortex-antivortex molecules, both pinning- and symmetry-induced ones. Color coding shows the energy of those vortex states.

state, as two vortices reside in the central and corner hole, but their ground-state flux-band is only $\Delta\Phi = 0.17\Phi_0$. Similarly, the broken symmetry $L = 3$ state with all vortices in the corners is the ground state in a short interval of $\Delta\Phi = 0.11\Phi_0$. Just like in the superconducting square with 2×2 holes [134], $L = 4$ vortices reside in the corners and show enhanced stability in the ground state ($\Delta\Phi = 1.95\Phi_0$). However, the most dominant state in Fig. 4.2 is the $L = 5$ one, where all holes are occupied by a single vortex ($\Delta\Phi = 3.63\Phi_0$). Therefore, while for the square with an 2×2 holes high symmetry states as $L = 2$ and $L = 4$ were pronouncedly low-energy states, we notice that in the present system the states which have a vortex in the central hole, and are fourfold symmetric dominate the ground state, i.e. $L = 1$ and $L = 5$. Note that the $L = 4$ state is still very comfortable with the fourfold symmetry although it does not have a central vortex, but e.g. $L = 3$ with a central vortex is not in the ground state because it does not obey the symmetry of the sample. Because of their very low energy, $L = 1, 4, 5$ states overshadow other states like the $L = 2$ and $L = 3$. The $L = 3$ state has several allotropes, i.e. it can have vortices across the sample diagonal, one vortex in the center and two on the side, or all three out of the center. Only one configuration can satisfy the four-fold symmetry of the sample and that is the $L = 4 - 1$ state, with four vortices in corner holes and an *antivortex* in the center. This vortex-antivortex (V-Av) state is indeed found stable in our system, with relatively high energy, but still lower than most higher vorticity states (which suggests that it can be experimentally realized in decreasing magnetic field).

The physical origin of this V-Av state is however different from the V-Av state described in previous sections and found in Refs. [47, 112, 114, 118, 125, 135] where the V-Av molecules appear due to the imposed symmetry of the sample. For instance adding holes only reinforce the symmetry argument and do not cause *per se* the V-Av state. Therefore we will refer to this state as the symmetry induced V-Av in contrast to the newly found V-Av state which is *fully stabilized by pinning* of all vortices and the antivortex. In Fig. 2.23 we show the $\Phi - T$ phase diagram for both versions of the $L = 3$ vortex-antivortex state (for taken parameters $a = 20\xi(0)$, $a_h = 3\xi(0)$, $l_h = 4\xi(0)$, $a_c = 1.5\xi(0)$, see Fig. 2.21). We observed two fully independent islands in the $\Phi - T$ phase space corresponding to the two manifestations of the V-Av state. The symmetry-induced one is situated in the high temperature regime, where confinement imposed by the sample boundaries is effectively very large. It should be noted here that the ΔT stability range for the symmetry-induced V-Av state is on average just 1% larger than in the case of 2×2 holes (since the order parameter inside the molecule is in any case severely suppressed). At lower temperatures, the GL equations are strongly non-linear and symmetry arguments cannot account for the nucleation of the V-Av state. Nevertheless, a second generation V-Av state does stabilize, thanks to the large spacing between the holes (preventing vortex-antivortex annihilation) and the large size of the sample (diminishing the effect of encircling screening currents). The pinning-stabilized V-Av state: 1) occupies far larger $\Phi - T$ area compared to the symmetry induced one, a wide region of $\approx 10\Phi_0$ and $\approx 0.6T_c$, and 2) it is found stable even *in negative applied field*, where central antivortex is a natural state and vortices are subjected to an increasing expulsion pressure. In principle, several vortex states are found stable at negative fields in Fig. 2.22, which is a manifestation of the flux-trapping effect [136, 137]. However, out of all $L = 3$ states, $L = 4 - 1$ shows maximal resilience to negative flux.

To emphasize again, the size of the sample is playing a crucial role for the V-Av state. While the symmetry-induced V-Av exists only for small samples [compared to the coherence length $\xi(T)$] the pinning-stabilized V-Av requires a large sample. This is illustrated in Fig. 2.24(a) for a square with five holes. When the sample is larger, the flux stability region of the pinning stabilized V-Av state becomes larger as well. This we can attribute to the weakened influence of the Meissner current on the inside vortices because of the larger distance. One also notices the extremely large flux interval (from $-7.5\Phi_0$ to $17\Phi_0$) for stability of the $L = 3$ pinning-stabilized V-Av state. However, penetration field for new vortices *must decrease* for larger samples (see e.g. [138] for the case of large BiSCCO disks). It is already known that magnetic field higher than H_{c1} is needed for penetration of vortices into mesoscopic superconductors, but this factor decreases to unity in bulk systems. Nevertheless, latter factor decreases with size of the sample much slower than the square power increase of the area of the sample. As a consequence,

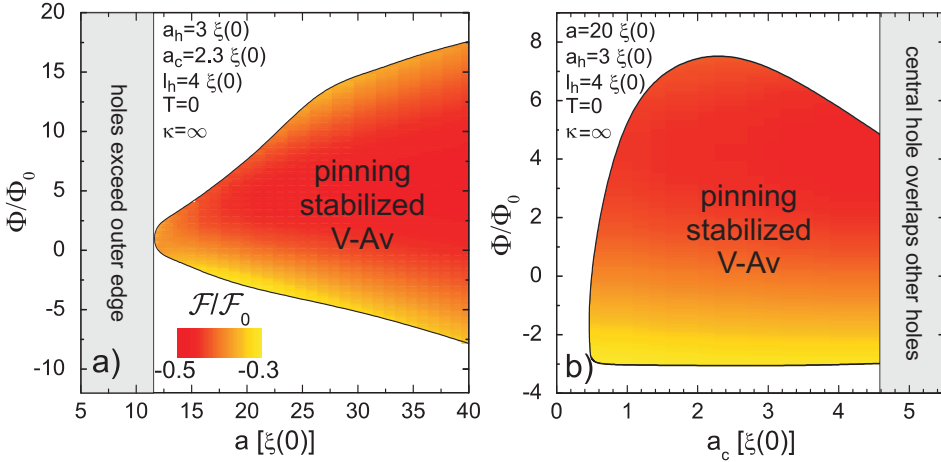


Figure 2.24: The stability diagram vs. applied field (i.e. magnetic flux) for the pinning-induced vortex-antivortex state, (a) as a function of the sample size for a fixed temperature, and (b) as a function of the size of the central hole.

the threshold flux for penetration of new vortices in our sample *increases* as a function of $a/\xi(0)$. We also observed the changing curvature of the latter dependence (at $a/\xi(0) \approx 25$); from the calculation of threshold magnetic field, we found that samples with size of 10 - $25\xi(0)$ exhibit almost identical demagnetization effects i.e. similar vortex penetration field which then gradually decreases for sizes above $25\xi(0)$.

The size of the central hole is equally important as the sample size, as it relates to the ability of V-Av pair to annihilate. Consequently, this second generation V-Av state *cannot be stabilized* in the absence of the central hole [see Fig. 2.24(b)]. The effect of decreasing the central hole size is also indicated in Fig. 2.24(b) - the upper boundary of the flux stability interval is decreasing, due to facilitated V-Av annihilation (at high fields, vortices are pushed towards the center of the sample), while the lower boundary is in fact *not influenced* by the size of the central hole. Note that the lower boundary lies in the negative field region, where vortices have expulsion tendency, and pinning of any strength stabilizes the central antivortex with ease.

The latter stability of the pinned V-Av state in the negative field forms a base for the realization of this state in experiment. Namely, abrupt increase of the magnetic field from a low negative value (that stabilizes one antivortex in the sample) to a large positive one (allowing for penetration of multiple vortices in outer holes) may result in the desired V-Av state at low temperatures. Alternatively, following the results of Fig. 2.23, one can think of an abrupt temperature decrease. We performed a corresponding simulation, where we started from the symmetry-induced V-Av state (which is the ground state for $L = 3$ at temperatures near

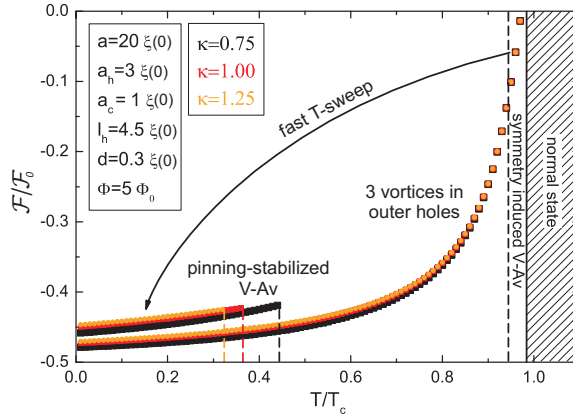


Figure 2.25: The energy of V-Av molecules as a function of temperature, for different values of the Ginzburg-Landau parameter κ . In numerical simulations, an abrupt cooling enables direct transition between two kinds of V-Av states.

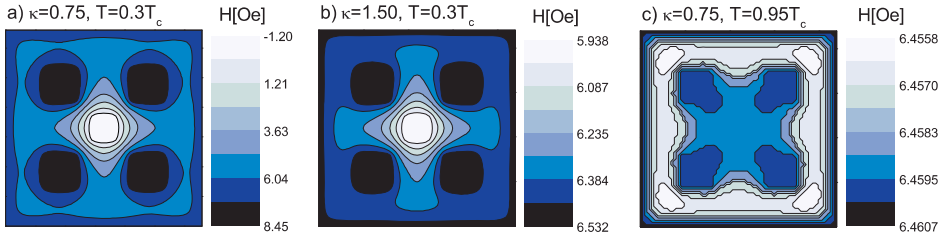


Figure 2.26: Calculated magnetic field profiles in the sample: (a,b) for the pinning-stabilized V-Av state and two values of κ , and (c) the corresponding profile for the symmetry-induced V-Av state. Parameters: $H_a = 6.46\text{Oe}$, $\xi(0) = 0.2\mu\text{m}$, $a = 4.0\mu\text{m}$, $a_h = 0.6\mu\text{m}$, $a_c = 0.2\mu\text{m}$, $l_h = 0.9\mu\text{m}$, $d = 0.05\mu\text{m}$

T_c) and then applied a steep temperature decrease. Without taking into account the experimentally relevant temperature gradient over time, the simulations were always able to land into the pinning-stabilized V-Av state at low temperatures. This is illustrated in Fig. 2.25 where also the influence of κ is depicted. Stronger screening of the magnetic field into the holes, which can be realized by decreasing κ or by taking a thicker sample, enhances the pinning, and consequently favors the V-Av state of second generation, *in contrast* to the symmetry-induced V-Av which is disfavored by low values of κ due to the effective attraction of vortices into a single bundle (see section 2.2.2).

Although quite difficult to realize (never being the ground-state of the system), the second generation V-Av state is much more suitable for direct experimental

visualization than its symmetry-induced ancestor. Firstly, samples can be made larger, and spacing between vortices and the antivortex are sufficient for their identification. Second, the Cooper-pair density is significantly higher inside the V-Av molecule, since temperature may be far below T_c . Third, the magnetic field profile in the sample is sufficiently inhomogeneous, with pronounced amplitudes, benefiting from the size of the V-Av state and its stability for low values of κ . This is shown in Fig. 2.26 where the magnetic field profile in and nearby the sample is calculated for two values of κ for the second generation V-Av and for one value for the symmetry-induced V-Av (given in real units). For taken parameters, the magnetic field contrast inside the symmetry-induced V-Av molecule is of the order of 0.01 Oe, while that of the second generation V-Av can be above 10 Oe, thus three orders of magnitude larger.

2.5 Conclusions

The existence of geometry induced antivortices in the presence of a *homogeneous* magnetic field has been predicted theoretically several years ago [47]. Up to now, the experimental verification is lacking. With numerical simulations, using both the linear and full non-linear Ginzburg-Landau theory, we investigated how to engineer superconducting samples to stabilize and enhance the vortex-antivortex state.

We propose how to design the superconducting sample without taking away the conceptual novelty of the nucleation of the vortex-antivortex pair in a homogeneous magnetic field, as opposed to the idea of placing e.g. a magnetic dot on top of the sample. We pursued the idea to introduce holes which will act as pinning centers, and in doing so, pull the vortices away from the antivortex and additionally provide a strong immunity for the state against imperfections and defects. First we elaborated on the size and position of these holes. We determined optimal parameters for the square and triangle geometry. For instance, in a square geometry, we managed to enlarge the separation between vortex and antivortex with a factor of 8, compared to the case without holes.

We then investigated the influence of several kinds of geometric defects on the V-Av state. For all the imperfections we studied, we found that the holes cause a substantial increase of the stability of the V-Av configuration with respect to sample imperfections compared to the case of a sample without holes.

The geometry-induced antivortices are known to be a consequence of the symmetry of the sample. Therefore, we focused on the competition of different sources of symmetry in a mesoscopic superconductor. We concluded that a collection of pinning centers are by far the most efficient in imposing their symmetry, while the shape of the outer boundary of the sample has a less important role. Thinking further along this line, we studied circular disks, perforated by a number of sym-

metrically placed holes, and found states with *giant antivortices* with vorticity up to -7. However, we found that this spectacular configuration is also highly sensitive to imperfections in geometry.

Further, the effect of the non-linearity of the first GL equation and the magnetic screening represented by the second GL equation was critically examined, allowing us to investigate the influence of temperature and non-zero thickness of the sample on the V-Av state. We constructed phase diagrams for different values of the GL parameter κ for the perforated and the plain square system showing the stability region of the V-Av state in the $\phi - T$ parameter space. The introduction of holes decreases the temperature range in which the V-Av is stable. For small (large) holes, a decrease of κ increases (decreases) the temperature range in which the V-Av is stable. During the second order transition from the multivortex to the vortex-antivortex state, asymmetric vortex-antivortex are encountered. Such asymmetric states are counterintuitive since the V-Av state is known to be a consequence of symmetry and yet must manifest in an asymmetric way during the transition from the conventional multivortex to the V-Av state. These asymmetric states are however stable in a very narrow temperature range ($\sim 10^{-3}T_c$).

We also showed that a small value of κ disfavors the vortex-antivortex state in all investigated geometries (square, perforated square, perforated triangle), contrary to the findings of Ref. [125] where a vortex-antivortex state in a type-I triangle is predicted to be more stable. We mainly concentrated our discussion on square samples but we believe that our main conclusions hold for any geometry.

Finally, using a square superconducting geometry with five holes, we found a second generation of the $L = 3$ vortex-antivortex (V-Av) state in a uniform field. This state is purely induced by pinning, and is NOT caused by the symmetry of the sample, contrary to the previously found V-Av molecules. This novel state is energetically favored in rather large mesoscopic samples, but it is never the ground state of the system. Consequently, more elaborate techniques are needed for its stabilization in experiment, such as an abrupt increase of field (from negative to positive value), or an abrupt cooling of the symmetry-induced V-Av state. However, the very large $\Phi - T$ stability range of the second generation V-Av state, the very comprehensive size of the V-Av molecule, and the large variation in amplitudes of both superconducting order parameter and stray magnetic field inside the molecule (further enhanced for lower κ and temperature), should all lead to facilitated experimental observation of this fascinating state.

The results presented in this chapter were published as:

- R. Geurts, M. V. Milošević and F. M. Peeters, *Symmetric and Asymmetric Vortex-Antivortex Molecules in a Fourfold Superconducting Geometry*, Phys. Rev. Lett. **97**, 137002 (2006)

- R. Geurts, M. V. Milošević and F. M. Peeters, *Stabilization of vortex-antivortex configurations in mesoscopic superconductors by engineered pinning*, Phys. Rev. B **75**, 184511 (2007)
- R. Geurts, M. V. Milošević and F. M. Peeters, *Second generation of vortex-antivortex states in mesoscopic superconductors: Stabilization by artificial pinning*, Phys. Rev. B **79**, 174508 (2009)

Chapter 3

Vortex matter in two-gap superconductors

We study the effects of the coupling between two electronic condensates in two-gap mesoscopic superconductors using numerical simulations in the framework of Ginzburg-Landau theory. In applied magnetic field, we derive the dependency of the vortex size on the sample size and the strength of the Josephson coupling. In addition, we elaborate on the dependence of the critical temperature and field on the parameters of coupled condensates. We demonstrate further the existence and stability of non-composite states, for which the two condensates comprise different vorticity. Moreover, we also found pronounced asymmetric non-composite states and we show their experimentally observable magnetic response. Finally we introduce the magnetic coupling between condensates, and study in particular the case where one band is type II and the other type I, i.e. the sample is effectively of I.x type. The calculated $M(H)$ loops show a clear signature of the mixed type of superconductivity, which we find to be strongly affected by the ratio of the coherence lengths in the two condensates.

3.1 Introduction

MgB₂ is the first superconductor unambiguously shown to possess two superconducting gaps [58]. Since its discovery in 2001 [56], a lot of research was conducted on this specific material as well as on two-band superconductors in general. In its class of binary compounds and metallic superconductors, MgB₂ turns out to have the highest critical temperature known today, $T_c = 39$ K. Its bulk critical field is strongly anisotropic: 3.5 T along the c -axis of the crystal and 17 T in the ab -plane and can reach fields as high as 43 T in films [139–141].

While the mechanism of its superconductivity is not yet entirely understood, it has been experimentally proven that MgB_2 has two separate superconducting gaps. For example, in Refs. [142, 143] the possibility of imaging only the π - or σ -band is demonstrated. On the theoretical side, one must consider two order parameters to describe the superconducting properties of MgB_2 . One of the first Ginzburg-Landau (GL) descriptions of multigap superconductors was developed by Zhitomirsky and Dao, starting from microscopic theory [71]. Fitting to experimental results, the authors pinpointed the values of several GL parameters relevant for MgB_2 , and derived analytical expressions for the critical parameters. In Ref [144], the same authors discussed the anisotropy of H_{c2} in the GL-framework. They considered only the direct exchange of Cooper pairs between condensates, i.e. the so called ‘Josephson’ coupling. Askerzade *et al.* investigated a different type of interaction between the bands - the drag effect [145, 146], which is described in the GL-formalism through the coupling of the gradient terms of the two condensates. The apparent agreement with experiment led these authors to fitting parameters for the GL-model of MgB_2 .

MgB_2 is generally accepted to be a type-II superconductor. However, in a very clean sample, Moshchalkov *et al.* provided estimates that one of the bands could be considered as type-I and the other as type-II [41, 147]. The resulting system exhibits behavior that cannot be attributed to either type, thus the classification as type 1.5 seemed credible. Indeed, the authors found a strong clustering of vortices, a phenomenon which they ascribed to a *combination* of attractive and repulsive vortex-vortex interaction. Actually, Ref. [148] reported a positive surface energy for vortices whenever the coherence lengths of the two bands are comparable. In Ref. [76] the semi-Meissner state was predicted theoretically for a two-gap superconductor and superconductors which do not belong in either of the two classes type-I or type-II, were discussed. The possibility of vortices carrying non-integer flux was studied in Refs. [149–154].

Surprisingly, virtually all studies done to date on two-gap superconductors (TGS) up-to-date concern bulk samples. It is known however that mesoscopic superconductivity bears a number of fascinating phenomena different from bulk, ranging from specific vortex states to enhancement of critical parameters by quantum tailoring. The only existing example of such a study is the one of Chibotaru *et al.* on mesoscopic disks [74, 155]. As a novelty, the authors found that non-composite vortex states (when bands have different vorticity) can be realized in a TGS and can even be thermodynamically stable. However, those results turned to be specific to the case of very weak coupling and not realistic for MgB_2 .

In this chapter we analyze the fundamental properties and vortex matter of mesoscopic disk-shaped two-gap superconductors using the Ginzburg-Landau formalism, where the electronic exchange between condensates occurs through Josephson coupling, and magnetic exchange between condensates is allowed for. The latter

mechanism has not yet been studied in detail up to now. The chapter is organized as follows. In Section II, after describing the theoretical approach, we focus on the effects of Josephson coupling on the the size of a vortex core, the unique vortex states and their $H - T$ stability regions, and the critical temperature and field as a function of coupling strength. In Section III, we introduce the screening of the magnetic field into the theoretical formalism, and illustrate the influence of the magnetic coupling between condensates on the vortex states, particularly in the case of type 1.x superconductivity. Magnetic signatures of the different features are discussed in the light of potential observation by magnetometry. Finally, our findings are summarized in Sec. IV.

3.2 Josephson coupling

3.2.1 Theoretical formalism

It is widely accepted that the high critical temperature of MgB₂ arises due to the coupling of the superconducting bands which effectively reinforce each other. However, the exact nature of the coupling is not fully understood, and possible scenarios are the exchange of electrons, Cooper pairs, interaction between the respective supercurrents, interaction through the internal magnetic field, etc. Microscopic ab-initio calculations have not been able to pinpoint the key interaction. In what follows, we will consider the Josephson coupling between the bands, resulting from the tunneling of the Cooper pairs from one band to another. This is incorporated in the Ginzburg-Landau (GL) energy functional through an interaction term dependent on the order parameter of both bands and proportional to Γ , the Josephson coupling strength:

$$\Delta F = \int \left[\sum_{n=1}^2 \left(\frac{1}{2m_n} \left| (-i\hbar\nabla - \frac{2e}{c}\vec{A})\Psi_n \right|^2 + \alpha_n |\Psi_n|^2 + \frac{1}{2}\beta_n |\Psi_n|^4 \right) - \Gamma(\Psi_1^*\Psi_2 + \Psi_2^*\Psi_1) \right] dV, \quad (3.1)$$

where $\alpha_n = \alpha_{n0}(1 - T/T_{cn})$ and β_n are the GL coefficients, and n is the band index. This results in a set of nine parameters describing a two-gap system: α_{10} , α_{20} , β_1 , β_2 , the Cooper-pair mass m_1 and m_2 , Γ , and critical temperatures T_{c1} and T_{c2} . We then introduce temperature independent units, in order to rewrite Eq. (3.1) in a dimensionless form. We express the free energy of the system in units of $F_{10} = \alpha_{10}^2/\beta_1$, length in units of ξ_{10} ($\xi_{n0} = \hbar/\sqrt{-2m_n\alpha_{n0}}$), the vector potential in $A_0 = \hbar c/2e\xi_{10}$, the order parameters in $\Psi_{n0} = \Psi_{n0}(T = 0, \Gamma = 0, H = 0) = \sqrt{-\alpha_{n0}/\beta_n}$ and the temperature in T_{c1} . This reduces the set of necessary parameters to just five: $\delta = \Psi_{10}/\Psi_{20}$, $\alpha = \xi_{10}^2/\xi_{20}^2$, $m = m_1/m_2$, $T_{cr} = T_{c2}/T_{c1}$

and $\gamma = \Gamma/\alpha_{10}$. In addition, we have two external tuneable parameters, the actual temperature T and the applied field H . We first consider an extreme type-II case, and neglect the self-induced magnetic field in the sample.

The minimization of the energy functional leads to the two-band GL equations. After the scaling described above, the equations for the order parameters read:

$$\begin{cases} (-i\nabla - \vec{A})^2 \psi_1 - (1 - T - |\psi_1|^2) \psi_1 - \frac{\gamma}{\delta} \psi_2 = 0, \\ \frac{1}{\alpha} (-i\nabla - \vec{A})^2 \psi_2 - \left(1 - \frac{T}{T_{cr}} - |\psi_2|^2\right) \psi_2 - \frac{\gamma\delta}{m\alpha} \psi_1 = 0. \end{cases}$$

In the following analysis we neglect the screening of the magnetic field. This is justified for an extreme type-II material, or any sufficiently thin sample. An applied vector potential $A = (\frac{1}{2}Hy, -\frac{1}{2}Hx, 0)$ results in a magnetic response resulting from a total supercurrent:

$$\vec{j}_s = \Re \left[\psi_1 (i\nabla - \vec{A}) \psi_1^* \right] + \frac{m}{\delta^2} \Re \left[\psi_2 (i\nabla - \vec{A}) \psi_2^* \right]. \quad (3.2)$$

Let us here address several direct implications of Josephson coupling. It is clear from Eq. (3.1) that the sign of γ determines the relative phase shift between the order parameters in the two condensates - either ≈ 0 when $\gamma > 0$ or $\approx \pi$ when $\gamma < 0$ - in order for the coupling term to provide a negative energy contribution. However, the sign of γ has no influence on observables such as the Cooper-pair density and magnetic response of the sample. The general consequence of γ coupling is an injection of Cooper pairs from one band into the other and vice versa, thus increasing the stability of the superconducting state. In other words, the average Cooper-pair density always increases with γ . In the absence of an applied field, the ratio $\chi = \psi_1/\psi_2$ can be found from

$$\frac{\gamma\delta}{m\alpha} \chi^4 + \left(1 - \frac{T}{T_{cr}}\right) \chi^3 - (1 - T) \chi - \frac{\gamma}{\delta} = 0, \quad (3.3)$$

analytically derived from the GL-equations. From this we find that in the limit $\gamma \rightarrow \infty$ a constant ratio $\psi_1/\psi_2(H=0) = \sqrt{\sqrt{m\alpha}/\delta}$ is reached, independent of temperature.

The next section is dedicated to an analysis of the size of the vortex core. Before we get into the physics of the problem, we here address some numerical issues following from mapping of the superconducting *disk* on a *square* numerical grid. For obvious reasons, the influence of the resolution of the numerical grid N , on the observed vortex size R_V , is significant. In Fig. 3.1(a) we show the R_V vs. N (definition of R_V is given in the next section). With increasing grid density, the numerical error decreases, and the vortex size converges towards the R_0 value with dependence $R_V = R_0 + b/N$. By a fitting procedure R_0 and b can be determined and the corresponding curves are represented by the solid lines in the figure. The

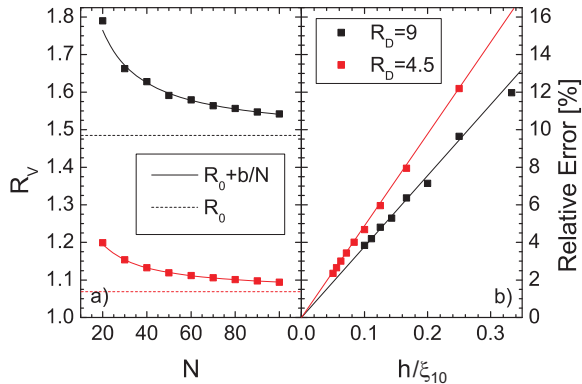


Figure 3.1: (a) The dependence of the observed vortex size R_V on the number of grid points in the numerical mesh N . (b) The relative error in found vortex size vs. grid spacing h , for two different sizes of the superconducting disk.

dashed lines are the asymptotes with value R_0 . In Fig. 3.1(b) the relative error is plotted as a function of h , the grid spacing (proportional to sample size and inversely proportional to N). We conclude that due to numerics the vortex size is always slightly overestimated, with overshoot increasing for smaller samples (where influence of the boundaries is more pronounced). Nevertheless, with a resolution of 10 points per coherence length we get a relative error under 5%. Although higher grid density obviously improves the results, we refrain from using a density above 10 points/ ξ , in order to optimize the speed of the calculation.

3.2.2 Size of the vortex core

The coherence length is the characteristic length scale over which the order parameter changes. It is therefore intuitive that the size of a vortex core is proportional to the coherence length in bulk superconductors. In single-gap materials, the coherence length is proportional to $1/\sqrt{1 - T/T_c}$ in the temperature range where the Ginzburg-Landau theory is valid. Here we show that in two-gap superconductors the coherence length is strongly affected by the coupling parameter γ , generally in an opposite manner from temperature. For comparison, we can use the coherence length obtained from the expression for the second critical field derived in Ref. [71], through the relation $H_{c2} = \Phi_0/2\pi\xi^2$, with Φ_0 being the flux quantum. Deviations are a priori expected, since already experiments of Refs. [142, 143] found a discrepancy between the vortex size and the coherence length deduced from the second critical field.

To estimate the coherence length, we will numerically determine the size of the vortex core, a quantity which is not uniquely defined. In the following calculations,

we examine the single-vortex state in a MgB₂ superconducting disk exposed to a field providing three flux quanta through the sample. For a definition of the vortex size, two possibilities are considered in literature: (i) The vortex size is determined by the distance from the center of the vortex to the contour where the Cooper-pair density (CPD) recovers to some percentage of its maximal value in the sample, denoted as $R_{V,CPD}$; (ii) The vortex size is the distance from the center of the vortex to the first contour where the supercurrent j_s reaches its maximum, denoted as $R_{V,j}$. The problem of the first definition is the arbitrary threshold value for the criterion, but also the fact that we have two Cooper pair densities, which makes the single vortex size ambiguous. As a threshold we take 80 %, since this allows for a more precise vortex size determination, and we will consider only the first condensate. On the other hand, the second definition involves coupled condensates and thus provides us with a unique vortex size. We therefore adopt the second definition to describe the vortex size in the rest of this work. Contrary to bulk case, in our mesoscopic disks both definitions render a vortex size dependent on the radius of the disk R_D , as vortex currents in the center of the sample can interact with Meissner currents decaying from the edge inwards. However, while $R_{V,CPD}$ in each band saturates for $R_D \rightarrow \infty$, this is not the case for $R_{V,j}$: it develops a linear dependence on R_D . We extracted the exact dependence of both definitions of the vortex size R_V on the disk size R_D , which led us to a universal formula (valid for both definitions, but with different coefficients):

$$\left(\frac{1}{R_{V0}}\right)^2 + \left(\frac{c}{R_D}\right)^2 = \left(\frac{1}{R_V - hR_D}\right)^2, \quad (3.4)$$

where R_{V0} is the vortex size independent of the sample size, c is a length coefficient and h is the slope of R_V vs. R_D for large R_D . From fitting of our numerical data, collected at different T , γ , α and m , we obtained $\{c = 1.90, h = 0\}$ for $R_{V,CPD}$ and $\{c = 3.40, h = 0.006\}$ for $R_{V,j}$. These coefficients are valid for single gap superconductors *as well as* for two-gap superconductors, even when coherence lengths of the two condensates are very different (e.g. for small α , see Fig. 3.2). The function gives an excellent estimate of the vortex size for anisotropic mass, i.e. $m = 1$, for disks larger than 5ξ . As shown in Fig. 3.2, deviation from the given function does occur for specific choices of m and α , especially for small disks, but the relative error remains under 5%.

Both previously given definitions of R_V are illustrated in Fig. 3.3. When disks are too small, the vortex size is not always predictable by the disk size only, e.g. when $T > T_{cr}$ and $\gamma < 0.1$, when the coherence lengths differ much and the interaction of the vortex with the Meissner currents becomes too different in the two bands. We found however that when $R_D > 10\xi_{10}$ these mesoscopic effects only have a minor influence and the correspondence between R_V and R_D becomes predictable again. With the established dependence of the vortex size on the size of the sample, we

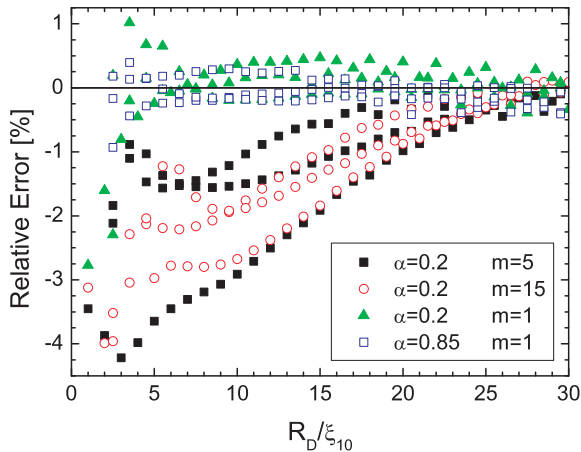


Figure 3.2: The relative error of the result of Eq. (3.4) compared to the observed vortex size, as a function of disk size, for indicated different values of parameters m and α , each with three different combinations of γ and T in order to cover as large as possible parameter space in the analysis.

can more precisely determine the actual influence of coupling γ on the vortex size. In particular we will look at the behavior of $R_{V0,j}$ as a function of T , T_{cr} and γ (parameters α and m remain fixed at realistic values for MgB₂).

In Fig. 3.4 the independent vortex size R_{V0} is plotted versus γ , for different temperatures T and T_{cr} . The dots represent the result of the simulations. The general behavior can be described by following the observed trends: i) Increasing T induces an increase of the vortex size whereas increasing γ has the opposite effect. ii) Deviation from the latter monotonic behavior occurs when $T \approx T_{cr}$ and the coupling is weak, see e.g. the curve at $T = T_{cr} = 0.4$. The reason for the initial positive slope is that the second band is revived by the presence of coupling but retains its own character (i.e. a larger coherence length) since coupling is still weak. iii) For $T > T_{cr}$, curves with different T_{cr} but identical T merge at $\gamma = 0$ since then only the first condensate survives and fully determines the vortex size. In Fig. 3.4, the solid curves represent an estimate of the vortex size based on the general relation between the coherence length and the upper critical field in a single gap bulk superconductor $H_{c2} \propto 1/\xi^2$,

$$\xi = \frac{\sqrt{2}}{\sqrt{g_+(\alpha, T, T_{cr}) + \sqrt{g_-(\alpha, T, T_{cr})^2 + 4\frac{\gamma^2}{m}}}}, \quad (3.5)$$

with $g_{\pm}(\alpha, T, T_{cr}) = 1 - T \pm \alpha \left(1 - \frac{T}{T_{cr}}\right)$, based on the analytical expression for

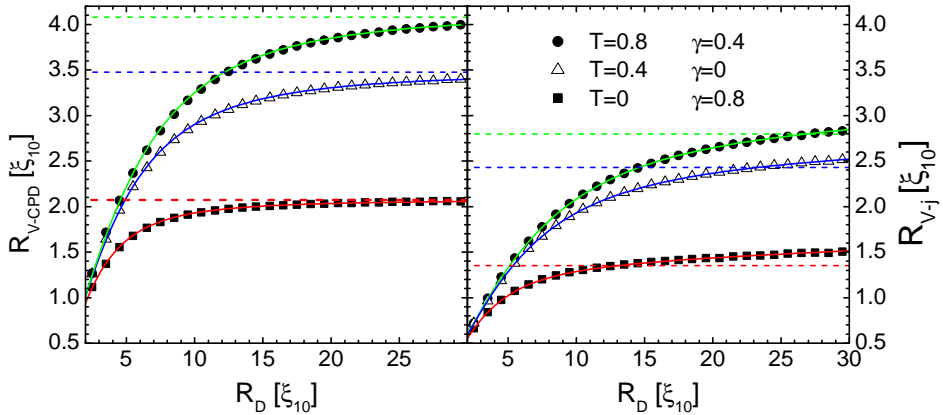


Figure 3.3: Vortex size, determined through the decay of the Cooper-pair density R_{V-CPD} (a) and determined through the maximum of encircling currents R_{V-j} (b), as a function of the radius of the superconducting disk R_D . The solid dots represent the numerical results, while solid lines show the fit using Eq. (3.4). The dashed lines indicate R_{V0} , the fitting parameter corresponding to the sample-independent vortex size.

the critical field of a bulk two-gap superconductor,

$$H_{c2}(T) \propto 1 - T + \alpha \left(1 - \frac{T}{T_{c2}} \right) + \sqrt{\left(1 - T - \alpha \left(1 - \frac{T}{T_{c2}} \right) \right)^2 + 4 \frac{\gamma^2}{m}}, \quad (3.6)$$

taken from Ref. [71]. We find that the vortex size in our samples scales to the coherence length as $R_{V0} = 1.78\xi$, which we use to plot the curves in Fig. 3.4. These theoretical curves coincide rather well with the data for $\gamma > 0.25$. The reason for this is that, when coupling becomes sufficiently strong, both order parameters tend to have a similar spatial distribution and thus also exhibit a similar vortex size and coherence length. A good correspondence between the data and the fitted curves is also found for $T \gg T_{cr}$, i.e. when the second condensate exists solely due to the coupling to the first condensate, or in the case of weak coupling and the second condensate is almost depleted, so that it does not influence the vortex size. Two regions of discrepancy include $T \approx T_{cr}$ (R_{V0} behaves non-monotonic), and $T \ll T_{cr}$ and weak coupling. For the latter case, the formula still predicts $R_{V0}(\gamma = 0)$ to be independent of T_{cr} , while this is clearly not the case. In this regime the vortex size is found to behave more like that of a single gap superconductor, but with a different critical temperature. By fitting we determined a function that describes

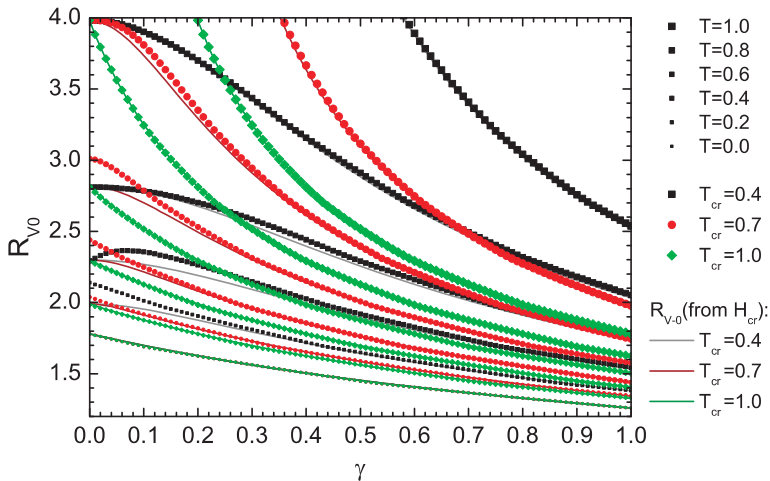


Figure 3.4: R_{V0} as a function of γ and temperature, for $\gamma < 1$ and for different values of T_{c2} . $\alpha = m = 1$.

the behavior of the vortex size accurately in this regime as

$$R_{V0} = \frac{1.78}{\sqrt{1 - T/\sqrt{T_{cr}} + \gamma}}. \quad (3.7)$$

This equation is generally applicable, and effectively shows our initial premise that γ has an opposite influence to T .

We notice however that Eq. (3.5) also contains the dependence on α and m . However, this formula can not adequately describe the vortex size for m, α much different from 1, since the properties of the two condensates can no longer be described by a single coherence length. In general we can state that the relation between coherence length and critical field does not hold anymore when the individual coherence lengths differ too strongly. In Fig. 3.5 we plot the numerically obtained R_V as a function of m , for small parameter α (with thus an acute difference between coherence lengths in two condensates). The analytic estimate of Eq. (3.5) is monotonously increasing with m in this case, and is obviously not useful for comparison with non-monotonically evolving curves in Fig. 3.5.

Let us first analyze the limiting case of extremely large m . Following from Eq. (3.2.1), the second condensate decouples from the first one in this limit. At the same time, as seen in Eq. (3.2), the influence of the second condensate on the total current in the system increases. Therefore, the size of the vortex $R_{V,j}$ will be fully determined by the second condensate (and its nominal coherence length $\xi_2(T)$), provided that the temperature is below T_{cr} . Otherwise, the vortex size is determined solely by the first condensate (and $\xi_1(T)$), since the coupling between the condensates is entirely suppressed and the second condensate fully depletes.

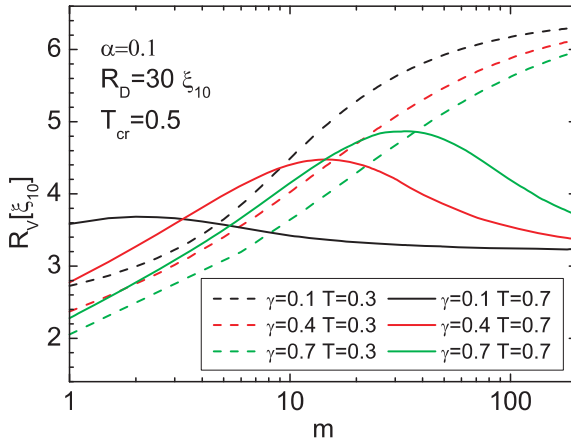


Figure 3.5: The apparent vortex size in a disk with radius $R = 30\xi$ as a function of m , for different γ and T . The ratio of coherence lengths in two condensates is fixed at $\xi_{20}/\xi_{10} = 3.162$, i.e. $\alpha = 0.1$.

This helps us understand the behavior of the vortex size as a function of m , shown in Fig. 3.5. At $T < T_{cr}$, the initial increase of m decreases the coupling of the second condensate to the first (m has an opposite effect from γ , see Eq. (3.2.1)). This causes an increase of the apparent vortex size, due to much larger coherence length of the second condensate ($\alpha = 0.1$), and at the same time the increase of m makes the supercurrent of the second band stronger and thus more deterministic for the magnetically detectable size of the vortex (see Eq. (3.2)). Above T_{cr} these two effects become competing, since the first will deplete the second condensate and therefore reduce its influence while the second enhances the influence of the second condensate. These competing effects result in the non-monotonic behavior of the vortex size vs. m in Fig. 3.5. At low m , the influence of the large coherence length in the second condensate dominates, whereas at large m the coupling disappears and the second condensate depletes. At very large m , all curves for $T > T_{cr}$ saturate to the same value, namely the size of the vortex core in the first condensate, in the absence of a second one.

In Fig. 3.6 we demonstrate some peculiarities of the dependence of the vortex size on parameter α . α was swept down from 1 to 0.05 in a disk with parameters $m = \delta = 1$, $T_{cr} = 0.5$ and $R_D = 30\xi_{10}$. In the absence of coupling, this sweep increases ξ_{20} while ξ_{10} is kept constant, as the length unit of the GL equations. In the presence of coupling, both the resulting ξ_2 and the resulting ξ_1 will be influenced (i.e. the Cooper-pair correlation length in each of the condensates, different from the nominal coherence lengths in each condensate separately). Intuitively, one expects that coupling causes vortex cores in two condensates to have similar behavior, and tend towards similar sizes; instead, for decreasing α at temperatures

$T = 0.45$ and $T = 0.7$ an increase of R_{V2} is observed while R_{V1} decreases! For stronger coupling this effect becomes even more prominent, compared to the vortex size at $\alpha = 1$. At lower temperatures (shown for $T = 0$ in Fig. 3.6), the behavior of $R_{V,j}(\alpha)$ for $T = 0$ is in better concordance with the intuition: R_{V1} increases as R_{V2} increases, with the effect growing with coupling. However this effect is weak, and still reverses for e.g. $\gamma = 0.5$ below $\alpha \sim 0.1$.

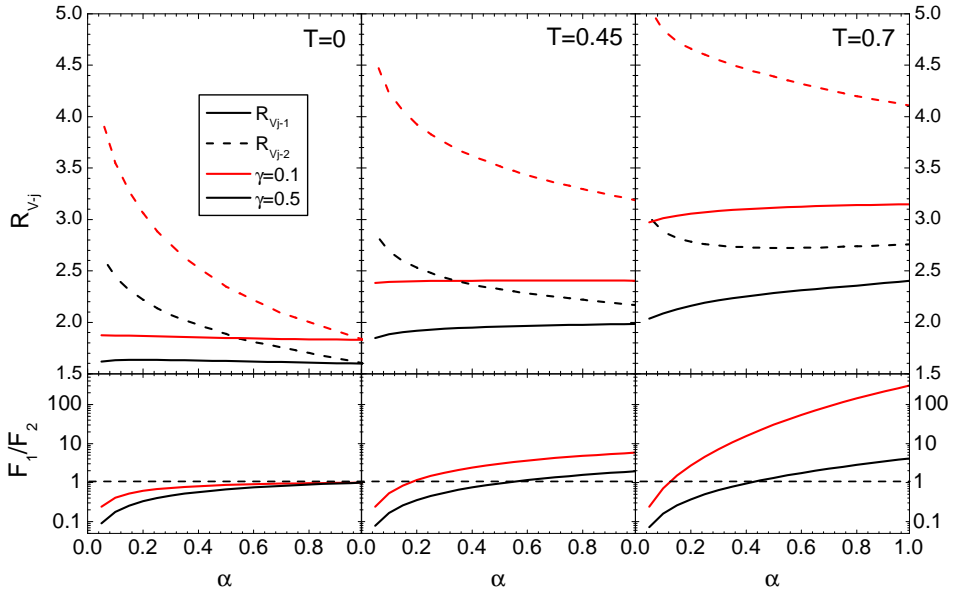


Figure 3.6: Top: R_V in each condensate as a function of α , for different γ , T . Bottom: Ratio of condensation energies of the two condensates (logarithmic scale) vs. α . When equal to 1, condensates influence each other with equal strength since $m = 1$.

The complex behavior of this system is the consequence of the competition of two opposite effects. An important quantity here is the ratio of the order parameters since this determines which terms in the GL equations dominate. Equivalently we can look at the ratio of the condensation energies, $F_1/F_2 = \int |\psi_1|^4 / \int |\psi_2|^4$, as shown in the bottom panel of Fig. 3.6. From the solution of Eq. (3.3) we find that $\chi = \psi_1/\psi_2$, the ratio of order parameters in zero field, goes to zero when $\alpha \rightarrow 0$. Actually both ψ_1 and ψ_2 diverge at this point, but ψ_2 at a faster pace. When $\chi < 1$, i.e. $\psi_1 < \psi_2$, the second condensate will remain practically unaffected by the first condensate. R_{V2} will therefore be determined by the intrinsic coherence length of the second band at the given temperature. However, at the same time the first band will still get a strong injection of Cooper-pairs, thus decreasing the coherence length and increasing the superconductivity in the first band. For $\chi > 1$, we obtain

the opposite. The second band now experiences an influx of Cooper pairs from the first band, but much weaker than previously described, since ψ_1 does not diverge as fast as ψ_2 . This has as a consequence that the second band manages to retain its own character¹. The first band in this case dominates but is nevertheless coupled to the second condensate. When α decreases, also χ decreases and the second band becomes more influential. This will initially demonstrate as an increase of R_{V1} , i.e. the vortex size of the first band attempts to follow that of the second. Ultimately, at small α the injection of Cooper-pairs dominates (since also χ becomes lower than 1), and the coherence length and vortex size in the first condensate shrink.

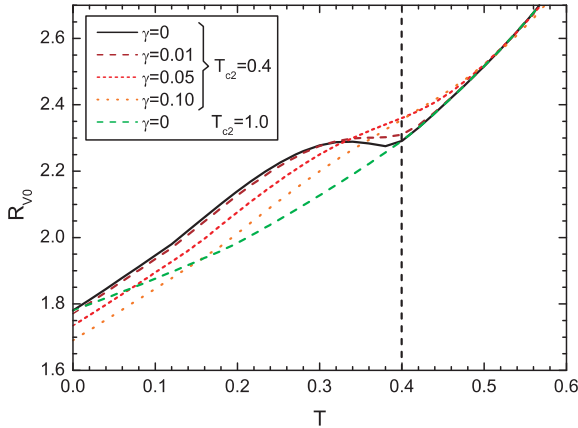


Figure 3.7: The size-independent vortex size R_{V0} as a function of temperature (for fixed T_{c1} and T_{c2}), for several values of γ . $R_D = 10\xi_0$, $m = 1$, and $\alpha = 1$.

Finally we draw the attention to one more interesting artefact. In Fig. 3.7 we show the calculated vortex size as a function of temperature, for very weak coupling, i.e. small γ , and $m = \alpha = 1$. The observed kink corresponds to the critical temperature of the second band, and smears out when γ is increased. The $\{\gamma = 0, T_{cr} = 0.4\}$ curve starts at the same value as the $\{\gamma = 0, T_{cr} = 1\}$ curve, since at $T = 0$ there is no dependence of vortex size on T_{cr} . This behavior is observable by magnetic-force, scanning Hall probe, or scanning tunneling microscopy, and we expect its experimental verification.

For the $\{\gamma = 0, T_{cr} = 1\}$ curve, the superconducting state and supercurrents in both condensates are identical. Therefore the vortex size defined on separate condensates as well as on the combined system will be equal. For this reason the curve coincides with the $\{\gamma = 0, T_{c2} = 0.4\}$ case for $T > T_{c2} = 0.4$, since then the

¹Unless partially for $T > T_{cr}$ when the existence of the band is completely due to the coupling (notice the change of curvature for the vortex size in the second band vs. α in the $T = 0.7$, $\gamma = 0.5$ data)

second band is depleted and only the first band superconducts.

3.2.3 H-T phase diagrams

In increasing magnetic field, more vortices penetrate the superconducting system. It is known that the symmetry of the vortex states is strongly affected by the symmetry of the mesoscopic sample, as detailed in Refs. [47, 116]. With increasing temperature, the symmetry of the sample is even stronger imposed on the vortex matter, and it is therefore no surprise that in mesoscopic disks most vortex state configurations collapse into a giant-vortex at high temperature. We can construct an $H - T$ diagram for mesoscopic samples, indicating the area of stability of states with different vorticity. Two-gap systems make there no exception, but do comprise several particularities. In Fig. 3.8 we displayed the full stability regions of all possible vortex states with vorticity $L < 7$ in a superconducting disk with parameters $\{T_{c2} = 0.44, \delta = 1.33, \alpha = 0.844, m = 1\}$ [74, 155], which is very similar to MgB_2 except for the coupling parameter, where we took significantly smaller $\gamma = 0.01$. This choice provides more complexity to the vortex states, as it allows for different vorticities and vortex arrangements in the two bands.

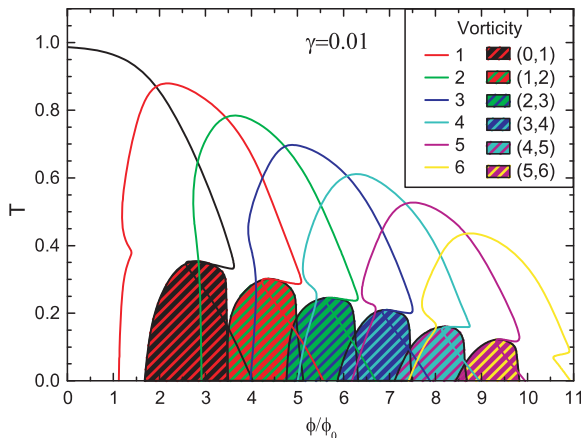


Figure 3.8: The magnetic flux-temperature stability regions for different vortex states (vorticity L) in a two-band disk of size $R_D/\xi_{10} = 4$, and with $T_{c2} = 0.44$, $\delta = 1.33$, $\alpha = 0.844$ and $\gamma = 0.01$. In color-coded areas, the vortex state is non-composite and cannot be represented by a single L , but rather as (L_1, L_2) state, where vorticities in two condensates are given respectively.

Indeed, one difference from the single-gap superconducting disks is directly visible in Fig. 3.8, where the stability regions of composite vortex states are *mushroom shaped*. In other words, with increasing temperature, one can exit the stability

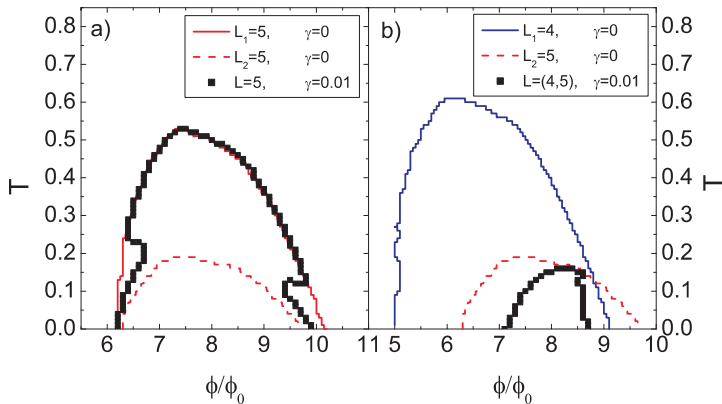


Figure 3.9: Illustration on how the stability flux-temperature regions of composite (a) and non-composite states (b) arise from the single-gap picture.

range of a particular L -state, but then find it again at higher temperatures. This shape has the following origin: At high temperatures ($T_{c2} \ll T < T_{c1}$) the second gap would be completely depleted if it wasn't for the coupling. In other words, the second band depends completely on the first band, and therefore has the same behavior and features like the $H(T)$ -boundary. However, for low temperatures ($T \lesssim T_{c2}$) the second band is still active and retains its own character, and therefore the stability region boundary follows quite closely the single-gap stability region.

In the mushroom-shaped areas, the vortex states are composite, meaning that the vorticity in the two bands is the same. However, in the shaded areas we found non-composite vortex states - where vorticity differs from one band to the other. As a consequence, the overall, apparent vorticity of the sample is no longer integer!

As clearly shown in Fig. 3.9(a), the full $H - T$ stability region of a composite vortex state is related to the union of the $H - T$ stability regions for the given state in the two corresponding single-gap condensates. On the other hand, the non-composite states are found at the intersection of two corresponding single-gap stability regions [see Fig. 3.9(b), for the $(L_1, L_2) = (4, 5)$ state].

With increasing coupling parameter γ , the vortex states in the two condensates are linked together, and moreover reinforce each other. In Fig. 3.10 we show the stability region of the composite $L = 4$ state, for three values of γ , where the $H - T$ stability region grows with γ . We conclude that increasing γ *stabilizes* the composite states, but for the same reason *destabilizes* the non-composite states. We discuss the latter further in the following section.

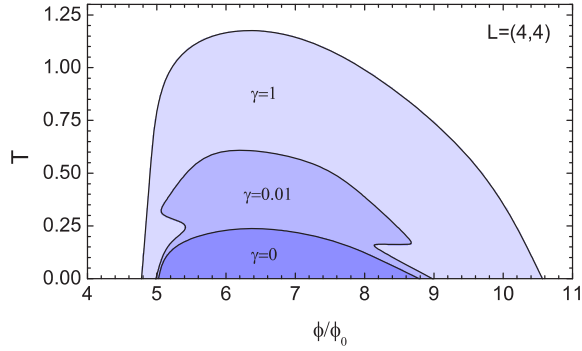


Figure 3.10: The stability region of the $L = 4$ composite vortex state, for three different strengths of coupling γ .

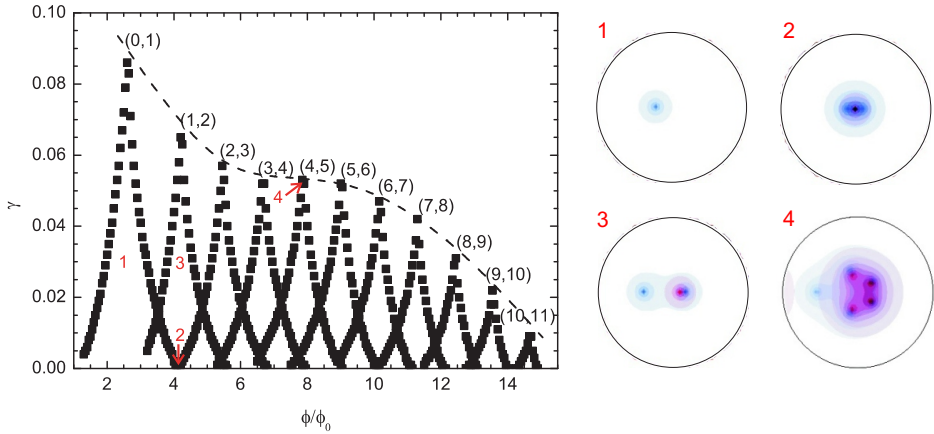


Figure 3.11: The stability regions in $\phi - \gamma$ parameter space of non-composite states with different vorticities in the two bands. Parameters of the sample are $R_D/\xi_{10} = 4$, $\alpha = \delta = m = 1$ and $T = 0$. In insets at the top of the figure, we superimposed the logarithmic plots of the Cooper pair density in the two gaps on each other (red/blue shades for condensates 1/2 respectively) for states indicated in the phase diagram by the red numbers.

3.2.3.1 Non-composite vortex states

The existence of non-composite states, i.e. states with different vorticity in the bands, depends strongly on the coupling. They survive only at weak Josephson coupling between the bands, while only composite states are possible at large γ values. This is illustrated in Fig. 3.11, where we show that the region of stability of non-composite states shrinks with increasing coupling, but also that lower vorticity non-composite states are more resilient to γ . Another interesting aspect of non-

composite states is their strong affinity to asymmetry. In both condensates vortices attempt to form a symmetric shell, but due to coupling and different respective number of vortices, the final state becomes asymmetric in most cases. For that reason, the asymmetry is more apparent at larger coupling γ . We show several examples through the log-plots of the Cooper pair density of the chosen states in Fig. 3.11. Note that the non-composite state not necessarily contains vortices in both condensates; for example, inset 1 in Fig. 3.11 is the $(0, 1)$ state. Due to coupling, the total energy is minimized when regions with depleted order parameter in two condensates are on top of each other. As a result, the vortex of the second band is attracted to the boundary of the sample, where the circulating Meissner currents strongly suppress the order parameter in the first band. Inset 2 is the $(1, 2)$ state for $\gamma = 0$, i.e. the condensates are decoupled. This non-composite state is therefore two-fold symmetric, but when we increase γ we enhance the asymmetric $(1, 2)$ state, as shown in inset 3. One vortex of the second band is attracted to the vortex of the first band, and the other is attracted to the edge of the sample. Finally we show in inset 4 the $(4, 5)$ state, at the verge of its stability region, showing maximally pronounced asymmetry. Four vortices in both bands sit on top of each other, and the remaining, fifth vortex of the second band, breaks the symmetry and is gradually pulled out of the sample. The found states look similar to what was found earlier for Coulomb bound classical particles [128], although underlying physics is very different.

A two-gap mesoscopic system is a prime example of a vortex system with competing interactions. Besides the vortex-vortex interactions in each band, one must take into account the coupling between order parameters across the bands, and the mesoscopic effect of the compression of vortices to the interior by the circulating Meissner current that is maximal at the edge. For example, consider the $(0, 1)$ state, where an outward force originates from the coupling between the vortex in the second condensate and the suppression of superconductivity at the edge of the first one. However, this action competes with the inward force exerted by the Meissner current. This purely mesoscopic effect leads to a tuneable position of the vortex in this non-composite state: while the Meissner current is roughly the same at a given magnetic field, the changed coupling between the condensates brings the vortex further to the boundary. This is shown in Fig. 3.12, as a transition from a non-composite $(0, 1)$ vortex state to a composite $L = 0$ vortex state with increasing coupling.

As fascinating as they are, the non-composite states are difficult to find in the ground-state. For example, when the coherence length of the two bands is the same, then the energy landscape in both bands - considered as separate single-gap superconductors - are proportional, i.e. $F_1 = \alpha\delta^2/mF_2$. All possible vortex states thus have their ground state in the same phase space region. The total energy of the system, $F = F_1 + F_2$, will therefore be proportional to the single-gap energy with as

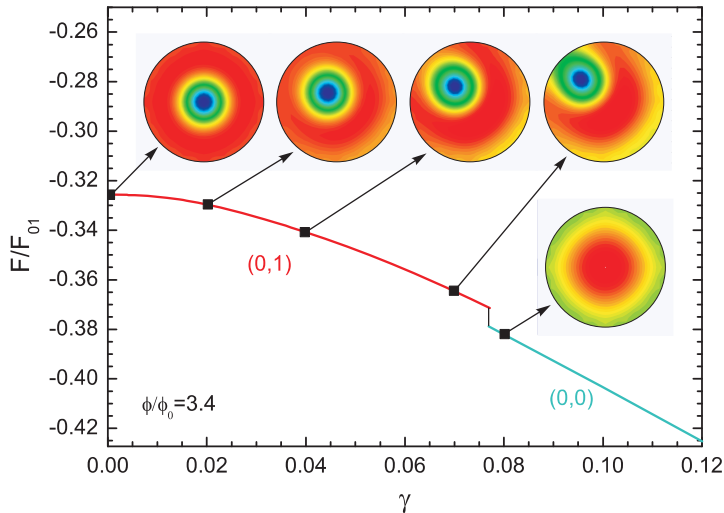


Figure 3.12: Calculated free energy of the non-composite $(0,1)$ state, as a function of Josephson coupling between the bands. Insets show contour plots of the Cooper-pair density in the second gap, illustrating how the asymmetry gradually increases with γ for taken MgB_2 parameters and size of the disk $R_D = 5\xi_{10}$. The γ -sweep was done along the vertical dashed line in Fig. 3.13.

a direct consequence that non-composite states always will have higher (or equal) energy compared to the composite states. To realize non-composite states as the ground state, one therefore needs to make the discrepancy between the coherence lengths as large as possible. This can be done by taking α significantly different from zero, or by taking temperature close to T_{c2} , when $T_{c1} > T_{c2}$. In Fig. 3.13 we show the stability and ground state regions of the non-composite states in a disk of size $R = 5\xi_{10}$ at temperature $T = 0.4$ (and $\alpha = 0.5$).

These asymmetric states can be observed in mesoscopic two-band samples. As main candidates for such an experiment, we select the imaging of only the π -band, as was done recently in Ref. [142]. Alternatively, scanning Hall magnetometry or magnetic force microscopy can both reveal the asymmetric magnetic response of the sample in the case of a non-composite state. We will revisit this point in the section devoted to magnetic coupling.

3.2.3.2 The superconducting-normal phase boundary

As mentioned in preceding sections, in Refs. [71, 146] an expression was derived for the second critical field of a bulk two gap superconductor, given by Eq. (3.6). That expression contains the dependence of the critical field not just on γ , but on m and α as well. We have shown that that dependence does not describe the vortex

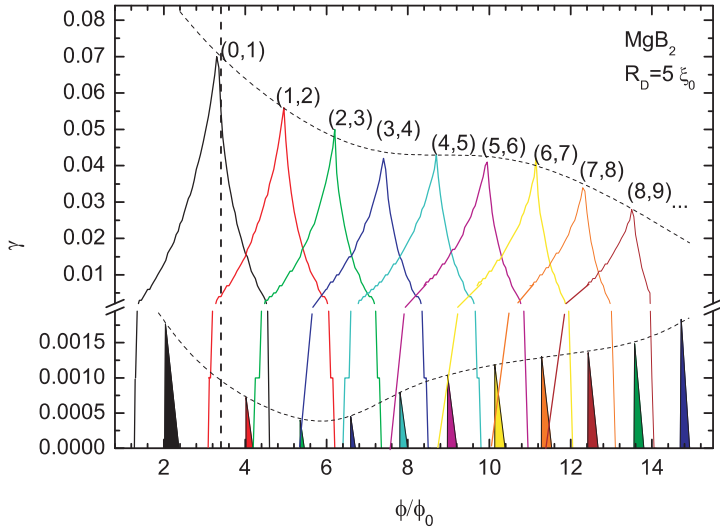


Figure 3.13: The stability regions and the ground state (colored) regions in $\phi - \gamma$ -space of the non-composite states. Taken parameters are $R_D/\xi_{10} = 5$, $\alpha = 0.844$, $\delta = 1.33$, $m = 1$, $T_{c2} = 0.44$ and $T = 0.1$, corresponding to MgB_2 .

properties in the two-band samples, but at this point we check its applicability for the estimation of the upper critical field of mesoscopic two-band disks at a given temperature. Our results for the dependence of the upper critical field on the mass ratio in two bands are shown in Fig. 3.14(a), and demonstrate perfect agreement with Eq. (3.6), provided that the found critical field is scaled by its value at zero temperature and in absence of coupling.

Eq. (3.6) is further applicable for the estimation of the $H - T$ superconducting-to-normal phase boundary. Namely, equating that expression to zero gives the expression for the critical temperature of the two-band sample:

$$T_c = \frac{1}{2} \left(1 + T_{cr} + \sqrt{(1 - T_{cr})^2 + 4 \frac{\gamma^2}{m\alpha} T_{cr}} \right). \quad (3.8)$$

This means that the critical temperature of a two gap superconductor is always equal or higher than the sum of the critical temperatures of the two bands, in the case as if there was no coupling. This observation is in contradiction with findings of Ref. [156], where it is claimed that also a lower T_c is possible, depending on the parameters. The authors obtained these results from a microscopic derivation.

Above expressions were originally derived for bulk samples. It is already known that the upper critical field in mesoscopic superconductors is higher than in bulk [157], and it is therefore intuitively clear that Eq. (3.6) would not work for the case of two-gap mesoscopic disks. In Fig. 3.15 we show the numerically obtained

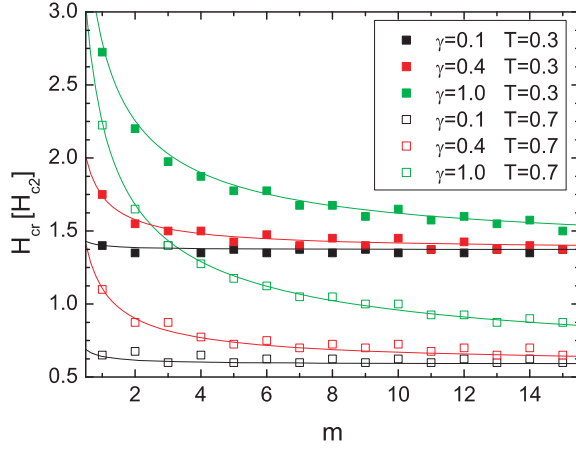


Figure 3.14: (a) The critical field of the mesoscopic disk H_{cr} as a function of the mass ratio in two condensates. Parameters used are $R_D = 4\xi_{10}$, $T_{c2} = 0.5$, $\alpha = 0.1$. (b) Idem but now as a function of α .

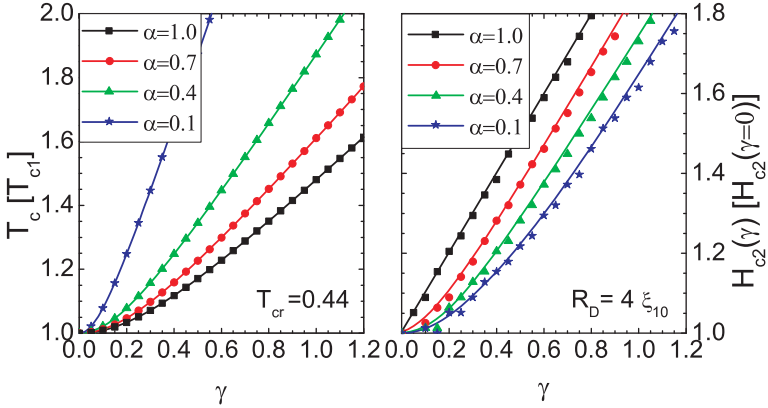


Figure 3.15: (a) The critical temperature T_{cr} of a two-band mesoscopic disk as a function of Josephson coupling γ , in absence of magnetic field. (b) The upper critical field H_{cr} vs. γ for $T = 0$. Dots represent the numerical data, and the solid line is the result of Eqs. (3.6-3.8).

critical temperature T_{cr} and upper critical field H_{cr} (corresponding to bulk H_{c2}) versus γ in disks of size $R = 4\xi_{10}$. We found that both the dependence of critical temperature and field on γ obey the dependencies given in Eqs. (3.6-3.8), provided that the critical field is scaled to its value in the absence of coupling and at zero temperature. In Fig. 3.16 we show the calculated $T_c(H)$ boundary for different coupling strengths. Eq. (3.6) can also be inverted to describe the dependence of T_c

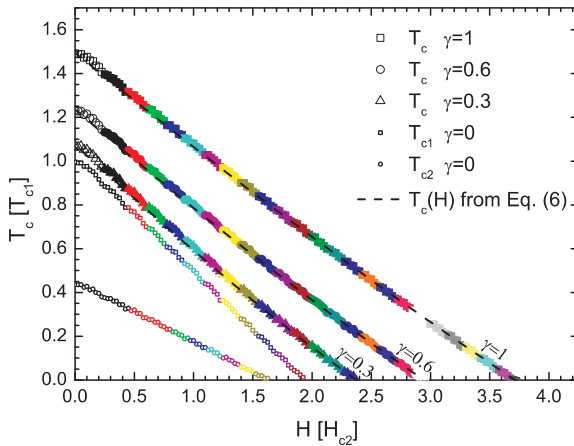


Figure 3.16: The superconducting-normal phase $H(T)$ boundary for the sample with parameters $R_D = 4\xi_0$, $\delta = 1.33$, $\alpha = 0.844$, $T_{c2} = 0.44$ and $m = 1$, for different values of the Josephson coupling strength. Different colors of the dots mean different vorticities. Dashed lines are obtained from Eq. (3.6) with a prefactor described in the text.

on the applied field. Although derived for bulk, we find that latter equation nicely fits the $H(T)$ -curves in Fig. 3.16 for a mesoscopic disk, after the aforementioned scaling of the magnetic field.

3.3 Magnetic coupling

In the previous section, we assumed the existence of a Josephson coupling between two superconducting bands, but we neglected the screening of the magnetic field. In applied magnetic field, the magnetic response of a two-band superconductor follows from the induced supercurrent:

$$\begin{aligned}
 -\kappa_1^2 \Delta \vec{A} = \vec{j}_s &= \Re \left[\psi_1 \left(i\nabla - \vec{A} \right) \psi_1^* \right] \\
 &+ \frac{m}{\delta^2} \Re \left[\psi_2 \left(i\nabla - \vec{A} \right) \psi_2^* \right].
 \end{aligned}
 \tag{3.9}$$

Conventionally, the demagnetization and screening effects in mesoscopic superconductors are expressed through the Ginzburg-Landau parameter κ , being equal to the ratio of penetration depth λ and coherence length ξ . For that reason, we reformulate the equations of section (3.2.1) to introduce κ_2 , the GL parameter of the second condensate instead of the parameter δ , the ratio of the order parameters in two bands. We start from the definitions of ξ and λ :

$$\lambda_{n0}^2 = \frac{m_n c^2 \beta_n}{16\pi \alpha_{n0} e^2} \quad \xi_{n0}^2 = \frac{\hbar^2}{2m_n \alpha_{n0}},$$

to derive:

$$\frac{\kappa_1^2}{\kappa_2^2} = \frac{m}{\delta^2 \alpha}, \quad (3.10)$$

which we then substitute in the GL equations to obtain:

$$(-i\nabla - \vec{A})^2 \psi_1 - (1 - T - |\psi_1|^2) \psi_1 = \frac{\gamma \alpha \kappa_1}{m \kappa_2} \psi_2, \quad (3.11)$$

$$(-i\nabla - \vec{A})^2 \psi_2 - \alpha \left(1 - \frac{T}{T_{c2}} - |\psi_2|^2 \right) \psi_2 = \frac{\gamma}{\sqrt{m\alpha}} \frac{\kappa_2}{\kappa_1} \psi_1, \quad (3.12)$$

$$\begin{aligned} -\Delta \vec{A} = \vec{j}_s &= \frac{1}{\kappa_1^2} \Re \left[\psi_1 (i\nabla - \vec{A}) \psi_1^* \right] \\ &+ \frac{\alpha}{\kappa_2^2} \Re \left[\psi_2 (i\nabla - \vec{A}) \psi_2^* \right]. \end{aligned} \quad (3.13)$$

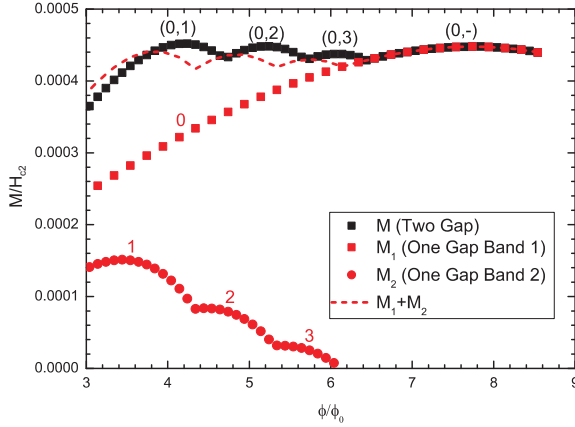


Figure 3.17: Magnetization versus applied magnetic field ($M(H)$) loops for a two-gap disk with radius $R_D = 10\xi_{10}$, and two condensates as single-gap samples, in the absence of Josephson coupling. Magnetic coupling is included in the calculations, with parameters $\kappa_1 = 3.68$, $\kappa_2 = 0.66$, and $\alpha = 0.06$.

This form of two-band Ginzburg-Landau equations is particularly convenient for comparison with the conventional types of superconductivity. In the single-gap bulk samples, the value of κ above or below $1/\sqrt{2}$ determines the superconductor being of second or first type, respectively. For a two-band sample, this distinction is much more difficult to establish, since Eqs. (3.11-3.13) show the direct influence of not only κ_1 and κ_2 , but also the Josephson coupling and the squared ratio of coherence lengths in two condensates α .

Eq. (3.13) also shows that two bands are directly coupled through the screening currents, and this type of coupling we refer to as magnetic coupling. In Fig. 3.17

we show the calculated magnetization of the disk with radius $R = 10\xi_{10}$ as a function of the applied field (in absence of Josephson coupling), to illustrate how the magnetic field couples the two bands. We observe: (i) the magnetization of the coupled system is somewhat higher than the sum of the two uncoupled systems; (ii) the found cusps are wider, since the Meissner currents in one band are screening out the field in the other band and flux entry is made more difficult. The net field in the interior of the sample is therefore lower, and the critical field is increased. This is in accordance with existing experimental findings on MgB_2 .

However, the information available in literature is also often confusing. For example, we identified two sets of parameters, both believed to be correct for MgB_2 . From Refs. [41, 148] we extracted $\kappa_1 = 3.68$, $\kappa_2 = 0.66$, $\alpha = 0.068$ which should be valid for a clean sample (single crystal). In these works the strength of the Josephson coupling, γ , is not estimated. In the dirty limit, the compound is definitely a type-II material. Substituting former values into Eq. (3.10) we obtain $\delta^2/m \approx 0.59$. On the other hand, from Refs. [71, 74, 155] we obtain $T_{c2} = 0.56T_{c1}$, and $\delta = 1.33$. For usual Mg^{11}B_2 we have $\gamma = 0.4$, $m = 1$ and $\alpha = 0.844$. For the Mg^{10}B_2 we found $\gamma = 0.28$. For irradiated MgB_2 samples a mass ratio $m \approx 14$ has been observed together with $\alpha = 0.059$ [74, 155]. Therefore, in the remainder of the chapter we will not restrict ourselves just to the particular values of the parameters, but rather focus on new physics between the two types of superconductivity and its manifestations.

3.3.1 Magnetic vs. Josephson coupling

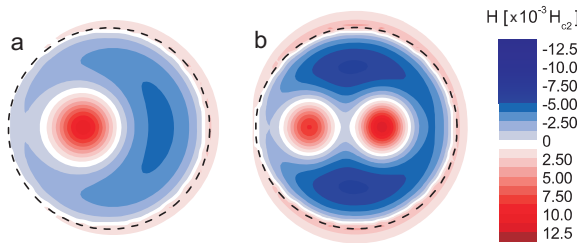


Figure 3.18: The magnetic response of the non-composite $(0,1)$ and $(1,2)$ vortex states in a mesoscopic two gap superconducting disk with parameters $R_D = 10\xi_0$, $\kappa_1 = 10$, $\kappa_2 = 2$, $\alpha = 0.3$, $\gamma = 0.01$ and $T = 0$. The applied field in (a) is $0.04H_{c2}$ ($\phi/\phi_0 = 2$) and in (b) $0.08H_{c2}$ ($\phi/\phi_0 = 4$). The dashed line shows the sample boundary.

As mentioned above, one of the most fascinating properties of a two-band system is the possible appearance of non-composite and fractional states. We argued that those could be observed in experiment through their magnetic response. Using the

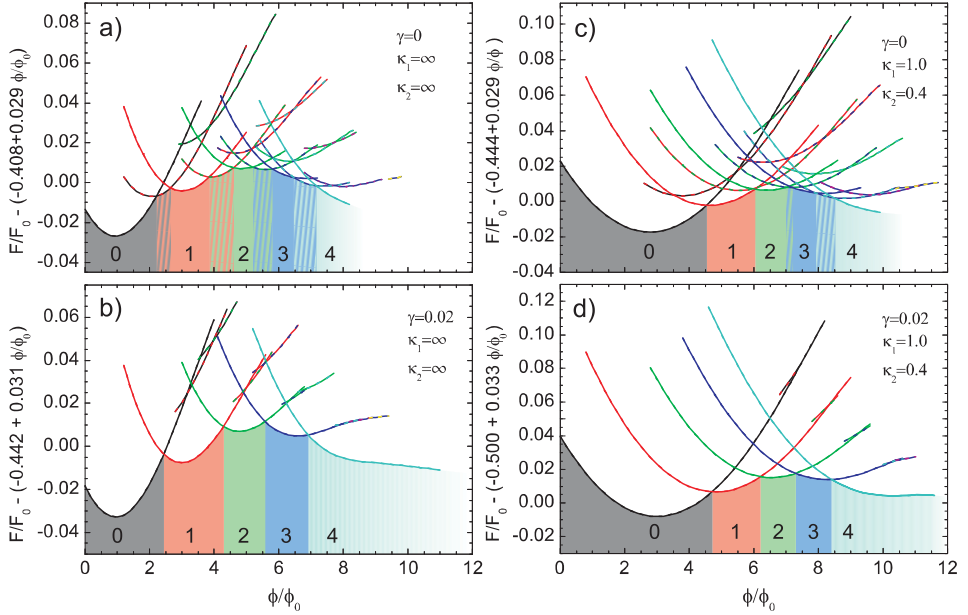


Figure 3.19: Free energy as a function of magnetic flux for found composite and non-composite states with $L \leq 4$. A linear background is subtracted from all curves to enhance readability (as indicated in the labels). The colors of the curves correspond to the vorticity, and also indicate the combinations involved in the (two-colored) non-composite states. The ground state is indicated by the color-coded shaded areas below the curves. Parameters of the sample are $R_D = 7.5\xi_0$, $T = 0.2$, $T_{cr} = 0.5$, $\alpha = 0.3$, and $m = 1$.

preceding theoretical formalism, we can now calculate the magnetic field in and around the sample, in response to the applied magnetic field. In Fig. 3.18 we show the magnetic field profile emanating from the mesoscopic superconducting disk in the non-composite (0,1) and (1,2) vortex state. The asymmetry induced by the Josephson coupling is clearly visible and can be directly imaged in magnetic force microscopy or scanning Hall probe magnetometry experiments. Additionally, the integrated magnetic field from such measurements will reveal the fractional flux carried by these states of non-integer total vorticity.

In Fig. 3.19 we show the effect of both Josephson and magnetic coupling on the free energy and the vortex states. Fig. 3.19(a) shows the energy landscape when superconducting condensates are decoupled. As could be expected, all $(L, L + 1)$ non-composite states are stabilized in the ground state, at intermediate fields between composite L and $L + 1$ states. $(L, L + 2)$ states also exist, but have significantly higher energy. The same holds for $(L + 1, L)$ fractional states, having far higher energy than the corresponding $(L, L + 1)$ state. This can be entirely inverted for a different choice of parameters, particularly α , which determines the

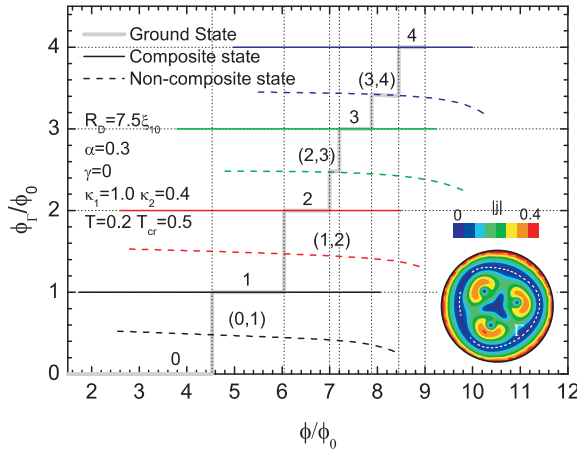


Figure 3.20: The flux quantization in a two gap superconductor bands only coupled by the magnetic field. ϕ_L is the flux measured through the contour Γ , defined as the contour where the supercurrent equals zero, as illustrated by the white dashed line in the inset. The thick solid grey line in the graph depicts the ground-state as a function of applied field.

relative coherence lengths and consequently the ratio of the vortex energy in the two bands. In the present calculation, we therefore omit the curves corresponding to $(L + 1, L)$ states.

In Fig. 3.19(b) the Josephson coupling is added. This directly results in stabilization of the composite states in the ground state, and non-composite ones have much higher energy. Generally, the $(L, L + n)$ energy increases further and energy levels follow each other as magnetic field and n are increased.

In Fig. 3.19(c) we introduced the magnetic coupling, in absence of the Josephson one. This broadens the stability intervals of all vortex states - composite and non-composite - as a consequence of the magnetic screening which lowers the effectively experienced field by the sample and enhances superconductivity. However, the magnetic response of the sample is generally of oblate shape (due to the symmetry of the disk), and asymmetric states are less favorable than in case (a). For that reason, pronouncedly asymmetric $(0,1)$ and $(1,2)$ states are not present in the ground state. However, higher non-composite states can be found in the ground state since the ring-like arrangement of vortices and their fields in both condensates enhance each other, and also follow better the overall symmetry of the stray magnetic field. Nevertheless, Josephson coupling is still able to completely remove the non-composite states from the ground state, as shown in Fig. 3.19(d). Arguably, at higher vorticity non-composite states could appear in the ground state, since the order parameters in the two bands will become increasingly similar with increasing vorticity.

In Fig. 3.20 we illustrate the flux-quantization in a two gap superconducting disk. As is already known, the flux in single-band mesoscopic samples is not quantized, but it always is within a contour determined by the zero current. Therefore we compute the flux ϕ_Γ penetrating the two-band sample through a contour Γ inside the sample on which $\vec{j}_s = 0$. The result is plotted in the presence of magnetic coupling between the bands to still have some non-composite vortex states left in the ground state. While composite states contain an integer number flux quanta in the contour Γ , non-composite states exhibit fractional flux [74, 155]. By plotting the whole stability regions of the states, we noticed that this flux decreases with increasing applied magnetic field (i.e. the applied flux ϕ). We pinpoint this effect in addition to the findings of Ref. [74, 155], where the authors found the decrease of flux through contour γ with increasing temperature. The reason for the change of the fractionally quantized flux with applied field or temperature is that one of the condensates always depletes faster than the other (in the present case, the second one). At sufficiently high field or temperature, only one band superconducts, and the flux through contour Γ changes towards its quantized level in the surviving band. In the present case, the first band is stronger, and the fractional flux decreases towards vorticity in the first band, i.e. $L = 1$. If the considered non-composite state was a $(2, 1)$ one, the fractional flux would increase towards $L = 2$ level with increasing field or temperature.

3.3.2 Magnetization curves

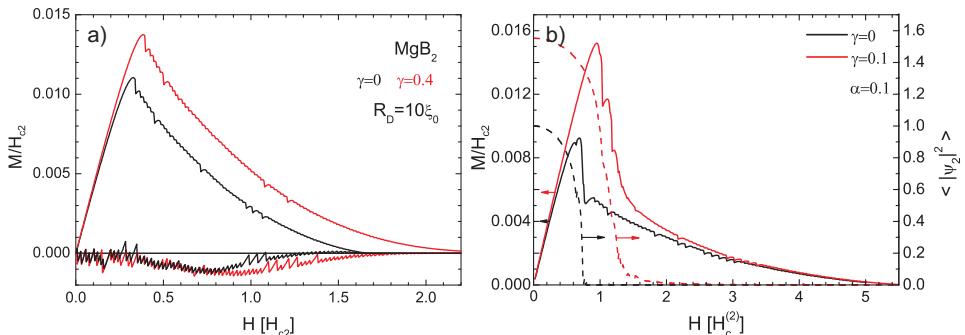


Figure 3.21: a) $M(H)$ loops obtained by sweeping up and down the magnetic field for a MgB_2 single-crystal disk of radius $R_D = 10\xi_{10}$. b) Solid curves represent magnetization as a function of applied magnetic field for $\gamma = 0$ (black) and $\gamma = 0.1$ (red), and parameters of the sample $\kappa_1 = 1$, $\kappa_2 = 0.2$, $\alpha = 0.1$, $R_D = 10\xi_{10}$ and $T = 0$. Dashed curves represent the mean Cooper pair density in the second condensate.

We define the magnetization as: $M = \frac{1}{4\pi V} \int \Delta H_z dV$, where ΔH represents the

induced magnetic field. In Fig. 3.21a we plot the $M(H)$ -loop in a MgB_2 disk with radius $R_D = 10\xi_0$ and thickness $d = \xi$ at $T = 0$, taking the parameters of Ref. [41], i.e. $\kappa_1 = 3.68$, $\kappa_2 = 0.66$, $\alpha = 0.068$. Although the second band is conventionally type-I, the shape of the $M(H)$ -loop suggests that the whole system still behaves like a type-II superconductor, i.e. there is no indication of a type 1.5 superconductivity reported by Moshchalkov *et al* [41]. We additionally plotted the magnetization in absence of Josephson coupling, which also does not show any qualitative deviation of type-II behavior. The only influence of the Josephson coupling is an apparent increase of critical field and a stronger magnetic response, which is a direct consequence of currents being strengthened by coupling. However, when we take lower values of the GL parameters, for example $\kappa_1 = 1$ and $\kappa_2 = 0.2$, we find, as shown in Fig. 3.21b a behavior of the magnetization versus field that is neither type-II nor type-I like. This state is characterized by a steep drop of the magnetization at a field close to the thermodynamical critical field H_c of the second condensate ($H_c^{(2)}$). Due to finite demagnetization effects, characteristic of type-I samples, the transition is at a lower field than $H_c^{(2)}$. At this transition field, superconductivity ceases in the second gap, and the magnetization undergoes a steep drop. The origin of this effect is clearly visible in the figure, where also the mean Cooper pair density in the sample is plotted - the magnetization drop coincides with the depletion of the second band. Beyond the transition field, the flux continues to enter the sample gradually, exhibiting the type-II mixed state of the first condensate, and the overall behavior of magnetization can be treated as a superposition of type-I (steep drop) and type-II (gradual decrease) behavior of the two condensates, each being of different type. The influence of the Josephson coupling is also striking, as it smoothes out the drop in the magnetization: the second condensate still depletes but at a slower rate due to the exchange of Cooper pairs with the first condensate. The slope of the decrease of the mean Cooper pair density in the second condensate still seems to match the slope of the drop in magnetization with a remarkable accuracy, although the transition becomes less abrupt and more reminiscent of a type-I intermediate state with bundles of flux penetrating the sample.

In Fig. 3.22 we demonstrate the influence of the ratio of the coherence lengths, α on the magnetic behavior of the sample. In Eq. (3.13), the supercurrents due to the second condensate have a prefactor of α/κ_2^2 . Therefore, it is not κ_2 alone which determines the type of the band and an effective $\kappa_2^{eff} = \kappa_2/\sqrt{\alpha}$ can be introduced. Essentially, this suggests that the self induced field should be proportional to α , and the results in Fig. 3.22 are supportive of this. The level of magnetization to which the sample jumps after the magnetization drop should be independent of α , since the second condensate is depleted there. However it turns out that the larger the magnetization is before the drop, the lower it becomes after the drop. This follows from the fact that, before the magnetization drop, the second condensate is able

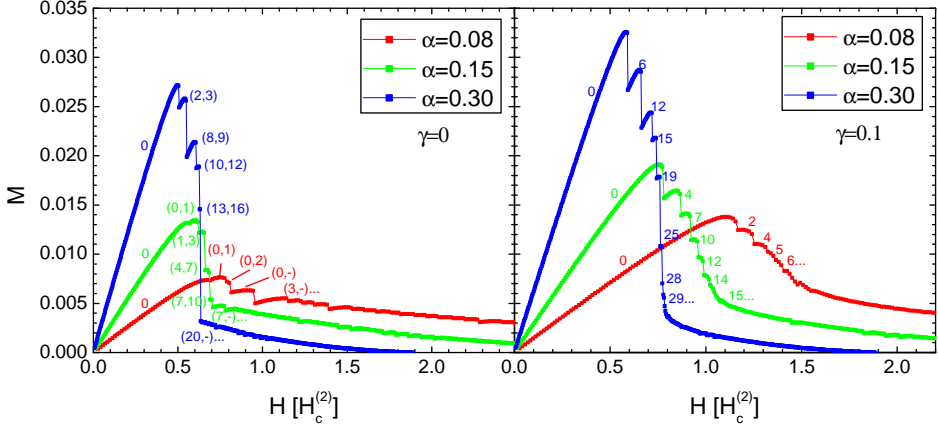


Figure 3.22: Magnetization of the sample versus the applied field for different values of the ratio between the coherence lengths in two condensates α . Left: without Josephson coupling, right: with Josephson coupling. Other parameters of the sample are $\gamma = 0$, $\kappa_1 = 1$, $\kappa_2 = 0.2$, $R_D = 10\xi_{10}$ and $T = 0$.

to provide a better screening of the magnetic field for the first condensate when α is larger, but when the second condensate ceases, the first condensate experiences a large difference in the felt magnetic field, which in turn allows for a larger flux penetration and thus a lower diamagnetic response of the sample.

It should be stressed here that the field at which the second condensate depletes and the magnetization drops is also influenced by α . The smaller the coherence length of the second condensate (higher α), the smaller the transition field. This difference is even more prominent in the presence of Josephson coupling. In other words, the apparent demagnetization effect in the type-I part of the magnetization curve is clearly influenced by the parameter α .

Finally, in Fig. 3.23 we also show the magnetization corresponding to the sweep-down of the applied magnetic field. At the point where the second condensate revives the magnetization jumps up, since there the type-I condensate contributes to the diamagnetic signal. This jump is less abrupt when γ is non-zero.

3.3.3 Type-1.x vortex states

It is already known that vortices repel each other in type-II superconductors, form Abrikosov lattice in bulk samples, but are compressed into geometry dependent multi-vortex states and even giant vortex states in mesoscopic superconductors. In type-I samples however, flux penetrates the sample in the form of lamellae or tubular flux bundles [158]. As we showed above, two band superconductors can

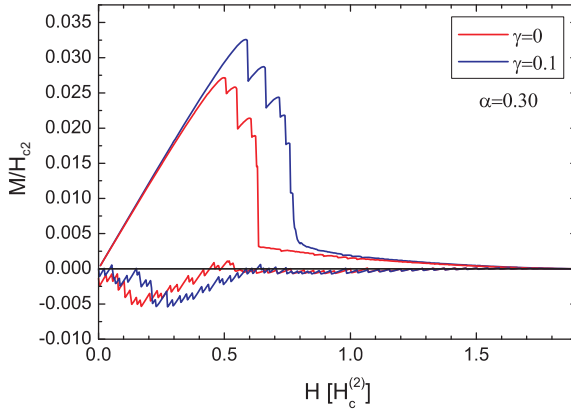


Figure 3.23: Full sweep up and down $M(H)$ loops with and without coupling. Taken parameters are $\alpha = 0.3$, $\kappa_1 = 1$, $\kappa_2 = 0.2$, $R_D = 10\xi_{10}$ and $T = 0$.

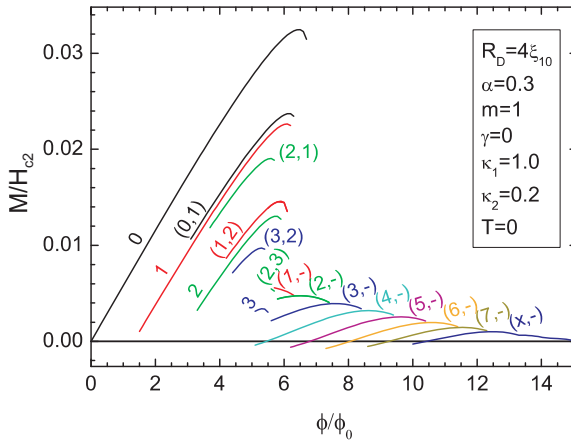


Figure 3.24: $M(H)$ for all stable vortex states in a mesoscopic type-1.x superconducting disk.

show a bit of both behaviors, called type-1.5 superconductivity by Moshchalkov *et al.* [41]. While we demonstrated the type 1.x behavior through the magnetization loops, they mainly discussed the vortex-vortex interaction in two-band superconductors, claiming that it should be short range repulsive and long range attractive. This of course assumes composite vortex states, or strong Josephson coupling in our model. However, as we have seen above, a plethora of other vortex states are possible, not all composite. Therefore, the vortex-vortex interaction should be discussed separately within bands (intra-band), and separately between them (inter-band). While leaving the detailed analysis for the future, we here show sev-

eral prime examples of vortex states that can be found in two-band mesoscopic disks, that show type-1.x behavior (however different from Ref. [41]). For example, we take the disk with radius $10\xi_{10}$ with parameters of the condensates $\kappa_1 = 1$, $\kappa_2 = 0.2$ and $\alpha = 0.3$. As shown in Fig. 3.25(a-b), at larger applied field providing 30 flux quanta through the sample, we found a composite $L = 24$ vortex state. Due to absence of Josephson coupling, two allotropic modifications of the vortex state were found possible. In both, the vortices in type-I condensate merge into a single domain, either a ring domain (a), or a giant-bubble (b), which is typical for type-I samples. Actually they are still single vortices, but have huge overlap, mimicking a normal domain. Vortices in the type-II condensate remain separate however, but are forced by magnetic coupling to obey the symmetry of the intermediate state of the type-I condensate. They therefore form more or less a conventional multi-shell state under the giant vortex in (b), but are forced to make an unconventional state with dense shells within the ring domain in (a). This type-I-II competition is even more pronounced in the presence of Josephson coupling, as shown in Fig. 3.25(c). In the first condensate, one can distinct three giant $L = 2$ vortices and two $L = 3$ multi-vortex clusters. This is also the situation in the second condensate, however the multi-vortices are now even closer and also overlap more, mimicking perfect giant vortices. Due to the Josephson coupling, both condensates influence each other; as a consequence, the type-I intermediate state is forced to split into as many bubbles as possible, and vortices in type-II condensate must group under those bubbles. As a result, a multi-vortex of multi-vortices is formed, clearly a signature of type-1.x behavior.

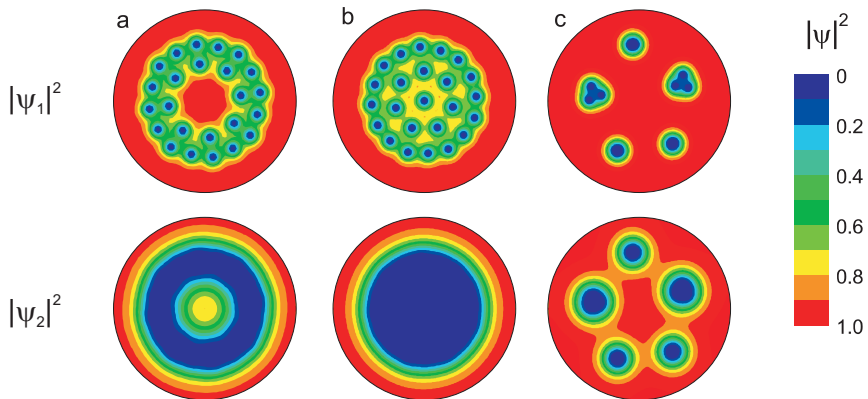


Figure 3.25: Cooper pair density contour plots of the first (left) and second (right) condensate. $\kappa_1 = 1$, $\kappa_2 = 0.2$, $\alpha = 0.3$, $R_D = 15\xi_{10}$. In (a) and (b) $\phi/\phi_0 = 30$, $L = 24$, $\gamma = 0$. In (c) $\phi/\phi_0 = 15$, $L = 12$, $\gamma = 0.02$.

3.4 Conclusions

In summary, we presented a theoretical Ginzburg-Landau (GL) study of the superconducting state of two-band mesoscopic disks, where both the influence of Josephson and of magnetic coupling between the superconducting bands are discussed. In cases when screening of the magnetic field can be neglected, we found the dependence of the size of the vortex core on the strength of the Josephson coupling and showed that it generally has an influence opposite to the one of temperature. In limiting cases, our numerical findings agree well with analytic expressions available in literature. We also found a fitting function, which gives an excellent estimate of the size of the vortex core as a function of the size of the mesoscopic disk. In our further analysis of the vortex states, we focussed mainly on exotic, non-composite states, where two condensates comprise different number of vortices and the apparent total vorticity of the sample is fractional. We reported asymmetric vortex states following from competing interactions in the two-band mesoscopic system, and showed how some states can be manipulated by e.g. coupling between the bands. We indicate how such states can be experimentally observed. Fractional states can even be found in the ground state, but typically far from the S/N boundary. We give the expression for the upper critical field of a two-band mesoscopic disk as a function of temperature, which is similar to analytic estimations for bulk, however scaled to its value at zero temperature for zero coupling between the condensates.

When magnetic screening and coupling between the bands is included in the simulations, we characterized the response of the sample through the competition of the GL parameters of the two-bands (with special attention to the case when one band is type-II and the other is type-I). However, we show that this is insufficient, and that Josephson coupling and the ratio of the coherence lengths in the two bands also play an important role. Although we did not find evidence for type-1.5 superconductivity in clean MgB₂ disks, we did find its manifestation for a different choice of relevant parameters. The magnetization vs. applied field shows a distinct jump at the field where type-I condensate ceases, and the overall shape of the curve can surely be characterized as type-1.x like. This is also evident in the found vortex states in the latter case, which are a combination of single vortices and lamellar domains.

The results presented in this chapter were published as:

- R. Geurts, M. V. Milošević and F. M. Peeters, *Vortex matter in mesoscopic two-gap superconducting disks: Influence of Josephson and magnetic coupling*, Phys. Rev. B **81**, 214514 (2010)

Chapter 4

Enhanced stability of the vortex-antivortex molecule in two-gap mesoscopic superconductors

Using the Ginzburg-Landau theory, we will now study stable symmetry-induced vortex-antivortex molecules in two-band mesoscopic superconductors in the presence of a homogeneous magnetic field. We find the conditions under which the two Cooper-pair condensates *cooperatively broaden* the field-temperature stability range of the vortex-antivortex state and predict unique fractional states in which the antivortex is present in just one of the condensates. With changing temperature re-entrant behavior of the vortex-antivortex states is observed.

Intuitively, one expects that the current of the superconducting vortices in a homogeneous magnetic field can only turn in one particular direction, *bundling* the flux inside the vortex core. While true for bulk superconductors, this is not always the case in mesoscopic superconductors where confinement plays an important role, and where the symmetry of the sample can stimulate the creation of one or more antivortices, i.e. vortices with currents circulating in the opposite direction, thus *expelling* flux [47]. The existence of such vortex-antivortex (V-Av) states can be understood from Ginzburg-Landau (GL) theory close to the superconducting/normal state (S/N) boundary, where GL equations for the superconducting order parameter become linear and the order parameter distribution must obey the symmetry of the sample. As a result, for e.g. vorticity $L = 3$ in a square sample, a state with a central antivortex surrounded by four vortices ($L = 4 - 1 = 3$) becomes the ground

state. This particular V-Av state was studied extensively in Ref. [114, 115, 117], also further away from the S/N boundary. The main findings were that the V-Av state was highly sensitive to defects or imperfections, and that the V-Av molecule is very compact (smaller than the coherence length ξ), both serious drawbacks regarding the experimental realization. To overcome these problems it was shown in Chapter 2 of this thesis that nano-engineered pinning can make the V-Av state more robust against imperfections and can multiply enlarge the V-Av molecule. Nevertheless, direct observation of the V-Av state remained one of the main experimental challenges in mesoscopic superconductivity to date.

In parallel to the above line of research, studies of superconducting MgB₂ captured the scientific attention all over the world [141]. Among other things, this exciting material possesses two superconducting gaps [58]. In other words, it hosts two superconducting condensates, and their mutual coupling (e.g. Josephson and magnetic ones), in combination with different intrinsic length scales and temperature-dependent properties, makes the net behavior highly non-trivial. Furthermore, the effect of the boundary of the sample in the mesoscopic regime can be very different for the two condensates, and can lead to novel physics. For example, non-composite vortices (with displaced cores in two bands) and fractional vortex states (with non-integer net flux) have been predicted in two-band mesoscopic samples in Refs. [74, 155] and were extensively studied in Chapter 3 of this thesis.

4.1 Theoretical formalism and sample parameters

Motivated by the above, we here investigate the symmetry-induced V-Av states in two-gap superconductors. Our theoretical investigation is based on the two-band GL theory, which reduces to solving the dimensionless GL equations [71, 159] self-consistently:

$$\left\{ \begin{array}{l} (-i\nabla - \vec{A})^2 \psi_1 - (\chi_1 - |\psi_1|^2) \psi_1 - \gamma \psi_2 = 0, \\ (-i\nabla - \vec{A})^2 \psi_2 - \alpha (\chi_2 - |\psi_2|^2) \psi_2 - \alpha \frac{n_1}{n_2} \gamma \psi_1 = 0, \\ -\Delta \vec{A} = \frac{1}{\kappa_1^2} \vec{j}_1 + \frac{\alpha}{\kappa_2^2} \vec{j}_2. \end{array} \right. \quad (4.1)$$

In these equations the order parameter is expressed in W (defined as $W^2 = 8\pi^2 T_c^2 / 7\zeta(3)$), lengths are measured in ξ_1 ($\xi_1^2 = \hbar^2 v_1^2 / 6W^2$), and the vector potential in $A_0 = 2\pi\xi_1 / \phi_0$. $v_{i=1,2}$ are the Fermi velocities in the two bands which define the parameter $\alpha = (v_1/v_2)^2$, a measure for the squared ratio of the intrinsic coherence lengths in the two bands. The temperature dependence is captured by $\chi_i = S_i / (n_i \eta) - \ln(T/T_c)$, with $S_1 = \lambda_{22} - n_1 \eta S$, $S_2 = \lambda_{11} - n_2 \eta S$, $S = (n_1 \lambda_{11} + n_2 \lambda_{22} - \sqrt{(n_1 \lambda_{11} - n_2 \lambda_{22})^2 + 4n_1 n_2 \lambda_{12}^2}) / (2n_1 n_2 \eta)$ and $\eta = \det \Lambda =$

$\lambda_{11}\lambda_{22} - \lambda_{12}^2$. $\Lambda = \begin{vmatrix} \lambda_{11} & \lambda_{12} \\ \lambda_{21} = \lambda_{12} & \lambda_{22} \end{vmatrix}$ is the (symmetric) coupling matrix, using the notation of Ref. [75]. This notation differs from the other used in literature as the partial density of states n_i is taken out of the matrix, which makes our Λ symmetric. From above expressions one can obtain the intrinsic critical temperatures, i.e. the temperatures at which the gaps would deplete in the absence of inter-band coupling: $T_{c,i} = T_c \exp(-S_i/n_i\eta)$. $\gamma = \lambda_{12}/n_1\eta$ determines the strength of the Josephson coupling. n_i represent the partial density of states in the two bands (preserving $n_1 + n_2 = 1$). The intrinsic GL parameters of each band are defined by $\kappa_1^2 = \frac{9}{8\pi} \frac{c^2}{\hbar^2 e^2} \frac{\Psi_0^2}{N(0)n_1 v_1^4}$ and $\kappa_2^2 = \kappa_1^2 \alpha^2 n_1/n_2$. The supercurrents j_i in Eq. (4.1) are calculated as $\vec{j}_i = \mathcal{R} \left[\psi_i^* \left(-i\nabla - \vec{A} \right) \psi_i \right]$. With the Neumann boundary condition that no supercurrent can pass through the boundary of the sample, we solve this system of equations self-consistently by mapping it on a regular square grid. Details on the numerical procedure can be found in Ref. [160] or in Section 1.8 of this thesis. The boundary condition on the supercurrent in this calculation has an additional important consequence, as it directly separates the length scales of the two order parameters, even very close to T_c (see Ref. [75]). In that sense, the removal of the (incomplete) terms of higher-order in $\tau = 1 - T/T_c$ in the standard GL model is not mandatory. Although incomplete, those terms capture important physics in the mesoscopic regime.

Without loss of generality, we consider a square geometry of the superconductor. In order to enlarge the V-Av molecule, we will mainly use this geometry with 2×2 holes (unless stated otherwise). All the obtained results can anyhow be extrapolated to the case of a plain square, as the symmetry of the sample, and thus the physical origin of the V-Av therein, is the same. The size of the sample will be further denoted by w . The holes are also of square shape (with size w_h), centered at a distance $2d_h$ from each other. In what follows, we consider the sample with $w = 10\xi_1$, $w_h = 1.5\xi_1$, and $d_h = 1.75\xi_1$. In principle, we have eight parameters to fully characterize the superconducting properties: v_1 , α , n_1 , λ_{11} , λ_{12} , λ_{22} , W (set by T_c) and $N(0)$ (entering κ_i). After scaling the sizes by ξ_1 and temperatures by T_c , and setting $N(0)$ small so that $\kappa_i \gg 1$, i.e. we are in a type-II superconducting regime, and are left with α , n_1 , λ_{11} , λ_{12} , λ_{22} as free parameters.

4.2 Stability region of the V-Av state

Without mutual coupling, the two bands are independent of each other and would cease at respective temperatures $T_{c,i}$. In this case, one can apply the earlier single-band findings, and conclude that $L = 4 - 1$ V-Av state should be found directly below the S/N boundary and extend down to temperatures at which the size of the sample measures $\sim 7\xi(T)$ [118, 135]. However, in the two-gap picture, two

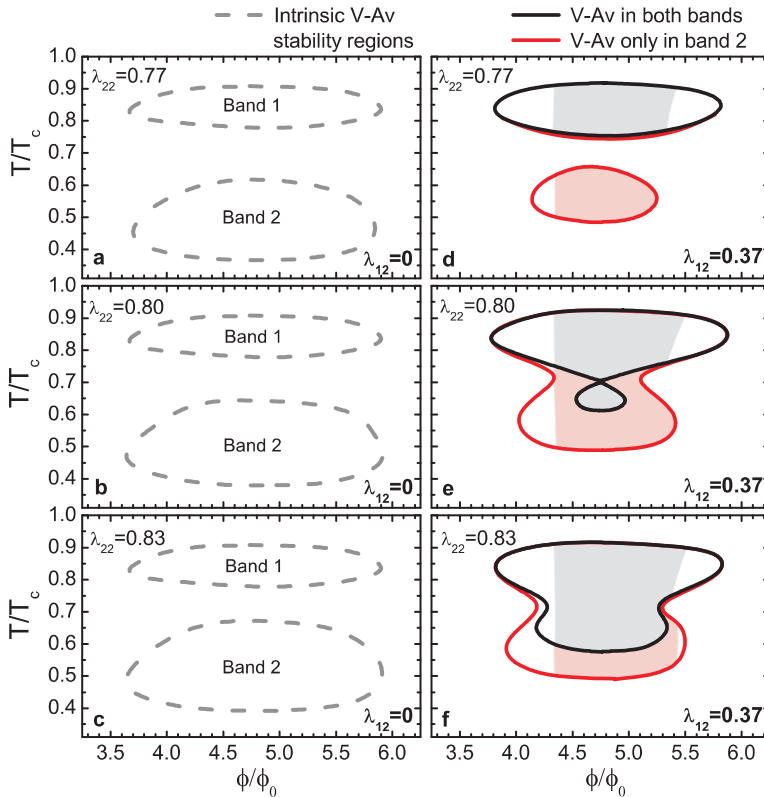


Figure 4.1: $\phi - T$ stability regions of the $L = 4 - 1$ V-Av state in a square with 2×2 holes, in the absence of Josephson coupling (left) and for non-zero coupling (right). The region in which the V-Av state is the ground state of the system is shaded. The parameters other than shown are $\alpha = 0.3$, $\lambda_{11} = 23$, $n_1 = 0.04$ and $\kappa_1 \gg 1$.

condensates have different length scales and critical temperatures, so their V-Av stability regions - in the absence of coupling - would be displaced in a magnetic flux-temperature ($\phi - T$) diagram, as illustrated in the left column of Fig. 4.1. In Figs. 4.1(a-c), we increase λ_{22} , and with it the critical temperature of the second band $T_{c,2}$. As a result, the V-Av stability region of the second band shifts up in temperature because the S/N boundary of the second band follows $T_{c,2}$. This picture is of course unrealistic and any introduced coupling between the two bands will couple their V-Av stability regions (though in a non-trivial manner, see the right panel of Fig. 4.1). One immediately assumes that the band dominant in superconducting properties will impose its vortex configuration on the weaker band, and this is certainly the case for $T > T_{c,2}$, where the first band is mostly in a V-Av state, and the second band superconducts solely due to the coupling. However, at

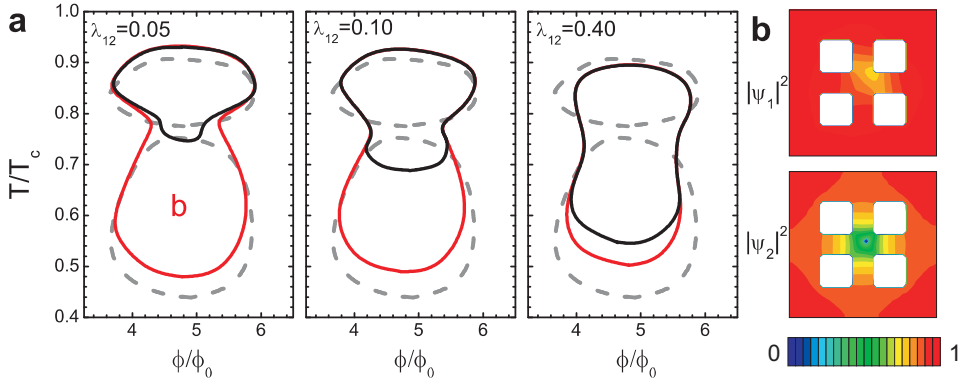


Figure 4.2: (a) The stability regions in of the $L = 4 - 1$ V-Av state in a perforated square, as a function of increasing Josephson coupling (via λ_{12}). Other parameters are $\alpha = 0.3$, $\lambda_{11} = 23$, $\lambda_{22} = 0.94$, $n_1 = 0.04$ and $\kappa_1 \gg 1$. (b) The Cooper-pair density in the two coupled condensates for the fractional antivortex state indicated in (a).

lower temperatures the second band hosts the V-Av state, and in order to impose it on the first band one needs $\alpha n_1/n_2 \ll 1$, as that factor regulates the influence of ψ_2 on ψ_1 in Eq. (4.1). In Fig. 4.1, we used $\alpha n_1/n_2 = 0.0125$. The Josephson coupling was introduced via the non-zero λ_{12} , and other constants in the Λ matrix are of the same order as ones readily found in the literature [41, 73, 75, 161, 162], though given in different notation $\lambda_{\mu\nu}^{(lit)} = n_\mu \lambda_{\mu\nu}$. Obviously, for $\lambda_{12}^{(lit)} \ll \lambda_{21}^{(lit)}$ it is very likely that an extended V-Av region in the $\phi - T$ space will be realized.

Therefore, as a main result we find that the superconducting condensate in a square confinement can potentially sustain the V-Av state *to far lower temperatures* when a second band is present. To ideally extend the stability region of the V-Av state, the lower boundary of the V-Av stability region in the first band should be close to the upper boundary of the V-Av region in the second, i.e. around $T_{c,2}$. In cases when the V-Av state in the second band is found at much lower temperatures than the one of the first band (see Fig. 4.1(d)), or for insufficiently strong coupling (see Fig. 4.2(a)), no enlargement of the stability region of the V-Av state is realized. Instead, one finds only at high temperatures an island of *integral V-Av state* (thus the V-Av molecule exists in both bands¹). As temperature is lowered, the $L = 4 - 1$ state disappears and reappears only in the second band while the vortex state in the first band is a simple $L = 3$ multivortex (as shown in Fig. 4.2(b)). We refer to such a state as a *fractional V-Av state*. Remarkably, this state is asymmetric, i.e. the antivortex in the second band is not centered as a consequence of the coupling to the low-order parameter regions of the first band.

In Fig. 4.1(e), with λ_{22} (and $T_{c,2}$) increased compared to Fig. 4.1(d), one observes

¹Note that vortex cores in two bands are not necessarily on top of each other.

two separate regions of integral V-Av state - the top one dominated by the first band and the bottom one dominated by the second band. Here *re-entrance* of the integral V-Av state is realized by sweeping temperature up or down! For further increased λ_{22} ($T_{c,2}$), the stability regions of the V-Av states in the two bands *merge* into a large region of an integral V-Av state. A similar effect is found with increasing Josephson coupling (by increasing λ_{12} , see Fig. 4.2(a)), where the integral V-Av state expands at the expense of the fractional antivortex state (which finally disappears). During this process, we also note a decrease of the critical temperature of the V-Av region in Fig. 4.2. Namely, increasing λ_{12} increases the coupling constant γ , but also induces a strong decrease of the intrinsic critical temperatures $T_{c,i}$ which all combine to a decreasing overall T_c .

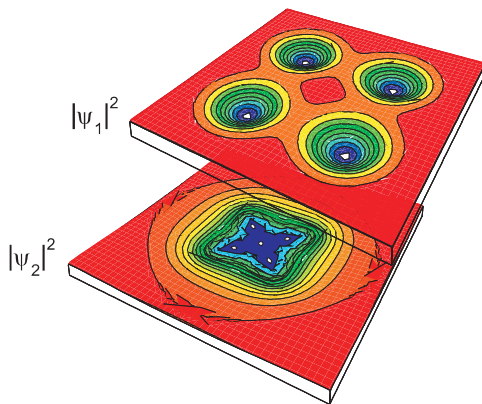


Figure 4.3: 3D plots of the Cooper-pair density of the first (top) and the second band (bottom) for the fractional $L = 4/L = 4 - 1$ state, demonstrating the V-Av in the second band which is pinned by the vortices of the first band through only magnetic coupling. The used parameters are $w = 16\xi_1$, $\alpha = 0.25$, $n_1 = 0.95$, $\lambda_{11} = 1$, $\lambda_{12} = 0$, $\lambda_{22} = 19$, $\phi/\phi_0 = 5$, $T = 0.6$, $\kappa_1 = 0.5$ and $\kappa_2 = 0.54$.

4.3 Fractional antivortex states

Although the fractional vortex states are suppressed in the presence of strong Josephson coupling (as is e.g. the case in MgB₂), we discuss here further the unique fractional states involving an antivortex in one of the bands. In Fig. 4.2(b) we showed the Cooper pair density plots of ψ_1 and ψ_2 respectively for a state with $L = 3$ multivortex state in the first band (with three vortices trapped by holes) and the $L = 4 - 1$ V-Av state in the second band. This fractional antivortex state can be stable in a relatively large part of $\phi - T$ space for the perforated square

(see Figs. 4.1,4.2), however this is not the case for a plain square where suppression of the order parameter inside each vortex core in one band must be similarly matched in the other band (whereas inside the holes this is not required). Yet, another type of a fractional antivortex state can be realized in the absence of holes, shown in Fig. 4.3. In this case, we have the $L = 4$ state in one band, with four separated vortices, and the $L = 4 - 1$ V-Av state in the second band. While the vortices in the first band adopt a fourfold symmetric position due to their mutual repulsion, the vortex state in the second band becomes fourfold symmetric due to the magnetic field generated by the first band. Moreover, the vortices of the first band now act as *magnetic pinning centers* for the second band, and help to realize a much expanded V-Av molecule in a plain square with V-Av distance of $\sim 1.4\xi_1$ (in Ref. [47], this distance was below the coherence length). Note that this effect does not strictly depend on sample geometry, as four vortices in the $L = 4$ state form a square configuration even in a sufficiently large circular superconducting disk. Finally, we point out that this unique fractional state may even be realized in two square single-gap superconductors, placed on top of each other and coupled through a thin oxide layer. [163]

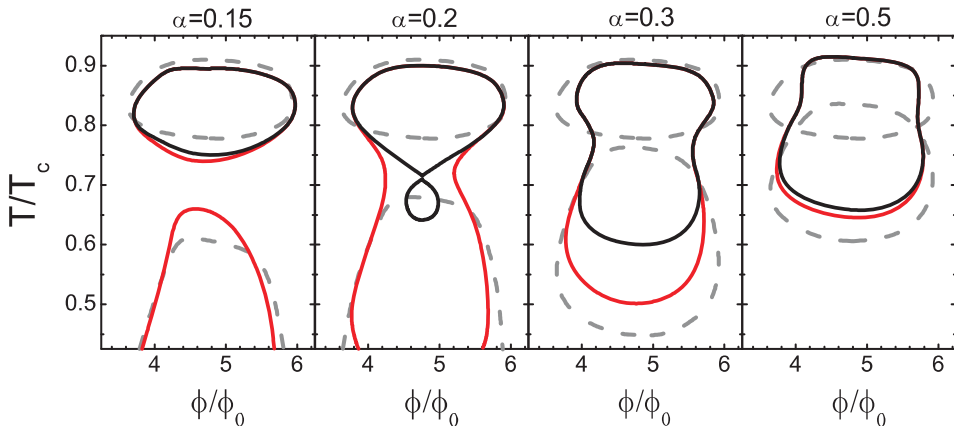


Figure 4.4: The evolution of the stability region of the integral $L = 4 - 1$ V-Av state in a perforated square as a function of the increasing α and thus decreasing Fermi velocity and coherence length of the second band. Other parameters are $n_1 = 0.04$, $\lambda_{11} = 23$, $\lambda_{12} = 0.2$ and $\lambda_{22} = 0.96$.

4.4 Other conditions for enhanced V-Av state

In mesoscopic superconductivity, one of the key parameters is the coherence length of the Cooper-pair condensate. In Fig. 4.4, we show the calculated V-Av $\phi - T$

stability regions for increasing parameter α , i.e. decreasing the Fermi velocity v_2 and consequently the intrinsic coherence length ξ_2 of the second band. We observe that by increasing α , the stability region of the integral V-Av state first expands but subsequently shrinks as α approaches unity. As ξ_2 decreases, the intrinsic critical temperature of the second band $T_{c,2}$ does not change, but its value for a given field *increases* (i.e. $T_c(H)$ boundary tilts upwards). This moves the intrinsic V-Av stability regions in two bands closer together which enables their merging into a larger stability region for the integral V-Av state, as already explained in our discussion of Fig. 4.1. At the same time, decreasing ξ_2 increases the size of the sample compared to ξ_2 , and a higher temperature is needed to enhance the effect of confinement and induce the V-Av state in the second band. This shrinks the V-Av stability region in the second band in the $\phi - T$ space. Note also that increasing α strengthens the influence of the first band on the second one (see Eq. (4.1)) which also contributes to the reduction of the stability region of the V-Av state for $\alpha \rightarrow 1$.

Although earlier we found that in order to increase the $\phi - T$ stability region of the integral V-Av state one needs a low $\alpha n_1/n_2$ value, we notice now that this can not be achieved when α is extremely low. Instead, one should opt for a low n_1/n_2 ratio. Note however that increasing n_1 directly increases $T_{c,1}$ and decreases $T_{c,2}$, and thus results in a gradual separation of the stability region of the V-Av state into two. Increasing n_1 further also diminishes the effect of the second band on the first one, and the integral V-Av state can no longer be found at low temperatures (although it is present in the second band). Finally, increasing n_1 decreases the nominal κ of the first band, which is known to generally reduce the stability region of the V-Av state (see Ref. [118, 135]).

4.5 Discussion on the validity of the two-gap GL formalism

Currently there exists controversy in the literature [75, 164, 165] concerning the validity of the two-band GL formalism as used in this work. The essence lies in the fact that the GL theory is a series expansion, valid only in the direct vicinity of the critical temperature, where the order parameter is small. In our two-gap GL theory, terms with different order of accuracy however occur, some of which are incomplete. Furthermore, only near T_c , the GL equations can be justified microscopically, using e.g. Gorkov's approach [24].

The initial critique was formulated by Kogan and Schmalian in Ref. [75]. The

authors noticed that in the general two-gap GL equations,

$$\begin{cases} a_1\Delta_1 + b_1\Delta_1|\Delta_1|^2 - \gamma\Delta_2 - K_1\Pi^2\Delta_1 = 0, \\ a_2\Delta_2 + b_2\Delta_2|\Delta_2|^2 - \gamma\Delta_1 - K_2\Pi^2\Delta_2 = 0, \end{cases} \quad (4.2)$$

not all terms are of the same order in the reduced temperature $\tau = 1 - T/T_c$, while the single-gap GL equation has all terms of order $\tau^{3/2}$:

$$a\Delta + b\Delta|\Delta|^2 - K\Pi^2\Delta = 0, \quad (4.3)$$

since $\Delta \propto \tau^{1/2}$, $a \propto \tau$ and $\Pi^2 \propto \xi^{-2} \propto \tau$. The authors assume that the same relation should hold for the individual condensates in a two-gap superconductor, since there is only one T_c at which both bands simultaneously deplete, i.e. $\Delta_1 \propto \tau^{1/2}$ and $\Delta_2 \propto \tau^{1/2}$, at least within the GL domain, $\tau \ll 1$. This assumption is reasonable since Josephson coupling between the two bands is inevitable. By combining both equations of Eqs. (4.2) and collecting only terms up to order $\tau^{3/2}$, the authors are able to derive two *independent* GL equations, each describing one band with GL parameters in function of the old parameters. In fact the two order parameters turn out to be proportional to each other which leads to the conclusion that a two-gap superconductor effectively behaves as a single-gap superconductor, at least in the regime where the GL theory is justified, near T_c . As a consequence, the authors rule out the possibility to describe effects of (1) the bands having different phase, (2) different coherence lengths between the bands, (3) non-composite and fractional vortices and (4) type-1.5 superconductivity, within the GL formalism.

In a follow-up work, Shanenko *et al.* derived the two-gap GL equations from microscopic theory [166], but up to a higher precision in τ , to the order $\tau^{5/2}$. In doing so, they found that away from T_c , the order parameters are no longer proportional. This again allows for all the four effects ruled out above. For instance, the different coherence lengths in two bands were studied and confirmed by Komendova *et al.* using this formalism in Ref. [167]. The same conclusion was reached by Silaev *et al.* in Ref. [168] by studying the size of a vortex core in the microscopic Eilenberger approach, thus valid over the entire temperature range from T_c to zero. Additionally, these authors investigated the vortex-vortex potential and found non-monotonic behavior for a range of parameters, proving the existence of type-1.5 superconductivity. Moreover, the difference in coherence lengths is an experimental fact as was shown for instance in experiments able to address the two bands separately [142]. The possibility of two bands having different phases is also an experimental fact, confirmed by observing the Leggett mode [169], first predicted in 1966 [170].

We agree that *quantitatively* the results of the two-gap formalism employed in this work can not be justified by a microscopic derivation. On the other hand, the formalism suggested by Kogan *et al.* reduces effectively to an single-gap theory,

and as such is unable to capture - even *qualitatively* - the majority of the physics that distinguishes two-band from single-band superconductors.

The extended GL model, developed by Shanenko *et al.* [166], is far better in this respect, but is currently developed only in the absence of applied magnetic field. Our GL approach is a *phenomenological* model for two-gap superconductors, as was the original intention of Ginzburg and Landau.

Therefore we believe that the features specific to two-band superconductors, observed in our numerical experiments, at least are *qualitatively* correct. Additionally it is already well established, in comparison with experiments, that for single-band superconductors, the GL theory indeed stays valid deep into the superconducting state.

Another remark made in Ref. [75] was that the parameters for the GL model, as we used in Chapter 4, cannot be chosen arbitrarily, as they all should lead to a simultaneous depletion of both gaps at T_c . This means in practice that the intrinsic critical temperatures $T_{1,2}$ are intimately correlated with the coupling constant γ . This also follows directly from a microscopical derivation, as performed e.g. in Ref. [73, 75]. The GL formalism, with parameters from microscopical derivation for the general case of a dirty two-band superconductor is derived in the appendix to this chapter.

4.6 Lawrence-Doniach model

In addition to two-band superconductors the results presented in this and the previous chapter are of direct relevance for superconducting bilayers. These systems consist of two superconducting layers with an insulating layer in between. When the insulating layer is sufficiently thin, Cooper pairs can tunnel through, and the two layers are coupled through Josephson coupling. In 1971 Lawrence and Doniach presented a GL model for a infinite stack of layers [171]. The application to the case of just two layers is straight-forward. Moreover the resulting equations turn out to be formally equivalent to the two-gap equations studied in this chapter, and casting the parameters from one model into the other turns out to be rather simple. Physically this means that any particular solution found in the two-gap GL formalism has a counterpart in the LD GL model and vice versa.

The Lawrence-Doniach (LD) Ginzburg-Landau (GL) energy functional for two layers reads:

$$F = \int \sum_{n=1}^2 \left(\frac{1}{2m_n} \left| \left(-i\hbar\nabla - \frac{2e}{c} A \right) \Psi_n \right|^2 + (\alpha_n + \Gamma) |\Psi_n|^2 + \frac{1}{2} \beta_n |\Psi_n|^4 \right) - \Gamma (\Psi_1^* \Psi_2 + \Psi_2^* \Psi_1), \quad (4.4)$$

with Γ the Josephson coupling, proportional to the tunneling constant and inversely

proportional to the thickness of the insulating layer, and $\alpha_n = -\alpha_{n0} \ln(T/T_{cn})$. ($\alpha_{n0} < 0$ and $\beta_n > 0$). From it the two dimensionless LD GL equations can be derived:

$$\begin{cases} -\left(\tau_1 - \frac{\gamma}{\delta}\right) \psi_1 + \psi_1 |\psi_1|^2 + \Pi^2 \psi_1 - \gamma \psi_2 = 0, \\ -\left(\tau_2 - \frac{\gamma}{\delta m \alpha}\right) \psi_2 + \psi_2 |\psi_2|^2 + \frac{1}{\alpha} \Pi^2 \psi_2 - \frac{\gamma}{m \alpha \delta^2} \psi_1 = 0, \end{cases} \quad (4.5)$$

with $\psi_n = \Psi_n / \Psi_{n0}$, $\Psi_{n0} = \sqrt{-\alpha_{n0} / \beta_n}$, $\alpha = m_2 \alpha_{20} / m_1 \alpha_{10}$, $m = m_1 / m_2$, $\delta = \sqrt{\alpha_{20} \beta_1 / \alpha_{10} \beta_2} = \Psi_{20} / \Psi_{10}$, $\gamma = -\Gamma \delta / \alpha_{10}$, $\tau_n = -\ln(T/T_{cn})$, $\Pi = -i \nabla - A/A_0$, $A_0 = \hbar c / 2e \xi$ and $\xi = \hbar / \sqrt{-2m_1 \alpha_{10}}$.

The fundamental difference between the LD GL model and the two-gap GL model is that in the former case the Josephson coupling does not increase the critical temperature above the maximum of the two intrinsic critical temperatures while in the latter case it does. This is intuitive, as Cooper pairs which tunnel to the one of the superconductors are in fact lost in the other. Notice however that the intrinsic' critical temperature of the two bands in a two-gap system has no real physical meaning, as it can never be directly observed due to the ever-present Josephson coupling. On the contrary, the intrinsic critical temperatures of the two layers are physical, as they are the critical temperatures when the layers are separated far from each other. In fact, the critical temperature of a double-layered LD system turns out to be always between the intrinsic critical temperature of the bands, as we will show in the subsection below.

First we want to show however how the solutions of the two-gap GL model presented in this chapter can be mapped onto the LD GL model, defined by the set of equations:

$$\begin{cases} \left(\frac{S_1}{n_1 \eta} - \tau\right) \psi_1 + |\psi_1|^2 \psi_1 + \Pi^2 \psi_1 - \gamma \psi_2 = 0, \\ \left(\frac{S_2}{n_2 \eta} - \tau\right) \psi_2 + |\psi_2|^2 \psi_2 + \frac{1}{\alpha} \Pi^2 \psi_2 - \frac{n_1}{n_2} \gamma \psi_1 = 0, \end{cases} \quad (4.6)$$

with $\tau = -\ln(T/T_c)$. Identification with the LD equations (4.5) gives:

$$\begin{aligned} \ln\left(\frac{T_{c1}}{T_c}\right) &= -\frac{S_1}{n_1 \eta} + \frac{\gamma}{\delta}, \\ \ln\left(\frac{T_{c2}}{T_c}\right) &= -\frac{S_2}{n_2 \eta} + \frac{\gamma}{m \alpha \delta}, \end{aligned} \quad (4.7)$$

with the condition $m \alpha \delta^2 = n_2 / n_1$. Since α and n_2 / n_1 are fixed, this is a relation between δ and m . One of them can be chosen freely.

4.6.1 Critical temperature

The critical temperature of a general n -component GL system can be found by dropping: (i) the non-linear terms, as they are negligible at T_c and (ii) the derivative terms, as the critical temperature is defined in the absence of a magnetic field, where the order parameters is homogenous. Thus we are left with a homogenous system of n linear equations, with n unknowns, the order parameters ψ_n . Above T_c we know only the trivial solution $\psi_n = 0$ can exist, which means that the determinant of the system should be different from zero. However, exactly at T_c , a non-trivial solution $\psi_n \neq 0$ appears, which mathematically corresponds to the determinant becoming zero. For the two-layer system discussed here, the determinant equation,

$$\begin{vmatrix} -\tau_1 + \frac{\gamma}{\delta} & -\gamma \\ -\frac{\gamma}{m\alpha\delta^2} & -\tau_2 + \frac{\gamma}{\delta m\alpha} \end{vmatrix} = 0, \quad (4.8)$$

gives the solution:

$$T_c = \sqrt{T_1^* T_2^*} \exp \left[\frac{1}{2} \sqrt{\ln^2 \left(\frac{T_1^*}{T_2^*} \right) + \frac{4\gamma^2}{m\alpha\delta^2}} \right] \quad (4.9)$$

with

$$\begin{aligned} T_1^* &= T_{c1} \exp \left(-\frac{\gamma}{\delta} \right), \\ T_2^* &= T_{c2} \exp \left(-\frac{\gamma}{m\alpha\delta} \right). \end{aligned} \quad (4.10)$$

When $\gamma = 0$, we get $T_c = \max(T_{c1}, T_{c2})$ as expected. When increasing γ from 0, T_c decreases. In the limit $\gamma \rightarrow \infty$, we obtain

$$T_c = T_{c1}^r T_{c2}^{1-r}, \quad (4.11)$$

with $r = 1/(m\alpha + 1)$. T_c is a weighted geometric mean of T_{c1} and T_{c2} and thus always lies in between these values.

4.7 Conclusions

We demonstrated that the V-Av state can be stabilized in mesoscopic two-gap superconductors in a far larger portion of the field-temperature phase diagram than is the case for single-gap samples. To realize this enhancement, the best conditions are provided by a low density of states in the band with higher intrinsic T_c and comparable but lower Fermi velocity (and coherence length) as compared to the second band. V-Av states in two-band samples are richer than their single-band counterparts, and appear in integral and fractional form, either of which can show re-entrant behavior as a function of temperature. Re-entrant integral

V-Av state is observable through e.g. the symmetry of the magnetic field profile obtained by Scanning Hall Probe Microscopy [172]. The re-entrant V-Av state in the second band can be verified experimentally by only imaging of that band [142]. The splitting of the stability regions of the V-Av state in two bands can also be realized by control of the local density of states, which might be attainable through local carrier injection [173]. Our theoretical findings are therefore of broad fundamental and experimental interest, they relate to bilayer structures of two single-band mesoscopic superconductors with appropriate properties, and should ultimately lead to direct detection of the yet unobserved vortex-antivortex state in a homogeneous magnetic field.

As a final remark we pointed the attention to the formal equivalence of the two-gap GL formalism to a Lawrence-Doniach GL model describing a system consisting of two Josephson coupled superconducting layers. This extends the relevance of the presented calculations and suggests further work on this easily controllable system in experiments.

Appendix

GL equations for two-gap superconductors using microscopic parameters

In Ref. [73], Gurevich derived the GL equations for dirty two-gap superconductors from microscopic theory. Here we show how these GL equations can be cast into dimensionless form and we find expressions for the free energy, the current and the boundary conditions for two-gap superconductors. The results of Ref. [75], where the GL equations were derived in the clean limit, are recovered by putting the interband scattering rate to zero. The latter equations forms the theoretical framework of Chapter 4.

Definitions

Starting point is the free energy density, as derived by Gurevich:

$$\begin{aligned} F = & a_1|\Psi_1|^2 + \frac{b_1}{2}|\Psi_1|^4 + c_1|\Pi\Psi_1|^2 \\ & + a_2|\Psi_2|^2 + \frac{b_2}{2}|\Psi_2|^4 + c_2|\Pi\Psi_2|^2 \\ & - a_i\Re(\Psi_1\Psi_2^*) + 2b_i(|\Psi_1|^2 + |\Psi_2|^2)\Re(\Psi_1\Psi_2^*) + c_i\Re(\Pi\Psi_1\Pi^*\Psi_2^*), \end{aligned} \tag{4.12}$$

with $\Pi = -i\nabla - \vec{A}$, the covariant derivative².

²Actually, Gurevich used a different definition for the covariant derivative, $\Pi_G = \nabla + i\vec{A}$. This does however not change the physics, since this different definition is equivalent to a reversal of the field and a complex conjugation of the two order parameters, leaving the free energy invariant.

The coefficients are defined as (the i in the subscript is short for ‘interaction’):

$$\begin{aligned}
 a_1 &= \frac{N_1}{2} \left[\ln \frac{T}{T_1} + \frac{\pi \hbar \gamma_{12}}{4k_B T} \right], \\
 b_1 &= N_1 \left[\frac{7\zeta(3)}{16\pi^2 (k_B T)^2} - \frac{3\pi \hbar \gamma_{12}}{384 (k_B T)^3} \right], \\
 c_1 &= \hbar N_1 D_1 \left[\frac{\pi}{16k_B T} - \frac{7\zeta(3) \hbar \gamma_{12}}{8\pi^2 (k_B T)^2} \right], \\
 a_2 &= \frac{N_2}{2} \left[\ln \frac{T}{T_2} + \frac{\pi \hbar \gamma_{21}}{4k_B T} \right], \\
 b_2 &= N_2 \left[\frac{7\zeta(3)}{16\pi^2 (k_B T)^2} - \frac{3\pi \hbar \gamma_{21}}{384 (k_B T)^3} \right], \\
 c_2 &= \hbar N_2 D_2 \left[\frac{\pi}{16k_B T} - \frac{7\zeta(3) \hbar \gamma_{21}}{8\pi^2 (k_B T)^2} \right], \\
 a_i &= \frac{N_1}{2} \left[\frac{\lambda_{12}}{w} + \frac{\pi \hbar \gamma_{12}}{4k_B T} \right] + \frac{N_2}{2} \left[\frac{\lambda_{21}}{w} + \frac{\pi \hbar \gamma_{21}}{4k_B T} \right], \\
 b_i &= \frac{\pi}{384 (k_B T)^3} (\hbar \gamma_{12} N_1 + \hbar \gamma_{21} N_2), \\
 c_i &= \frac{7\zeta(3)}{(4\pi k_B T)^2} (D_1 + D_2) (\hbar \gamma_{12} N_1 + \hbar \gamma_{21} N_2)
 \end{aligned} \tag{4.13}$$

where D_m are the *intra*band diffusivities due to nonmagnetic impurity scattering, $2\gamma_{mm'}$ are the *inter*band scattering rates, $\lambda_{mm'}$ are the electron-phonon constants: the diagonal terms λ_{11} and λ_{22} quantify *intra*band pairing and λ_{12} and λ_{21} describe *inter*band coupling, and N_m are the partial densities of states. We have the relations $N_1 \lambda_{12} = N_2 \lambda_{21}$ and $N_1 \gamma_{12} = N_2 \gamma_{21}$. Furthermore, we have intrinsic critical temperatures, defined as:

$$\begin{aligned}
 T_1 &= T_{c0} \exp(-(\lambda_0 - \lambda_-)/2w), \\
 T_2 &= T_{c0} \exp(-(\lambda_0 + \lambda_-)/2w),
 \end{aligned} \tag{4.14}$$

with

$$\begin{aligned}
 w &= \lambda_{11} \lambda_{22} - \lambda_{12} \lambda_{21}, \\
 \lambda_0 &= \sqrt{\lambda_-^2 + 4\lambda_{12} \lambda_{21}}, \\
 \lambda_{\pm} &= \lambda_{11} \pm \lambda_{22},
 \end{aligned} \tag{4.15}$$

and T_{c0} is to be determined from the quadratic equation in $x = \ln T_{c0}$

$$U p - (U w + \lambda_0) x + w x^2 = 0, \tag{4.16}$$

which has two roots:

$$\ln T_{c0} = \frac{U w + \lambda_0 \pm \sqrt{(U w + \lambda_0)^2 - 4U w p}}{2w}, \tag{4.17}$$

with

$$\begin{aligned}
 U &= \psi\left(\frac{1}{2} + \frac{2\eta}{\pi^2}\left(1 + \frac{\lambda_{21}}{\lambda_{12}}\right)\right) - \psi(1/2), \\
 2p &= \lambda_0 + \frac{\lambda_-(\lambda_{12} - \lambda_{21}) - 4\lambda_{21}\lambda_{12}}{\lambda_{12} + \lambda_{21}},
 \end{aligned} \tag{4.18}$$

with ψ the digamma function and $\eta = \hbar\gamma_{12}\pi/4k_B T_c$, a dimensionless expression quantifying the interband scattering rate. When there is no interband scattering ($\eta = 0$), we have $U = 0$ and we get $T_{c0} = \exp(\lambda_0/w)$ (+) or $T_{c0} = 1$ (-). The solution with the minus sign has to be chosen:

$$\ln T_{c0} = \frac{Uw + \lambda_0 - \sqrt{(Uw + \lambda_0)^2 - 4Uwp}}{2w}, \tag{4.19}$$

in correspondence with the results of Kogan in Ref. [75] where the GL equation for a clean two-gap superconductor were derived and where the minus sign for S was chosen.

Derivation of GL equations

GL equations for the order parameters

To obtain the GL equations for the two order parameters, one has to vary the free energy, Eq. (4.12), with respect to Ψ_1^* ,

$$\begin{aligned}
 \delta\mathcal{F} &= \int a_1\Psi_1\delta\Psi_1^* + b_1\Psi_1|\Psi_1|^2\delta\Psi_1^* + c_1(\Pi\Psi_1)(\Pi^*\delta\Psi_1^*) \\
 &\quad - \frac{a_i}{2}\Psi_2\delta\Psi_1^* + b_i[2\Psi_1\Re(\Psi_1\Psi_2^*) + (|\Psi_1|^2 + |\Psi_2|^2)\Psi_2] \delta\Psi_1^* \\
 &\quad + \frac{c_i}{2}(\Pi\Psi_2)(\Pi^*\delta\Psi_1^*),
 \end{aligned} \tag{4.20}$$

and to Ψ_2^* . In this way, the first two Ginzburg-Landau equations are obtained:

$$\begin{aligned}
 &a_1\Psi_1 + b_1|\Psi_1|^2\Psi_1 + c_1\Pi^2\Psi_1 - \frac{a_i}{2}\Psi_2 \\
 &+ b_i[(|\Psi_1|^2 + |\Psi_2|^2)\Psi_2 + 2\Psi_1\Re(\Psi_1\Psi_2^*)] + \frac{c_i}{2}\Pi^2\Psi_2 = 0, \\
 &a_2\Psi_2 + b_2|\Psi_2|^2\Psi_2 + c_2\Pi^2\Psi_2 - \frac{a_i}{2}\Psi_1 \\
 &+ b_i[(|\Psi_1|^2 + |\Psi_2|^2)\Psi_1 + 2\Psi_2\Re(\Psi_1\Psi_2^*)] + \frac{c_i}{2}\Pi^2\Psi_1 = 0.
 \end{aligned} \tag{4.21}$$

In this derivation, the boundary conditions naturally emerge, analogous to the single-gap case, which was presented in Section 1.7.2. It suffices to focus on the terms with derivatives:

$$\begin{aligned}
 \delta\mathcal{F}_\Pi &= \int c_1(\Pi\Psi_1) \cdot (\Pi^*\delta\Psi_1^*) + \frac{c_i}{2}(\Pi\Psi_2)(\Pi^*\delta\Psi_1^*) \\
 &= \int (\Pi\Phi) \cdot (\Pi^*\delta\Psi_1^*),
 \end{aligned} \tag{4.22}$$

with

$$\Phi = c_1 \Psi_1 + \frac{c_i}{2} \Psi_2. \quad (4.23)$$

Now the last derivative, Π^* , is expanded:

$$\begin{aligned} \delta \mathcal{F}_\Pi &= \int (\Pi \Phi) \cdot (\Pi^* \delta \Psi_1^*) \\ &= \int (\Pi \Phi) i \nabla (\delta \Psi_1^*) - (\Pi \Phi) A \delta \Psi_1^* \\ &= \int -i \delta \Psi_1^* \nabla \cdot \Pi \Phi + i \nabla (\delta \Psi_1^* \Pi \Phi) - \delta \Psi_1^* A (\Pi \Phi), \end{aligned} \quad (4.24)$$

where the vector calculus identity $\nabla \cdot (a \vec{b}) = \vec{b} \cdot \nabla a + a \nabla \cdot \vec{b}$ with $a = \delta \Psi_1^*$ and $\vec{b} = \Pi \Phi$ was used in the last step. By taking the first and the last term and resubstituting Π , we obtain

$$\begin{aligned} \delta \mathcal{F}_\Pi &= \int \delta \Psi_1^* \Pi^2 \Phi + i \nabla (\delta \Psi_1^* \Pi \Phi) \\ &= \int \delta \Psi_1^* \Pi^2 \Phi dV + i \oint \delta \Psi_1^* \vec{n} \cdot (\Pi \Phi) dS, \end{aligned} \quad (4.25)$$

making use of the Gauss theorem. The variation of the free energy has to be zero for all variations of $\delta \Psi_1^*$, which can only be satisfied when

$$\begin{aligned} \Pi^2 \Phi + a_1 \Psi_1 + b_1 \Psi_1 |\Psi_1|^2 - \frac{a_i}{2} \Psi_2 + b_i [2 \Psi_1 \Re(\Psi_1 \Psi_2^*) + (|\Psi_1|^2 + |\Psi_2|^2) \Psi_2] &= 0 \\ \vec{n} \cdot (\Pi \Phi) &= 0. \end{aligned} \quad (4.26)$$

The last equation is the boundary condition, with \vec{n} the unit vector normal to the surface of the superconductor. From the variation with respect to $\delta \Psi_2^*$ the other boundary condition is obtained. The two boundary conditions thus become:

$$\begin{cases} \vec{n} \cdot (c_1 \Pi \Psi_1 + \frac{c_i}{2} \Pi \Psi_2) = 0 \\ \vec{n} \cdot (c_2 \Pi \Psi_2 + \frac{c_i}{2} \Pi \Psi_1) = 0 \end{cases}, \quad (4.27)$$

which can be simplified by linear transformations from which the final form of the boundary conditions is obtained:

$$\begin{cases} \vec{n} \cdot (\Pi \Psi_1) = 0, \\ \vec{n} \cdot (\Pi \Psi_2) = 0, \end{cases} \quad (4.28)$$

GL equation for the vector potential

In fact, we omitted a term in the GL free energy, the one representing the magnetic energy. The extra term is:

$$F_{mag} = \frac{1}{8\pi} (\vec{H} - \vec{H}_0)^2 \quad (4.29)$$

with $\nabla \times \vec{A} = \vec{H}$. In dimensionless units, the vector potential is expressed in units of $A_0 = \frac{\phi_0 c}{2\pi\xi} = \frac{\hbar c}{2e\xi}$, the magnetic field in units of the intrinsic second critical field of the first band $H_{c2}^{(1)} = A_0/\xi$ and we get:

$$\frac{F_{mag}}{F_0} = \kappa_1^2 (\nabla \times \vec{A} - \vec{H}_0)^2 \quad (4.30)$$

with

$$\kappa_1^2 = \frac{A_0^2}{8\pi F_0 \xi^2} = \frac{\pi^3}{3584\zeta(3)} \frac{c^2}{e^2} \frac{1}{N_1 D_1^2}. \quad (4.31)$$

Using variational analysis, the third GL (i.e. the Maxwell) equation can be derived. Only terms in the free energy containing the magnetic vector potential, \vec{A} , have to be considered:

$$\frac{F_A}{F_0} = c_1 |\Pi\Psi_1|^2 + c_2 |\Pi\Psi_2|^2 + c_i \Re(\Pi\Psi_1 \Pi^* \Psi_2^*) + \kappa_1^2 (\nabla \times \vec{A} - \vec{H}_0)^2 \quad (4.32)$$

We first focus on the last term. The vector potential is varied by $\delta\vec{A}$ and only terms linear in the variation are kept:

$$\begin{aligned} \delta\mathcal{F}_M &= \kappa_1^2 \int (\nabla \times A + \nabla \times \delta A)^2 - 2(\nabla \times A_0) \cdot (\nabla \times (A + \delta A)) + \dots \\ &= 2\kappa_1^2 \int (\nabla \times A)(\nabla \times \delta A) - (\nabla \times \delta A)(\nabla \times A_0) + \dots \\ &= 2\kappa_1^2 \int (\nabla \times \delta A) \cdot (\nabla \times (A - A_0)) + \dots \end{aligned} \quad (4.33)$$

Now the identity $\nabla \cdot (a \times b) = b \cdot (\nabla \times a) - a \cdot (\nabla \times b)$ with $a = \delta A$ and $b = \nabla \times (A - A_0)$ is used to obtain:

$$\delta\mathcal{F}_M = 2\kappa_1^2 \int \delta A \cdot [\nabla \times \nabla \times (A - A_0)] + \nabla \cdot [\delta A \times (\nabla \times (A - A_0))] + \dots \quad (4.34)$$

By using Gauss' identity $\int \nabla \cdot \vec{c} = \oint dS \cdot \vec{c}$, the last term can be replaced by a surface integral. Since the integration has to be done over the whole space, the surface is at infinity where $A = A_0$ and thus this term vanishes. We are left with

$$\delta\mathcal{F}_M = 2\kappa_1^2 \int \delta A \cdot [\nabla \times \nabla \times (A - A_0)] + \dots \quad (4.35)$$

Now we consider the other terms that contain the vector potential A :

$$\begin{aligned} \delta\mathcal{F}_j &= - \int \delta A \cdot [2c_1 \Re(\Psi_1^* \Pi \Psi_1) + 2c_2 \Re(\Psi_1^* \Pi \Psi_1) \\ &\quad c_i \Re(\Psi_2^* \Pi \Psi_1) + c_i \Re(\Psi_1^* \Pi \Psi_2)] + \dots \end{aligned} \quad (4.36)$$

According to variational analysis, $\delta\mathcal{F}$ has to be zero for all δA which can only be true if the term after δA is zero, from which we get the third (Maxwell) GL equation:

$$-\kappa_1^2 \Delta \vec{A} = \vec{j}_s = c_1 \Re(\Psi_1 \Pi \Psi_1^*) + c_2 \Re(\Psi_2 \Pi \Psi_2^*) + \frac{c_i}{2} \Re(\Psi_1 \Pi \Psi_2^*) + \frac{c_i}{2} \Re(\Psi_2 \Pi \Psi_1^*) \quad (4.37)$$

As such one can state that the effective values for $\kappa_{1,2}$ become temperature dependent.

The GL free energy

Finally the free energy expression is revisited, which will reduce to an integral over the sample interior and will make the computation possible using a finite simulation region. We start by examining the kinetic terms of the free energy:

$$\mathcal{F}_\Pi = \int c_1 |\Pi \Psi_1|^2 + c_2 |\Pi \Psi_2|^2 + \frac{c_i}{2} (\Pi \Psi_1 \Pi^* \Psi_2^* + \Pi^* \Psi_1^* \Pi \Psi_2) \quad (4.38)$$

We will analyze this by separating the expression into two parts, consisting of the outer and the inner terms, and start with the outer terms:

$$\begin{aligned} & \int c_1 |\Pi \Psi_1|^2 + \frac{c_i}{2} \Pi^* \Psi_1^* \Pi \Psi_2 \\ &= \int c_1 \Pi \Psi_1 \Pi^* \Psi_1^* + \frac{c_i}{2} \Pi^* \Psi_1^* \Pi \Psi_2 \\ &= \int \Pi^* \Psi_1^* \Pi \Phi \\ &= \int i \nabla \Psi_1^* \Pi \Phi - A \Psi_1^* \Pi \Phi \end{aligned} \quad (4.39)$$

where we used $\Phi = c_1 \Psi_1 + \frac{c_i}{2} \Psi_2$. Then we use the identity $\nabla \cdot (a\vec{b}) = \vec{b} \cdot \nabla a + a \nabla \cdot \vec{b}$ with $a = \Psi_1^*$ and $\vec{b} = \Pi \Phi$ to obtain

$$\begin{aligned} & \int -i \Psi_1^* \nabla \Pi \Phi + i \nabla \cdot (\Psi_1^* \Pi \Phi) - A \Psi_1^* \Pi \Phi \\ &= \int \Psi_1^* \Pi^2 \Phi + i \oint \Psi_1^* \vec{n} \cdot \Pi \Phi \\ &= \int \Psi_1^* \Pi^2 \Phi \end{aligned} \quad (4.40)$$

where we dropped the last term because of the earlier derived boundary condition. When we substitute this into the first GL equation we get

$$\int -a_1 |\Psi_1|^2 - b_1 |\Psi_1|^4 + \frac{a_i}{2} \Psi_2 \Psi_1^* - b_i [2 |\Psi_1|^2 \Re(\Psi_1 \Psi_2^*) + (|\Psi_1|^2 + |\Psi_2|^2) (\Psi_1^* \Psi_2)] \quad (4.41)$$

For the inner terms we do the same and obtain:

$$\int -a_2|\Psi_2|^2 - b_2|\Psi_2|^4 + \frac{a_i}{2}\Psi_1\Psi_2^* - b_i [2|\Psi_2|^2\Re(\Psi_1\Psi_2^*) + (|\Psi_1|^2 + |\Psi_2|^2)(\Psi_1\Psi_2^*)] \quad (4.42)$$

When we add both results we get:

$$\begin{aligned} \mathcal{F}_{\Pi} = \int & -a_1|\Psi_1|^2 - b_1|\Psi_1|^4 - a_2|\Psi_2|^2 - b_2|\Psi_2|^4 + a_i\Re(\Psi_1\Psi_2^*) \\ & -4b_i(|\Psi_1|^2 + |\Psi_2|^2)\Re(\Psi_1\Psi_2) \end{aligned} \quad (4.43)$$

Substituting this into the total free energy functional, all terms except the ones with b 's as coefficients are eliminated:

$$\mathcal{F} = \int -\frac{b_1}{2}|\Psi_1|^4 - \frac{b_2}{2}|\Psi_2|^4 - 2b_i(|\Psi_1|^2 + |\Psi_2|^2)\Re(\Psi_1\Psi_2^*). \quad (4.44)$$

Dimensionless GL theory

To switch to a dimensionless GL model, an energy scale, $W^2 = 8\pi^2(k_B T_c)^2/7\zeta(3)$, and an length scale $\xi^2 = \hbar D_1/W\chi$ is introduced with $\chi^2 = 56\zeta(3)/\pi^4$ and ζ the Riemann zeta function ($\zeta(3) \approx 1.202$). The free energy is expressed in units of $F_0 = N_1 W^2/2$, the order parameters in units of W , and the covariant derivatives are by their dimensionless counterparts. Then we obtain the coefficients of the dimensionless two-gap GL model:

$$\begin{aligned} a_1 &= \ln \frac{T}{T_1} + \frac{\eta}{T} \\ a_2 &= \frac{N_2}{N_1} \ln \frac{T}{T_2} + \frac{\eta}{T} \\ b_1 &= \left[1 - \frac{4}{\pi^2} \frac{1}{\chi^2} \frac{\eta}{T} \right] \frac{1}{T^2} \\ b_2 &= \left[\frac{N_2}{N_1} - \frac{4}{\pi^2} \frac{1}{\chi^2} \frac{\eta}{T} \right] \frac{1}{T^2} \\ c_1 &= \left[1 - \chi^2 \frac{\eta}{T} \right] \frac{1}{T} \\ c_2 &= \frac{D_2}{D_1} \left[\frac{N_2}{N_1} - \chi^2 \frac{\eta}{T} \right] \frac{1}{T} \\ a_i &= 2 \left[\frac{\lambda_{12}}{w} + \frac{\eta}{T} \right] \\ b_i &= \frac{6}{\pi^2} \frac{1}{\chi^2} \frac{\eta}{T^3} \\ c_i &= \left(1 + \frac{D_2}{D_1} \right) \chi^2 \frac{\eta}{T^2} \end{aligned} \quad (4.45)$$

The limit for a clean superconductor is obtained by putting $\eta = 0$, and substituting T by 1 everywhere, except in the logarithms (otherwise the temperature dependence would be lost). This substitution is indeed justified near the critical temperature, which is the strict validity region of the GL theory. Definitions $\alpha = D_1/D_2$ and $\gamma = \lambda_{12}/w$ lead to:

$$\begin{aligned}
 a_1 &= \ln \frac{T}{T_1}, \\
 a_2 &= \frac{N_2}{N_1} \ln \frac{T}{T_2}, \\
 b_1 &= 1, \\
 b_2 &= \frac{N_2}{N_1}, \\
 c_1 &= 1, \\
 c_2 &= \frac{1}{\alpha} \frac{N_2}{N_1}, \\
 a_i &= 2\gamma.
 \end{aligned} \tag{4.46}$$

The GL equations now become:

$$\begin{cases} \ln \frac{T}{T_1} \Psi_1 + |\Psi_1|^2 \Psi_1 + (\Pi \Psi_1)^2 - \gamma \Psi_2 = 0, \\ \ln \frac{T}{T_2} \Psi_2 + |\Psi_2|^2 \Psi_2 + \frac{1}{\alpha} (\Pi \Psi_2)^2 - \frac{N_1}{N_2} \gamma \Psi_1 = 0, \end{cases} \tag{4.47}$$

which is equivalent to the GL equations derived by Kogan in Ref. [75]. Notice however that the definition of γ in terms of microscopic parameters differs however by a factor $1/N_1$. This is explained by the different definition of the λ -matrix. In the current derivation we use the convention found throughout the majority of literature while Kogan employs a different notation where Λ is symmetric. We have that $\lambda_{\nu\mu}^{(lit)} = n_\mu \lambda_{\nu\mu}^{(Kogan)}$ and thus:

$$\left(\frac{\lambda_{12}}{w} \right)_{lit.} = \left(\frac{\lambda_{12}}{n_1 w} \right)_{Kogan}. \tag{4.48}$$

Summary

Summarizing this appendix, from the two-gap GL free energy density,

$$\begin{aligned}
 \frac{F}{F_0} &= a_1 |\Psi_1|^2 + \frac{b_1}{2} |\Psi_1|^4 + c_1 |\Pi \Psi_1|^2 \\
 &+ a_2 |\Psi_2|^2 + \frac{b_2}{2} |\Psi_2|^4 + c_2 |\Pi \Psi_2|^2 \\
 &- a_i \Re(\Psi_1 \Psi_2^*) + 2b_i (|\Psi_1|^2 + |\Psi_2|^2) \Re(\Psi_1 \Psi_2^*) + c_i \Re(\Pi \Psi_1 \Pi^* \Psi_2^*) \\
 &+ \kappa_1^2 (\nabla \times \vec{A} - \vec{H}_0)^2,
 \end{aligned}$$

the two-gap GL equations can be obtained:

$$\begin{aligned}
& a_1 \Psi_1 + b_1 |\Psi_1|^2 \Psi_1 + c_1 \Pi^2 \Psi_1 - \frac{a_i}{2} \Psi_2 \\
& + b_i [(|\Psi_1|^2 + |\Psi_2|^2) \Psi_2 + 2 \Psi_1 \Re(\Psi_1 \Psi_2^*)] + \frac{c_i}{2} \Pi^2 \Psi_2 = 0 \\
& a_2 \Psi_2 + b_2 |\Psi_2|^2 \Psi_2 + c_2 \Pi^2 \Psi_2 - \frac{a_i}{2} \Psi_1 \\
& + b_i [(|\Psi_1|^2 + |\Psi_2|^2) \Psi_1 + 2 \Psi_2 \Re(\Psi_1 \Psi_2^*)] + \frac{c_i}{2} \Pi^2 \Psi_1 = 0 \\
& -\kappa_1^2 \Delta(\vec{A} - \vec{A}_0) = \vec{j}_s = c_1 \Re(\Psi_1 \Pi \Psi_1^*) + c_2 \Re(\Psi_2 \Pi \Psi_2^*) \\
& \quad + \frac{c_i}{2} \Re(\Psi_1 \Pi \Psi_2^*) + \frac{c_i}{2} \Re(\Psi_2 \Pi \Psi_1^*)
\end{aligned}$$

with boundary conditions:

$$\begin{cases} \vec{n} \cdot (\Pi \Psi_1) = 0 \\ \vec{n} \cdot (\Pi \Psi_2) = 0 \end{cases}$$

When the GL equations are obeyed, the total energy of the system can be expressed through the integral over the interior of the sample

$$\mathcal{F} = \int_V -\frac{b_1}{2} |\Psi_1|^4 - \frac{b_2}{2} |\Psi_2|^4 - 2b_i (|\Psi_1|^2 + |\Psi_2|^2) \Re(\Psi_1 \Psi_2^*) + (\vec{A} - \vec{A}_0) \cdot \vec{j}_s$$

with dimensionless coefficients, defined as:

$$\begin{aligned}
a_1 &= \ln \frac{T}{T_1} + \frac{\eta}{T} \\
a_2 &= \frac{N_2}{N_1} \ln \frac{T}{T_2} + \frac{\eta}{T} \\
b_1 &= \left[1 - \frac{4}{\pi^2} \frac{1}{\chi^2} \frac{\eta}{T} \right] \frac{1}{T^2} \\
b_2 &= \left[\frac{N_2}{N_1} - \frac{4}{\pi^2} \frac{1}{\chi^2} \frac{\eta}{T} \right] \frac{1}{T^2} \\
c_1 &= \left[1 - \chi^2 \frac{\eta}{T} \right] \frac{1}{T} \\
c_2 &= \frac{D_2}{D_1} \left[\frac{N_2}{N_1} - \chi^2 \frac{\eta}{T} \right] \frac{1}{T} \\
a_i &= 2 \left[\frac{\lambda_{12}}{w} + \frac{\eta}{T} \right] \\
b_i &= \frac{6}{\pi^2} \frac{1}{\chi^2} \frac{\eta}{T^3} \\
c_i &= \left(1 + \frac{D_2}{D_1} \right) \chi^2 \frac{\eta}{T^2} \\
\kappa_1^2 &= \frac{\pi^3}{3584 \zeta(3)} \frac{c^2}{e^2} \frac{1}{N_1 D_1^2}.
\end{aligned}$$

For given geometry, field and temperature, the behavior of a Two-Gap GL superconductor can be described in a 7-dimensional parameter space, representing the material properties, consisting of

$$T_1, T_2, \gamma, \frac{N_2}{N_1}, \eta, \frac{D_2}{D_1}, \kappa_1.$$

Note that these 7 parameters are not independent. Furthermore, their connection to microscopic parameters prohibits us to choose them completely arbitrarily: a set of microscopic parameters leading to these intuitive parameters has to exist and moreover, has to consist of rather realistic values. The corresponding 7 parameters from microscopic theory are:

$$\lambda_{11}, \lambda_{12}, \lambda_{21}, \lambda_{22}, \eta, \frac{D_2}{D_1}, \kappa_1$$

with the relations defined in Eqs. (4.14), (4.15), (4.16) and (4.17).

Chapter 5

Topologically trapped vortex molecules in Bose-Einstein condensates

During the last decade, intense experimental and theoretical activity has induced dramatic achievements in Bose-Einstein condensation in trapped alkali-metal gases at ultralow temperatures [92, 93]. The atomic Bose-Einstein condensates (BECs) differ fundamentally from the helium BEC, having significantly non-uniform density, very high low-temperature condensate fraction, and being pure and dilute, so that interactions can be accurately parametrized in terms of the scattering length. As a result, a relatively simple nonlinear Schrödinger equation (the Gross-Pitaevskii (GP) equation) gives a precise description of the atomic condensates and their dynamics [174].

It is already well established that the GP equation has rotating solutions with a well-defined angular momentum, defining the *vortex states* [175]. Vortices as topological singularities in BEC have been readily observed in experiment [176, 177], and are also found in liquid helium [20] and in superconductors [48]. The exciting new property of atomic BECs is that intrinsic interactions in the system are directly dependent on the mean particle density [178], which gives them a unique degree of freedom for studies of vortex matter. Another interesting aspect of dilute Bose condensates is that their density can be locally suppressed *optically*. As experimentally shown by Tung *et al.* [179], vortex lines in BEC show great affinity towards weak spots created by focussed laser beams, which results in a very profound vortex pinning and provides yet another tool for vortex manipulation [180].

Vortices in BEC are accompanied by the appropriate distribution of the phase

φ of the order parameter ψ , where the number of successive 2π changes along the perimeter corresponds to the vorticity of the vortex state, i.e. the topological charge. Therefore, using the known phase distribution, particular vortex states can be predefined in the system by the so-called *phase imprint* technique [181], where an uniform light pulse projects a designed mask onto the condensate. However, the gradient of the imprinted phase ($\nabla\varphi$) must always be parallel to the rotational velocity of the condensate, i.e. the *antivortex* is fundamentally unstable for a positive angular momentum. Note also that imprinted multiple 2π change, i.e. a *multiquantum* vortex, was never found stable against decomposition into single vortices in conventional BEC setups [182, 183].

Motivated by these recent developments in vortex physics, in this chapter we exploit a uniquely defined BEC system that combines above essentials; our atomic BEC is confined, exposed to engineered spatial pinning, and is cylindrically rotated. Knowing that vortex solitons are strongly influenced by symmetry in non-linear media [184–186], we impose a particular *symmetry* on the system by chosen arrangement of the vortex-trapping optical beams. As we will show, this results in the nucleation of vortex molecules of matching symmetry in the ground state, which may comprise unconventional phase profiles containing a *stable antivortex*, or a *multiquantum* vortex.

For the purpose of this work, we solve the stationary Gross-Pitaevskii (GP) equation, in a rotating frame with frequency Ω around the z -axis:

$$\left(-\frac{\hbar^2}{2m}\Delta + V_c + g|\psi|^2 - \Omega L_z - \mu\right)\psi = 0, \quad (5.1)$$

where V_c stands for confinement potential, $g = 4\pi\hbar^2 a/m$ is the non-linearity with a being the s -wave scattering length, $L_z = -i\hbar(x\partial_y - y\partial_x)$ is the angular momentum operator, μ denotes chemical potential, and ψ is the order parameter normalized to the number of particles in the condensate N . The energy of a particular state is then given by $E = \mu - \frac{g}{2} \int dV |\psi|^4$. We take the usual parabolic-like confinement potential characterized by the frequency ω_\perp in the (x, y) plane and ω_z in the z -direction. Our numerical method treats the GP equation in all three dimensions, but in the present work we take $\omega_z \gg \omega_\perp$ forcing the condensate in a quasi two-dimensional, oblate (pancake) shape. In that case, Eq. (5.1) can be written in dimensionless and discretized form as

$$\begin{aligned} \frac{U_x^{i-1,i}\psi_{i-1,j}}{b_x^2} + \frac{U_x^{i+1,i}\psi_{i+1,j}}{b_x^2} + \frac{U_y^{j-1,j}\psi_{i,j-1}}{b_y^2} + \frac{U_y^{j+1,j}\psi_{i,j+1}}{b_y^2} \\ = \left(\frac{2}{b_x^2} + \frac{2}{b_y^2} - g'|\psi_{i,j}|^2 - V + \mu\right)\psi_{i,j}, \end{aligned} \quad (5.2)$$

where $b_{x,y}$ are the lattice constants of the Cartesian grid, and the link variable is defined as $U_{\alpha=x,y}^{m,n} = \exp\left[-i\int_{\mathbf{r}_m}^{\mathbf{r}_n} \mathbf{A}_\alpha(\mathbf{r})d\alpha\right]$, with $A_{x(y)} = (-)\frac{1}{2}\Omega y(x)$. The dis-

tances, angular velocity and energy are expressed in the fundamental scales of the harmonic trap, i.e. $r_0 = \sqrt{\hbar/m\omega_\perp}$, $\omega_0 = \omega_\perp$, and $E_0 = \hbar\omega_\perp$ respectively. The 2D nonlinearity $g' = 2aN\sqrt{2\pi m\omega_z/\hbar}$ (found by averaging the GP equation over the z-direction) now depends on N since we chose wave function normalized to unity. Therefore, for fixed g , N is a measure of the importance of interactions in the condensate, and directly reflects on the vortex phase diagram. Note also that for low non-linearities, i.e. when g' is small, vortex states in parabolic confinement are stable only for velocities of the condensate close to $\Omega = \omega_\perp$, i.e. when the gas dissolves due to centrifugal forces. To enhance the vortex stability, we have chosen a modified confinement potential $V_c = \frac{1}{2}r_\perp^2 + \frac{1}{10}r_\perp^4$. Such empowered confinement enables the condensate to survive higher angular velocities ($\Omega > \omega_\perp$), and is feasible in experiment by combining optical and magnetic trapping (e.g. for ^{87}Rb , a magnetic trap with frequency $75.5 \times 2\pi$ Hz in combination with a laser beam with waist $25 \mu\text{m}$ and power 1.2 mW [187]).

5.1 Vortex-antivortex molecules as the ground state

In this chapter, we consider ^{23}Na BEC, with somewhat lower interaction than ^{87}Rb , and consequently lower non-linearity. With the above expression for V_c , we use the effective perpendicular parabolic confinement with $\omega_\perp = 4.39 \times 2\pi$ Hz, and the unit of length becomes $r_0 = 10 \mu\text{m}$. To obtain the pancake shape of the condensate, we take $\omega_z = 10\omega_\perp$. The non-linearity parameter for a condensate consisting of 10^4 sodium atoms becomes $g' = 44$. In what follows, we implement laser pinning in the formalism, and model it as a Gaussian potential well $V_p = \exp(-16(r/w_p)^2)$ (r is the distance from the pinning center) as depicted schematically in the inset of Fig. 5.1c. We use a set of N_p laser beams on a single ring, and compare first the energy in the absence and presence of pinning, as shown in Fig. 5.1c. The resulting total potential in the BEC, introduced by confinement and laser beams, is taken as

$$V = V_c(\vec{r}) + a_p \sum_{j=1, N_p} V_p(\vec{r} - \vec{r}_j)$$

with $\vec{r}_j = d_p [\cos(j2\pi/N_p)\vec{e}_x + \sin(j2\pi/N_p)\vec{e}_y]$. With increasing angular velocity $\omega = \Omega/\omega_\perp$, vortices stabilize in the system, and each vortex state exhibits a distinct energy. In the $N_p = 0$ case, for chosen parameters, individual vortices form multi-vortex patterns denoted by (L_c, L) , where L_c gives the number of vortices in the central part of the condensate i.e. $L_c = \lim_{\epsilon \rightarrow 0} \frac{i}{2\pi\epsilon} \oint_{|\vec{r}|=\epsilon} d \left(\log \frac{\psi}{|\psi|} \right)$, and L is the total vorticity. In the $N_p \neq 0$ case, the ordering of laser beams imposes its symmetry on the vortex states, with N_p vortices pinned by the laser beams, and the remaining ones sitting in the central region of the condensate. As a remarkable phenomenon,

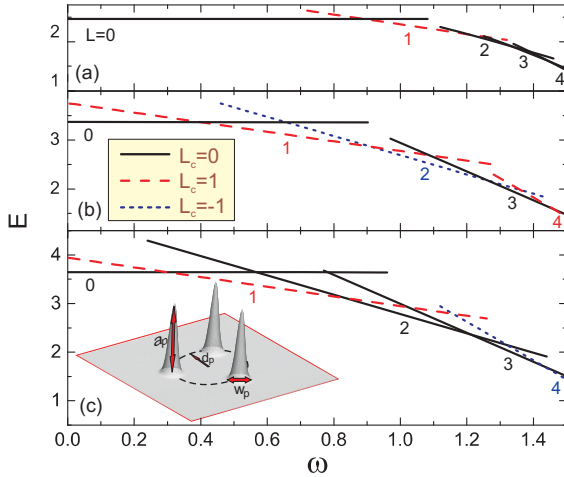


Figure 5.1: Energy versus angular velocity of a ^{23}Na condensate with $g'=20$ (i.e. with $N \approx 5000$ atoms), in the case of no laser pinning ($N_p = 0$, a), and three ($N_p = 3$, b), and five ($N_p = 5$, c) laser beams in a polygonal setting (with $d_p = 0.5$, $w_p = 0.4$, $a_p = 500$). Different lines correspond to states with different total vorticity L . The colors and style of the lines indicate the vorticity in the center of the condensate (L_c). The inset depicts the used energy profile for each pinning site, and notation of the parameters.

the system may preserve the symmetry even for $L < N_p$; e.g. for $L = N_p - 1$, still N_p vortices nucleate and are pinned, but must be accompanied by a central *antivortex* in order to simultaneously match the total angular momentum and the symmetry of the pinning potential. Energy levels of such vortex-antivortex molecules are indicated in Fig. 5.1 for $N_p = 3$ and $N_p = 5$ by the dotted (blue) curves.

Vortex-antivortex (V-Av) phenomena has already been of interest in BEC, mainly due to the fact that the excitation energy of a vortex-antivortex pair in non-rotating condensate is *lower* than the one of a single vortex. For that reason, it was assumed that the actual nucleation of a vortex occurs through the generation of a V-Av pair and the subsequent expulsion of the antivortex [188, 189]. While this may hold in ideally non-interacting BEC, V-Av appearance is seriously hampered by even small perturbations in the system, particularly in the rotating one. Yet, Crasovan *et al.* demonstrated that a V-Av pair may be stable in an interacting non-rotating BEC, however *only as an excited state* (ground state remains vortex-free) [190, 191] and the dynamics of such a state was recently analyzed in Ref. [192]. In addition, vortex-antivortex clusters were studied in Ref. [193, 194], the stabilization of vortex-antivortex lattices was considered in Ref. [195] and a superposed vortex-antivortex state was investigated in Ref. [196], however all only for the case of *non-rotating* systems. Here we show that states comprising an antivortex can be

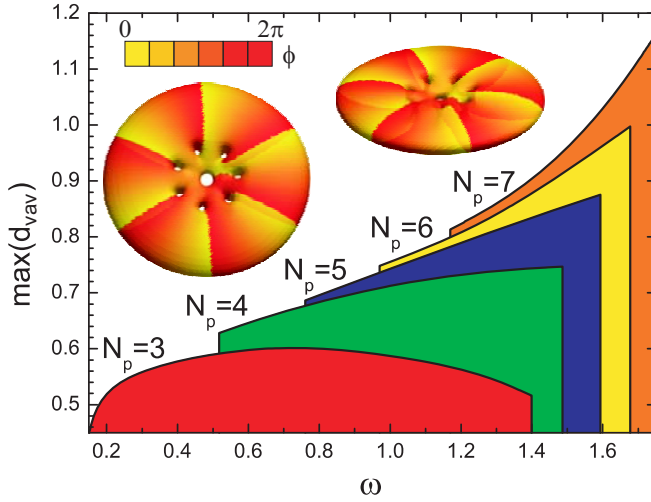


Figure 5.2: Histogram of vortex-antivortex (V-Av) distance in stable molecules found for different number of equidistant laser beams on a ring, as a function of angular velocity for $g' = 40$. Maximal V-Av separation increases for more used pinning beams, and insets show two oblique views of the superimposed density/phase 3D plots of the condensate for $\omega = 1.71$ and $N_p = 7$.

stabilized as the *ground state* in a rotating BEC by engineered pinning. Moreover, by using a different number of laser beams, antivortex can be realized at *different angular velocities*. Fig. 5.2 shows the ω -stability range of V-Av states with one antivortex found for $N_p = 3 - 7$, thus all states having vorticity $L = N_p - 1$. With increasing N_p , not only V-Av states appear for higher angular momenta, but they can also be spread over a larger area of the condensate. When artificially spreading the laser beams further apart (increasing d_p , see Fig. 5.1), vortices spontaneously follow and increase their distance from the central antivortex (d_{vav}) which facilitates the experimental verification of the V-Av molecule. Fig. 5.2 also shows the maximal d_{vav} that can be reached by increasing d_p for $w_p = 0.5$, $a_p = 500$ and $g' = 40$. The insets of Fig. 5.2 show isosurfaces of density 10^{-6} on which the phase distribution is superimposed for a condensate in the V-Av state for $N_p = 7$, $g' = 22$ and $\omega = 1.71$.

5.2 Novel phase transitions

As much as V-Av states are novel and exciting study objects, our system actually exhibits even richer vortex structures beyond V-Av phenomena. To illustrate this, we constructed a full vortex phase diagram, shown in Fig. 5.3 as a function of ω

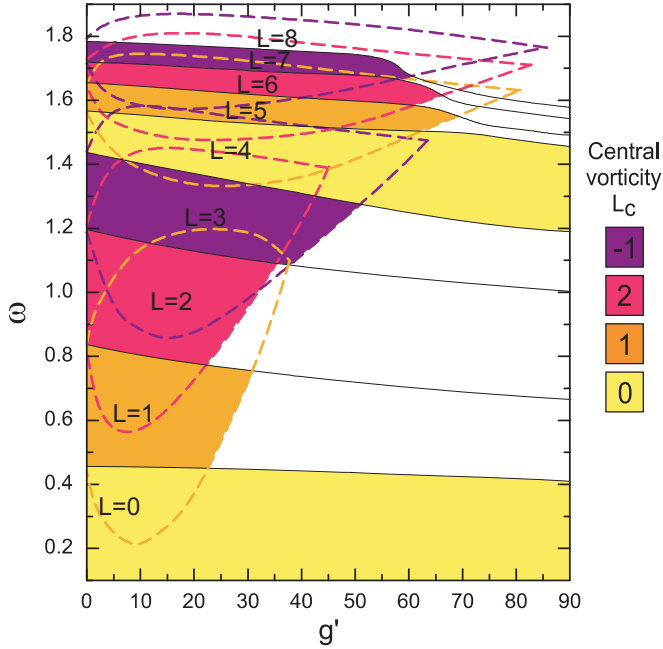


Figure 5.3: Equilibrium vortex phase diagram as a function of the angular velocity and non-linearity of the condensate, for $N_p = 4$, $d_p = 0.71$, $w_p = 0.4$ and $a_p = 500$. Coloring scheme illuminates the vorticity in the center of the condensate, between the pinning beams. Solid lines show the transitions in the ground state, while dashed curves illustrate the whole region of stability for different vortex states. In white areas, the vortex structure does not fully obey the fourfold symmetry of the pinning.

and non-linearity g' , for $N_p = 4$, i.e. a square arrangement of laser beams. As shown before, for constant g' , the vorticity increases with increasing ω . Note however that our strategic pinning setup enforces the N_p -fold symmetry of the vortex states, which leads to specific transitions in the central region of the condensate. As illustrated by a color gradient in Fig. 5.3, the central vorticity changes as $L_c = \text{mod}(L + 1, N_p) - 1$, where an antivortex may nucleate as discussed above. Nevertheless, N_p -fold symmetry tends to remain preserved for other vorticities as well, which results in the compression of excess $L - kN_p$ ($k \in \mathbb{N}^+$) vortices in the center of the condensate into a *multiquantum vortex* (also called *giant vortex*). This result complements earlier studies of such vortices in conventional BEC setups, where a multi-quanta vortex was found *unstable* towards decay into single-quantum vortices [182, 183]. For $N_p = 4$, we show the 0, 1, 2, -1, 0, 1, 2, -1 sequence with increasing ω in Fig. 5.3, for total vorticity $L = 0 - 7$. Doubly quantized vortex was realized for $L = 2$ and $L = 6$ states in the center of the condensate.

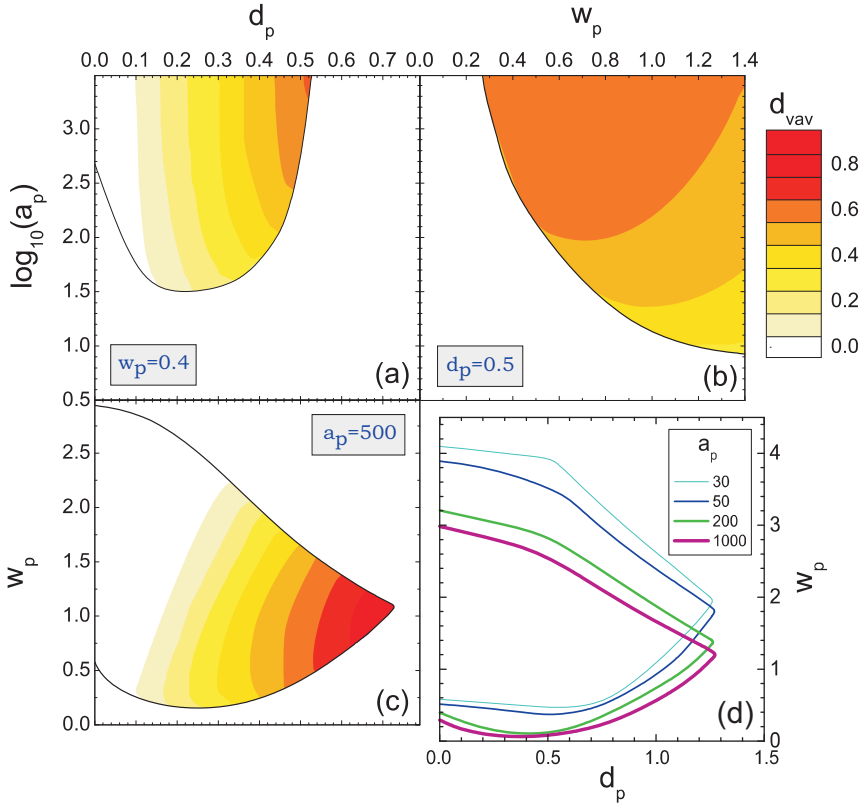


Figure 5.4: Influence of the optical parameters of the laser beams on the stability of the special vortex molecules found for $N_p = 4$. (a-c) V-Av stability and spacing in a two-parameter space, thus for either fixed amplitude, separation, or focused width of the beams ($g' = 40$, $\omega = 1.25$). (d) The stability region of the doubly quantized vortex in the center of a $L = 6$ state, for different values of a_p ($g' = 40$, $\omega = 1.6$).

While the existence of stable multiquantum vortices was already predicted in several theoretical papers for condensates in a confinement potential with a quartic component [197–200], our giant vortices are solely a consequence of the symmetry induced by the pinning centers, as can be deduced from Fig. 5.4(d) for the $L = 6 = 4 + 2$ state: The giant vortex state is not stable when w_p is too small. By doing two separate simulations of a condensate in conventional parabolic confinement - thus without quartic component - exposed to 4 pinning beams, we were able to confirm this statement: We found a giant vortex in both the ground states for $L = 2$ (with $g = 20$, $\omega = 0.85$, $d_p = 0.8$, $w_p = 0.6$, $a_p = 50$) and $L = 6 = 4 + 2$ ($g = 40$, $\omega = 0.85$, $d_p = 1.3$, $w_p = 1.6$, $a_p = 200$). This general behavior holds for arbitrary number of pinning beams. In other words, vortex molecules comprising

multi-quantum vortices are stable in our system, contrary to conventional behavior of BEC. Moreover, we report here a unique way of engineering locally the phase imprint of the condensate, by either changing angular velocity, or the non-linearity (e.g. by condensing more constituent atoms). The limits of this procedure are: (i) the deconfinement of the condensate at large ω , and (ii) the maximal g' at which vortex-vortex interaction overwhelms the optical pinning, resulting in a vortex structure that does not fully obey the imposed geometry (white areas in Fig. 5.3).

5.3 Stability and control of special vortex states

Obviously, the exact parameters of the strategically placed laser beams are very deterministic for the resulting vortex structure in the condensate. Here we briefly discuss the influence of beam intensity, distance between adjacent beams, and their focussed waist on V-Av and multi-quantum states. Our results are summoned in Fig. 5.4. Figs. (a)-(c) relate to V-Av molecules in fourfold pinning, and help visualize their stability and size in a two-parameter space. As a general conclusion, we find that a larger amplitude of the pinning (a_p , see inset of Fig. 5.1) is always beneficial to the V-Av state. Simply, stronger imposed pinning reflects better its symmetry on the vortex state. For the same reason, strong overlap between pinning profiles of the beams should be avoided (i.e. $w_p \lesssim 3d_p$ is desirable). As shown in Fig. 5.4, the distance between the central antivortex and pinning vortices can be increased by increasing the spacing between the beams (d_p); this is nevertheless a limited option, as vortices may not follow the imposed pinning at large distances from the center of the condensate. For considered parameters, we realized maximal V-Av distance of approximately $0.9r_0$, which is of the order of $10\mu\text{m}$ for the sodium condensate, and thus feasible for experimental observation. The used beam width of $w_p = 0.2 - 1.5r_0$ and sub- r_0 distances for beam ordering are also very realistic values for the available experimental techniques.

Fig. 5.4(d) shows the stability region of a doubly quantized vortex in a fourfold geometry of the $L = 6$ state ($4 \times 1 + 2$). Similarly to the V-Av case, imposed symmetry of the pinning is essential for the nucleation of the double vortex. Relatively weaker pinning by wider laser beams can significantly enhance the stability of the multi-quantum vortex, while the clarity of its separation from the surrounding vortices is best achieved for high beam amplitudes and narrow beam waists. However, the needed d_p is quite low, as confinement between the pinning beams must remain firm for the stabilization of the multi-quantum vortex. Such small spacing is unfavorable for experimental observation, but can be significantly improved in the case of larger N_p and larger vorticity. This analysis and the complete investigation of *all* stable vortex states in this phenomenologically rich system will be presented

elsewhere.

5.4 Conclusions

In summary, using a novel concept of polygonal optical pinning, we demonstrated yet unpredicted vortex states in rotating atomic Bose-Einstein condensates. We realized a stable antivortex for positive angular momentum, as well as a multi-quantum vortex, which up to now was assumed to be unstable in BEC. Both are found as the ground state for a wide range of parameters. New ground-state transitions found by increasing angular velocity of the condensate, by changes in the optical pinning setup, or by changing the number of constituent atoms, open up ways to further studies employing quantum phase engineering [181] and submicron coherence and matter-wave interference effects [201].

The results presented in this chapter were published as:

- R. Geurts, M. V. Milošević and F. M. Peeters, *Topologically trapped vortex molecules in Bose-Einstein condensates*, Phys. Rev. A **78**, 053610 (2008)

Summary

In this thesis, I have investigated vortex-antivortex states in three different mesoscopic quantum systems: single-gap superconductors, two-gap superconductors, and Bose-Einstein condensates. These states are remarkable in the sense that in usual conditions, vortices and antivortices can never coexist. Indeed, opposites attract, and when vortex and antivortex meet they annihilate, a situation similar to the behavior of particles and antiparticles described by high energy physics.

These opposites, the *vortices* and *anti-vortices* are the subject of this thesis. They are just tiny whirlpools, consisting of particles rotating around a common axis. The only distinction between the two is that the *direction* of the rotation is *opposite*. However, they are not just simple whirlpools: they arise as a consequence of the laws of quantum mechanics, a fact which is manifested by the quantization of the amount of rotation they can carry.

While vortex-antivortex pairs can be induced in a quantum system using various techniques, it seems that their immediate annihilation can only be prevented by some effective energy input. This could be e.g. an inhomogeneous magnetic field, as generated by a magnet, or by the (anti-)vortices getting pinned by inhomogeneities. Intuitively, this is the only condition in which a vortex and an antivortex can coexist. Nevertheless, the equations describing the physics of quantum systems such as superconductors, superfluids and Bose-Einstein condensates, offer another possibility to stabilize this, as we often call it, vortex-antivortex molecule: *symmetry*. Indeed, in *mesoscopic* quantum systems (systems with a size comparable to density variations therein), the boundaries of the system, or the confinement imposed by them, play a crucial role. That this could lead to the appearance of vortex-antivortex states in superconductors was first realized in 2000. One of our contributions was to generalize this concept to Bose-Einstein condensates as well. Eleven years later, still no experimental confirmation of symmetry-induced vortex-antivortex states has been reported. Should we therefore abandon this general prediction of quantum mechanics and go with the intuitive idea that indeed vortex and antivortex can not coexist without energy input, or, should we believe the prescription of quantum mechanics and conclude that we just have not observed

it yet, probably due to the high requirements concerning sample fabrication and detector resolution.

For both superconductors and for Bose-Einstein condensates, we have shown to be able to weaken the severe requirements of a perfectly symmetric boundary / confinement potential, by introducing the idea of symmetrically placed pinning centers, which take the dominant role in imposing the symmetry on the system, rather than the confinement. Additionally the technique turns out to provide more tolerance to sample imperfections, and enables a larger size of the vortex-antivortex molecule, facilitating experimental observation.

In **Chapter 1**, a brief history and overview of superconductivity, Bose-Einstein condensation and the theories describing them is given. Furthermore the numerical techniques, employed for the results of this thesis were presented.

Chapter 2 dealt with symmetry-induced vortex-antivortex states in mesoscopic single-gap superconductors. A proposal to design the superconducting sample is given but without taking away the conceptual novelty of the nucleation of the vortex-antivortex pair in a *homogeneous* magnetic field, as opposed to the idea of placing e.g. a magnetic dot on top of the sample. We pursued the idea of introducing holes which will act as pinning centers, and in doing so, pull the vortices away from the anti-vortex and additionally provide improved immunity against sample imperfections and defects. First we elaborated on the size and position of these holes. We determined optimal parameters for the square and triangle geometry. For instance, in a square geometry, we managed to enlarge the separation between vortex and antivortex with a factor 8 compared to the case without holes. We then investigated the influence of several kinds of geometric defects on the vortex-antivortex (V-Av) state. For all the imperfections we studied, we found that the holes cause a substantial increase of the stability of the V-Av configuration with respect to sample imperfections as compared to the case of a sample without holes.

The geometry-induced antivortices are known to be a consequence of the symmetry of the sample. Therefore, we focused on the competition of different sources of symmetry in a mesoscopic superconductor. We concluded that the pinning centers are by far the most efficient in imposing their symmetry, while the shape of the outer boundary of the sample has a less important role. Thinking further along this line, we studied circular disks, perforated by a number of symmetrically placed holes, and found giant-antivortices up to a vorticity of -7.

Further, the effect of the non-linearity of the first GL equation and the magnetic screening represented by the second GL equation was critically examined, allowing us to investigate the influence of temperature and non-zero thickness of the sample on the V-Av state. We constructed phase diagrams for different values of the GL

parameter κ for the perforated and the plain square system showing the stability region of the V-Av state in the $\phi - T$ parameter space. We found that the introduction of holes decreases the temperature range in which the vortex-antivortex state is stable, and analyzed the dependence of this effect on the Ginzburg-Landau parameter κ . The asymmetric vortex-antivortex state, which is found on the transition from multivortex to vortex-antivortex is found to be stable only in a very narrow temperature range ($\sim 10^{-3}T_c$). We also showed that a small value of κ disfavors the vortex-antivortex state in all investigated geometries (square, perforated square, perforated triangle). We mainly concentrated our discussion on square samples but we believe that our main conclusions hold for any geometry.

Finally, using a square superconducting geometry with five holes, we found a second generation of the $L = 3$ vortex-antivortex (V-Av) state in a uniform field. This state is purely induced by pinning, and is NOT caused by the symmetry of the sample, contrary to the previously found V-Av molecules. This novel state is energetically favored in rather large mesoscopic samples, but it is never the ground state of the system. Consequently, more elaborate techniques are needed for its stabilization in experiment, such as an abrupt increase of field (from negative to positive value), or an abrupt cooling of the symmetry-induced V-Av state. However, the very large $\Phi - T$ stability range of the second generation V-Av state, the very comprehensive size of the V-Av molecule, and the large variation in amplitudes of both superconducting order parameter and stray magnetic field inside the molecule (further enhanced for lower κ and temperature), should all lead to facilitated experimental observation of this fascinating state.

In **Chapter 3**, a theoretical Ginzburg-Landau study of the superconducting state of two-band mesoscopic disks is presented, as a preparation on the investigation of V-Av states therein, since the two-band GL theory is still in an immature status. Both the influence of Josephson and of magnetic coupling between the superconducting bands are discussed. In cases when screening of the magnetic field can be neglected, we found the dependence of the size of the vortex core on the strength of the Josephson coupling and showed that it generally has an influence opposite to the one of temperature. In limiting cases, our numerical findings agree well with analytic expressions available in literature. We also found a fitting function, which gives an excellent estimate of the size of the vortex core as a function of the size of the mesoscopic disk. In our further analysis of the vortex states, we focused mainly on exotic, non-composite states, where two condensates comprise different number of vortices and the apparent total vorticity of the sample is fractional. We reported asymmetric vortex states following from competing interactions in the two-band mesoscopic system, and showed how some states can be manipulated by e.g. coupling between the bands. We indicated how such states can be experimentally observed. Fractional states can even be found in the ground state, but

typically far from the S/N boundary. We gave the expression for the upper critical field of a two-band mesoscopic disk as a function of temperature, which is similar to analytic estimations for bulk, however scaled to its value at zero temperature for zero coupling between the condensates.

With magnetic screening and coupling between the bands included in the simulations, we characterized the response of the sample through the competition of the GL parameters of the two-bands (with special attention to the case when one band is type-II and the other is type-I). However, we showed that these criteria are insufficient, and that Josephson coupling and the ratio of the coherence lengths in the two bands also play an important role. Although we did not find evidence for type-1.5 superconductivity in clean MgB₂ disks, we did find its manifestation for a different choice of relevant parameters. The magnetization vs. applied field shows a distinct jump at the field where type-I condensate ceases, and the overall shape of the curve can surely be characterized as type-I.x like. This is also evident in the found vortex states in the latter case, which are a combination of single vortices and lamellar domains.

In **Chapter 4**, we demonstrated that the V-Av state can be stabilized in mesoscopic two-gap superconductors in a far larger portion of the field-temperature phase diagram than is the case for single-gap samples. To realize this enhancement, the best conditions are provided by a low density of states in the band with higher intrinsic T_c and comparable but lower Fermi velocity (and coherence length) as compared to the second band. V-Av states in two-band samples are richer than their single-band counterparts, and appear in integral and fractional form, either of which can show re-entrant behavior as a function of temperature. The re-entrant integral V-Av state should be observable through e.g. the symmetry of the magnetic field profile obtained by Scanning Hall Probe Microscopy. The re-entrant V-Av state in the second band can be verified experimentally by only imaging of that band. The splitting of the stability regions of the V-Av state in two bands can also be realized by control of the local density of states, which might be attainable through local carrier injection.

We discussed the validity of the two-gap GL formalism and justified our use of it as a phenomenological theory able to describe *at least* qualitatively important phenomena occurring in two-gap superconductors. As a final remark we pointed the attention to the formal equivalence of the two-gap GL formalism to a Lawrence-Doniach GL model describing a bilayer system, consisting of two superconducting layers, separated by an insulating layer, sufficiently thin to allow for Josephson coupling of the two layers. This extends the relevance of the presented calculations to bilayers of two single-band superconducting films.

In **Chapter 5**, we presented our investigations on rotating Bose-Einstein conden-

sates. As the superconductors studied in previous chapters, Bose-Einstein condensates are mesoscopic quantum systems and feature vortices as well. Moreover, the Gross-Pitaevskii equation, which describes the behavior of Bose-Einstein condensates, is similar to the Ginzburg-Landau equations. Motivated by these parallels, we translated the idea of symmetrically positioned pinning centers to Bose-Einstein condensates. Co-rotating laser beams, capable of locally depleting the condensate, now take the role of the pinning centers.

Using this novel concept of polygonal optical pinning, we demonstrated yet unpredicted vortex states in rotating atomic Bose-Einstein condensates. We realized a stable vortex-antivortex state for positive angular momentum, as well as a multi-quantum vortex, which up to now was assumed to be unstable in BEC. Both are found as the ground state for a wide range of parameters. New ground-state transitions found by increasing angular velocity of the condensate, by changes in the optical pinning setup, or by changing the number of constituent atoms, open up ways to further studies employing quantum phase engineering and submicron coherence and matter-wave interference effects.

Outlook

The study of vortex physics has gone a long way in the past two decades, but still has a long way to go. The mechanism to pin vortices in bulk superconductors has led to the dramatic increase of the critical current, and has made the application of superconductors in high-field magnets possible. However concerning vortex applications on the small scale, rapid single flux quantum logic is still in its infancy. When these superconducting devices ever are going to be used for commercial applications they will have to be able to compete with the existing semiconductor technology. They will thus have to be scaled down, and mesoscopic and geometrical effects will play a major role. A clear understanding of geometry induced vortex phenomena may thus be of vital importance. How to model these phenomena effectively, what are the limitations of the Ginzburg-Landau theory, which corrections should be applied, and which unknown effects still have to be taken into consideration? In order to answer these questions, theory and experiment will have to go hand in hand to make progress.

With the discovery of multiband superconductivity in MgB_2 and the Fe-pnictides over the last decade this field has experienced a massive resurgence of interest. The vortex physics in these materials is very rich due to an intricate interplay of several competitions (inter- and intraband vortex repulsion and attraction, boundary effects). Detailed description of the intermediate state of type-1.5 materials is still lacking. For that matter, the intermediate state of type-I multiband materials, especially weakly coupled ones, is completely unexplored. For example, OsB_2 shows all the characteristics of a type-I superconductor and, according to the penetration depth measurements, it is definitely a two-band material. However, more sophisticated experimental methods will be needed to conclusively distinguish between type-I and type-II superconductivity. Moreover, a lot of interesting physics can be found on the border between type-I and type-II materials. Many researchers suggest the existence of type-1.5 superconductivity or a semi-Meissner state. While the theorists can argue indefinitely as to whether or not such a state is possible, it is up to experimentalists to resolve the issue and provide reliable experimental data that would help to resolve the dispute. Other theoretical questions in the

multiband arena involve e.g. the consequences of other types of coupling, for instance the gradient coupling, present in dirty multiband samples (considering that most experimental samples are dirty). In the Fe-based superconductors many experiments are consistent with an extended s -wave (s_{\pm}) order parameter, and the influence of this symmetry on the vortex matter is still not explored. Furthermore, in ARPES measurements on these materials, up to four separate gaps show up [202] and theoretical investigations are increasingly focussing on superconductivity in systems of three or more bands. It is now well understood that this is a very fertile area for new physics due to the intrinsic frustration that additional bands introduce into the problem. For example, all choices of the sign of order parameters for a system of three bands with an odd number of repulsive interactions result in suppression of superconductivity in at least one band. For systems of four or five bands the situation is more complex, but is again generally frustrated if more than one interaction is repulsive. Therefore, such systems are bound to produce exciting vortex physics, and will also require theoretical investigation in the future.

Samenvatting

In deze thesis heb ik vortex-antivortextoestanden onderzocht in drie verschillende mesoscopische kwantumsystemen: één-band supergeleiders, twee-band supergeleiders en Bose-Einstein condensaten. Deze toestanden zijn bijzonder omdat in normale omstandigheden vortices en antivortices nooit samen kunnen bestaan. Inderdaad, tegengestelden trekken elkaar aan, en wanneer vortex en antivortex elkaar ontmoeten annihilieren ze, gelijkaardig aan het gedrag van deeltjes en antideeltjes in de hoge-energie fysica.

Deze tegengestelden, de *vortices* en *antivortices* zijn het onderwerp van deze thesis. Beide zijn minuscule draaikolkjes, bestaande uit deeltjes die ronddraaien rondom een gemeenschappelijke as. Het enige verschil is dat de *richting* van de draaiing *tegengesteld* is. Vortices zijn echter geen ordinaire draaikolken: zij ontstaan als gevolg van de wetten van de kwantummechanica, wat zich manifesteert via de kwantisatie van de hoeveelheid draaiimpuls die ze kunnen dragen.

Hoewel vortex-antivortexparen geïnduceerd kunnen worden in een systeem op verschillende manieren, lijkt hun onmiddellijke annihilatie slechts voorkomen te kunnen worden in de aanwezigheid van een effectieve energie-input. Dit kan bijvoorbeeld een inhomogeen magneetveld zijn, of door het verankeren of 'pinnen' van de (anti-)vortices aan inhomogeniteiten. Intuïtief lijkt dit de enige voorwaarde waarop een vortex en antivortex samen kunnen bestaan. Desalniettemin voorzien de vergelijkingen die de fysica van kwantumsystemen - zoals supergeleiders en Bose-Einstein condensaten - beschrijven een andere mogelijkheid om deze vortex-antivortex *molecule*, zoals we het vaak noemen, te stabiliseren: *symmetrie*. Inderdaad, in *mesoscopische* kwantumsystemen (systemen met een grootte vergelijkbaar met de lengteschaal van de deeltjesdichtheidsvariëaties erin) spelen de randen van het systeem, of de opsluiting die ze opleggen, een cruciale rol. Dat dit kan leiden tot het verschijnen van vortex-antivortextoestanden in supergeleiders werd voor het eerst gerealiseerd in 2000. Eén van onze verdiensten was om dit concept te veralgemenen naar Bose-Einstein condensaten.

Elf jaar later is het bestaan van de symmetrie-geïnduceerde vortex-antivortextoestanden nog steeds niet experimenteel bevestigd. Moeten we daarom deze algemene

voorspelling van de kwantummechanica laten varen en ons op het intuïtieve idee beroepen dat vortex en antivortex inderdaad niet samen kunnen bestaan zonder effectieve energie-input, of, moeten we het voorschrift van de kwantummechanica toch geloven en concluderen dat we de vortex-antivortextoestand simpelweg nog niet geobserveerd hebben, waarschijnlijk te wijten aan de hoge vereisten gesteld aan de samplefabricatie en detectorresolutie?

Eën van de verdiensten van ons onderzoek is dat we, zowel voor supergeleiders als voor Bose-Einstein condensaten, hebben aangetoond dat de hoge vereisten inzake een perfect symmetrische samplerand of opsluitingspotentialaal sterk verzwakt kunnen worden, dankzij het idee om symmetrisch geplaatste pinningcentra toe te voegen die, eerder dan de samplerand, de dominante rol gaan spelen in het oplossen van de symmetrie. Daarbovenop demonstreerden we dat deze techniek een heel grote tolerantie ten aanzien van sample-imperfecties tot gevolg heeft, en dat ze de vortex-antivortexmoleculen vele malen vergroot, allebei factoren die de experimentele observatie sterk ten goede komen.

In **Hoofdstuk 1** werd een beknopte geschiedenis en een overzicht van supergeleiding, Bose-Einstein condensaten en de respectievelijke theorieën gegeven. Ook werden de numerieke methodes, gebruikt om de resultaten van deze thesis te bekomen, voorgesteld.

Hoofdstuk 2 behandelt symmetrie-geïnduceerde vortex-antivortextoestanden in mesoscopische één-band supergeleiders. We doen een voorstel om het supergeleidende sample te ontwerpen, zonder te raken aan het concept van vortex-antivortexnucleatie in een *homogeen* magneetveld, in tegenstelling tot het idee van de plaatsing van een magnetische stip bovenop het sample. We streefden het idee na symmetrisch gepositioneerde gaten in het sample aan te brengen die als pinning centra optreden, en op die manier de vortices wegtrekken van de centraal gelegen antivortex. Daarbovenop voorzien de holtes een versterkte immuniteit tegen sampleimperfecties en -defecten. Eerst hebben we de invloed van de positie en de grootte van deze gaten uitgewerkt. We bepaalden de optimale parameters voor zowel de vierkante als driehoekige geometrie. Voor de vierkante geometrie slaagden we erin de afstand tussen vortex en antivortex met een factor 8 te vergroten ten opzichte van het geval zonder gaten.

Vervolgens onderzochten we de invloed van verschillende soorten geometrische defecten op de vortex-antivortex toestand. Voor alle beschouwde imperfecties vonden we dat de introductie van gaten een aanzienlijke toename van de stabiliteit van de vortex-antivortextoestand ten opzichte van sampleimperfecties veroorzaakt.

Van de door geometrie geïnduceerde antivortices is geweten dat ze een gevolg zijn van de symmetrie van het sample. Daarom hebben we ons toegespitst op de competitie van verschillende bronnen van symmetrie in een mesoscopische supergeleider. We kwamen tot de conclusie dat de pinningcentra veruit het efficiëntst zijn

in het opleggen van de symmetrie vergeleken met de buitenrand van het sample. Verder denkende in deze lijn bestudeerden we cirkelvormige schijven geperforeerd door een aantal symmetrisch gepositioneerde gaten en vonden giant-antivortices met een vorticeit tot -7.

Verder werd het effect van de niet-lineariteit van de eerste Ginzburg-Landau (GL) vergelijking en de magnetische afscherming, beschreven door de tweede GL vergelijking, grondig onderzocht, wat toeliet de invloed van de temperatuur en de eindige dikte van het sample op de vortex-antivortex toestand te beschouwen. We construeerden phasediagrammen voor verschillende waarden van de GL parameters κ voor het geperforeerde en het gewone vierkante systeem, en toonden de stabiliteitsgebieden van de vortex-antivortex toestand in de flux-temperatuur parameter ruimte. We vonden dat de introductie van gaten het temperatuursinterval waarbinnen de vortex-antivortex toestand stabiel is, verkleint, en analyseerden de afhankelijkheid van dit effect op κ . De asymmetrische vortex-antivortex toestand, die gevonden wordt op de overgang van de multivortex naar vortex-antivortex toestand, wordt stabiel bevonden slechts in een extreem nauw temperatuursbereik ($\sim 10^{-3}T_c$). We toonden ook dat een kleine waarde van κ de vortex-antivortex toestand benadeelt in alle onderzochte geometriën (vierkant, geperforeerd vierkant, geperforeerde driehoek). We hebben onze discussie voornamelijk beperkt tot vierkante samples, maar we geloven dat onze hoofdconclusies blijven gelden voor eender welke geometrie.

Tenslotte vonden we in een vierkante geometrie met vijf gaten een tweede generatie van de $L = 3$ vortex-antivortex toestand in een uniform veld. Deze toestand is enkel en alleen geïnduceerd door pinning, en is *niet* veroorzaakt door de symmetrie van het sample, in tegenstelling tot de hierboven besproken vortex-antivortex moleculen. Deze nieuwe toestand wordt energetisch voordelig in eerder grote mesoscopische samples, maar is nooit de grondtoestand van het systeem. Bijgevolg zijn ingewikkeldere technieken nodig voor de stabilisatie ervan in het experiment, zoals een abrupte afkoeling van de symmetrie-geïnduceerde vortex-antivortex toestand. Het erg grote flux-temperatuur stabiliteitsgebied van de tweede-generatie vortex-antivortex toestand, de erg grote vortex-antivortex molecule, en de grote variaties van de amplitudes van zowel de supergeleidende ordeparameter en het magnetische veld binnenin de molecule (verder versterkt door lage κ en temperatuur), zouden allen moeten leiden tot een vergemakkelijkt experimentele observatie van deze fascinerende toestand.

In **Hoofdstuk 3** werd een theoretische Ginzburg-Landau studie gepresenteerd van de supergeleidende toestand in twee-band mesoscopische schijven als voorbereiding op het onderzoek van de vortex-antivortices daarin, omdat de twee-band GL theorie nog in een onvolwassen stadium verkeert. Zowel de invloed van de Josephson koppeling als de magnetische koppeling worden behandeld. In gevallen waarin de afscherming van het magneetveld verwaarloosd kan worden, vonden we de afhanke-

lijkheid van de grootte van de vortexkern van de sterkte van de Josephson koppeling en toonden dat die in het algemeen een effect had tegengesteld aan dat van de temperatuur. In limietgevallen komen onze numerieke resultaten goed overeen met analytische uitdrukkingen beschikbaar in de literatuur. We vonden ook een pasfunctie die een voortreffelijke schatting van de grootte van de vortexkern geeft in functie van de grootte van de mesoscopische schijf. In onze verdere analyse van de vortextoestanden legden we de nadruk vooral op exotische, niet-samengestelde vortextoestanden, waar twee condensaten een verschillend aantal vortices bevatten en de schijnbare vorticeiteit van het sample fractioneel is. We brengen verslag uit van asymmetrische vortextoestanden als gevolg van de competitie tussen de verschillende interacties in twee-band systemen, en toonden hoe sommige toestanden gemanipuleerd kunnen worden door bijvoorbeeld de koppeling tussen de banden. We geven aan hoe dergelijke toestanden experimenteel geobserveerd kunnen worden. Fractionele toestanden kunnen zelfs gevonden worden in de grondtoestand, maar typisch ver van de supergeleiding/normaal-grens. We geven de uitdrukking voor het hoogste kritische veld van een twee-band mesoscopische schijf als een functie van de temperatuur, gelijkaardig aan de analytische schattingen voor bulk, maar geschaald naar de waarde bij temperatuur nul en in de afwezigheid van koppeling tussen de condensaten.

Wanneer magnetische afscherming en interbandkoppeling mee in rekening worden gebracht in de simulaties, karakteriseerden we de respons van het sample via de competitie van de GL parameters κ_1 en κ_2 van de twee banden (met extra aandacht aan het geval waarbij één band type-II is en de andere type-I). We toonden echter dat deze criteria ontoereikend zijn, en dat Josephson koppeling en de verhouding van de intrinsieke coherentielengtes in de twee banden een belangrijke rol spelen. Hoewel we geen bewijs vonden voor type-1.5 supergeleiding in zuivere MgB₂ schijven, vonden we de manifestatie ervan voor een andere keuze van de relevante parameters. De magnetisatie-versus-magneetveld curves tonen een onderscheiden sprong bij het veld waar type-I supergeleiding wordt vernietigd, en de gehele vorm van de curve kan zeker gekarakteriseerd worden als type-1.x-achtig. Dit blijkt ook in de vortextoestanden in het laatste geval, die een combinatie zijn van enkelvoudige vortices en lamellaire domeinen.

In **Hoofdstuk 4** demonstreerden we dat de vortex-antivortextoestand in mesoscopische twee-band supergeleiders gestabiliseerd kan worden in een veel groter deel van het flux-temperatuur fasediagram dan het geval is bij een-band supergeleiders. De beste condities om deze verbetering te realiseren zijn een lagere toestandsdichtheid in de band met de hoogste intrinsieke kritische temperatuur en een vergelijkbare maar lagere Fermisnelheid (en coherentielengte) vergeleken met de andere band. Vortex-antivortextoestanden in twee-band samples hebben een rijkere fenomenologie dan hun een-band tegenhangers, en verschijnen zowel in gehele als fractionele vorm, en vertonen herintredend gedrag in functie van de temperatuur.

De herintredende gehele vortex-antivortex toestand zou waarneembaar moeten zijn via bijvoorbeeld de symmetrie van het profiel van het magneetveld verkregen door Scanning Hole Probe microscopie. De herintredende vortex-antivortex toestand in de tweede band kan experimenteel geverifieerd worden door enkel die band te meten. Het opsplitsen van de stabiliteitsgebieden van de vortex-antivortextoestand in de twee banden kan ook gerealiseerd worden via het beheersen van de lokale toestandsdichtheid, wat mogelijk kan zijn via lokale dragersinjectie.

We bespraken de geldigheid van het twee-band GL-formalisme en rechtvaardigden het gebruik ervan als een fenomenologische theorie die in staat is om op zijn minst kwalitatief de belangrijke fenomenen die zich voordoen in twee-band supergeleiders te beschrijven. Als laatste opmerking richtten we onze aandacht naar de formele equivalentie tussen het twee-band GL-formalisme en een Lawrence-Doniach GL-model dat een dubbellaagsysteem, gescheiden door een isolerende laag, voldoende dun om Josephson koppeling toe te laten, beschrijft. Dit breidt de relevantie van de voorgestelde berekeningen uit tot dubbellagen van twee één-band supergeleidende films.

In **Hoofdstuk 5** stelden we ons onderzoek naar roterende Bose-Einstein condensaten voor. Net zoals de supergeleiders bestudeerd in de voorgaande hoofdstukken, zijn Bose-Einstein condensaten mesoscopische kwantumsystemen, en vertonen zij vortices. Bovendien is de Gross-Pitaevskii vergelijking, die het gedrag van Bose-Einstein condensaten beschrijft, gelijkaardig aan de eerste Ginzburg-Landau vergelijking. Gemotiveerd door deze parallellen, extrapoleerden we het idee om symmetrisch gepositioneerde pinningcentra toe te voegen naar Bose-Einstein condensaten. Meedraaiende laserstralen, in staat om het condensaat plaatselijk te vernietigen, nemen nu de rol aan van de pinningcentra. Gebruikmakende van dit nieuwe concept van polygonale optische pinning, toonden we het bestaan aan van eerder niet voorspelde vortextoestanden in roterende Bose-Einstein condensaten. We realiseerden een stabiele vortex-antivortextoestand voor een positieve waarde van de draaiïmpuls, maar ook een meervoudig gekwantiseerde vortex, die tot nu toe verondersteld werd onstabiel te zijn in Bose-Einstein condensaten. Beide toestanden werden gevonden in de grondtoestand voor een ruim bereik van de parameters. Nieuwe grondtoestandovergangen, gevonden door het toename van de draaisnelheid van het condensaat, door veranderingen in de opstelling van de optische pinning, of door het aanpassen van het aantal atomen in het condensaat, maken de weg vrij voor verdere studies die gebruik maken van kwantumfaseontwerp en submicron- coherentie en materie-golf interferentie-effecten.

Curriculum vitae



Roeland GEURTS

Born on May 4th, 1983
in Duffel / Belgium

Contact information

Departement Fysica
Universiteit Antwerpen (Campus Groenenborger)
Groenenborgerlaan 171
B-2020 Antwerpen, Belgium.

Tel: +32 (0)3 265 35 39
e-mail: roeland.geurts@ua.ac.be

Education

- 2001-2005: Master in Science, Physics at Universiteit Antwerpen, Antwerpen (Belgium)
- 2005-2011: Teaching Assistant and PhD in Science, Physics at Universiteit Antwerpen, Antwerpen (Belgium)

Teaching experience

- 2005-2011: ‘Biostatistics’ to the students of pharmaceutical, biomedical, biochemical and veterinary sciences.

Research interests and technical expertise

- Ginzburg-Landau theory, 2D and 3D mesoscopic superconductors, influence of the geometry on vortex configurations, antivortices.
- Finite difference and finite element methods to solve (non-)linear differential equations
- Programming in Fortran, MATLAB, COMSOL, Basic, C++/C, Java

List of publications

1. R. Geurts, M. V. Milošević and F. M. Peeters, *Symmetric and Asymmetric Vortex-Antivortex Molecules in a Fourfold Superconducting Geometry*, Phys. Rev. Lett. **97**, 137002 (2006)
2. R. Geurts, M. V. Milošević and F. M. Peeters, *Stabilization of vortex-antivortex configurations in mesoscopic superconductors by engineered pinning*, Phys. Rev. B **75**, 184511 (2007)
3. R. Geurts, M. V. Milošević and F. M. Peeters, *Topologically trapped vortex molecules in Bose-Einstein condensates*, Phys. Rev. A **78**, 053610 (2008)
4. R. Geurts, M. V. Milošević and F. M. Peeters, *Second generation of vortex-antivortex states in mesoscopic superconductors: Stabilization by artificial pinning*, Phys. Rev. B **79**, 174508 (2009)
5. R. Geurts, M. V. Milošević and F. M. Peeters, *Vortex matter in mesoscopic two-gap superconducting disks: Influence of Josephson and magnetic coupling*, Phys. Rev. B **81**, 214514 (2010)
6. M. V. Milošević and R. Geurts, *The Ginzburg-Landau theory in application*, Phys. C, **470**, 791 (2010)

Bibliography

- [1] H. Kamerlingh Onnes, Koninklijke Nederlandse Akademie van Wetenschappen Proceedings Series B Physical Sciences **14**, 818 (1911).
- [2] R. de Bruyn Ouboter, Scientific American **276**, 98 (1997).
- [3] J. File and R. G. Mills, Phys. Rev. Lett. **10**, 93 (1963).
- [4] W. Meissner and R. Ochsenfeld, Naturwissenschaften **21**, 787 (1933).
- [5] F. London and H. London, Proceedings of the Royal Society of London. Series A - Mathematical and Physical Sciences **149**, 71 (1935).
- [6] V. L. Ginzburg and L. D. Landau, Zh. Eksp. Teor. Fiz. **20**, 1064 (1950).
- [7] F. London, *Superfluids* (John Wiley & Sons, Inc., New York, 1950), p. 152.
- [8] B. S. Deaver and W. M. Fairbank, Phys. Rev. Lett. **7**, 43 (1961).
- [9] R. Doll and M. Näbauer, Phys. Rev. Lett. **7**, 51 (1961).
- [10] A. A. Abrikosov, Sov. Phys. JETP **5**, 1174 (1957).
- [11] J. Bardeen, L. N. Cooper, and J. R. Schrieffer, Phys. Rev. **108**, 1175 (1957).
- [12] B. D. Josephson, Physics Letters **1**, 251 (1962).
- [13] Department of Energy, Progress in development of superconducting materials, <http://en.wikipedia.org/wiki/Superconductivity> (2011).
- [14] J. G. Bednorz and K. A. Müller, Zeitschrift für Physik B Condensed Matter **64**, 189 (1986).
- [15] M. K. Wu, J. R. Ashburn, C. J. Torng, P. H. Hor, R. L. Meng, L. Gao, Z. J. Huang, Y. Q. Wang, and C. W. Chu, Phys. Rev. Lett. **58**, 908 (1987).
- [16] M. A. Subramanian, C. C. Torardi, J. C. Calabrese, J. Gopalakrishnan, K. J. Morrissey, T. R. Askew, R. B. Flippen, U. Chowdhry, and A. W. Sleight, Science **239**, 1015 (1988).
- [17] H. Takahashi, K. Igawa, K. Arii, Y. Kamihara, M. Hirano, and H. Hosono, Nature (London) **453**, 376 (2008).
- [18] U. Essmann and H. Trauble, Physics Letters A **24**, 526 (1967).
- [19] A. B. Pippard, Proceedings of the Royal Society of London. Series A. Mathematical and Physical Sciences **216**, 547 (1953).
- [20] Tilley & Tilley, *Superfluidity and superconductivity* (Institute of Physics Pub,

- Bristol Philadelphia, Pa, 1994).
- [21] H. F. Hess, R. B. Robinson, R. C. Dynes, J. M. Valles, and J. V. Waszczak, *Phys. Rev. Lett.* **62**, 214 (1989).
 - [22] H. Fröhlich, *Advances in Physics* **3**, 325 (1954).
 - [23] A. M. Clogston, *Phys. Rev. Lett.* **9**, 266 (1962).
 - [24] L. Gor'kov, *Sov. Phys. JETP* **36**, 1364 (1959).
 - [25] G. Berdiyrov, *Vortex Structure and Critical Parameters in Superconducting Thin Films with Arrays of Pinning Centers*, PhD thesis, Universiteit Antwerpen, 2007.
 - [26] M. Zehetmayer, M. Eisterer, J. Jun, S. M. Kazakov, J. Karpinski, A. Wisniewski, and H. W. Weber, *Phys. Rev. B* **66**, 052505 (2002).
 - [27] D. N. Zheng, A. M. Campbell, J. D. Johnson, J. R. Cooper, F. J. Blunt, A. Porch, and P. A. Freeman, *Phys. Rev. B* **49**, 1417 (1994).
 - [28] E. Brandt and M. Das, *J. Superconduct. and Novel Magn.* **24**, 57 (2011).
 - [29] A. Shepelev, *Superconductor* (InTech, 2010), chap. The Discovery of Type II Superconductors (Shubnikov Phase).
 - [30] J. E. Kunzler, E. Buehler, F. S. L. Hsu, and J. H. Wernick, *Phys. Rev. Lett.* **6**, 89 (1961).
 - [31] K. Dulon, Iter newslines (2010), <http://www.iter.org/newsline/140/340>.
 - [32] F. London, *Phys. Rev.* **74**, 562 (1948).
 - [33] D. Einzel, *Journal of Low Temperature Physics* **163**, 215 (2011).
 - [34] C. E. Gough, M. S. Colclough, E. M. Forgan, R. G. Jordan, M. Keene, C. M. Muirhead, A. I. M. Rae, N. Thomas, J. S. Abell, and S. Sutton, *Nature (London)* **326**, 855 (1987).
 - [35] P. D. Gennes, *Superconductivity of metals and alloys* (Advanced Book Program, Perseus Books, Reading, Mass, 1999).
 - [36] J. Pearl, *Applied Physics Letters* **5**, 65 (1964).
 - [37] L. Kramer, *Phys. Rev. B* **3**, 3821 (1971).
 - [38] E. H. Brandt, *Phys. Rev. B* **34**, 6514 (1986).
 - [39] A. Chaves, F. M. Peeters, G. A. Farias, and M. V. Milošević, *Phys. Rev. B* **83**, 054516 (2011).
 - [40] F. Mohamed, M. Troyer, G. Blatter, and I. Luk'yanchuk, *Phys. Rev. B* **65**, 224504 (2002).
 - [41] V. Moshchalkov, M. Menghini, T. Nishio, Q. H. Chen, A. V. Silhanek, V. H. Dao, L. F. Chibotaru, N. D. Zhigadlo, and J. Karpinski, *Phys. Rev. Lett.* **102**, 117001 (2009).
 - [42] C. P. Bean and J. D. Livingston, *Phys. Rev. Lett.* **12**, 14 (1964).
 - [43] I. V. Grigorieva, W. Escoffier, J. Richardson, L. Y. Vinnikov, S. Dubonos, and V. Oboznov, *Phys. Rev. Lett.* **96**, 077005 (2006).

- [44] H. J. Zhao, V. R. Misko, F. M. Peeters, V. Oboznov, S. V. Dubonos, and I. V. Grigorieva, *Phys. Rev. B* **78**, 104517 (2008).
- [45] A. Kanda, B. J. Baelus, F. M. Peeters, K. Kadowaki, and Y. Ootuka, *Phys. Rev. Lett.* **93**, 257002 (2004).
- [46] H. J. Fink and A. G. Presson, *Phys. Rev.* **151**, 219 (1966).
- [47] L. F. Chibotaru, A. Ceulemans, V. Bruyndoncx, and V. V. Moshchalkov, *Nature (London)* **408**, 833 (2000).
- [48] M. Tinkham, *Introduction to superconductivity* (Dover Publications, Mineola, N.Y, 2004).
- [49] W. A. Little and R. D. Parks, *Phys. Rev. Lett.* **9**, 9 (1962).
- [50] R. Benoist and W. Zwerger, *Zeitschrift für Physik B Condensed Matter* **103**, 377 (1997).
- [51] H. Suhl, B. T. Matthias, and L. R. Walker, *Phys. Rev. Lett.* **3**, 552 (1959).
- [52] L. Y. L. Shen, N. M. Senozan, and N. E. Phillips, *Phys. Rev. Lett.* **14**, 1025 (1965).
- [53] J. W. Hafstrom and M. L. A. MacVicar, *Phys. Rev. B* **2**, 4511 (1970).
- [54] G. W. Crabtree, D. H. Dye, D. P. Karim, S. A. Campbell, and J. B. Ketterson, *Phys. Rev. B* **35**, 1728 (1987).
- [55] D. P. Almond, M. J. Lea, and E. R. Dobbs, *Phys. Rev. Lett.* **29**, 764 (1972).
- [56] J. Nagamatsu, N. Nakagawa, T. Muranaka, Y. Zenitani, and J. Akimitsu, *Nature (London)* **410**, 63 (2001).
- [57] Y. Wang, T. Plackowski, and A. Junod, *Phys. C* **355**, 179 (2001).
- [58] W. Pickett, *Nature (London)* **418**, 733 (2002).
- [59] W. L. McMillan, *Phys. Rev.* **167**, 331 (1968).
- [60] E. G. Maksimov, *Proceedings of the P. N. Lebedev Institute* **86**, 105 (1977).
- [61] S. L. Bud'ko, G. Lapertot, C. Petrovic, C. E. Cunningham, N. Anderson, and P. C. Canfield, *Phys. Rev. Lett.* **86**, 1877 (2001).
- [62] T. Yokoya, T. Kiss, A. Chainani, S. Shin, M. Nohara, and H. Takagi, *Science* **294**, 2518 (2001).
- [63] V. Guritanu, W. Goldacker, F. Bouquet, Y. Wang, R. Lortz, G. Goll, and A. Junod, *Phys. Rev. B* **70**, 184526 (2004).
- [64] Y. Nakajima, T. Nakagawa, T. Tamegai, and H. Harima, *Phys. Rev. Lett.* **100**, 157001 (2008).
- [65] A. Wälte, G. Fuchs, K.-H. Müller, A. Handstein, K. Nenkov, V. N. Narozhnyi, S.-L. Drechsler, S. Shulga, L. Schultz, and H. Rosner, *Phys. Rev. B* **70**, 174503 (2004).
- [66] G. Seyfarth, J. P. Brison, M.-A. Méasson, J. Flouquet, K. Izawa, Y. Matsuda, H. Sugawara, and H. Sato, *Phys. Rev. Lett.* **95**, 107004 (2005).
- [67] G. Seyfarth, J. P. Brison, M.-A. Méasson, D. Braithwaite, G. Lapertot, and

- J. Flouquet, *Phys. Rev. Lett.* **97**, 236403 (2006).
- [68] Y. Kasahara, T. Iwasawa, H. Shishido, T. Shibauchi, K. Behnia, Y. Haga, T. D. Matsuda, Y. Onuki, M. Sigrist, and Y. Matsuda, *Phys. Rev. Lett.* **99**, 116402 (2007).
- [69] F. Hunte, J. Jaroszynski, A. Gurevich, D. C. Larbalestier, R. Jin, A. S. Sefat, M. A. McGuire, B. C. Sales, D. K. Christen, and D. Mandrus, *Nature (London)* **453**, 903 (2008).
- [70] D. R. Tilley, *Proceedings of the Physical Society* **84**, 573 (1964).
- [71] M. E. Zhitomirsky and V.-H. Dao, *Phys. Rev. B* **69**, 054508 (2004).
- [72] A. Gurevich, *Phys. Rev. B* **67**, 184515 (2003).
- [73] A. Gurevich, *Physica C* **456**, 160 (2007).
- [74] L. F. Chibotaru, V. H. Dao, and A. Ceulemans, *Europhys. Lett.* **78**, 47001 (2007).
- [75] V. G. Kogan and J. Schmalian, *Phys. Rev. B* **83**, 054515 (2011).
- [76] E. Babaev and M. Speight, *Phys. Rev. B* **72**, 180502 (2005).
- [77] S. J. Bending, *Adv. Phys.* **48**, 449 (1999).
- [78] G. Binnig and H. Rohrer, *IBM J. Res. Dev.* **30**, 355 (1986).
- [79] L. Y. Vinnikov, J. Karpinski, S. M. Kazakov, J. Jun, J. Anderegg, S. L. Bud'ko, and P. C. Canfield, *Phys. Rev. B* **67**, 092512 (2003).
- [80] H. F. Hess, R. B. Robinson, R. C. Dynes, J. M. Valles, and J. V. Waszczak, *Phys. Rev. Lett.* **62**, 214 (1989).
- [81] J. R. Kirtley, C. C. Tsuei, M. Rupp, J. Z. Sun, L. S. Yu-Jahnes, A. Gupta, M. B. Ketchen, K. A. Moler, and M. Bhushan, *Phys. Rev. Lett.* **76**, 1336 (1996).
- [82] P. E. Goa, H. Hauglin, M. Baziljevich, E. Il'yashenko, P. L. Gammel, and T. H. Johansen, *Superconduct. Sc. Tech.* **14**, 729 (2001).
- [83] A. Tonomura, H. Kasai, O. Kamimura, T. Matsuda, K. Harada, J. Shimoyama, K. Kishio, and K. Kitazawa, *Nature (London)* **397**, 308 (1999).
- [84] S. L. Adler and T. Piran, *Rev. Mod. Phys.* **56**, 1 (1984).
- [85] Q. Du, *Mathematics of Computation* **67**, pp. 965 (1998).
- [86] N. Schlömer, D. Avitabile, and W. Vanroose, arXiv:1102.1212 (2011).
- [87] R. Kato, Y. Enomoto, and S. Maekawa, *Phys. Rev. B* **47**, 8016 (1993).
- [88] R. Prozorov, E. B. Sonin, E. Sheriff, A. Shaulov, and Y. Yeshurun, *Phys. Rev. B* **57**, 13845 (1998).
- [89] Bose, *Zeitschrift für Physik* **26**, 178 (1924).
- [90] A. Einstein, *Sitzungsberichte der Preußischen Akademie der Wissenschaften, Physikalisch-mathematische Klasse* **1924**, 261 (1924).
- [91] W. Ketterle, *Rev. Mod. Phys.* **74**, 1131 (2002).
- [92] M. H. Anderson, J. R. Ensher, M. R. Matthews, C. E. Wieman, and E. A.

- Cornell, Science **269**, 198 (1995).
- [93] K. B. Davis, M. O. Mewes, M. R. Andrews, N. J. van Druten, D. S. Durfee, D. M. Kurn, and W. Ketterle, Phys. Rev. Lett. **75**, 3969 (1995).
- [94] M. R. Andrews, C. G. Townsend, H.-J. Miesner, D. S. Durfee, D. M. Kurn, and W. Ketterle, Sciencekh **275**, 637 (1997).
- [95] J. R. Abo-Shaeer, C. Raman, J. M. Vogels, and W. Ketterle, Science **292**, 476 (2001).
- [96] E. Gross, Il Nuovo Cimento (1955-1965) **20**, 454 (1961).
- [97] L. P. Pitaevskii, Sov. Phys. JETP **13** (1961).
- [98] W. Bao, D. Jaksch, and P. A. Markowich, J. Comp. Phys. **187**, 318 (2003).
- [99] A. Klein, D. Jaksch, Y. Zhang, and W. Bao, Phys. Rev. A **76**, 043602 (2007).
- [100] S. Bargi, J. Christensson, H. Saarikoski, A. Harju, G. Kavoulakis, M. Manninen, and S. Reimann, Physica E **42**, 411 (2010).
- [101] V. L. Berezinsky, Sov. Phys. JETP **32**, 493 (1971).
- [102] J. M. Kosterlitz and D. J. Thouless, J. Phys. C **6**, 1181 (1973).
- [103] M. R. Beasley, J. E. Mooij, and T. P. Orlando, Phys. Rev. Lett. **42**, 1165 (1979).
- [104] A. M. Kadin, M. Leung, and A. D. Smith, Phys. Rev. Lett. **65**, 3193 (1990).
- [105] K. Epstein, A. M. Goldman, and A. M. Kadin, Phys. Rev. Lett. **47**, 534 (1981).
- [106] M. V. Milošević, G. R. Berdiyrov, and F. M. Peeters, Phys. Rev. Lett. **95**, 147004 (2005).
- [107] M. J. Van Bael, J. Bekaert, K. Temst, L. Van Look, V. V. Moshchalkov, Y. Bruynseraede, G. D. Howells, A. N. Grigorenko, S. J. Bending, and G. Borghs, Phys. Rev. Lett. **86**, 155 (2001).
- [108] M. Lange, M. J. V. Bael, Y. Bruynseraede, and V. V. Moshchalkov, Phys. Rev. Lett. **90**, 197006 (2003).
- [109] M. Lange, M. J. Van Bael, A. V. Silhanek, and V. V. Moshchalkov, Phys. Rev. B **72**, 052507 (2005).
- [110] M. V. Milošević and F. M. Peeters, Phys. Rev. Lett. **93**, 267006 (2004).
- [111] M. V. Milošević and F. M. Peeters, Phys. Rev. Lett. **94**, 227001 (2005).
- [112] L. F. Chibotaru, A. Ceulemans, V. Bruyndoncx, and V. V. Moshchalkov, Phys. Rev. Lett. **86**, 1323 (2001).
- [113] L. F. Chibotaru, G. Teniers, A. Ceulemans, and V. V. Moshchalkov, Phys. Rev. B **70**, 094505 (2004).
- [114] A. S. Mel'nikov, I. M. Nefedov, D. A. Ryzhov, I. A. Shereshevskii, V. M. Vinokur, and P. P. Vysheslavtsev, Phys. Rev. B **65**, 140503 (2002).
- [115] J. Bonča and V. V. Kabanov, Phys. Rev. B **65**, 012509 (2001).
- [116] B. J. Baelus and F. M. Peeters, Phys. Rev. B **65**, 104515 (2002).

- [117] T. Mertelj and V. V. Kabanov, *Phys. Rev. B* **67**, 134527 (2003).
- [118] R. Geurts, M. V. Milošević, and F. M. Peeters, *Phys. Rev. Lett.* **97**, 137002 (2006).
- [119] L. F. Chibotaru, A. Ceulemans, G. Teniers, and V. V. Moshchalkov, *Phys. C* **369**, 149 (2002).
- [120] A. K. Geim, S. V. Dubonos, I. V. Grigorieva, K. S. Novoselov, F. M. Peeters, and V. A. Schweigert, *Nature (London)* **407**, 55 (2000).
- [121] F. M. Peeters, V. A. Schweigert, and B. J. Baelus, *Physica C: Superconductivity* **369**, 158 (2002).
- [122] B. J. Baelus, K. Kadowaki, and F. M. Peeters, *Phys. Rev. B* **71**, 024514 (2005).
- [123] V. A. Schweigert and F. M. Peeters, *Phys. Rev. B* **57**, 13817 (1998).
- [124] P. S. Deo, V. A. Schweigert, F. M. Peeters, and A. K. Geim, *Phys. Rev. Lett.* **79**, 4653 (1997).
- [125] V. R. Misko, V. M. Fomin, J. T. Devreese, and V. V. Moshchalkov, *Phys. Rev. Lett.* **90**, 147003 (2003).
- [126] V. M. Bedanov and F. M. Peeters, *Phys. Rev. B* **49**, 2667 (1994).
- [127] E. H. Brandt, *J. Low Temp. Phys.* **53**, 41 (1983).
- [128] G. A. Farias and F. M. Peeters, *Solid State Communications* **100**, 711 (1996).
- [129] P. T. Jochym and K. Parlinski, *Phys. Rev. B* **65**, 024106 (2001).
- [130] N. A. B. *et al.*, Formation of two-dimensional colloidal sphere arrays on micro-patterns, in *FNANO Proceedings*, Snowbird, USA, 2005.
- [131] C. Carballeira, V. V. Moshchalkov, L. F. Chibotaru, and A. Ceulemans, *Phys. Rev. Lett.* **95**, 237003 (2005).
- [132] M. V. M. V. V. Khotkevych and S. J. Bending, *Rev. Sci. Instrum.* **79**, 123708 (2008).
- [133] M. V. Milošević, G. R. Berdiyrov, and F. M. Peeters, *Appl. Phys. Lett.* **91**, 212501 (2007).
- [134] G. R. Berdiyrov, B. J. Baelus, M. V. Milošević, and F. M. Peeters, *Phys. Rev. B* **68**, 174521 (2003).
- [135] R. Geurts, M. V. Milošević, and F. M. Peeters, *Phys. Rev. B* **75**, 184511 (2007).
- [136] J. Jurisson and R. J. Oakes, *Phys. Lett.* **2**, 187 (1962).
- [137] E. Coskun, *Appl. Math. Comp.* **106**, 31 (1999).
- [138] M. R. Connolly, M. V. Milošević, S. J. Bending, and T. Tamegai, *Phys. Rev. B* **78**, 132501 (2008).
- [139] L. Lyard, P. Samuely, P. Szabo, T. Klein, C. Marcenat, L. Paulius, K. H. P. Kim, C. U. Jung, H.-S. Lee, B. Kang, S. Choi, S.-I. Lee, J. Marcus, S. Blanchard, A. G. M. Jansen, U. Welp, G. Karapetrov, and W. K. Kwok, *Phys.*

- Rev. B **66**, 180502 (2002).
- [140] C. Buzea and T. Yamashita, *Supercond. Sc. Tech.* **14**, R115 (2001).
- [141] X. X. Xi, *Rep. Prog. Phys.* **71**, 116501 (2008).
- [142] M. R. Eskildsen, M. Kugler, S. Tanaka, J. Jun, S. M. Kazakov, J. Karpinski, and O. Fischer, *Phys. Rev. Lett.* **89**, 187003 (2002).
- [143] M. Iavarone, G. Karapetrov, A. E. Koshelev, W. K. Kwok, G. W. Crabtree, D. G. Hinks, W. N. Kang, E.-M. Choi, H. J. Kim, H.-J. Kim, and S. I. Lee, *Phys. Rev. Lett.* **89**, 187002 (2002).
- [144] V. H. Dao and M. E. Zhitomirsky, *Eur. Phys. J. B* **44**, 183 (2005).
- [145] I. N. Askerzade, *Physica C: Superconductivity* **390**, 281 (2003).
- [146] I. N. Askerzade, A. Gencer, and N. G. clü, *Superconductor Science and Technology* **15**, L13 (2002).
- [147] T. Nishio, V. H. Dao, Q. Chen, L. F. Chibotaru, K. Kadowaki, and V. V. Moshchalkov, *Phys. Rev. B* **81**, 020506 (2010).
- [148] J.-P. Wang, *Phys. Lett. A* **374**, 58 (2009).
- [149] E. Babaev, *Phys. Rev. Lett.* **89**, 067001 (2002).
- [150] E. Babaev, *Phys. Rev. Lett.* **94**, 137001 (2005).
- [151] E. Babaev, *Nuclear Physics B* **686**, 397 (2004).
- [152] Y. Tanaka, *Phys. Rev. Lett.* **88**, 017002 (2001).
- [153] Y. Tanaka, *J. Phys. Soc. Japan* **70**, 2844 (2001).
- [154] E. Babaev, J. Jäykkä, and M. Speight, *Phys. Rev. Lett.* **103**, 237002 (2009).
- [155] L. F. Chibotaru and V. H. Dao, *Phys. Rev. B* **81**, 020502 (2010).
- [156] M. Eisterer, *Supercond. Sc. Tech.* **20**, R47 (2007).
- [157] V. V. Moshchalkov, L. Gielen, C. Strunk, R. Jonckheere, X. Qiu, C. V. Haesendonck, and Y. Bruynseraede, *Nature (London)* **373**, 319 (1995).
- [158] G. R. Berdiyrov, A. D. Hernandez, and F. M. Peeters, *Phys. Rev. Lett.* **103**, 267002 (2009).
- [159] R. Geurts, M. V. Milošević, and F. M. Peeters, *Phys. Rev. B* **81**, 214514 (2010).
- [160] M. Milošević and R. Geurts, *Physica C: Superconductivity* **470**, 791 (2010), Vortex Matter in Nanostructured Superconductors.
- [161] C. Bersier, A. Floris, A. Sanna, G. Profeta, A. Continenza, E. K. U. Gross, and S. Massidda, *Phys. Rev. B* **79**, 104503 (2009).
- [162] A. A. Golubov, J. Kortus, O. V. Dolgov, O. Jepsen, Y. Kong, O. K. Andersen, B. J. Gibson, K. Ahn, and R. K. Kremer, *Journal of Physics: Condensed Matter* **14**, 1353 (2002).
- [163] H. Bluhm, N. C. Koshnick, M. E. Huber, and K. A. Moler, *Phys. Rev. Lett.* **97**, 237002 (2006).
- [164] E. Babaev and M. Silaev, arXiv:1105.3756 (2011).

- [165] V. G. Kogan and J. Schmalian, arXiv:1105.5090 (2011).
- [166] A. A. Shanenko, M. V. Milošević, F. M. Peeters, and A. V. Vagov, Phys. Rev. Lett. **106**, 047005 (2011).
- [167] L. Komendová, M. V. Milošević, A. A. Shanenko, and F. M. Peeters, Phys. Rev. B **84**, 064522 (2011).
- [168] M. Silaev and E. Babaev, Phys. Rev. B **84**, 094515 (2011).
- [169] G. Blumberg, A. Mialitsin, B. S. Dennis, M. V. Klein, N. D. Zhigadlo, and J. Karpinski, Phys. Rev. Lett. **99**, 227002 (2007).
- [170] A. J. Leggett, Prog. Theor. Phys. **36**, 901 (1966).
- [171] W. Lawrence and S. Doniach, Proceedings of the twelfth international conference on low temperature physics, in *Proceedings of the Twelfth International Conference on Low Temperature Physics*, edited by E. Kanda, p. 361, Academic Press of Japan, Kyoto, 1971.
- [172] A. Oral, S. J. Bending, and M. Henini, Appl. Phys. Lett. **69**, 1324 (1996).
- [173] Y. Koval, X. Jin, C. Bergmann, Y. Simsek, L. Özyüzer, P. Müller, H. Wang, G. Behr, and B. Büchner, **96**, 082507 (2010).
- [174] E. M. Lifshitz and L. P. Pitaevskii, *Statistical Physics* Vol. 2 (Pergamon, Oxford, 1980).
- [175] G. Baym and C. J. Pethick, Phys. Rev. Lett. **76**, 6 (1996).
- [176] M. R. Matthews, B. P. Anderson, P. C. Haljan, D. S. Hall, C. E. Wieman, and E. A. Cornell, Phys. Rev. Lett. **83**, 2498 (1999).
- [177] M. W. Zwierlein, J. R. Abo-Shaeer, A. Schirotzek, C. H. Schunck, and W. Ketterle, Nature (London) **435**, 1047 (2005).
- [178] F. Dalfovo, S. Giorgini, L. P. Pitaevskii, and S. Stringari, Rev. Mod. Phys. **71**, 463 (1999).
- [179] S. Tung, V. Schweikhard, and E. A. Cornell, Phys. Rev. Lett. **97**, 240402 (2006).
- [180] K. Kasamatsu and M. Tsubota, Phys. Rev. Lett. **97**, 240404 (2006).
- [181] J. Denschlag, J. E. Simsarian, D. L. Feder, C. W. Clark, L. A. Collins, J. Cubizolles, L. Deng, E. W. Hagley, K. Helmerson, W. P. Reinhardt, S. L. Rolston, B. I. Schneider, and W. D. Phillips, Science **287**, 97 (2000).
- [182] D. A. Butts and D. S. Rokhsar, Nature (London) **397**, 327 (1999).
- [183] A. E. Leanhardt, A. Görlitz, A. P. Chikkatur, D. Kielpinski, Y. Shin, D. E. Pritchard, and W. Ketterle, Phys. Rev. Lett. **89**, 190403 (2002).
- [184] Y. V. Kartashov, A. Ferrando, A. A. Egorov, and L. Torner, Phys. Rev. Lett. **95**, 123902 (2005).
- [185] V. M. Pérez-García, M. A. García-March, and A. Ferrando, Phys. Rev. A **75**, 033618 (2007).
- [186] M.-A. García-March, A. Ferrando, M. Zacarés, J. Vijande, and L. Carr, Phys.

- D **238**, 1432 (2009).
- [187] V. Bretin, S. Stock, Y. Seurin, and J. Dalibard, *Phys. Rev. Lett.* **92**, 050403 (2004).
- [188] C. Raman, J. R. Abo-Shaeer, J. M. Vogels, K. Xu, and W. Ketterle, *Phys. Rev. Lett.* **87**, 210402 (2001).
- [189] Q. Zhou and H. Zhai, *Phys. Rev. A* **70**, 043619 (2004).
- [190] L.-C. Crasovan, G. Molina-Terriza, J. P. Torres, L. Torner, V. M. Pérez-García, and D. Mihalache, *Phys. Rev. E* **66**, 036612 (2002).
- [191] L.-C. Crasovan, V. Vekslerchik, V. M. Pérez-García, J. P. Torres, D. Mihalache, and L. Torner, *Phys. Rev. A* **68**, 063609 (2003).
- [192] W. Li, M. Haque, and S. Komineas, *Phys. Rev. A* **77**, 053610 (2008).
- [193] M. Möttönen, S. M. M. Virtanen, T. Isoshima, and M. M. Salomaa, *Phys. Rev. A* **71**, 033626 (2005).
- [194] V. Pietilä, M. Möttönen, T. Isoshima, J. A. M. Huhtamäki, and S. M. M. Virtanen, *Phys. Rev. A* **74**, 023603 (2006).
- [195] G. Ruben, D. M. Paganin, and M. J. Morgan, *Phys. Rev. A* **78**, 013631 (2008).
- [196] M. Liu, L. H. Wen, H. W. Xiong, and M. S. Zhan, *Phys. Rev. A* **73**, 063620 (2006).
- [197] A. Aftalion and I. Danaila, *Phys. Rev. A* **69**, 033608 (2004).
- [198] I. Danaila, *Phys. Rev. A* **72**, 013605 (2005).
- [199] A. L. Fetter, B. Jackson, and S. Stringari, *Phys. Rev. A* **71**, 013605 (2005).
- [200] K. Kasamatsu and M. Tsubota, *Phys. Rev. Lett.* **97**, 240404 (2006).
- [201] P. Berman, *Atom interferometry* (Academic Press, 1997).
- [202] K. Nakayama, T. Sato, P. Richard, Y.-M. Xu, Y. Sekiba, S. Souma, G. F. Chen, J. L. Luo, N. L. Wang, H. Ding, and T. Takahashi, *Europhys. Lett.* **85**, 67002 (2009).

